Impact of bicycle tire parameters on the total rolling losses

Master thesis

K.H. Dijkman

Impact of bicycle tire parameters on the total rolling losses

Master thesis

by

K.H. Dijkman

Student number: 4832957
Project duration: February 20, 2023 – January 4, 2024
Supervisors: Dr. A. Dressel, TU Delft, daily supervisor
Dr. J.K. Moore, TU Delft, Assistant Professor
Ir. H. Ubbens, Team DSM, Aerodynamics Expert
P. Rooijakkers, Team DSM, R&D Expert

TU Delft

Abstract

The cycling industry is influenced by the approval of the tire pressure control system in competitive cycling. This system allows real-time adjustments to the tire-road interaction during races. The total rolling losses is the resistance resulting from tire-road interaction, incorporating resistance due to tire deformation and the dissipation of vibrational energy within the rider-bicycle system. This research investigates the influence of tire parameters on the total rolling losses during road cycling through three key measurements: ink print test, drum test, and rolling losses measurement. The ink print test captures the contact area between the tire and road surface under specified loads, revealing significant impacts of tire type, width, inflation pressure and vertical load on the contact patch shape. In addition, this study shows that an increase in contact patch measures is related to an increase in the rolling resistance coefficient (C_{rr}). The drum test extracts C_{rr} values related to pure rolling resistance by measuring the power needed to maintain constant velocity of a rotating drum when in contact with a loaded tire. Results indicate a significant influence of tire type, width, inflation pressure, vertical load and velocity on C_{rr} estimates. Combining C_{rr} obtain with drum testing with C_{rr} determined with total rolling losses measurements, provides insights into the contribution of vibrational losses to the total rolling losses. The study employs a novel bike trailer measurement technique to estimate total rolling losses, measuring the cyclist's power while cycling at constant speed with elimination of aerodynamic drag. Despite some limitations, the bike trailer method successfully identifies optimal tire parameters for minimizing rolling losses on different road surfaces at varying speeds.

K.H. Dijkman
Delft, January 2024

Contents

1

Introduction

The cycling industry is influenced by emerging technologies [1]. At the beginning of April 2022, the UCI has approved the use of the Scope Atmoz – Tire pressure control system (Scope Cycling, Eindhoven, The Netherlands) in competitive cycling. This system allows riders to control the tire pressure while cycling by inflating and deflating the tire with a button on the handlebars [2, 3]. Throughout the development of the Scope Atmoz, team DSM has provided their knowledge and experience regarding the system's application during racing [2]. Their vision is to redefine the sport through cooperation and innovation by pushing the boundaries of science and technology [4]. Participation in the development of new technologies, such as the Scope Atmoz, could contribute to the improvement of cycling performance. A tool that can be used to assess the impact of new technologies on the performance is performance modelling.

In competitive cycling, performance modelling is a useful tool for athletes, coaches and researchers to estimate the required power for road racing under different cycling conditions [1]. Models of cycling performance are based on physiological, environmental and equipment related parameters, which help to predict how changes in racing conditions affect the cycling performance [1, 5]. During cycling, the cyclist generates power to move forward, however, external factors create a resistance against this forward motion (see Fig.1.1). The power balance equation provides a mathematical model of the power produced by the cyclist ($P_{produced}$) and the sum of the power related to the resistances experienced during cycling ($P_{resistance}$) (see Eq. 1.1).

$$\frac{dE_{kin}}{dt} = P_{produced} - P_{resistance} \tag{1.1}$$

A difference between the produced power and the resistive power results in a change in kinetic energy (dE_{kin}/dt), which leads to an increase or decrease in cycling velocity. As the goal of competitive cycling is to finish in the least amount of time, it is desired to maintain a high and sustainable cycling velocity during the race. Assessment of the power provided by the cyclist and the factors influencing the resistive power, allows for effective strategy modifications during racing and training, which help to achieve this goal [1]. Team DSM implements this approach by developing race strategies for each athlete and each race based on performance modeling. During this process, factors associated with the resistances are modeled based on fundamental engineering and physical principles [1, 5].

The main driving resistances are aerodynamic drag, gravitational resistance, inertial resistance and the rolling losses [7, 8, 9]. These result from wind velocity, the slope of the road, acceleration and the interaction between the bicycle tire and the road surface, respectively [7]. Generally, aerodynamic drag is the major resistance with a contribution of 56-90% during steady-state cycling, while the rolling losses and gravitational losses both account for 10-20% of the total resistance [10, 11]. The presence of the peloton during road races can reduce aerodynamic drag by 40% compared to time-trial races [1, 11]. If the magnitude of the other resistances do not change, then this will result in a reduction in aerodynamic contribution to the total resistance with 17.4%, increasing the relative importance of other resistances [11]. In addition, rough road surfaces could increase the contribution of the total rolling losses up to 69% [9]. The presence of road irregularities results in the creation of vibrations at the tires and the transmission of these vibration to the rider [6, 12].

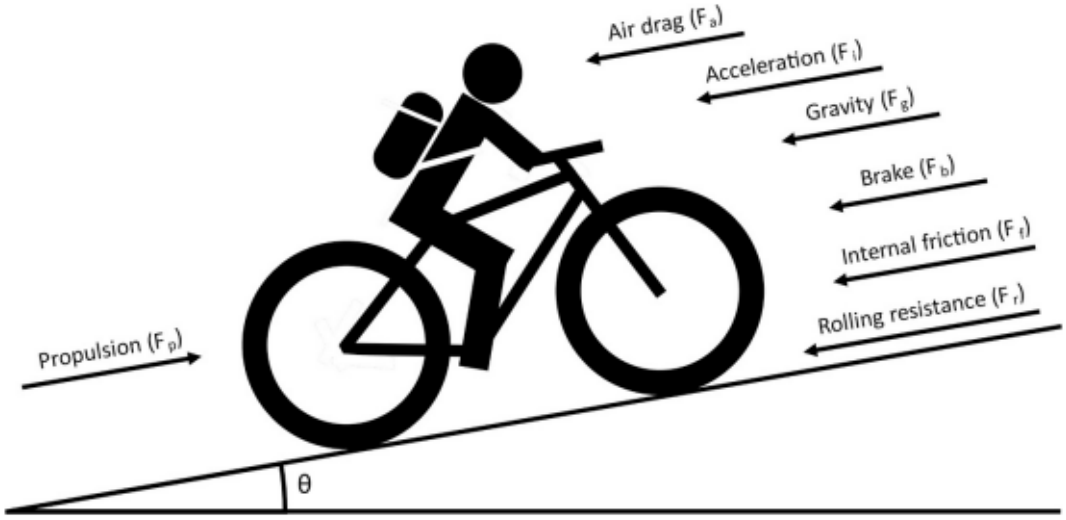

Figure 1.1: Schematic representation of the forces acting on the bike-rider system (figure taken from ([6])

The introduction of the Scope Atmoz and its utilization in competitive cycling will influence the interaction between the tire and the road surface by allowing adjustment of the inflation pressure during the race. This will affect the total rolling losses experienced during cycling. The total rolling losses is used to describe the combination of rolling resistance and rolling impedance. The rolling resistance mainly results from hysteresis losses due to tire deformations, which could be minimized by increasing the tire stiffness [6, 13]. The rolling impedance results from the transmission of vibrations from the road to the rider. The vibrational energy is dissipated within the bicycle frame, suspension system or cyclist [14]. In road cycling, most of the impedance losses result from the absorption of energy within the cyclist's body, as road race bicycles have minimal suspension features [15]. In contrast to rolling resistance, an increase in tire stiffness results in an increase of the impedance losses. The tire will be unable to deform around road irregularities, which results in more vibrations being transmitted to the cyclist [16, 17, 18].

This creates a trade-off between achieving low rolling resistance and low rolling impedance. The development of the Scope Atmoz has pointed out the need to find the inflation pressures that minimizes the total rolling losses while maintaining enough grip, cornering control and puncture protection [9, 19]. The value of the optimal pressure, referred to as the break-point pressure, depends on the road surface type and other tire parameters, such as tire width, construction and temperature [9, 20, 21]. The tire parameters influence the deformations, while the road surface type affects the generation of vibrations.

The inflation pressure affects the tire elasticity and the vertical load determines the amount of deflection [21]. Together they determine the total contact area (A) between the tire and the road (=contact patch), which can be approximated by dividing the vertical load ($F_N = mg$) by the inflation pressure (p) (see Eq. 1.2) [22]. The shape of the contact patch is influenced by the tire width, which is the longest lateral distance from sidewall to sidewall [23]. The contact patch shape can be approximated by an ellipse [22]. The ellipse will be more rounded (shorter and wider) for wide tires compared to narrow tires with the same inflation pressure and vertical load. It has been stated that this shorter contact patch will reduce the rolling resistance [17, 23], which means that contact patch shape and size influences the total rolling losses.

$$A = \frac{F_N}{p} \tag{1.2}$$

Previous research has already focused on the effect of different tire parameters on the rolling resistance, however, rolling impedance is often disregarded. However, it is essential to evaluate the impact of various parameters on both rolling resistance and rolling impedance. As it has been stated that consideration of rolling resistance in isolation from the vehicle itself leads to errors in estimation of the total energy losses [24]. Choices in tire parameters cannot rely on the assessment of one driving resistance in isolation, but each resistance should be assessed as part of the decision-making process

[8]. This results in the following research question:

How do the tire parameters influence the total rolling losses?

To provide an answer to this question, the following sub-questions will be used:

- How do changes in tire parameters influence the shape of the contact patch?
- What measurement technique can be used to assess the total rolling losses?
- What are the optimal tire pressures for different sets of parameters?
- How does the road roughness influence the optimal pressures?
- What is the individual contribution of rolling resistance and rolling impedance?

In order to address the research question and sub-questions, three types of measurements are conducted. The first assesses the influence of tire parameters on the contact patch shape. The second determines pure rolling resistance under various conditions. The third evaluates the total rolling losses. Combining the results of the total rolling losses and pure rolling resistance provides insights into the contribution of rolling impedance. These three measurements collectively help determine the optimal tire pressure for different parameter sets and various road surfaces.

This thesis is organized into distinct chapters to systematically explore and present the research findings. Chapter 2 provides information on the mechanisms associated with energy losses, with a specific focus on rolling resistance and rolling impedance. In addition, insights regarding the influence of tire parameters, road surface type and cycling velocity are derived from previous studies. This serves to provide a foundation regarding the context and scope of the current study. Chapter 3 serves to answer the sub-question of how to measure the total rolling losses. This is done be analyzing the existing measurement techniques and developing new methods based on specified requirements. Chapter 4 and 5, respectively, discuss the methods and results regarding the three types of measurements: contact patch, rolling resistance and total rolling losses. The research findings are presented in chapter 6, which serve to answer the research questions.

2

Literature review

This thesis focuses the assessment of the total rolling losses, which is one of the main resistive force experienced during cycling. This chapter provides background information on the total rolling losses and the mechanisms resulting in the loss of energy. In addition, some of the tire parameters and environmental factors associated with tire-road interaction are discussed. These could be used as a tool to minimize the total rolling losses and, consequently, reduce the total resistance experienced during cycling. The information presented in this discussion is derived from previous studies, dissertation, thesis reports and insights from bicycle (tire) manufactures. This provides a foundation for understanding and evaluating the experiments discussed in chapter 4 and 5.

2.1. The total rolling losses

The energy losses caused by the rolling interaction between the bicycle tire and the road surface can be described as total rolling losses. The total rolling losses incorporates both rolling resistance and rolling impedance [16, 20]. Section 2.1.1 and 2.1.2 will both focus on the underlying mechanisms that result in the loss of energy.

2.1.1. Rolling resistance

Rolling resistance can be defined as a resistive force, resistive moment, power drain or energy drain. In general, it is described as the resistance to relative motion between two bodies in rolling contact parallel to the plane of contact between them [22]. Energy is lost due to the deformation of the tire during the rolling motion and the deformation of the surface it is rolling on [6, 13, 22]. These deformations are responsible for the two main mechanisms behind rolling resistance: hysteresis losses and frictional losses [12, 24].

The amount of rolling resistance depends on the quality of the tire, which can be described by the rolling resistance coefficient (C_{rr}) [25]. This is a dimensionless number that represents the ratio between the rolling resistance force (F_r) and the wheel load (F_N) (see Eq. 2.1) [6, 7]. The use of a dimensionless number makes it easy to compare the effect of different tire parameters on the rolling resistance, due to assessing the amount of rolling resistance independent of the mass of the bike and the rider [25].

$$C_{rr} = \frac{F_r}{F_N} \tag{2.1}$$

Hysteresis losses

Around 90% of the energy loss due to rolling resistance results from tire hysteresis, which is caused by deformation of pneumatic tires in and around the contact patch [24]. In case a rigid wheel is in contact with a flat surface, the contact between the two is limited to a single point. However, pneumatic tires deform due to the load of the rider and the bike, which results in a contact area between the tire and the road surface. This area is defined as the contact patch [26].

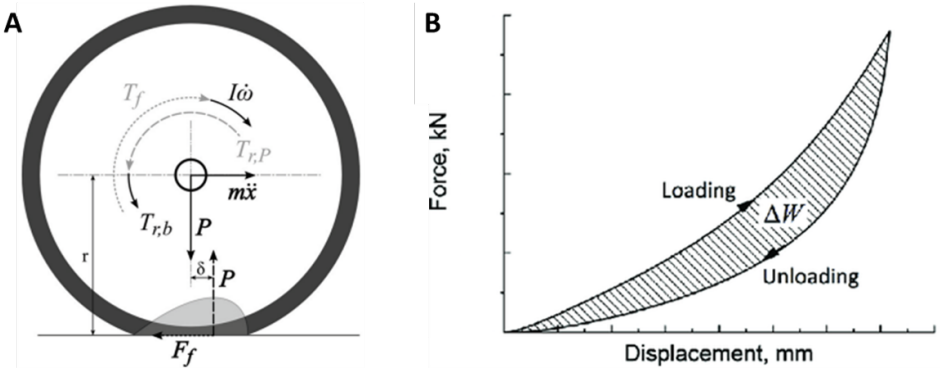

Figure 2.1: Explanation of resistive moment A) Ground reaction force on the tire when the wheel rolls across a flat surface (figure taken from [27]) B) Typical hysteresis loops, which shows the reaction force under loading and unloading of the tire (figure taken from [28])

The contact patch between the tire and the road results in a force distribution in reaction to the load put onto the wheel. In stationary position, this force distribution is symmetrical. However, when the tire is rotating, the contact pressure becomes asymmetric due to the tire getting deformed upon contact with the road surface and recovering to its initial shape as it leaves the contact patch (see Fig. 2.1A) [12, 27]. This results in the resultant vertical reaction force of the ground to the wheel ending up in front of the wheel, which creates a resistive moment to the driving force of the wheel [6, 27].

The asymmetric contact pressure results from hysteresis losses in the tire and road surface. Hysteresis means that the stiffness during compression is greater than during relaxation, which results in a difference in the force generation between deformation in loaded and unloaded conditions (See Fig. 2.1B) [22, 28]. The difference in force generation is caused by the dissipation of energy in the form of heat, resulting in the energy to deform the tire being greater than the energy that is recovered [26].

Frictional losses

Although rolling resistance mainly results from hysteresis losses, it also includes some frictional losses resulting from the interaction between the tire and the road surface [23, 24]. Generally, the frictional losses has a contribution of 5-10% to the rolling resistance [21]. However, this contribution significantly increases in cases of braking, accelerating and cornering [21, 29]. The mechanism behind frictional losses can be explained by making comparison between a rigid wheel and a deformable tire.

A rigid wheel has a single point of contact, which is either stationary or slides relative to the road surface, also called slipping [30, 31]. For the wheel to be able to roll across the flat surface, it needs to roll around the stationary contact point without slip [31]. The case of rolling without slip, can be called pure rolling and no frictional losses are experienced [30].

However, the deformation of the bicycle tire creates a contact area between the tire and road surface rather than a single point of contact. This means that there is combination between rolling and sliding within the contact patch [30, 31]. The elastic deformations of the tire may compensate for this relative motion between the tire and the road, which creates a region within the contact patch without relative motion, also called the stick zone (see Fig. 2.2)[30]. However, slip will occur in the areas where the elastic deformation cannot compensate for this relative motion. This slippage of the contact patch results in the generation of heat, which is the cause of frictional losses [12, 31].

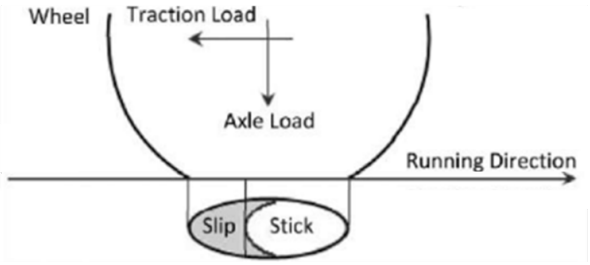

Figure 2.2: Slippage of part of the contact patch (figure taken from [22])

2.1.2. Rolling impedance

Rolling impedance, also referred to as suspension losses, transmission losses, or vibration losses, is the resistance to forward motion caused by surface roughness. This resistance results from lifting the rider-bike system over bumps many times per seconds leading to the generation of vibrations [16, 17, 20, 22, 32]. The vibrations are transmitted from the road to the rider's body via the tires and the bicycle frame, which mainly happens at the hand-bike interface and the saddle [33, 34]. The energy loss within the rider-bicycle system depends on the bicycle frame, suspension system and cyclist [14].

The generation of vibrations is influenced by the tire-road interaction. Pneumatic tires can act like an air-spring, which allows them to store energy [16]. The tires store energy by deflecting when hitting bumps on the road. While some of this energy is lost due to hysteresis, most of the energy is recovered as the tire returns to its original shape [20, 35, 36]. In case the tires fail to store the energy from the bumps, due to being unable to deform around them, then the rider and bicycle becomes the suspension system [16, 17].

The vibrational energy can be dissipated within the bicycle frame, suspension system or cyclist [14]. The bicycle frame and suspension system dampen the vibrations, which results in the loss of energy [37]. However, typical road racing bicycles are generally equipped with rigid frames and lack suspension systems to minimize weight and improve power transfer [15]. The minimal suspension features of road racing bicycles, suggest that most of the impedance losses during road racing results from energy dissipation by the cyclist.

The transmission of vibrations to the rider's body leads to heat generation due to tissue being rubbed against each other [13, 22, 36]. The body will get sore and heat up as a result of this energy conversion, which can be associated with discomfort [32, 36]. In addition, the energy absorbed in the body is lost from the energy that results in the forward motion of the bicycle [36]. This energy loss cannot jet be expressed by an equation, however, figure 2.3 provides experimental data that relates the absorbed energy to the amplitude and frequency of the vibration [14]. This shows that the size and frequency of bumps encountered during cycling influences the magnitude of energy losses due to rolling impedance.

2.2. Tire parameters

The energy losses during cycling can be minimized by optimizing bicycle components. In case of minimizing rolling losses, the tire parameters greatly influence the amount of energy loss [20, 35]. In section 2.2.1, 2.2.2 and 2.2.3, the influence of inflation pressure, tire width and tire type will be discussed.

2.2.1. Inflation pressure & Vertical load

The tire or inflation pressure has large effect on the value of C_{rr} and the total amount of rolling losses. The rolling losses is highly influenced by the hysteresis losses, which result from non-elastic deformations when the tire gets compressed [38]. An increase in inflation pressure, increases the stiffness coefficient of the air-spring of the pneumatic tire, which results in less deflection under the same vertical load [35]. The lower the amount of tire deformation, the lower amount of tire hysteresis losses, and thus the total rolling losses.

Previous research that is conducted within a laboratory setting, using a drum tester, has supported this theory [39]. The measurements have shown a decrease in C_{rr} with increasing levels of tire pressure [38]. In addition, the relation between C_{rr} and vertical loading has been assessed using the same methods. As the tire inflation pressure determines the tire elasticity, the vertical load influences the amount of deflection [21]. Together they determine the total contact area between the tire and the road. The area of the contact patch (A) can be approximated by dividing the vertical load (F_N) by the tire pressure (p) (see Eq.2.2)[22]. An increase of the vertical load, increases the area of contact, resulting in more tire deformations. For this reason rolling resistance measurements have shown that an increase in vertical loading results in an increase of C_{rr} [38, 39].

$$A = \frac{F_N}{p} \tag{2.2}$$

Velinsky et al. has stated that consideration of rolling resistance in isolation from the vehicle itself can lead to error in estimation of vehicle energy losses [24]. This means that energy losses caused by the transmission of vibrations cannot be disregarded. As mentioned, the test performed

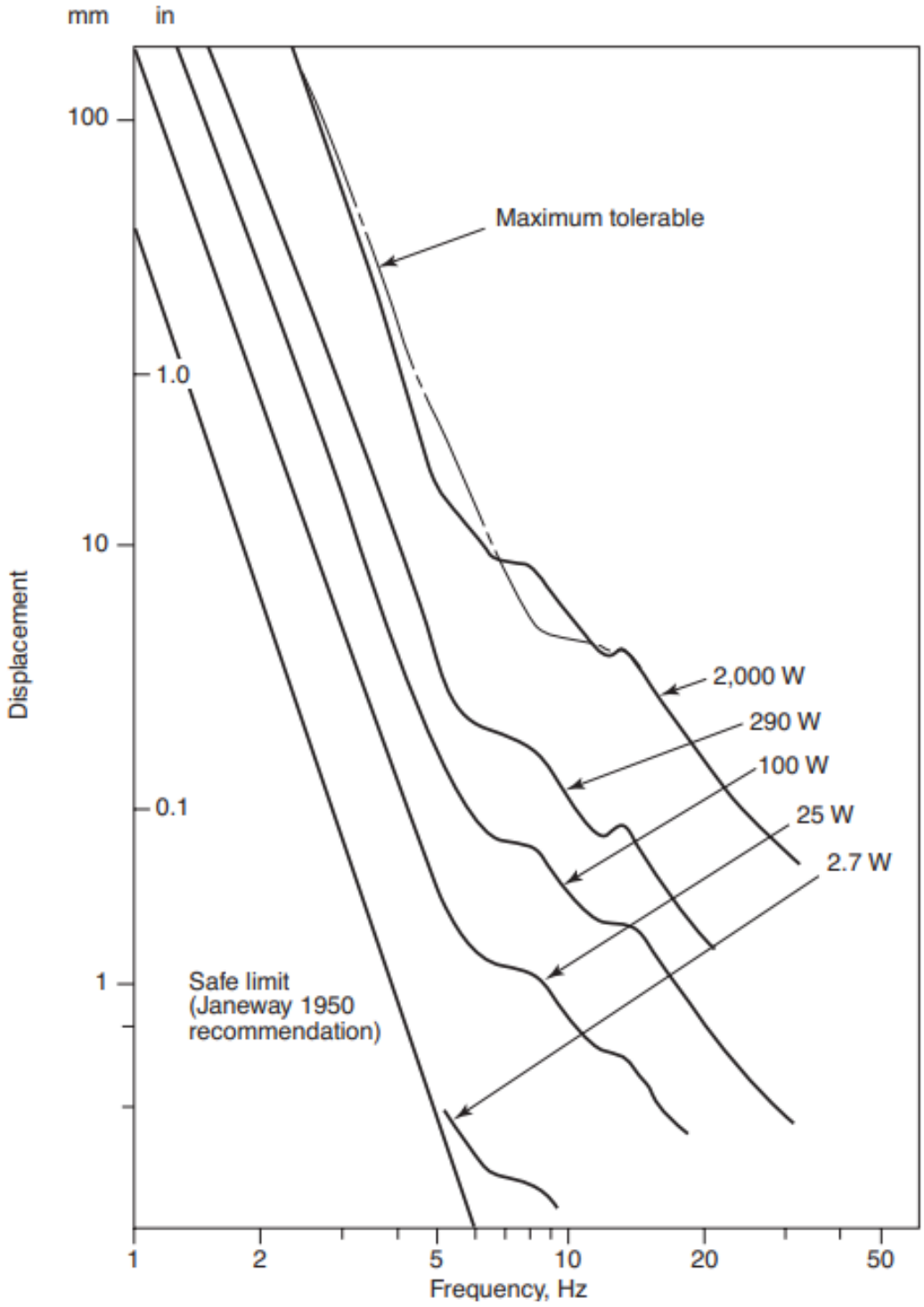

Figure 2.3: Experimental data that relates the absorbed power within the rider's body to the amplitude and frequency of the transmitted vibrations (figure taken from [14])

in laboratory settings show a decrease of C_{rr} with increasing pressures. However, these laboratory tests do not incorporate the effect of rolling impedance, as the energy-absorbing rider is excluded [14]. The incorporation of rolling impedance in the estimation of C_{rr}, leads to the concept of using lower pressures on rough road surfaces. This will decrease the tire stiffness and increase the ability to store energy from the bumps [18]. This means that fewer vibrations are transmitted to the rider, which leads to less impedance losses.

The use of pneumatic tires over solid wheels has given the advantage of an effective suspension system of the bicycle [35]. However, it has resulted in a trade-off between rolling resistance and rolling impedance (see Fig. 2.4). The rolling resistance is minimized by increasing the tire stiffness, as this minimizes tire deformation that causes hysteresis losses. On the other hand, rolling impedance can be minimized by reducing the tire stiffness, as the energy from the bumps can be stored which minimizes the transmission of vibrations to the cyclist. This trade-off between rolling resistance and rolling impedance could be characterized by the break-point pressure, which is defined as the tire pressure that results in the least amount of rolling losses [20]. In practice the break-point pressure is not always clearly visible. If that is the case, the break-point pressure can describe a range of optimal tire pressures (see Fig. 2.4) [17].

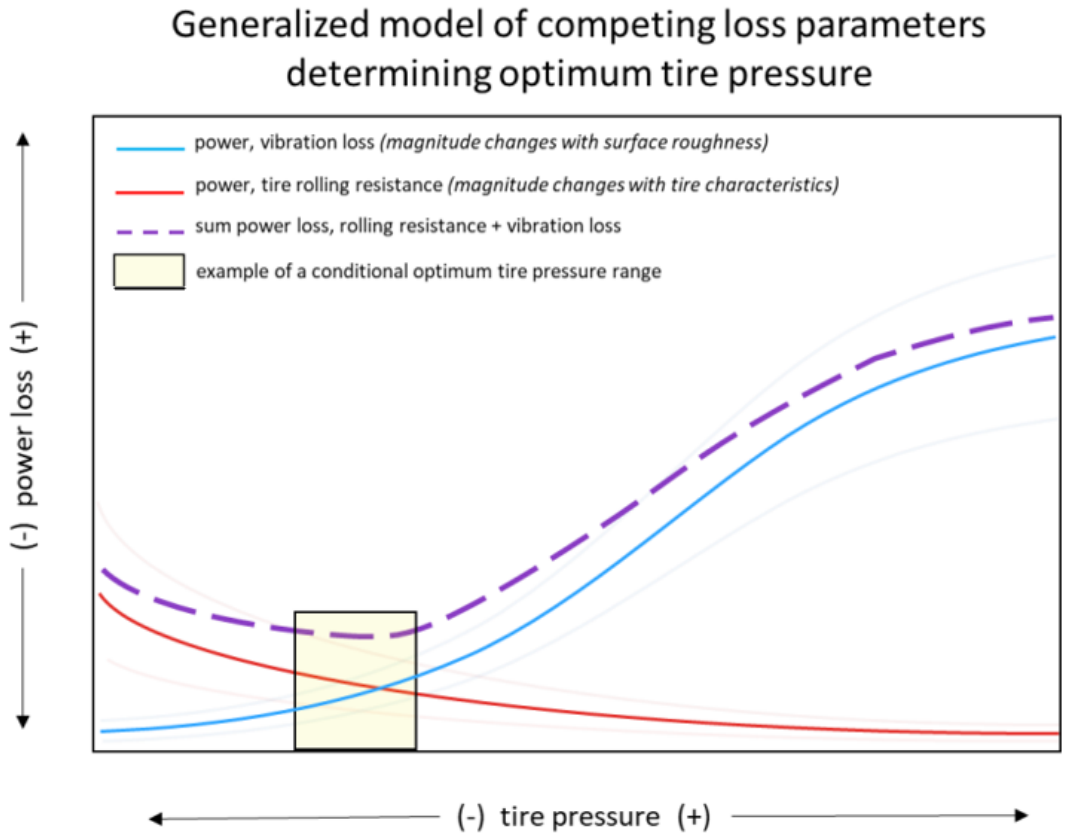

Figure 2.4: A hypothetical model that suggests that the total rolling losses, which is equal to the sum of the rolling resistance and transmission losses, has an optimum range of tire pressures (figure taken from [17])

2.2.2. Tire width

The tire width is defined as the longest lateral distance from sidewall to sidewall. This tire parameter has an influence on the shape of the contact patch [23]. The contact patch is generally assumed to be shaped as an ellipse, as shown in figure 2.5 [22]. When comparing a wide and narrow tire with the same tire pressure and deflected under the same load, then the total contact area will be approximately the same for both tires (see Eq.2.2) [18, 23]. However, the shape of the contact patch differs as the contact patch of a wide tire has a more rounded shape compared to a narrow tire [17, 23].

The length of the contact patch (s) affects the rolling resistance [17, 23, 26]. This can be explained by looking at rolling resistance as a resistive moment caused by the resultant vertical reaction force of the ground to the wheel ending up in front of the wheel. The length of the contact patch will influence the length of the moment arm and the magnitude of the total resistive moment on the wheel. It is stated that a shorter contact patch will result in a smaller moment arm and a smaller total resistive moment [26]. This means that less energy is needed to rotate the wheel. In figure 2.5, it is shown that the length of the contact patch of wide tires is smaller than that of narrow tires, which would indicate that wide

tires result in lower rolling resistance than narrow tires in case of using the same pressure and load.

The tire width also influences rolling impedance. *Silca* states that wider tires are better in absorbing bumps and imperfections of the road surface compared to narrow tires when using the same tire pressures. This means that fewer vibrations are transmitted to the rider resulting in lower rolling impedance [40]. Wider tires have a higher availability to deflect, which improves the compliance of the tire when rolling across bumps [40, 41]. This suggests a reduction the energy losses caused by rolling impedance. However, the connection between different parameters makes this more complicated.

Changes in tire width results in changes in the internal diameter of the tire-rim combination. An increase in internal diameter will increase the stress on the casing and rim walls when the same tire pressure is used, resulting in an increased tire stiffness [42]. To maintain equal stresses in the casing and rim, the tire pressure needs to be lowered [40]. This often results in the choice of using lower pressures when changing to wider tires [17, 42]. This relation between tire pressure and tire width, increases the complexity of assessing their effect on the total rolling losses.

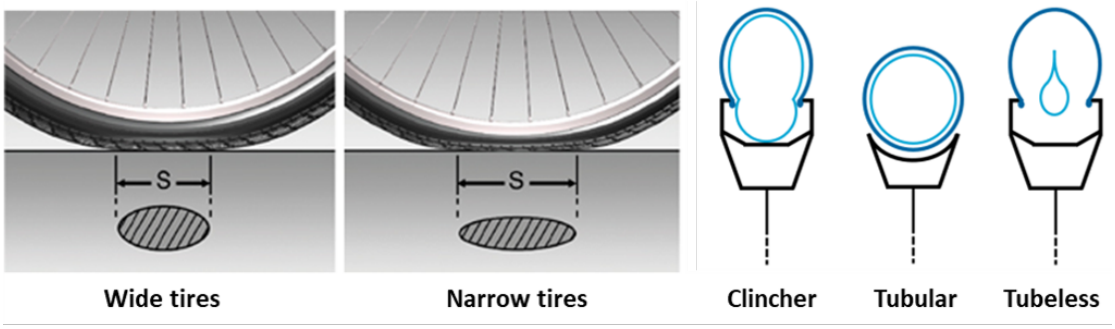

Figure 2.5: Contact patch differences between wide and narrow tire with same pressure and load (figure taken from [23]) and three type of tires (figure taken from[11])

2.2.3. Tubeless vs Tubular

A distinction can be made between three types of pneumatic tire constructions: clincher, tubular and tubeless (see Fig. 2.5) [43]. Two main tire types used in road racing are tubeless and tubular. A tubular tire consist of an inner tube completely surrounded by the outer tube, which are sewed together. The tire is glued on the rim at one side and makes contact with the road at the other side [43]. In contrast, the tubeless tire lacks an inner tube. This tire creates a cavity together with the rim that is sealed due to a combination of pressure and sealant within the cavity [43]. In general, the rolling resistance of tubeless tires is lower due to the lack of friction between the inner tube and outer tire [43]. However, the range of pressures at which tubeless tires run, are lower compared to tires with an inner tube [17].

2.3. Tire-road interaction

The interaction between the tire and the road has an influence on the optimal tire parameters to minimize the total rolling losses. This means that tire parameters should be adapted to the road surface of the race to optimize performance. Section 2.3.1 and 2.3.2 will further elaborate on this parameter selection.

2.3.1. Road surface

In section 2.1.2, rolling impedance is defined as the resistance due to surface roughness. The roughness of the road surface can refer to both the unevenness or the texture of the road. The road unevenness describes the larger scale bumpiness of the road, while the road texture describes the small scale road irregularities [44]. The presence of bumps, ruts and irregularities on the road surface leads to increased rolling losses, as the surface roughness results in the creation of vibrations and the transmission of these vibrations to the rider [6, 12]. Multiple sources have stated that the C_{rr} increases as the surface roughness increases [6, 12, 45, 46].

The most commonly used measures to assess road unevenness and texture are, respectively, the international roughness index (IRI) and the mean profile depth (MPD) [12, 44, 45]. First, the IRI is expressed in mm/m or m/km and represents the ratio between the accumulated vertical displacement of the vehicle's suspension system and the travelled distance [12, 47]. It can be difficult to relate IRI

directly to rolling resistance, due to being based on the vehicle response to the road profile, rather than representing the actual road profile [12]. Second, the MPD represents the average profile depth of two halves of the surface within a given baseline [12]. *Jackson et al.* states that an increase of MPD by 1 mm will result in an increase of C_{rr} by 17% to 30% when traveling at 48 km/h to 96 km/h [12]. This speed dependency of C_{rr} will further be discussed in section 2.3.2.

The type of road surface influences the break-point pressure. An increase of surface roughness results in a reduction of break-point pressure, which lead to the concept of using low to moderate tire pressures on rough surfaces [13, 20]. This is illustrated in figure 2.6, which present the estimation of C_{rr} on different road surfaces with increasing road roughness from a steel drum to machine roughened concrete [20]. It has been suggested that the change in break-point pressure is a result of an increase in rolling impedance when riding on rougher surfaces [20].

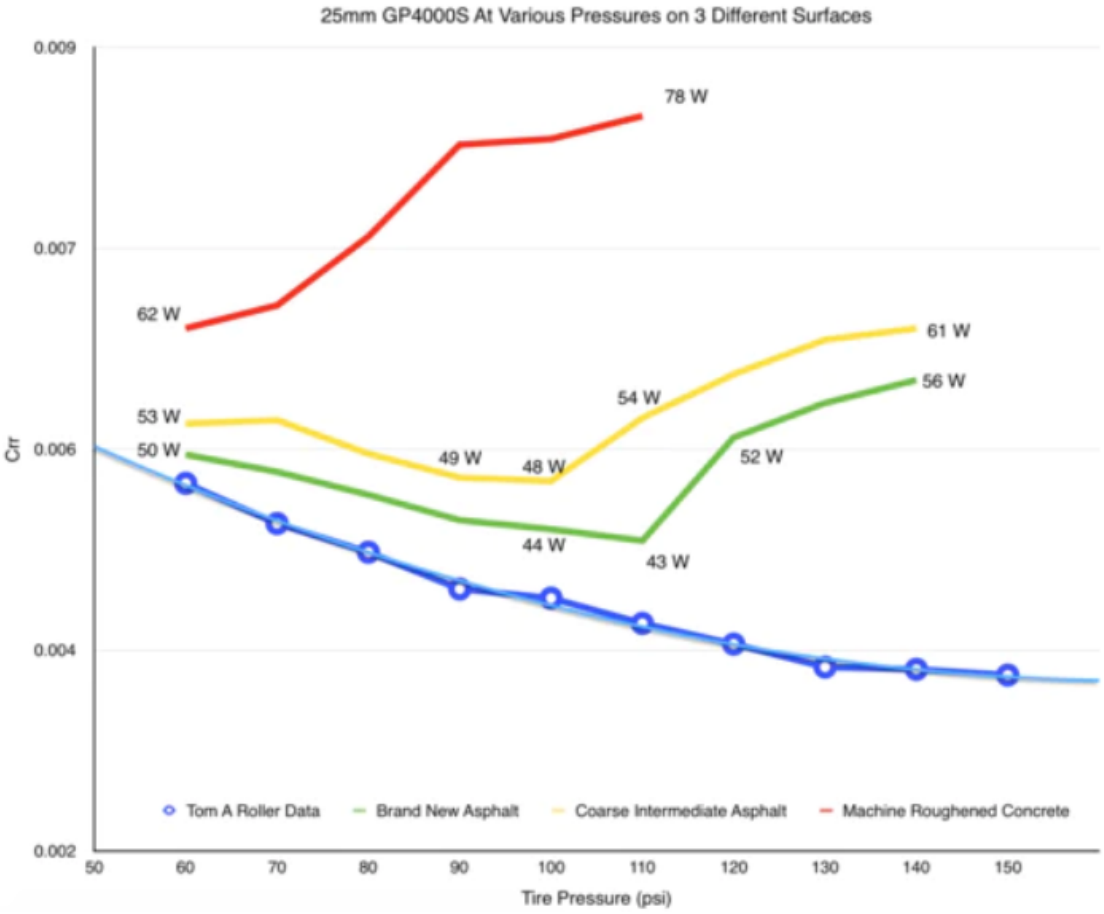

Figure 2.6: Estimation of C_{rr} from experiments on different road surfaces (figure taken from [20])

2.3.2. Cycling velocity

The total amount of rolling losses is proportionally related to the cycling velocity as it both increases the rolling resistance and impedance [21]. Speed dependency of rolling resistance can be assigned to the hysteresis losses. These losses result from the visco-elastic properties of the tire, which relates the stiffness of the tire to the rate of deformation [48]. An increase in cycling velocity increases the rate of deformation. This results in the difference in measured force between loading and unloading of the tire to increase, which means an increase of the hysteresis losses [22].

However, it should be mentioned that the effects of speed on rolling resistance is small for low and moderate speeds. Up to 40 km/h, the value of C_{rr} shows little to no changes. For this reason rolling resistance is often assumed to be independent of speed to distinguish energy losses due to rolling resistance and air drag [21].

The energy losses due to rolling impedance is also influenced by cycling velocity. This speed dependency has already been mentioned once in section 2.3.1. This showed that the combination of increased surface roughness with increased cycling velocity resulted in more percentage change of C_{rr} [12]. *Munera et al.* states that the higher velocities result in higher vibration amplitudes, in case equal pressures are used [33]. The influence of cycling velocity on rolling impedance has been assessed using acceleration measurements. This uses an effective value, which is extracted from acceleration frequencies measured at the rider-bike interface and allows to make conclusions about the influences of vibrations on the cyclist [49].

The test results are depicted in figure 2.7. It could be concluded that there is a linear relationship between the effective value and the increasing cycling velocity [49]. In addition, rougher surfaces show larger absolute changes in effective value, which means that cycling velocity and surface roughness both influence the transmission of road vibrations. Last, in comparison to rolling resistance, rolling impedance is affected by cycling velocity at speeds lower than 40 km/h. This might indicate taht the total rolling losses cannot be assumed to be constant at low speeds.

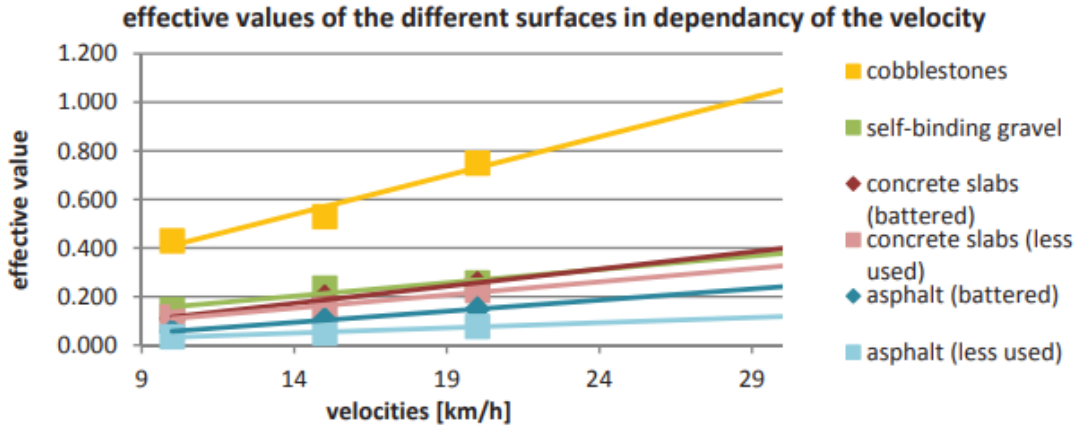

Figure 2.7: The estimated effective value at different speeds and road surfaces (figure taken from [49])

3

Experimental Design

Many measurement techniques exist to assess rolling resistance (see Table I). However, not all of these measurements are suitable to estimate the total rolling losses. The energy losses due to rolling impedance are often neglected due to exclusion of the energy-absorbing rider [14]. The goal is to find a measurement technique that determines the combined energy losses of rolling resistance and rolling impedance. This is achieved by analyzing existing measurement techniques, creating a list of requirements and performance criteria, and developing three possible measurement techniques. These techniques are then rated using the weighted criteria method within a decision matrix.

3.1. Existing Rolling resistance testing

Table I provides an overview of the measurement techniques currently used to assess the rolling resistance and, in some cases, the total rolling losses. For each measurement, the main working principles, advantages, and disadvantages are highlighted. In case of the Chung method, data regarding the reliability of the test setup has been reported.

Table I - Overview of existing rolling resistance measurement techniques

measurement technique	**Working principle**	**Technical evaluation**
Drum testing 	A bicycle wheel is pushed onto a rotating steel drum with a certain load. The contact between the drum and wheel will slow down the spinning drum due to the rolling resistance. Four measures can be used to quantify rolling resistance: force at tire spindle, torque at drum hub, motor power to keep drum rotating at constant speed or drum deceleration. Aerodynamic drag due to the rotation of the wheel combined with the bearing resistance should be removed from the measured resistance. In addition, correction formulas are applied to correct for the unrealistic contact patch shape.	*Disadvantages* - Unrealistic contact patch shape - Limited to added road texture - Excludes rider-bike interface *Advantages* + Can be used to measure pure rolling resistance + No aerodynamic disturbances + Adding road texture influences the estimation of C_{rr} [13, 36, 39, 44, 45, 50]

Table I - Overview of existing rolling resistance measurement techniques

measurement technique	Working principle	Technical evaluation
Rolling road 	Treadmill built from connected rigid slats, which could be replaced individually to change road profile. Simulation of road profiles result from changing thickness of some slats, which indicate bumps in the road. This simulation can be determined from scanning road profiles or assessing transmitted vibrations during on road testing. The rolling losses can be determined from power output of the cyclist. A high speed camera is used to assess effects of vibrations on the rider.	*Disadvantages* - Simulation of road profiles - Availability testing equipment *Advantages* + No aerodynamic drag influences + Controlled environment + Includes rider bike interface [51, 52, 53, 54, 55]
Tire trailer 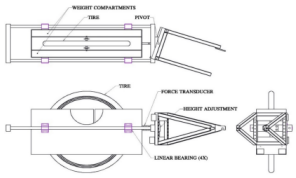	A trailer, in which a testing wheel is mounted, is towed by a vehicle. The trailer consists of two slots to add mass and one slot to mount the wheel. The mounted wheel is connected to the trailer with low friction linear bearings and a force transducer. The force transducer will directly measure the rolling resistance when getting pulled at constant speed. Influences of air drag are minimized by applying a covering or by performing test at low speeds.	*Disadvantages* - Grade sensitivity - road unevenness could reduce measurement accuracy - Excludes rider-bike interface - Sensitive to trailer angle (stay within 0.5 degree tolerance) *Advantages* + Testing on different roads + Directly measure force output + Removes influence air drag with cover [13, 44, 45]
Dynamoteric testing 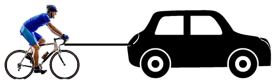	A vehicle tows a bike with cyclist along a certain distance. The bike is connected to the towing vehicle by a nylon cable in series with a dynamometer. The dynamometer reports the force needed to tow the bike at a constant speed. To minimize air drag, the test is performed in absence of wind. Besides, the air turbulence caused by the towing vehicle is minimized by choosing the correct cable length. In addition, the cyclist is still cycling without transmission chain to mimic the air flow experienced during cycling.	*Disadvantages* - Assumes constant rolling resistance to subtract air drag - The rolling resistance contribution reduces as speed increases - Requires desirable weather condition (absence wind) *Advantages* + Includes rider-bike interface + Can test on different roads + Directly measure force output [56, 57]

Table I - Overview of existing rolling resistance measurement techniques		
measurement technique	**Working principle**	**Technical evaluation**
Coast-down testing	Cyclist accelerates to a certain speed and then decelerates by stopping with pedaling or changing gears to stop the force transmission. The cyclist will pass multiple time switches, which records the time needed to pass a certain distance. Both C_{rr} and C_DA* are determined by minimizing error squared of the difference between real distance and estimated distance. The estimated distance is based on the time between two time switches and the initial and final velocities. Aerodynamic influences are minimized by using a coarse that is sheltered from the wind. In addition, wind conditions are monitored during testing	*Disadvantages* - Influenced by aerodynamics - Surface roughness could lead to measurement inconsistencies - Assumes rolling resistance to be independent of speed - No Braking/steering allowed - Needs constant body position - Irregular grades, subject behavior and braking forces (like cornering) could increase measurement variation >10% *Advantages* + Includes rider-bike interface + Typical error <1%. [27, 38, 58, 59, 60]
Chung method	Uses Golden Cheetah to solve for mathematical model based on power balance equation by using the cyclist's power output to match the elevation profile of the road. The test is performed by cycling multiple laps on the same track, which means that the net elevation is zero. The test requires the use of power meter and speed sensor to continuously track the cyclist. This data is used to determine the elevation profile, where at the end of each lap the net elevation should become zero. Environmental conditions (wind speed & Temperature) are also tracked. If wind speed exceeds 2 m/s, measurement is invalid. It is allowed to vary cycling speed, however, three rules need to be followed: 1. No braking 2. Remain cycling position 3. Constant tire pressure	*Disadvantages* - Aerodynamic drag has a large contribution to total resistance - Estimation of C_DA and C_{rr} can affect each other. - Assumes fixed C_DA over complete round - Not accounted for tilted position of the bike in curves - Exact rider paths are not recorded - rolling resistance is assumed to be independent of speed - Needs to follow strict rules *Advantages* + Can test on different road surfaces + Requires limited equipment + Includes rider-bike interface *Reliability:* Typical error of 0.0006 between analyst and has detected a 16% difference between C_{rr} values of different tires. [9, 19]

*C_DA is the product of the drag coefficient (C_D) and the frontal area (A). The drag coefficient is a dimensionless number that quantifies the drag force generated when an object moves through the air. The frontal area represents the size of the object perpendicular to the air flow.

Table I - Overview of existing rolling resistance measurement techniques

measurement technique	Working principle	Technical evaluation
Hill method 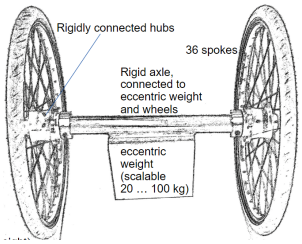	1 DoF pendulum consisting of 2 rigidly connected wheels and an eccentric weight placed onto the rigid connection. The eccentric weight is lifted to supply potential energy to the system, which is converted to heat due to the rolling resistance. A gyroscope and the geometric shape of the pendulum are used to determine the travelled distanced by measuring from the first peak-point of return. The C_{rr} determined from energy conversion principle (change in potential energy = work of rolling resistance ($F_N * s$)). Aerodynamic drag could be neglected. In addition, centrifugal forces due to the motion of the eccentric weight creates a dynamic loading of the tires, which is minimized using small eccentric weight close to center of the wheel axis. Other random disturbances can be removed by applying a minimum of 10 repetitions.	*Disadvantages* - Excludes rider-bike interface - Limited to low speeds - C_{rr} independent of velocity - Variation in vertical load *Advantages* + Testing on different surfaces + No aerodynamic influences [8, 49]
Instrumented Bicycle 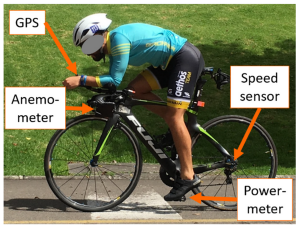	Estimates rolling losses by solving the force equilibrium. The main resistive forces are measured using many sensors (air drag, gravitational force, inertial force). The bike should be equipped with a power meter to measure athletes power output, GPS and gyroscope for cycling velocity, baroscope and accelerometer for slope of the road and differential pressure sensor for air velocity in cycling direction Aerodynamic influences are subtracted using wind and cycling velocity data combined with $C_D A$ values from wind tunnel testing. This provides an accuracy of 96.5%. The accuracy of the C_{rr} estimate increases with test length. The precision decreases from 0.005 (9 to 25m) to 0.002 (55 to 153 m) for test at 10km/h.	*Disadvantages* - Many sensors needed to measure all types of energy losses - Only performed at low speeds *Advantages* + Possible to use on any type of road surface + Includes total rider-bike interface [7]

3.2. Requirements & Performance criteria

The measurements described in table I are currently used only to assess the effect of rolling resistance and exclude or neglect the effects of rolling impedance on the estimation of C_{rr}, with the exception for the Rolling Road. Other measurements that include the rider-bike interface within the test setup, such as dynamometric testing, coast down testing, Chung method and the instrumented bicycle, are able to assess the combined effects of rolling resistance and impedance. However, the influence of rolling impedance on C_{rr} estimation is often not mentioned and neglected.

For example, field tests, such as Chung method or Coast-down method, apply the assumption of rolling resistance being independent of speed, which makes it possible to estimate C_{rr} and $C_D A$ by distinguishing the effect of rolling resistance and aerodynamic resistance. However, this assumption becomes problematic when assessing the total rolling losses, rather than the rolling resistance in isolation, as the rolling impedance is a speed dependent resistance (see section 2.3.2) [49]. The speed-dependent energy losses might be incorrectly assigned to aerodynamic resistance, even though, it results from rolling impedance and should contribute to C_{rr} estimation. To prevent this, the aerodynamic drag should be eliminated from the measurement results.

In addition, one of the research goals is to assess the effects of different road surfaces on optimal tire pressures. Therefore, there is a need to test on surfaces that vary in roughness. To enhance cycling performance during road races, it is recommended to conduct rolling losses estimation under road racing conditions. This implies that the test surface should reflect road surfaces encountered during racing. Moreover, it suggests that the shape of the contact patch during testing should reflect to the shape of the contact patch on a flat surface.

Requirement

- Adding the energy-absorbing rider responsible for rolling impedance losses [14].
- Being able to test on surfaces with different roughness to assess effects on optimal tire pressures.
- Realistic contact patch shape by testing on a flat surface.

Performance criteria

- Minimize aerodynamic drag as this increases accuracy of estimation
- Testing on representable ground surfaces to get results that are better applicable in practice
- Minimize risk of injury for participant to guarantee safety of participants during experiments
- Accessibility of equipment will make it possible to perform tests in the given time frame
- Minimizing the data set will prevent to get lost in big piles of information

The existing measurement techniques can be assessed based on the requirements. Drum testing, Hill method and tire trailers do not include rider-bike interface and only estimate the rolling resistance. However, combining these measurements with a total rolling losses estimation might help to distinguish the effect of rolling resistance and impedance on the total rolling losses. In addition, some test are limited to specific surface types. For example, coast-down testing can be used on different surfaces, however, road irregularities like bumps could result in measuring inconsistencies. This makes this measurement less suitable to test the influence road roughness. Last, measurements that include speed variation, such as the Chung method, makes it difficult to eliminate air drag. The variation in speed will cause a variation in air drag and rolling impedance. This will make it difficult to distinguish these two resistances.

3.3. Design Solutions

The requirements to test on surfaces that differ in roughness, combined with the need to eliminate aerodynamic influences, create a trade-off between laboratory testing and road testing. Laboratory testing provides a quick and consistent metric, however, it might be oversimplified as it does not include the road surface. On the other hand, road testing delivers a fully realistic metric, but is slower and can sometimes be inconsistent due to rider and condition variability [53]. This trade-off is addressed by proposing possible solution for minimizing aerodynamic drag and obtaining surface roughness that reflects the road racing circumstances. These solutions are depicted in figure 3.1.

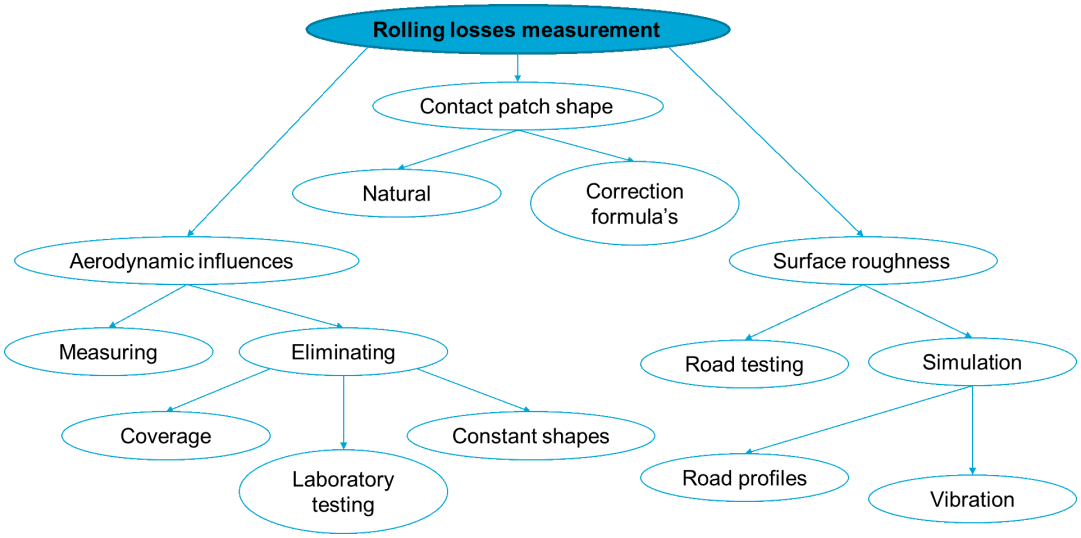

Figure 3.1: Design tree

3.4. Concepts

With the use of the design tree, three different concepts are created to determine the total rolling losses. These will be presented in section 3.4.1, 3.4.2 and 3.4.3 and will be assessed using the decision matrix.

3.4.1. The bike trailer

The bike trailer provides the possibility for road testing by applying a cover to eliminate air drag. The general idea is to create a see-through plastic cover around the cyclist, which is towed by a car. The air inside will move along with the cyclist, which means that no aerodynamic resistance will be experienced (see App. A. Figure 3.2 depicts the test setup.

The towing vehicle will pull the trailer at a constant speed across a minimum distance of 100m, which is determined based on previous research. Di Prampero et al. performed dynamometric test across a distance of 100m, and the instrumented bicycle mentioned a precision of 0.001 when measuring across a distance of 55 to 153 m [7, 56]. To remove possible gravitational resistance, the test needs to be performed on a leveled surface and in both directions. Last, to reduce effects of random disturbances, the test should be performed 10 times [8]. The total rolling losses could be estimated by averaging the results of the two direction and the repetitions.

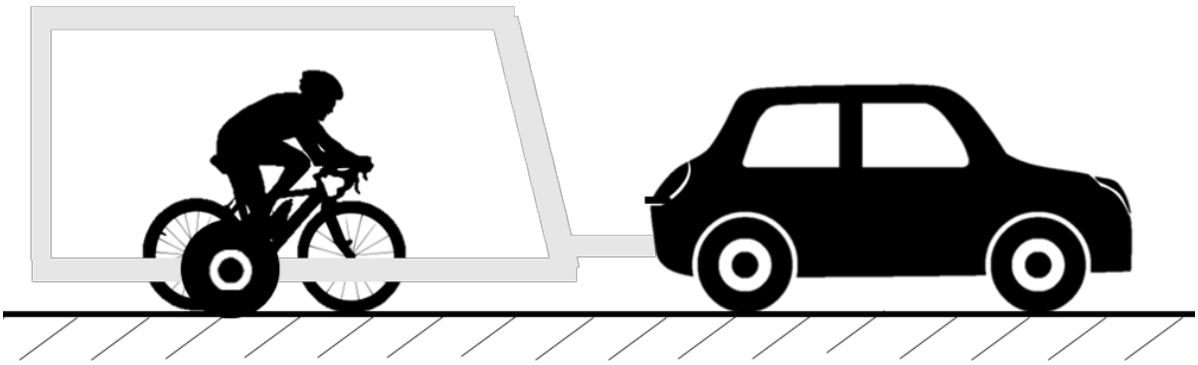

Figure 3.2: Concept 1; the bike trailer

There are two measures that could provide data regarding the rolling losses. First, a force cell (dynamometer or force transducer) can measure the force needed to pull the bike with the cyclist forward at a constant speed. This requires a connection between the bike and the trailer. However, the estimation of rolling losses will have a high sensitivity to trailer angle, as has been shown by the tire trailer method (0.5 degrees tolerance) [13]. Second, a power meter can record the power produced

by the cyclist to maintain constant velocity. The sensitivity to trailer angle will be removed, however, small variations in cycling velocity can exist as the cyclist propels itself forward. It is required to mount a speed sensor to the bike to verify constant velocity. The towing vehicle will help the cyclist maintain a constant velocity as the cyclist should match the speed of the trailer. The choice of measurement equipment depends on its availability.

3.4.2. The rolling road

The laboratory setting of the rolling road eliminates air drag by cycling in place on a treadmill. This means that actual road conditions need to be simulated to address the effects of road roughness on the total rolling losses. To simulate the road surface, data regarding the actual road surface need to be recorded. This can be done by using inertial profiles, which consist of an accelerometer, height sensor (=laser) and distance measuring equipment [44, 45]. Another option is to measure the vehicle response to surface roughness during road testing with the use of an accelerometer and match this to the response on the treadmill. However, this requires both field testing and laboratory testing to obtain bike-road and the total rolling losses.

The existing rolling road measurement could be applied (see table I), however, to reduce resources, it would be possible to build a smaller treadmill that only supports the back wheel of the bicycle (see Fig. 3.3). The front wheel will be connected to a sliding support that is linked with a force sensor to a fixed point. The force sensor records the resistance force, as the rolling losses will pull the cyclist away from the fixed point when the treadmill is on. In comparison to the tire trailer, this measurement setup will not exceed angle tolerances as the force sensor will always remain leveled between the front wheel support and fixed point [13].

The main advantages of this technique are that the test setup within a controlled environment creates a high reproducibility, aerodynamic resistance will not be present during testing, and only one parameter needs to be recorded. On the other hand, the biggest challenge is the availability of the test equipment. A treadmill is needed, which is rigid enough to avoid an increase ground hysteresis and it should be possible to adapt road roughness.

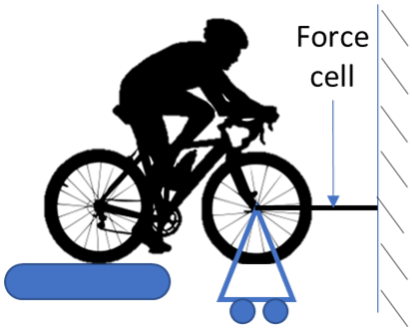

Figure 3.3: Concept 2: the rolling road

3.4.3. Instrumented bicycle

In Table I, the instrumented bicycle is discussed as a field test applicable to any road surface. This test estimates aerodynamic drag by measuring wind speeds and utilizing C_D values from wind tunnel testing. The power balance equation can be used to subtract all known resistive force from the cyclist's power output. The remaining energy can then be assigned to the total rolling losses. It should be noted that the number of sensors used to record all resistive forces could be minimized by testing on a levelled surface in both directions to eliminate the gravitational influences (F_g).

To determine the rolling losses, the cyclist's power output is recorded using a power meter. The aerodynamic resistance (F_a) can be determined using a differential pressure sensor to measure wind velocity in the cycling direction. The inertial resistance (F_i) can be determined using the bike's geometry. Last, the cycling velocity (v) could be determined with a gyroscope or speed sensor [7]. This approach relies on solving the power balance equation to obtaining the total rolling losses (F_r):

$$F_r v = (F_p - (F_g + F_a + F_i))v \tag{3.1}$$

The main advantage of this technique is the possibility to measure the impact of different road surfaces. However, relying on C_D values obtained from wind tunnel testing, imposes constraints on the cyclist's posture, requiring to match the posture of the wind tunnel test. In addition, variations cyclist size could influence the C_D due to changes in air flow around the cyclist. Test accuracy could be increased when minimizing aerodynamic influences by applying the following rule: if the difference between cycling velocity and measured wind velocity exceeds 2m/s, data should be removed from the total data set [58].

3.5. Decision Matrix

To make a reasonable choice between the different methods, the weighted criteria method can be applied. In this method, each measurement technique receives a rating from 1 to 5 for each predefined performance criteria. A higher score indicates better alignment with the criteria. The importance of each criterion is indicated by its weight. The weights are a number between 10 and 1, the higher the weight the more important the criteria. To make a difference in the importance of the criteria within the total score, a weighted score is determined for each criteria ($weight * score$). Summing up the weighted score from each criteria will result in the total score. The highest scores will indicate the most appropriate measurement technique to achieve the goal of measuring the influence of tire parameters and road roughness on the total rolling losses.

Table II presents the decision matrix used to rank the three concepts discussed in section 3.4. According to the decision matrix, the bike trailer will be the best option to measure the total rolling losses This results from the possibility to test on any road surface and the elimination of air drag (see App. A). However, it is crucial to address safety concerns during the design of the bike trailer, particularly focusing on the risk of injury to the participant. In comparison to the other two concepts, it won't be able to prevent falling by applying a harness. Additionally, in case the participant does fall during testing, then the structure of the trailer increases risk of injury. It is important that during the design of the bike trailer, the safety of the cyclist will be taken into account by addressing these concerns (see appendix B).

Table II - Decision matrix using weighted criteria principle

		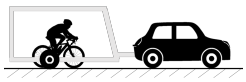 *Bike trailer*		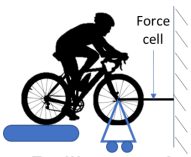 *Rolling road*		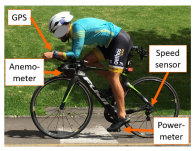 *Instrumented bicycle*	
Criteria	**Weight**	**Score**	**Weighted**	**Score**	**Weighted**	**Score**	**Weighted**
Road Surface	10	5	50	2	20	5	50
Aerodynamic drag	8	4	32	5	40	1	8
Safety Cyclist	7	2	14	4	28	5	35
Available equipment	5	5	25	1	5	3	15
Size data set	3	5	15	5	15	1	5
		Total	137	**Total**	108	**Total**	113

4

Methodology

The impact of the tire parameters on the total rolling losses are assessed through three different tests. First, ink prints are taken to evaluate the shape of the contact patch. Second, drum testing is used to determine the pure rolling resistance. Third, the effect of road type is assessed by performing rolling losses measurements. In chapter 5, the outcomes of each test are analyzed separately and combined. This chapter will provide the methods used for each measurement. Section 4.1 gives an overview of the tire parameters and tire-road parameters applied during testing. The test methods are presented in section 4.2, 4.3 and 4.4. In section 4.5, regression analysis is discussed, which can be applied to assess how the tire parameters and tire-road parameters affect the outcome of each test.

4.1. Test Parameters

In section 2.2 and 2.3, the effects of tire parameters and parameters related to tire-road interaction on the total rolling losses are highlighted based on previous studies. The upcoming experiments aim to extend this knowledge by exploring various settings for the discussed parameters. Table III presents an overview of the parameters used in each experiment

A distinct set of tire pressures is used for each tire, reflecting the impact of tire width and type on the usable range of inflation pressures (see section 2.2.2). During the experiments, there is an overlap in the applied inflation pressures between two different tires. This applies for both the difference in tire type, Tubular vs Tubeless (Corsa Pro), and the difference in tire width. In addition, for certain experiments, changes in specific parameters are not applicable due to limitation within the test setup.

Table III - Parameters assessed with each test

Parameter specification	**Ink prints**	**Drum testing**	**Rolling losses Measurement**
Tire & inflation pressure			
• 26mm Corsa Tubular	6.0, 7.5 bar	6.0, 6.8, 7.5 bar	NA
• 26mm Corsa Pro	5.3, 6.0 bar	5.3, 5.7, 6.0 bar	5.3, 5.7, 6.0 bar
• 28mm Corsa Pro	4.8, 5.3 bar	4.8, 5.3, 5.8, 6.0 bar	4.8, 5.3, 5.8 bar
• 30mm Corsa Pro	4.3, 4.8 bar	4.3, 4.8 bar	NA
Cycling velocity	NA	30, 40 km/h	30, 40 km/h
mass on rear wheel	21, 30, 38 kg	35, 45 kg	54 kg
Road Surface	NA	NA	Asphalt, Brick road

4.2. Ink Print measurements

As discussed in section 2.2.2, literature suggests that wider tires creates a wider and shorter contact patch compared to narrower tires. A shorter contact patch should be equivalent to a lower rolling resistance, as the moment arm reduces. The shape and size of the contact patch can be analyzed by creating a print of the contact area between the tire and ground when pressing a wheel onto a flat surface with a specified force. Various resources can be applied to create this print, such as paint, ink, pressure sensitive film or ultrasonic waves [61, 62, 63, 64].

Ink print measurements are one of the more accessible methods to assess the contact patch shape and only requires an ink pad, paper and some weights. The test setup described in section 4.2.1, is applied to four different tires, three different loads and two different pressures (see table III). All parameter combination are repeated three times from which the average and standard error is extracted.

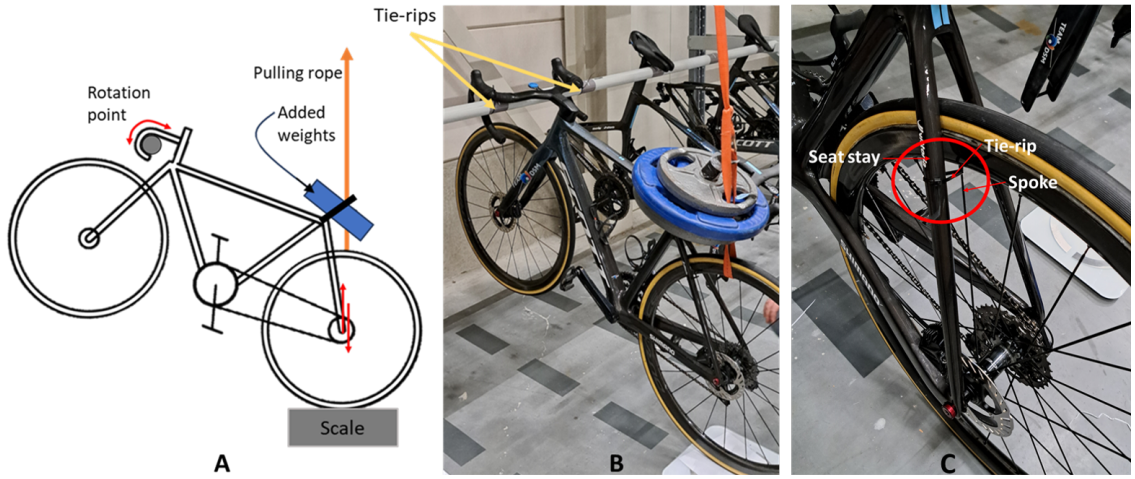

Figure 4.1: Ink print measurement setup A) schematic test setup B) Actual test setup C) Wheel locking mechanism

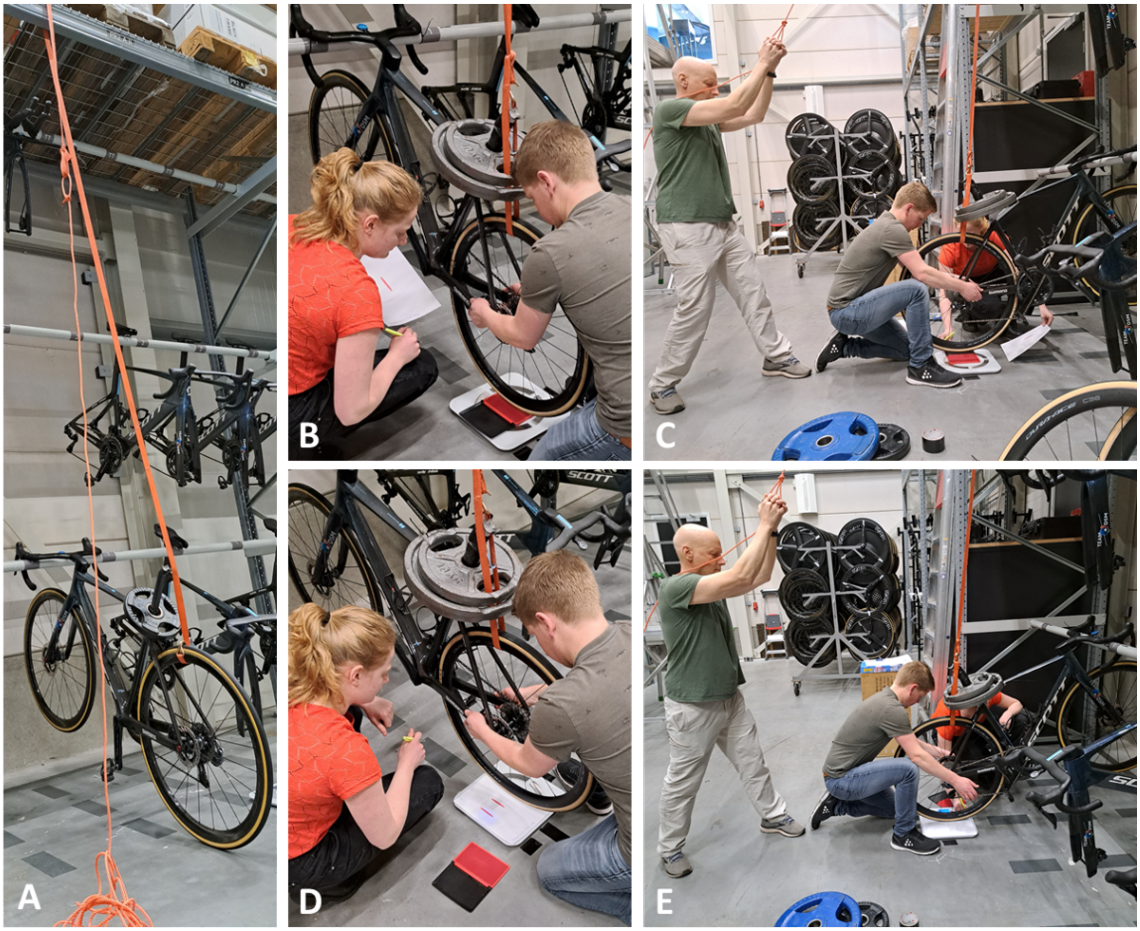

Figure 4.2: Measurement steps A) test setup B) Applying ink to the tire C) replacing the ink pad with a piece of paper D) placing the tire on the paper E) writing down the mass of the scale beside the ink print

4.2.1. Test setup

Figure 4.1 illustrates the setup that is used to take the ink prints. The handlebars of the bike are hooked to a beam and locked in place by tie-rips (see Fig. 4.1A&B). This creates a pivot point to lift the rear wheel and prevents the bicycle from tilting. In addition, the rotation of the rear wheel could contaminate the test results by elongating the ink print. For this reason, a tie-rip is used to connect the spoke of the wheel to the seat stay at the rear triangle of the bicycle (see Fig. 4.2C). Last, a scale is placed underneath the rear wheel to measure the exact load placed on the tire when taking the ink print.

Before starting the measurements, the test parameters should be set to the right values. The saddle of the bicycle is removed, which makes it possible to place the weights around the seat post. When switching the rear tire, it is made sure that all load and pressure combinations have been tested for that specific tire before moving on to the next tire.

The steps taken to obtain the ink prints are illustrated in figure 4.2. The measurements are performed with the help of three people. One person lifts the bike using the rope, one person lifts the bike at the rear wheel axis and carefully guides the rear wheel to the paper and the third person reads out the weight placed on the rear wheel.

The first step is to lift the rear wheel from the scale and place the ink pad underneath the tire. Second, the bike is put down onto the ink pad (Fig. 4.2B). The person who lifts the bike at the rear wheel axis, pushes the tire into the ink pad. This extra force increases the contact area during this step (see Eq. 2.2), which guarantees that the ink will spread at least across the entire area that will be measured. Third, the rear wheel is lifted and the ink pad is swapped with a piece of paper (Fig. 4.2C). Fourth, the rear wheel is gently placed onto the piece of paper (Fig. 4.2D). The person lifting at the wheel axis helps to stabilize the bike at the back to prevent the bike from bouncing when getting in contact with the paper. However, the wheel should absolutely not be pushed down. Last, the value of the scale is written down on the piece of paper next to the ink print (Fig.4.2E).

4.2.2. Data analysis

The ink prints are scanned into a PDF document and separately converted into a JPEG format [61]. These images are loaded into MATLAB, where an ellipse is fitted by hand on top of the ink print. An example is given in figure 4.3. The ellipse can be fitted by aligning the side of the ink print with the black line. After fitting the ellipse, MATLAB will extract the length, width and total area of the contact patch. Based on these three parameters of the contact patch, conclusion can be drawn regarding the effect of tire parameters on the size of the contact patch.

It should be noted that the estimation of contact measures is based on the pixel size of the image. For this reason, it is important to verify the mm/pixel conversion unit of the contact patch images before applying this method. To check whether the correct conversion unit is applied, the estimated length and width could be verified by measuring the contact patches by hand.

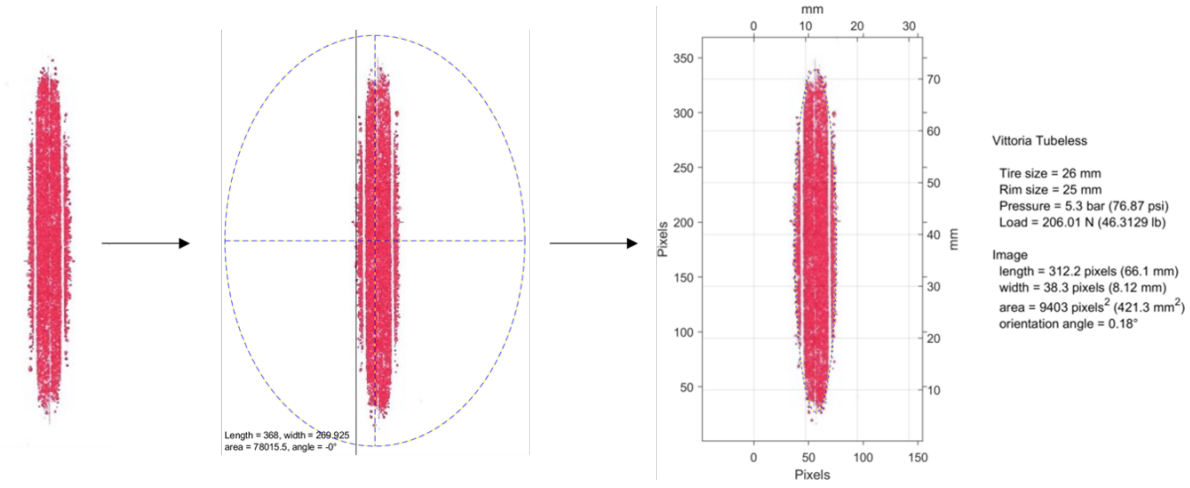

Figure 4.3: Steps taken to extract ink print measures 1) uploading the image 2) fitting ellipse 3) document the fitted ellipse

4.3. Drum testing

Drum test is a laboratory test setup, often used by tire manufacturers to assess the rolling resistance. It has been stated that drum testing can be used to assess pure rolling resistance, as almost all other disturbances are removed [44]. This means that the rolling resistance force should be equal to the force needed to keep a wheel moving at a constant speed [6][12]. In section 3.1, the working principles of drum testing have already been discussed. It is mentioned that there are four different types of output measures to quantify rolling resistance. In this research, the motor power to keep the drum rotating at constant speed is used as outcome measure.

During the measurements, all four tires were tested, each with three or four inflation pressures, at two speeds, and under two different loads. Due to limited time at the testing facility, all tires were prepared in advance. This involved placing each tire on a different wheel with the same characteristics. The goal was to repeat measurements for each parameter at least twice. In case the two measurements showed an absolute difference in outcome of 0.2 Watts, the test was repeated a third time. However, for some parameter combinations, only one trial was conducted due to time constraints toward the end. The final estimation of rolling resistance is obtained by extracting the average and standard error from all trials with the same parameter set.

4.3.1. Test setup

The measurements are performed on a drum with a diameter of 1.4 meter. Figure 4.4 shows the drum tester. Before starting the experiments, the wheel is attached, using the quick release in the center of the leverage. Afterwards, the leverage is leveled using the spirit level. Last, it should be checked whether all parameters are set to the correct values. In case the weight needs to be adjusted, the springs need to be pushed down as much as possible to prevent oscillation of the weights contaminating the results. In addition, it takes some time for the drum to calibrate to the set velocity. Therefore, it is recommended to perform one complete run to calibrate the velocity of the drum and minimize errors in the estimation of rolling resistance.

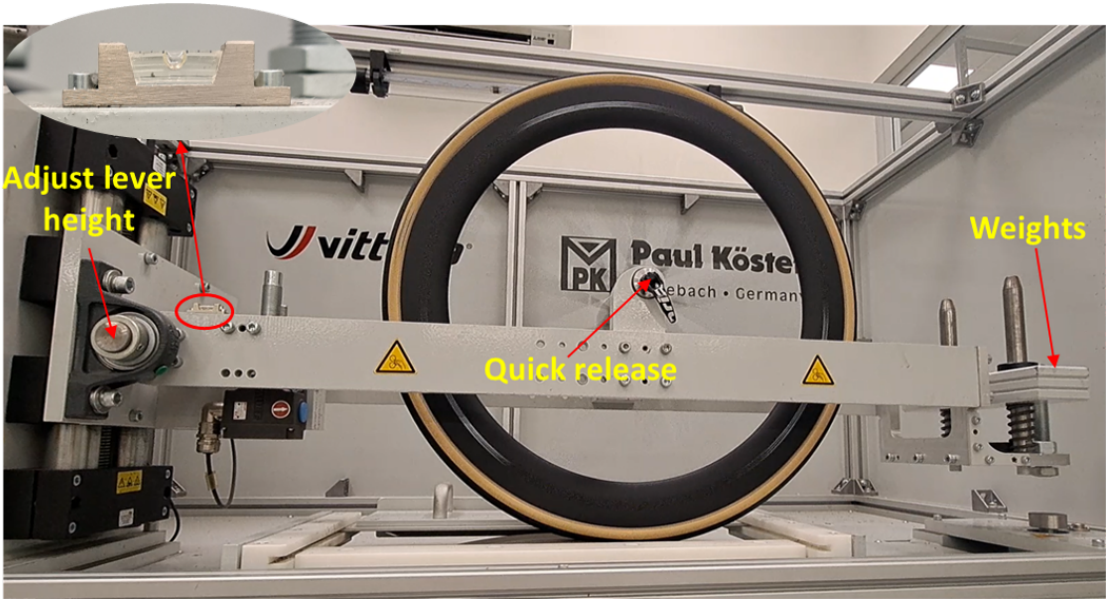

Figure 4.4: Drum tester available at Vittoria Headquarters

When all parameters are set, the test can be started. The test consists of a warm-up period of 2 minutes, a test period of 1 minute and a recovery period of 2 minutes. The warm-up period starts the moment the tire hits the drum. During this period, the power generated by the motor is gradually increases to match the set velocity. At the end of the warm-up period the power supplied by the motor to maintain a constant speed is stabilized. During the test period, the average power is recorded. The recovery period start when the tire is removed from the drum. The motor needs some time to adapt to changes in setting. After the test period, the average power (P_{drum}) required to keep the drum rotating at the specified speed (v) is given. These values are written down for further data analysis.

4.3.2. Data analysis

The drums curvature results in an overestimation of the rolling resistance when compared to the resistance experienced on a flat surface [65, 66]. This results from increased stress levels in the tire. Therefore, curvature correction should be applied to the drum force (F_{drum}) obtained from the measured power based on the radius of the tire (r_{tire}) and drum (R_{drum}) (see Eq.4.1 and4.2).

$$F_{drum} = \frac{P_{drum}}{v} \tag{4.1}$$

$$F_{rr} = F_{drum}\left(1 + \frac{r_{tire}}{R_{drum}}\right)^{\frac{1}{2}} \tag{4.2}$$

After applying the curvature correction, the estimated rolling resistance force (F_{rr}) is converted to C_{rr} by applying equation 2.1. The conversion to C_{rr} makes it possible to compare the outcomes of the different tests.

4.4. Rolling losses measurement

Current measurement techniques do not take into account the rider-bike interface and the effect of road surface texture. This means that the effect of rolling impedance is often overlooked. In chapter 3, an assessment of different measurement techniques is performed. This evaluation has led to the selection of one measurement technique — the bike trailer method. The bike trailer is a type of wind shield that creates an enclosed space around a cyclist and can be used to eliminate the air resistance experienced during cycling (see Appendix B).

For this measurement, a (semi-)professional road cyclist has been selected to participate in this study. All test runs are conducted with one participant ($m_{bike+cyclist} = 94kg$, $m_{rearwheel} = 54kg$). As shown in table III, this measurement technique is applied to two tires with three different pressures, at two speeds, and on two different surfaces. The road type is considered a categorical factor, asphalt or bricks (20x10 cm), as roughness measurements are not conducted (see Fig. 4.5). In total, three repetitions are taken for each parameter set. If the participant reports that one of the repetitions could be inaccurate due to contact with part of the trailer or the need to stop pedalling in the middle of the test run, an extra repetition is conducted.

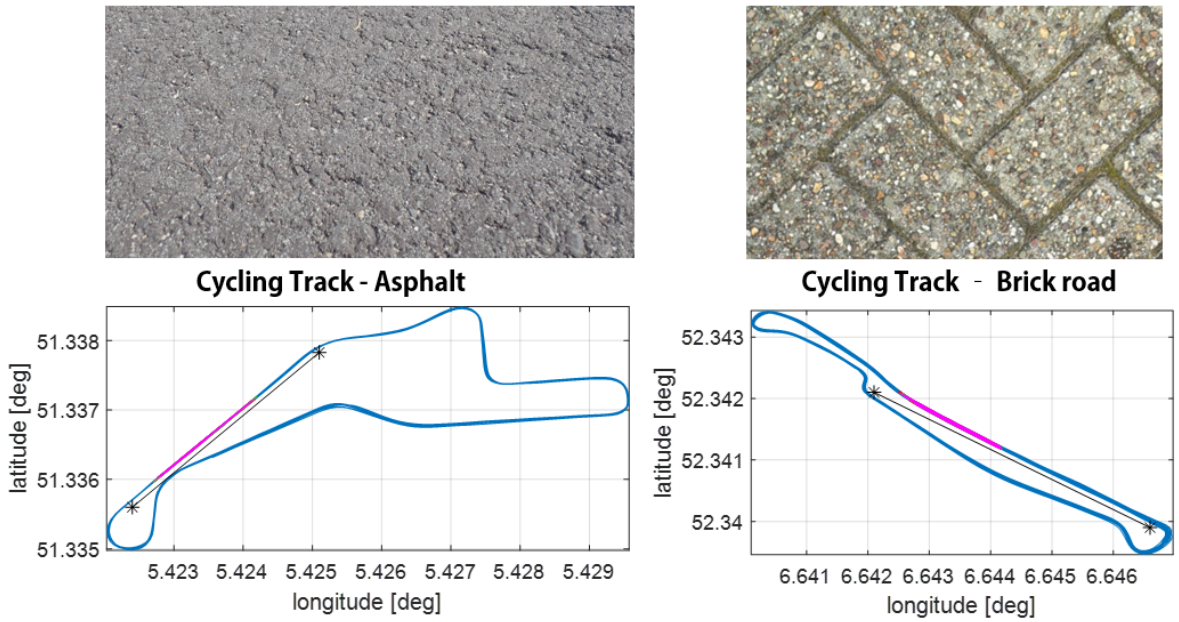

Figure 4.5: The cycling tracks on which the measurements are performed with test section highlighted in pink. The black line is created by identifying two points (*) and serves as threshold to eliminate all data points located under it. Note: the bricks have a dimension of 20x10 cm.

4.4.1. Test setup

Figure 4.6 depicts the test setup. During the experiments the bike trailer was towed by a car at a speed of 30 or 40 km/h across a straight road section, as cornering will influence the estimate for total rolling losses [21]. A test run consists of accelerating to desired speed, cycling at constant speed for approximately 150 meters and decelerating to a stop. The cyclist's bicycle is equipped with the DURA-ACE FC-R9200-P power crank (Shimano, Sakai, Osaka, Japan), a Wahoo RPM speed sensor mounted to the wheel-hub and a Wahoo head unit with GPS system (Wahoo Fitness, Atlanta, Georgia, USA) [67, 68]. The Wahoo head unit records information regarding cadence, cycling velocity, traveled distance, power, longitude and latitude with a sample frequency of 1 Hz. In addition, an anemometer is placed within the trailer to verify the absence of air drag.

The cyclist is instructed to match the speed of the trailer during the test runs, while not braking or changing gears. In addition, the cyclist is instructed to maintain the same position and muscle tension during each run. After a run is completed, the cyclist will give feedback about the performance of the run, which is used to eliminate failed runs from the data set during data processing.

To guarantee the participant's safety, several precautionary measures were taken. First, the cycling tracks were explored with dry runs, which indicates that the trailer, without the cyclist, was towed behind the car across the cycling track. Second, during the test runs, the cyclist and the car driver could communicate using a radio communication system, which allows the test to be aborted at any moment. In addition, braking was only allowed when mutually agreed through the radio system after which the cyclist was guided by the brake lights of the towing car. Last, the car driver already had experience with cyclists riding closely behind the car.

Figure 4.6: Test setup for the bike trailer measurement

4.4.2. Data analysis

The Wahoo head unit provides a CSV file of the test data (power, speed, cadence, distance, longitude, latitude). In addition, a GPX file is obtained, which is used to assess changes in altitude along the cycling track. To automatically select the data related to the specified test section depicted in figure 4.5), a MATLAB file is created which selects data based on six thresholds. The thresholds are minimum cadence, maximum change in velocity between two consecutive data points, minimum duration, percentage deviation from the average cadence, absolute deviation from the average cycling velocity and constant for median absolute deviation (MAD) with values of 75 RPM, 0.205 m/s, 8 seconds, 5%, 1 km/h and 2, respectively. These thresholds are applied in three different selections steps. Figure 4.7 provides an overview of the selection procedure from raw data to the final selection.

Preparation data: Since power cranks are used, the frictional losses within the drivetrain influence the raw power output (P_{raw}). The chain efficiency (η_{chain}) should be used to eliminate frictional losses and determine the power that is effectively transferred to the road ($P_{eff} = P_{raw}\eta_{chain}$). According to literature the chain efficiency is 97.66% [5]. The effective power will be used for all data selection steps and parameter estimations. During the data selection procedure, the terms 'raw power' or 'raw data' will refer to the data without transmission losses (P_{eff}). This is done to distinguish this data set from filtered data.

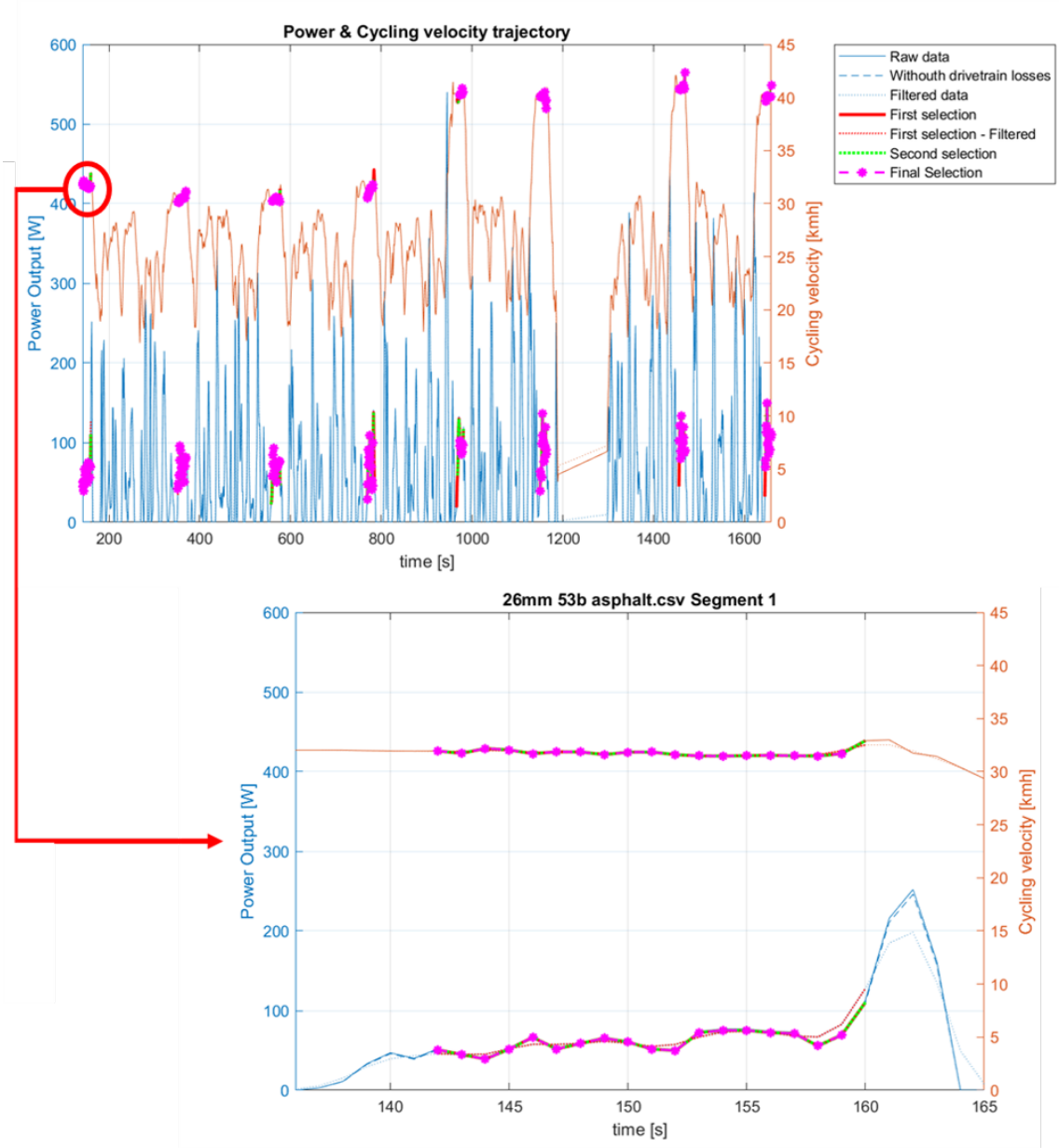

Figure 4.7: Data selection process from raw data to final selection. On top, the power and velocity data stored within one of the CSV files is depicted. This includes all runs performed with the 26mm Corsa Pro at 5.3 bar on Asphalt for both 30 and 40 km/h. On the bottom, the selection process of one segment is shown in more detail to illustrate the elimination of data points during each selection step

Several thresholds, including minimum cadence, change in velocity and deviations from the averages, are applied to filtered data. A first order low-pass filter with a cut-off frequency of 5 Hz is applied to attenuate high frequency noise. The purpose of smoothing the data with a low-pass filter is to better identify changes in the signal over time. The choice of cut-off frequency is based on the highest frequency of the signal of interest, which is a maximum cadence of 120 rpm (= 4 Hz). Cut-off frequencies in the range of 4 to 6 Hz are considered to find a cut-off frequency that keeps important signal features while effectively filtering out high-frequency components. It should be noted that the final rolling losses estimations are based on the raw data and filtering the data is only used as a tool during the selection process.

The last step before applying the selection process is to define the location of the test sections on the cycling tracks. This is done to ensure that only data points corresponding to the actual test are selected. In figure 4.5, a black line is depicted, which is located slightly under the part of the cycling

track where the test runs are performed. The line is created by specifying two points on the map (*) and determining the intercept and gradient of a line between those points. During the selection process, only the data taken on the cycling track that is located above this line will be assessed. In addition, to identify the start and end point of the test section, a minimum and maximum longitude are defined (Asphalt = [5.4227, 5.4242], Bricks = [6.6425, 6,6442]). These values are based on images of the cycling tracks, which are matched with the longitude and latitude coordinates.

First Selection: Data points are selected based on location, minimum cadence, and change in velocity between two consecutive points. First, data points are selected based on the location indicators defined in the previous paragraphs, namely, the black line and longitudinal range. Second, all points with a cadence higher than 75 rpm are selected. This threshold will help to identify whether the cyclist needed to stop pedalling during the test run. This results in either elimination of the complete run or part of the run. Third, the change in cycling velocity between two consecutive points are calculated and can not exceed 0.205 m/s. This threshold is based on change in kinetic energy being maximally 2 Watts, when assuming that the initial velocity is zero. Equation 4.3 can be applied to calculate the change in kinetic energy, which depends on the combined mass of the bike and cyclist (m), the current velocity (v_1) and the initial velocity (v_0) [5]. When applying the assumption of the initial velocity being zero, than equation 4.4 can be applied to determine the maximum change in velocity threshold (Δv).

$$\frac{dE_{kin}}{dt} = \frac{1}{2}mv_1^2 - \frac{1}{2}mv_0^2 \tag{4.3}$$

$$\Delta v = \sqrt{\frac{2\Delta E_{kin}}{m}} \tag{4.4}$$

Second selection: Data points are removed from the first selection based on deviation from the average cycling velocity, deviation from the average cadence, and a minimum duration of the segment. In this process, a segment is defined as a set of consecutive data points. First, the average cadence and cycling velocity are computed for each segment. These averages are used to calculate the difference between individual data points and the corresponding segment averages for both cycling velocity and cadence, which can not exceed 1 km/h and 5% of the average, respectively. This criterion aims to minimize speed variation within a segment, thereby upholding the assumption of cycling at a constant velocity. After elimination of specific data points, the length of each segment is determined, which should be greater or equal to 8 (representing a minimum duration of 8 seconds). Segments that do not comply will be removed completely. The duration constraint ensures that segments provide valid information regarding the rolling losses, as pedalling power is highly variable and should be average over multiple data points [14].

Final selection: An outlier detection method, using the median absolute deviation (MAD) as a measure of variability, is applied to eliminate data points whose power significantly deviates from the others within the segment. This method is suitable for outlier detection as the median is stable against the influence of outliers [69]. The MAD is calculated by determining the absolute deviation of the power for each data point (x_i) within the segment (x). This deviation is the difference between the power output of the data point and the segment's median power (see Eq. 4.5) [69]. In equation 4.6, the MAD-median rule for normally distributed data is given. The K-value is a constant, which is recommended to be 2, 2.5 or 3 [70]. All three recommended K-values were tested, which has resulted in selecting a K-value of 2 for this selection process.

$$MAD = median\,(x_i - median(x)) \tag{4.5}$$

$$\frac{\left|x_i - median(x)\right|}{MAD/0.6745} > K \tag{4.6}$$

It should be noted that this outlier detection method is only applied to the first and last elements within a segment, as consecutive data points are needed to estimate the total rolling losses. If one of the elements does not comply with the threshold, the element with the highest absolute deviation will be removed from the data set. Its consecutive element then becomes the new first or last element, depending on which element was removed. These steps are repeated until the segment size is reduced to the minimum duration or both elements comply with the threshold.

Post processing: Based on the participant's feedback regarding the performance of the test run, several complete segments are manually removed from the data set (see Appendix E). This completes the selection of data segments. Subsequently, the power losses attributed to a slight incline of the road are subtracted from the measured power output by extracting altitude data from GPS. Reference points are selected by pairing the altitudes with corresponding longitudes. A trend line is then created between the reference points, which allows for the estimation of altitude (h) at longitudes where no altitude data is available. Equation 4.7 is applied to determine the change in potential energy (dE_{pot}/dt) between two consecutive points (h_1, h_0) with a time step of 1 second ($t_1 - t_0$) [5]. The average change in potential energy is determined for each segment, which is subtracted from the segment's average power. The validity of this correction has been confirmed by comparing test runs conducted in opposite directions with the same parameter set (Bricks, 26 mm Corsa Pro, 6 bar at 30 and 40 km/h,).

$$\frac{dE_{pot}}{dt} = mg(h_1 - h_0)(t_1 - t_0) \tag{4.7}$$

The average corrected power of each segment can be converted to C_{rr} by applying equation 4.1 and 2.1. The average C_{rr} and standard deviation for each segment is used to determine the average C_{rr} and standard error for each parameter combination.

4.5. Regression Analysis

Regression analysis is a statistical tool used to assess the relationship between variables [71]. It provides answers to whether there is a significant relationship between independent and dependent variables and how strong this relationship is [71, 72]. Within this study, four regression analysis are conducted. The first two analysis focuses on understanding the impact of tire type, tire width, inflation pressure and vertical load on the length and width of the contact patch. It should be noted that this analysis is not applied to the area of the contact patch, as the contact area is described by a function of length and width ($A = 0.25lw$). The third analysis focuses on the impact of tire type, tire width, inflation pressure, vertical load and velocity on C_{rr} obtained with drum testing. The fourth analysis focuses on the impact of tire width, inflation pressure, velocity and road type on C_{rr} obtained with the rolling losses measurement. Figure 4.8 gives an overview of the independent and dependent variables within this study.

The dependent variables or response variables are the outcomes of each measurement. The parameters varied within this study are the independent variables or predictors (see Table III). The independent variables can be continuous or categorical. Continuous variables can take any value between their minimum and maximum, while categorical variables can only take on a number of possible values or classifications [73]. The tire type and road type are categorical variables, with the former being either tubeless or tubular, and the latter being either asphalt or bricks.

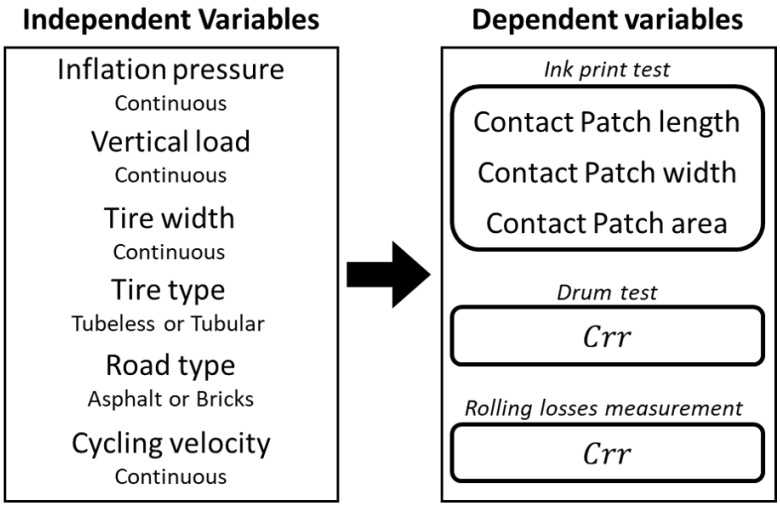

Figure 4.8: Independent and dependent variables with distinction between continuous and categorical independent variables

The relationship between two or more independent variables ($x_1, \ldots, x_n$) and one dependent variable (y) can be estimated with multiple linear regression (MLR) [74]. This is done by fitting a line to the observed data by minimizing the sum of the squared differences between the observations and the line itself [71]. The representation of the fitted line is given by equation 4.8. In which, β_0 is the intercept, $\beta_1, \ldots, \beta_n$ are the regression coefficients and ϵ is the model error or residual (= difference between the regression line and the actual observation).

$$y = \beta_0 + \beta_1 x_1 + \ldots + \beta_n x_n + \epsilon \tag{4.8}$$

The intercept indicates the value of the dependent variable if all independent variables were zero [71]. If the model includes categorical values and independent variables that, generally, would not be zero, then the intercept does not provide meaningful information. Instead, it serves as an anchor for the regression line.

The regression coefficients represent the change in the dependent variable due to the change in the corresponding independent variable, while all other independent variables remain constant [71]. For continuous independent variables, the value of β_i is the difference in the prediction of y when x increases by one unit. However, to assess the influence of categorical variables on the dependent variable, a variable ($x_{category}$) is created, which indicates the presence (1) or absence (0) of a category. One category is selected as base category to which all other categories are compared. The β related to a categorical variable represents the difference in prediction of y compared to the base category [71, 73]. Within this study, bricks and tubeless tires are applied as the base category for road type and tire type, respectively.

Interpretation of multiple linear regression analysis

Two steps are taken to interpret the results of the multiple linear regression. First, an assessment of the model fit is conducted through the interpretation of the F-test and the coefficient of determination (r^2). Second, an evaluation of the effect of the independent variables on the dependent variable is performed by interpreting the value, standard error, t-statistic and p-value of the regression coefficients.

The F-statistic is used to assess the significance of the model and is applied to test the null hypothesis of no relationship between the independent and dependent variables. The null hypothesis is rejected if the p-value is lower than 0.05. Rejection of the null hypothesis indicates that at least one of the independent variables significantly affects the dependent variable. In addition, the coefficient of determination (R^2) indicates how well the model explains the observed variation in the dependent variable relative to the mean. A higher R^2 indicates a better model fit. If R^2 is satisfactory, the effects of the individual variables can be assessed further [71].

As mentioned before, the regression coefficient represents the change in the dependent variable when the corresponding independent variable increases by one unit or deviates from the base category. The degree of uncertainty of β is represented by the standard error. In addition, a t-statistic is applied to determine whether the specific independent variable significantly affects the dependent variable. The null hypothesis of no significant effect can be rejected for a p-value below 0.05, indicating that the independent variable is significantly related to the dependent variable [71].

Assumptions of regression analysis

Multiple linear regression analysis relies on certain assumptions and requirements, namely, continuous response variables, linearity, little to no collinearity, independence of observations, normal distribution of residuals and homoscedasticity of residuals [71, 72, 73, 75]. Both, the continuous response variable and independence of observation depend on the design of the experiment. All observations are independently taken and are stored within a continuous output variable.

Collinearity results from correlation between two independent variables. This is assessed by calculating the variance inflation factor (VIF) for each independent variable (see Eq. 4.9). In this case, R^2 refers to the coefficient of determination, which is obtained by performing regression analysis for which one independent variable is used as dependent variable and the remaining independent variables as independent variables. The assumption of little to no collinearity holds if VIF < 10 [71, 76].

$$VIF = \frac{1}{1 - R^2} \tag{4.9}$$

Homoscedasticity and linearity can be assessed by plotting the standardized residuals against the fitted predicted values. The relationship between dependent and independent variables can be assumed linear if the errors are equally distributed around zero. In addition, homoscedasticity implies that the variance of the error does not change significantly across all levels of the independent variables. The residuals should be scattered randomly around zero, providing a relatively even distribution. It should be noted that a small variation has little effect on the significance of the test. However, the data should approximately meet homoscedasticity [71, 73, 75, 76].

Finally, a frequency distribution of the standardized residuals with a fitted normal distribution curve can be created to visually inspect the normality of the residuals [71, 75, 76]. It is important to note that meaningful conclusions can be drawn only if all assumptions are met [75]. Therefore, it is crucial to test apply these tests. Appendix C provides an analysis of the assumptions for the four regression analyses conducted within this study.

5

Results and Discussion

This chapter provides the results obtained from each test: the ink print test, drum test and rolling losses test (section 5.1, 5.2 and 5.3). In section 5.4, the results of the different measurements are compared to find a relation between contact patch shape and total rolling losses, and to distinguish the effects of rolling resistance and rolling impedance on the total rolling losses. It should be noted that for all results, the estimated values will be presented as mean $\pm$ standard error (SE).

5.1. Ink Print test

Table IV presents the outcomes of the ink print test by giving the mean $\pm$ standard error for the length, width and area of the contact patch for each combination of parameters. Appendix D presents all 73 ink prints with the fitted ellipse, which is used to extract the contact patch measures. The result within the table are visualised in figure 5.1 and 5.2.

Table IV - Estimation of length (l), width (w) and Area (A) of the contact patch obtained from ink print. Values given as $mean \pm SE$

Tubular	*6.0 bar*			*7.5 bar*		
26mm	**l** $[mm]$	**w** $[mm]$	**A** $[mm^2]$	**l** $[mm]$	**w** $[mm]$	**A** $[mm^2]$
• *21 kg*	59.6 ± 0.47	7.28 ± 0.033	341 ± 1.4	61.8 ± 0.35	7.94 ± 0.037	386 ± 3.9
• *30 kg*	73.9 ± 0.058	9.73 ± 0.043	564 ± 3.0	70.3 ± 0.16	9.21 ± 0.063	508 ± 3.6
• *38 kg*	81.1 ± 0.26	10.3 ± 0.023	658 ± 2.2	78.0 ± 0.20	9.96 ± 0.043	610 ± 3.0
Tubeless	*5.3 bar*			*6.0 bar*		
26mm	**l** $[mm]$	**w** $[mm]$	**A** $[mm^2]$	**l** $[mm]$	**w** $[mm]$	**A** $[mm^2]$
• *21 kg*	66.0 ± 0.16	8.08 ± 0.052	419 ± 3.7	65.0 ± 0.42	8.04 ± 0.15	410 ± 9.1
• *30 kg*	74.9 ± 0.16	8.60 ± 0.014	475 ± 1.8	74.6 ± 0.20	8.79 ± 0.012	515 ± 2.0
• *38 kg*	83.4 ± 0.38	9.40 ± 0.015	616 ± 3.7	81.1 ± 0.094	9.26 ± 0.023	590 ± 1.5
Tubeless	*4.8 bar*			*5.3 bar*		
28mm	**l** $[mm]$	**w** $[mm]$	**A** $[mm^2]$	**l** $[mm]$	**w** $[mm]$	**A** $[mm^2]$
• *21 kg*	66.0 ± 0.11	7.73 ± 0.078	401 ± 4.3	64.2 ± 0.095	7.59 ± 0.14	383 ± 6.9
• *30 kg*	76.8 ± 0.43	9.35 ± 0.077	564 ± 1.8	73.9 ± 0.20	9.23 ± 0.050	536 ± 4.3
• *38 kg*	82.9 ± 0.12	9.84 ± 0.046	641 ± 2.3	82.0 ± 0.29	9.62 ± 0.087	620 ± 3.4
Tubeless	*4.3 bar*			*4.8 bar*		
30mm	**l** $[mm]$	**w** $[mm]$	**A** $[mm^2]$	**l** $[mm]$	**w** $[mm]$	**A** $[mm^2]$
• *21 kg*	67.7 ± 0.58	9.84 ± 0.064	471 ± 3.0	64.6 ± 0.22	8.86 ± 0.031	444 ± 3.1
• *30 kg*	77.9 ± 0.31	7.59 ± 0.042	600 ± 1.9	74.3 ± 0.36	10.0 ± 0.031	543 ± 0.85
• *38 kg*	85.5 ± 0.43	9.23 ± 0.20	683 ± 9.7	83.2 ± 0.56	10.2 ± 0.086	660 ± 2.2

In figure 5.1, it can be observed that all measures of the contact patch - length, width and area - generally increase with an increase of vertical load. This is in agreement with the existing literature, as illustrated by equation 2.2. However, three parameter combinations, highlighted with red circles, have odd outcomes. First, for the 30mm Corsa Pro at 4.8 bar, the width of contact patch is larger for a low vertical load (21 kg) in comparison to the higher vertical loads (30, 38 kg). Second, for the 26mm

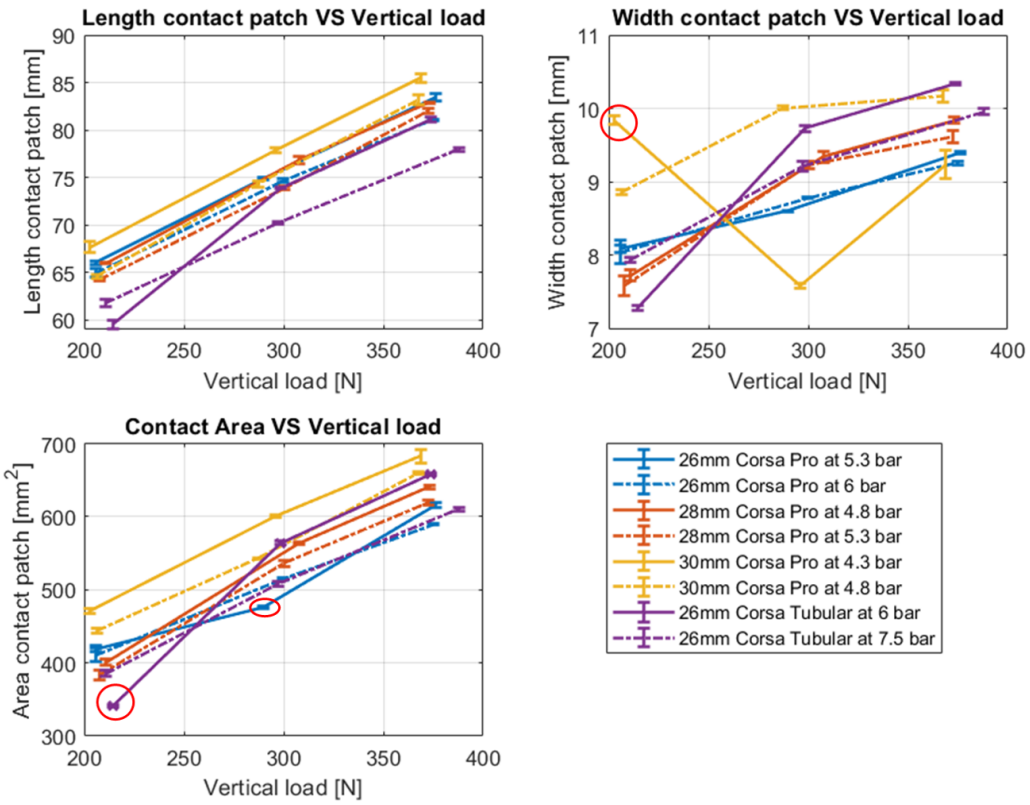

Figure 5.1: The length, width and area of the contact patch against vertical load

Corsa Tubular with 21 kg loading and the 26mm Corsa Pro with 30 kg loading, it can be observed that the contact area is larger at a lower pressure than at a higher pressure, when comparing the same tire deformed under the same load.

The influence of tire pressure on the shape of the contact patch is displayed more clearly in figure 5.2. The length of the contact patch generally decreases as inflation pressure increases, with the exception of the 26mm Corsa Pro Tubular with 21 kg loading. The same relation can be observed for the contact area, however, both the 26mm Corsa Pro Tubular with 21 kg loading and the 26mmm Corsa Pro with 30 kg loading deviate from the other parameter sets. The influence of inflation pressure on the contact patch width is more variable compared to the length and area of contact.

Deviations from the general trend could be a result of human error when taking the ink prints, as the consistency of the fitted ellipse on the ink print has been double checked (see appendix D). While taking the ink print, the tire should be placed carefully on the piece of paper to prevent bouncing, as this could result in an increase of contact area. The possibility exists that a small bounce has occurred, which could result in deviation from the general trend. In addition, as human judgement is involved with extracting the ink print parameters, a small bias could be introduced within the results as an absolute offset from the true value. This bias will have a larger influence on estimation of contact width compared to contact length, as the width's magnitude is approximately a eight times smaller compared to contact length. This could explain why the influence of the inflation pressure is more variable for the width of the contact patch compared to the contact length and area.

Table V and VI present estimated regression coefficients for the analysis that focuses on understanding the impact of tire type, tire width, vertical load and inflation pressure on the contact patch length and width, respectively. The regression analysis of the contact patch length has recorded a model p-value of $9.02\text{E} - 51$ and a R^2 of 0.97. Meanwhile, the regression analysis of the contact width recorded a model p-value of $5.79\text{E} - 26$ and an R^2 of 0.836. For both models this indicates that at least one independent variable significantly affects the assessed dependent variable, and that there is a good model fit.

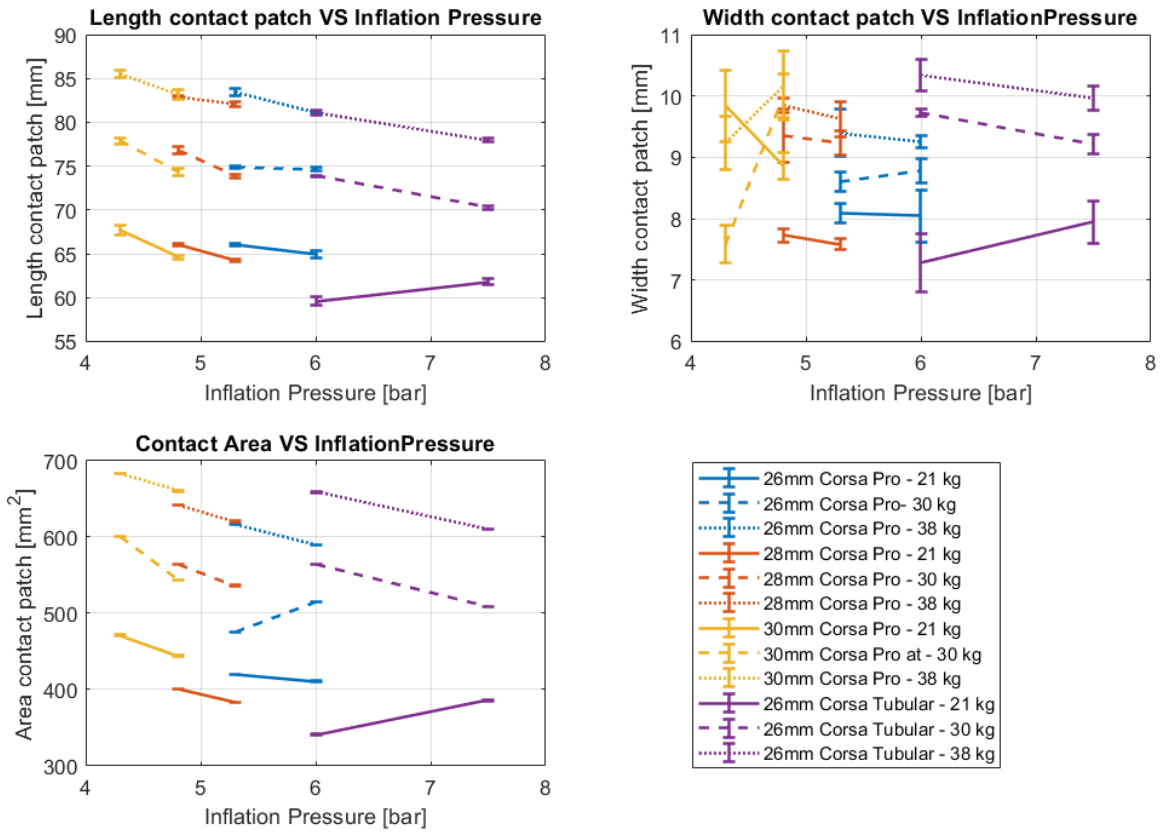

Figure 5.2: The length, width and area of the contact patch against inflation pressure

Tire type, inflation pressure and vertical load are significantly related to the contact patch length (p-values of 0.0080073, $2.514\text{E}{-6}$ and $1.5666\text{E}{-52}$, respectively). However, tire width is not significantly related to the length of the contact patch (p-value of 0.6867). On the other hand, the contact width is significantly affected by tire type, tire width and vertical load (p-values of 0.0015177, $1.724\text{E}-5$ and $1.0259\text{E}{-26}$, respectively), but not by inflation pressure (p-value of 0.29834). The sign of the regression coefficient estimates, in combination with the p-value, suggest that tubular tires have a shorter and wider contact patch compared to tubeless tires. In addition, wider tires increase the contact width, a higher inflation pressure decreases contact length and a higher vertical load increases both the length and width of the contact area. The variation in these factors subsequently affect the contact area, which is a function of the length and width of the contact patch.

Table V - Estimated regression coefficients for contact patch length

	Estimate	*SE*	*tStat*	*pValue*
(Intercept)	54.562	5.5617	9.8104	$1.1871\text{E}-14$
TireType_Tubular	-1.6215	0.59345	-2.7323	0.0080073
TireWidth	-0.060707	0.14987	-0.40507	0.6867
InflationPressure	-1.8124	0.35267	-5.1392	$2.514\text{E}-6$
VerticalLoad	0.10628	0.0023456	45.308	$1.5666\text{E}-52$

Table VI - Estimated regression coefficients for contact patch width

	Estimate	*SE*	*tStat*	*pValue*
(Intercept)	1.2151	1.4766	0.82292	0.41343
TireType_Tubular	0.52074	0.15756	3.3051	0.0015177
TireWidth	0.18406	0.039788	4.626	$1.724\text{E}-5$
InflationPressure	-0.098126	0.093629	-1.048	0.29834
VerticalLoad	0.010823	0.00062274	17.38	$1.0259\text{E}-26$

5.2. Drum testing

Table VII presents the outcomes of the drum test obtained from 95 observations, by giving the mean $\pm$ standard error for estimated C_{rr}. For some estimations, no standard error has been reported. This could mean that only one repetition has been performed for that specific parameter set due to time constraints, which applies to all pressures of the 26mm Corsa Pro at 30 km/h with 35kg loading and for 28mm Corsa Pro at 4.8 bar, 30 km/h and with 35kg loading. For all other cases, in which standard error has not been reported, the two or more repetition do not differ from each other.

Table VII - Estimated $C_{rr} \pm SE$ obtained with drum testing

Tire	**v [kmh]**	**p [bar]**	C_{rr} ±**SE** (load = 35kg)	C_{rr} ±**SE** (load = 45kg)
26mm Corsa Tubular	30	7.5	$0.00385 \pm 1.443\text{E} - 5$	$0.00365 \pm 1.587\text{E} - 5$
		6.8	0.00381	0.00377
		6.0	$0.00391 \pm 1.443\text{E} - 5$	0.00397
	40	7.5	$0.00383 \pm 3.061\text{E} - 5$	$0.00380 \pm 1.190\text{E} - 5$
		6.8	$0.00404 \pm 1.531\text{E} - 5$	$0.00391 \pm 1.190\text{E} - 5$
		6.0	0.00416	$0.00413 \pm 1.190\text{E} - 5$
26mm Corsa Pro	30	6.0	0.00248	$0.00248 \pm 1.587\text{E} - 5$
		5.7	0.00254	0.00254
		5.3	0.00263	0.00263
	40	6.0	$0.00276 \pm 1.531\text{E} - 5$	$0.00272 \pm 1.190\text{E} - 5$
		5.7	0.00281	$0.00275 \pm 1.190\text{E} - 5$
		5.3	0.00288	0.00286
28mm Corsa Pro	30	6.0	0.00257	0.00249
		5.8	$0.00264 \pm 2.041\text{E} - 5$	$0.00253 \pm 1.296\text{E} - 5$
		5.3	0.00274	$0.00261 \pm 1.122\text{E} - 5$
		4.8	-	0.00276
	40	6.0	0.00279	$0.00275 \pm 1.612\text{E} - 5$
		5.8	$0.00281 \pm 1.767\text{E} - 5$	$0.00277 \pm 8.418\text{E} - 6$
		5.3	$0.00289 \pm 2.794\text{E} - 5$	$0.00285 \pm 1.684\text{E} - 5$
		4.8	$0.00299 \pm 2.165\text{E} - 5$	$0.00299 \pm 2.572\text{E} - 5$
30mm Corsa Pro	40	4.8	$0.00302 \pm 1.531\text{E} - 5$	$0.00296 \pm 2.381\text{E} - 5$
		4.3	$0.00313 \pm 1.531\text{E} - 5$	$0.00304 \pm 1.190\text{E} - 5$

The estimated C_{rr} values range from 0.00248 to 0.00416. Drum tests performed in previous research has reported C_{rr} values in the range of 0.00362 to 0.00499 [39]. It can be concluded that the estimated C_{rr} has the appropriate magnitude when comparing them to values from previous studies. The difference could result from differences in test parameters. Figure 5.3 and 5.4 visualize the influence of the tire parameters on the estimation of C_{rr}.

Figure 5.3 can be used to compare the different tires under the same conditions. It can be observed that the tubular tire has a quite higher C_{rr} compared to the tubeless tires. While the estimates of C_{rr} for the tubeless tire with different widths and at the same pressure are comparable. In addition, it could be observed that the estimations of C_{rr} reduces as the inflation pressure increases, which is in agreement with the statements from literature (see section 2.2.1).

Figure 5.4 can be used to assess the effects of test parameters to each tire. It seems that the vertical load has little to no effect on the estimated rolling resistance. If an effect is visible, C_{rr} decreases as vertical load increases. However, this contradicts with literature, which states that an increase in vertical load results in an increase of C_{rr} (see section 2.2.1). In addition, the cycling velocity seems to affect the rolling resistance. Even though, in section 2.3.2, it is stated that for velocities up to 40 km/h, the speed-dependency of rolling resistance could be disregarded. To better understand the significance of these observations, it is essential to examine the multiple linear regression analysis.

Table VIII presents the estimated regression coefficients for the analysis, focusing on understanding the impact of tire type, tire width, vertical load, inflation pressure and cycling velocity on C_{rr}. The regression analysis has recorded a model p-value of $2.78\text{E} - 5$ and a R^2 of 0.997. This indicates that model is a good fit for prediction of C_{rr} and that at least one independent variable significantly affects the C_{rr} estimate.

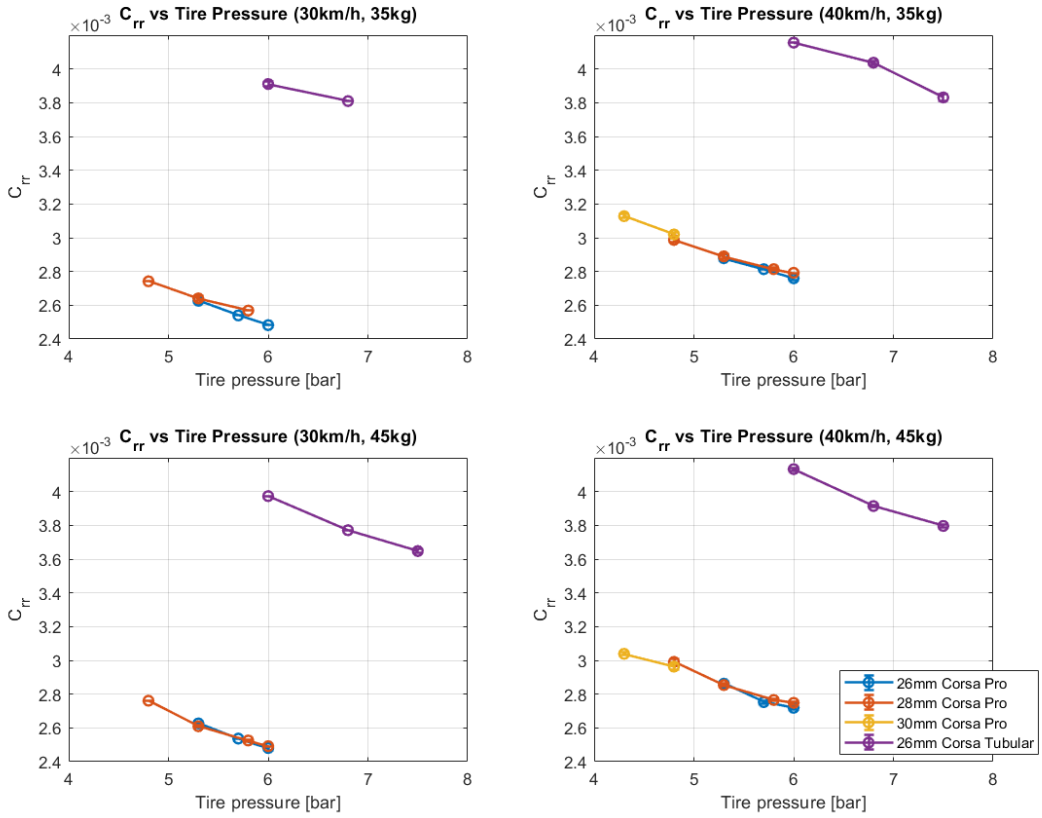

Figure 5.3: Drumtest Results - C_{rr} vs Tire pressures for 26mm, 28mm & 30mm Corsa Pro and 26mm Corsa Tubular under each tested condition: 30kmh & 35kg, 30kmh & 45kg, 40kmh & 35kg, 40kmh & 45kg

The p-values of the estimated regression coefficients indicate that all five independent variables significantly influence C_{rr}. The tubular tire has a significantly higher C_{rr} compared to tubeless tires (p-values is $3.3085\text{E} - 107$). In addition, both an increase in velocity or an increase in tire width, significantly increases C_{rr}. In contrast, an increase of inflation pressure or an increase of vertical load results in a significant decrease of C_{rr}. The significant negative relation between vertical load and C_{rr} is in contrast with previous studies. This difference might be caused do to the differences in contact pressures on a curved surface compared to a flat surface.

Last, despite the significant relationships between tire width, vertical load, and cycling velocity with C_{rr}, changes in these tire parameters by one unit (mm, kg, km/h) result in only a 0.01% to 1% change in C_{rr}. This can be determined from the absolute value of the regression coefficients, which are $6.8352\text{E} - 6$, $3.127\text{E} - 6$ and $2.2991\text{E} - 5$, respectively. However, *Grappe et al.* reported that a decrease of 0.02% of rolling resistance coefficient could already have a significant impact in racing performance [38]. Therefore, racing performance could still be significantly improved by changes of tire width and vertical load.

Table VIII - Estimated regression coefficients for C_{rr} of drum test

	Estimate	*SE*	*tStat*	*pValue*
(Intercept)	0.0029441	0.00010554	27.897	$8.9157\text{E} - 46$
TireType_Tubular	0.0014232	$9.8886\text{E} - 6$	143.92	$3.3085\text{E} - 107$
TireWidth	$6.8352\text{E} - 6$	$3.0718\text{E} - 6$	2.2251	0.028599
InflationPressure	-0.00019817	$6.1916\text{E} - 6$	-32.007	$1.3031\text{E} - 50$
VerticalLoad	$-3.127\text{E} - 6$	$5.8909\text{E} - 7$	-5.3082	$8.051\text{E} - 7$
Velocity	$2.2991\text{E} - 5$	$6.1176\text{E} - 7$	37.581	$2.1545\text{E} - 56$

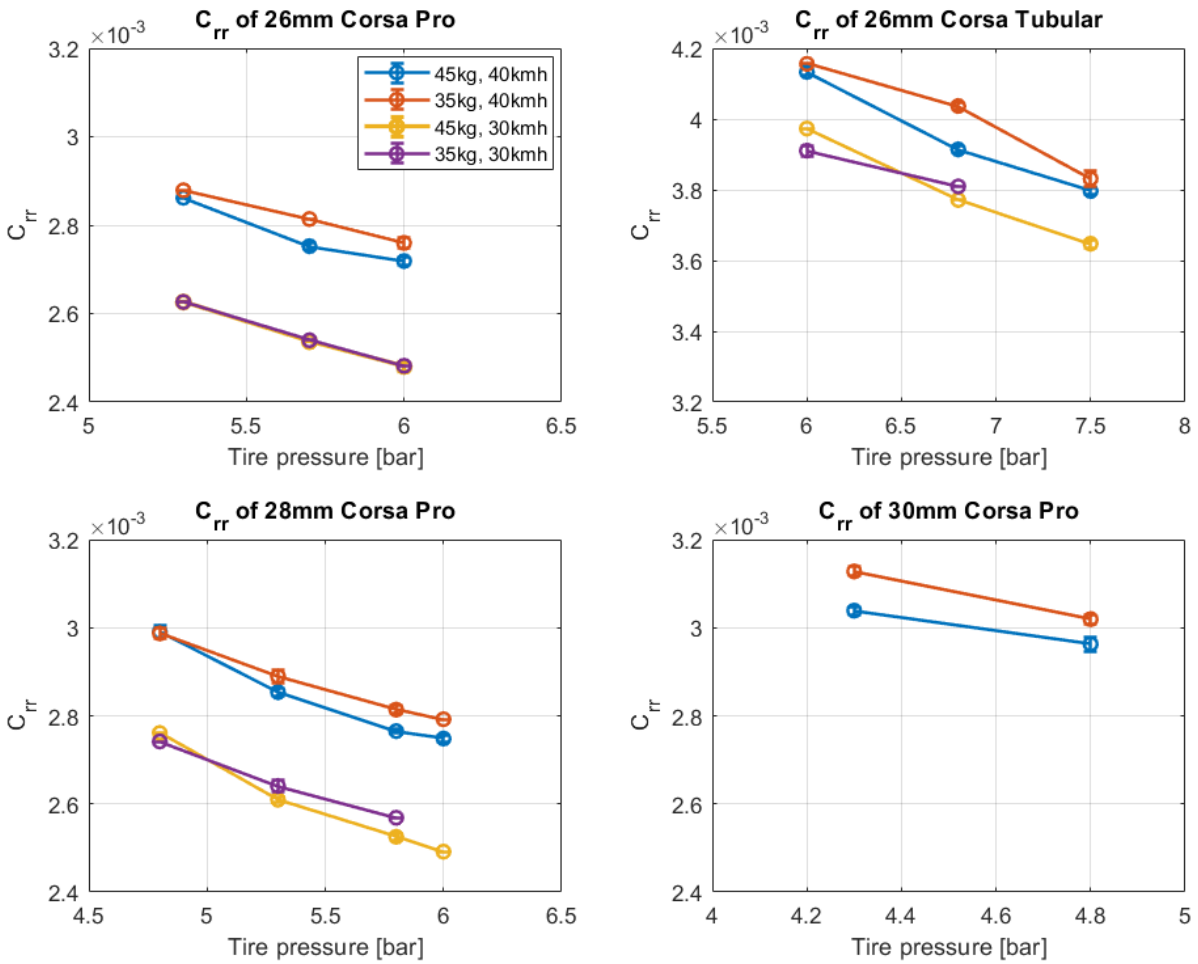

Figure 5.4: Drumtest Results - C_{rr} vs Tire pressures with all condition in one plot fro each tire (26mm, 28mm & 30mm Corsa Pro and 26mm Corsa Tubular)

5.3. Rolling losses measurement

Table IX presents the outcomes of the rolling losses measurements obtained from 83 observations by giving the mean $\pm$ standard error for estimated C_{rr}. The estimated values range from 0.001610 to 0.003174. The magnitude of this estimate is comparable to the C_{rr} values obtained with existing measurement techniques [77]. However, the values are within the lower limit of expected C_{rr} for bicycle tires. Figure 5.5 and 5.6 illustrates the influence of inflation pressure, cycling velocity and road surface on the estimation of C_{rr}.

Figure 5.5 depicts C_{rr} for different tire pressures. The trends of these lines differ from the trends visualised in figure 5.3 and 5.4, which presents the result of the drum test. The drum test obtained the lowest C_{rr} for the highest inflation pressure. However, the optimal C_{rr} obtained with road testing differs between low, moderate and high pressures. The trends of figure 5.5 are comparable to generalized model of the total rolling losses depicted in figure 2.4. By including the energy absorbing rider within the measurement setup, the trade-off between rolling resistance and rolling impedance had been visualised. This results in low and moderate inflation pressures being used more often during road racing.

From figure 5.5, it can also be observed that an increase in cycling velocity results in an increase in C_{rr}. This also applies for an increase of road roughness. However, the influence of velocity and road surface on C_{rr} is more clearly visualized in figure 5.6. It can be concluded that the total rolling losses on asphalt is smaller compared to the total rolling losses on bricks. In addition, this figure shows

that the differences in C_{rr} between 26mm and 28mm tire increases as cycling velocity increases. At a cycling velocity of 30 km/h, the maximum difference in C_{rr} is 0.00029 for all tire combination on bricks and 0.00011 for the tire combinations on asphalt. For a cycling velocity of 40 km/h, the maximum difference doubles for both asphalt and bricks, which is in the favor of the 28 mm Corsa Pro as it starts to outperform the 26 mm Corsa Pro at higher velocities.

Table IX - Estimated $C_{rr} \pm SE$ obtained with rolling losses measurement

Road	Tire	v [kmh]	p [bar]	# Runs	C_{rr} ±SE
Bricks	26mm Corsa Pro	30	6	6	$0.002306 \pm 1.4522\text{E}-4$
			5.7	2	$0.002466 \pm 5.9980\text{E}-4$
			5.3	3	$0.002471 \pm 3.9100\text{E}-4$
		40	6	8	$0.002731 \pm 1.1224\text{E}-4$
			5.7	4	$0.002725 \pm 3.5210\text{E}-4$
			5.3	3	$0.002871 \pm 4.9989\text{E}-4$
	28mm Corsa Pro	30	5.8	3	$0.002596 \pm 3.8205\text{E}-4$
			5.3	3	$0.002418 \pm 2.9822\text{E}-4$
			4.8	3	$0.002363 \pm 3.1182\text{E}-4$
		40	5.8	2	$0.003174 \pm 8.6482\text{E}-4$
			5.3	3	$0.002847 \pm 3.1097\text{E}-4$
			4.8	3	$0.002646 \pm 3.9360\text{E}-4$
Asphalt	26mm Corsa Pro	30	6	4	$0.001622 \pm 2.4322\text{E}-4$
			5.7	5	$0.001610 \pm 2.6916\text{E}-4$
			5.3	3	$0.001736 \pm 3.4381\text{E}-4$
		40	6	3	$0.001939 \pm 4.7584\text{E}-4$
			5.7	3	$0.001991 \pm 5.0787\text{E}-4$
			5.3	4	$0.002068 \pm 2.0760\text{E}-4$
	28mm Corsa Pro	30	5.8	3	$0.001692 \pm 3.5785\text{E}-4$
			5.3	3	$0.001613 \pm 3.8511\text{E}-4$
			4.8	3	$0.001727 \pm 3.1460\text{E}-4$
		40	5.8	3	$0.001804 \pm 5.5908\text{E}-4$
			5.3	3	$0.001774 \pm 5.2162\text{E}-4$
			4.8	3	$0.002011 \pm 3.5157\text{E}-4$

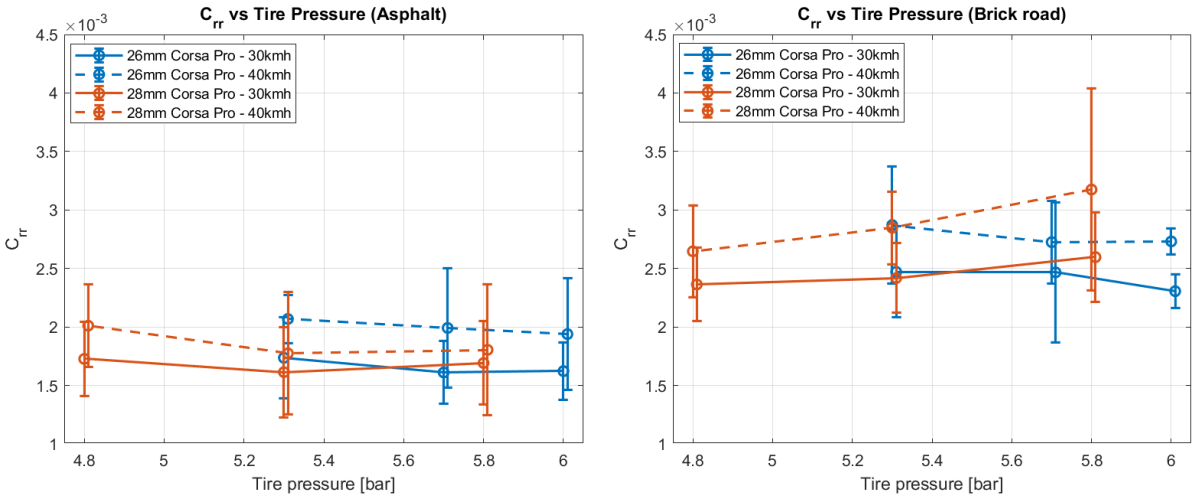

Figure 5.5: C_{rr} for different tire pressures for 26mm & 28mm Corsa Pro at 30 and 40 km/h on both asphalt and brick roads. Inflation pressures for estimates at 40 km/h are shifted with 0.01 to distinguish between error bars of each estimate

During road racing, the tire parameters should be carefully selected to minimize the total resistance. The total rolling losses during road racing can be minimized by adapting the tire and its inflation pressure to the specific road surface. To identify the optimal parameter set for high cycling velocities, it is crucial

to consider the road surface characteristics. For brick road at high cycling velocity, the 28mm Corsa Pro at 4.8 bar gives the lowest C_{rr} ($0.002646 \pm 3.9360\text{E} - 4$), while for asphalt the 28mm Corsa Pro at 5.3 bar gives the lowest C_{rr} ($0.001613 \pm 3.8511\text{E} - 4$). This shows that the surface roughness influences the appropriate tire pressure, also called the break-point pressure. However, it should be noted that the standard error of the mean C_{rr} is relatively high, which results in overlap of standard errors for different parameter sets. This questions the significance of the relations between the tire and road characteristics their impact on the C_{rr}.

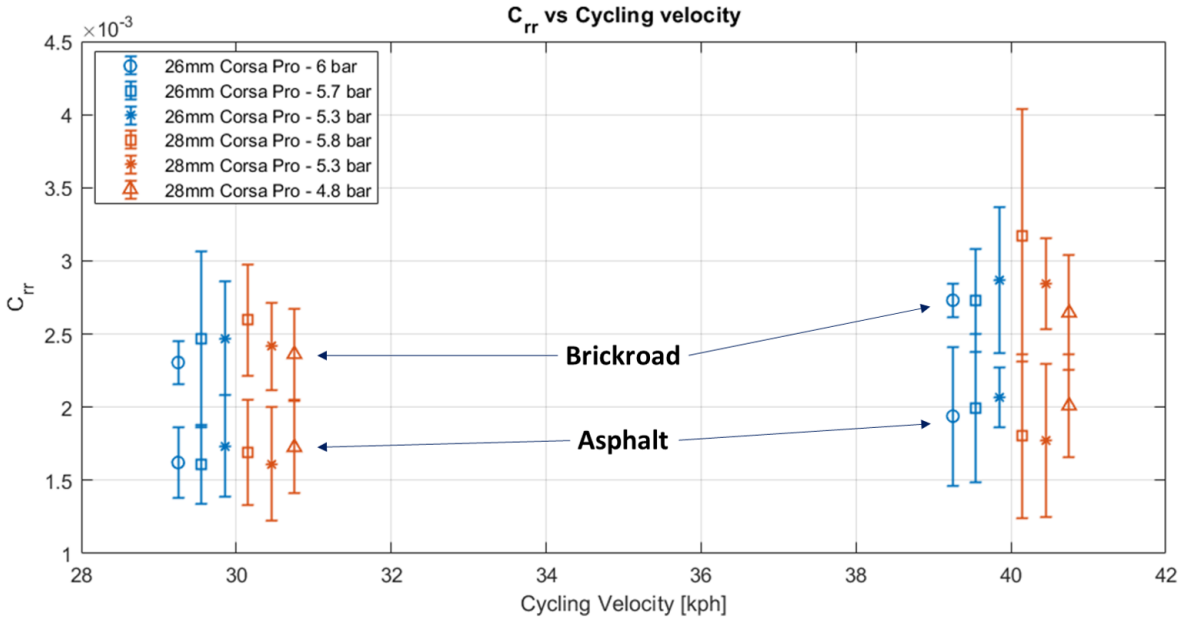

Figure 5.6: C_{rr} at 30 and 40 km/h for 26mm & 28mm Corsa on both asphalt and brick roads. The cycling velocity of all estimates is either 30 km/h or 40 km/h and depends around which value the estimate is centered

Multiple linear regression analysis is conducted to assess the significance of the impact of road type, tire width, inflation pressure, and cycling velocity on C_{rr}. Table X presents the estimated regression coefficients for this analysis, with a model p-value of $1.93\text{E}-20$ and a R^2 of 0.714. The p-value indicates that at least one independent variable significantly affects the C_{rr} estimate. While the R^2 suggests that the model provides a good fit, however, there might be some limitations when applying this model for prediction of C_{rr}. Nevertheless, conclusions could be drawn regarding the relationship between the dependent and independent variables.

Road type and cycling velocity have a significant influence on C_{rr} (p-value of $1.5021\text{E} - 20$ and $1.813\text{E} - 6$, respectively). The total rolling losses on asphalt roads is significantly lower compared to brick roads. In addition, an increase in cycling velocity results in an increase of the total rolling losses. On the other hand, the tire width and inflation pressure do not significantly affect the C_{rr}. This might result from the relative high standard error of C_{rr}. For future experiments, it is recommended to increase the number of data points within one test run to reduce the standard error of the estimate. This will boost statistical power, which allows for more robust and significant results.

Table X - Estimated coefficients Multiple linear regression

	Estimate	*SE*	*tStat*	*pValue*
(Intercept)	0.0013221	0.001409	0.93835	0.35096
RoadType_Asphalt	-0.000809	$6.4051\text{E} - 5$	-12.631	$1.5021\text{E} - 20$
TireWidth	$6.6141\text{E} - 6$	$3.8211\ e - 5$	0.1731	0.86303
InflationPressure	$-1.9458\text{E} - 5$	$9.3464\text{E} - 5$	-0.20818	0.83563
Velocity	$3.4262\text{E} - 5$	$6.6367\text{E} - 6$	5.1625	$1.813\text{E} - 6$

5.4. Combined Results

In this section, the result of the ink print measurements are combined with the results of the drum test to assess how contact patch shape influences the rolling resistance. In addition, the C_{rr} estimates obtained with drum test are plotted against the C_{rr} estimates of road testing to try to assess the separate contribution of rolling resistance and rolling impedance to the total rolling losses.

Figure 5.7 presents the relationship between the contact patch measures and the estimates of C_{rr} obtained with drum testing. To ensure comparable load conditions, this analysis incorporates the contact measures obtained with a 38 kg load and an interpolation of the C_{rr} obtained with 35 kg and 45 kg load on the drum. Generally, an increase of the length, width and area of the contact patch result in an increase in rolling resistance. In addition, the lower tire pressures are associated with a higher rolling resistance and larger contact length, width and area. The only exception is the 30mm Corsa Pro tire, which shows deviating results for the width of the tire pressure. This results from deviation in shape of the contact patch as shown in figure 5.1. In section 5.1, some possible explanations regarding this deviation are already discussed.

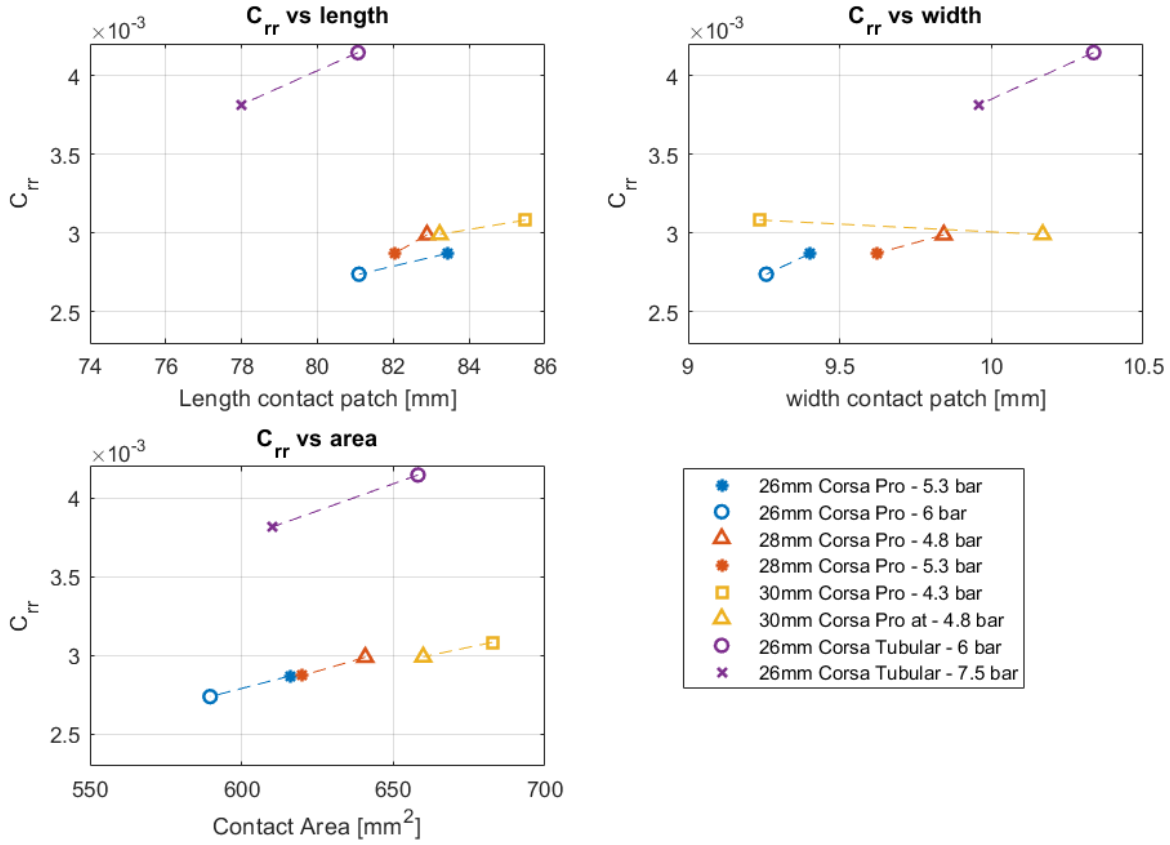

Figure 5.7: Relates the estimated parameters of drum test and ink print measurement with a load of 38 kg by plotting each contact measure against C_{rr} at 40 km/hh

In figure 5.8, the C_{rr} obtained on the drum surface, on asphalt and on bricks for varying inflation pressures is presented for both 30 and 40 km/h. It should be noted that the estimates for bricks and asphalt are obtained with a 54 kg load, while the estimates on the drum are obtained with a 45 kg load. It can be observed that the drum test results in higher estimates of C_{rr} compared to the estimates on asphalt, even though, the vertical load is smaller. In addition, C_{rr} estimates of the drum test are higher or equal to the estimates on brick roads. This is against expectations. It was expected that drum testing showed lower values compared to rolling losses test, due to the absence of rolling impedance, the smoothness of the drum surface and the lower vertical load.

There are some ideas that could explain the difference between expectation and measurement results. First, the gravitational influences on the total rolling losses during road testing might have been overestimated. The gravitational losses extracted based on changes in elevation, which were

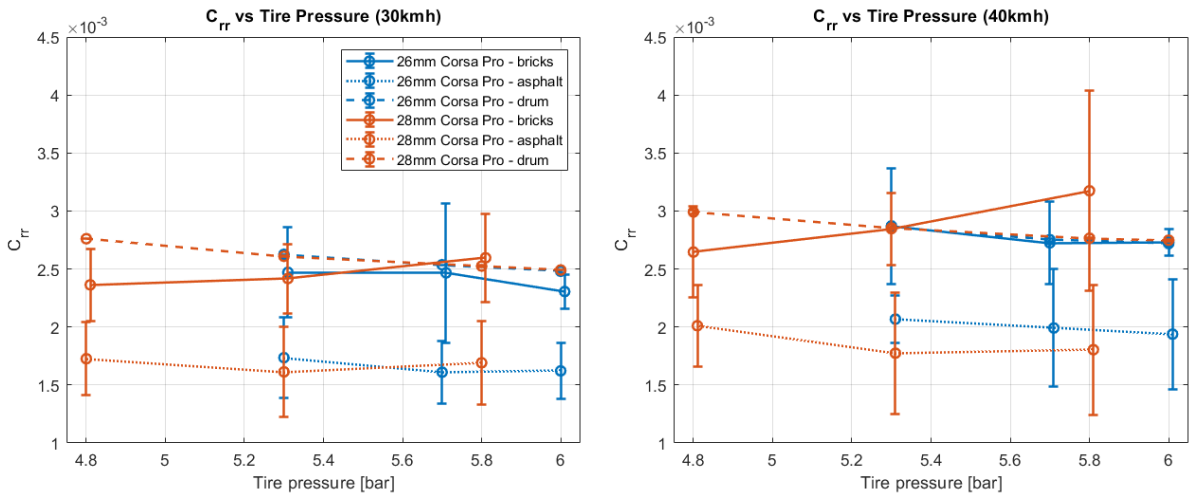

Figure 5.8: Estimated C_{rr} vs Inflation pressure for both road testing and drum testing

extracted from GPS data (see section 4.4). Second, during drum testing it was observed that the tire was bouncing on the drum during the measurement. This bouncing could have increased the estimation of C_{rr} by increasing the energy losses due to tire hysteresis. When the tire bounces on the drum, the tire constantly deforms and recovers. During each cycle of deformation and recovery some energy is lost due to hysteresis. This will explain why the magnitude of the estimated values of the drum test are more comparable to the brick road than the asphalt road, as the vibration of the road surface could introduce the same affect on hysteresis losses.

There are two less likely explanation for the difference between expectation and measurement results. First, the bouncing of the tire could result in rolling impedance losses. It has been stated that the vibrational energy experienced during cycling can be dissipated within the bicycle frame, suspension system or cyclist [14]. However, most vibrations are absorbed by the cyclist due to the design of road bicycles. In contrast, the drum tester could have a suspension system that dissipates the vibrational energy, which results in an increase of C_{rr}. This explanation is less likely, as the drum test still shows the trend in which rolling resistance decreases as inflation pressure increases, which does not include the trade-off between rolling resistance and rolling impedance.

Last, the curvature of the drum could result in an overestimation of the rolling resistance. It has been reported that the curvature of the drum creates a higher tension in the tire, which results in a higher rolling resistance estimation [14]. However, equation 4.2 is applied to correct for the curved surface by reducing the rolling resistance estimate, which means that it is not likely that this has resulted in the difference between expectation and measurement results. This means that the overestimation of gravitational losses, an increase in hysteresis losses due to bouncing or a combination of both might be the cause.

6

Conclusion

To conclude this master's thesis, the questions stated within the introduction should be answered. The main goal of this thesis is to understand how tire parameters influence the total rolling losses. Literature has shown that tire parameters and factors associated with tire-road interaction influence the total amount of rolling losses, however, this study does not establish significant relationships for all parameters discussed in the literature. The multiple linear regression analysis has verified that tire type, inflation pressure and vertical load affect the contact patch length, while tire type, tire width and vertical load affect the width of the contact patch. From this, it can be concluded that the area of the contact patch is influenced by all four variables, as contact area is a function of contact width and length. In addition, the estimation of C_{rr} on the drum is affected by tire type, width, inflation pressure, vertical load and velocity. On the other hand, the C_{rr} estimate from the rolling losses measurement is only significantly affected by road surface type and cycling velocity.

Other than the significant influence of tire type, tire width, inflation pressure and vertical load on the shape of the contact patch, several trends were observed. First, tubular tires have a wider and shorter contact patch compared to tubeless tires with the same parameters. This result from the sign of the regression coefficient corresponding to tire type. Second, the length, width and area of the contact patch, generally increase as vertical load increases. Third, the length and the area of the contact patch decrease as the inflation pressure increases. The effects of inflation pressure on the width of the contact patch are more variable, and no significant trend could be extracted. However, it can be stated that the width of the contact patch does increase with the tire width.

The ink print test was applied to assess the shape of the contact patch. However, the relationship in which an increase in C_{rr} is associated with an increase in the contact patch measures is extracted by conducting drum tests and total rolling loss measurements. In chapter 3, an analysis of existing measurement techniques and the development process of new measurement techniques has been discussed. The bike trailer measurement has been selected as the most appropriate measurement technique based on the possibility to eliminate the influence of aerodynamic drag and to test on different road surfaces. This technique has been able to identify differences in C_{rr} estimates when varying different parameters, however, the standard error of the mean is still very high. In addition, it is suspected that there is and underestimation of C_{rr} due to an overestimation of slope influence using the GPS data.

The bike trailer has proven to be a good technique to estimate the total rolling losses, however, the measurement technique can be improved by addressing these issues. First, the duration of the measurement should be increased to minimize the standard error. *Wilson* has stated that pedaling power is highly variable and requires averaging. To obtain a good estimate, the measurement time should be extended to 2 minutes [14]. To verify this, it is recommended to use the obtained data from this experiment to perform a power analysis, which results in the determination of the appropriate sample size for each test run. In addition, the effects of slope on the estimate should be handled better. The bike trailer measurement eliminates air drag and inertial resistance, which means that from the main resistances, only the rolling losses and gravitational losses are still present within the power estimate. This means that gravitational resistance could significantly influence the final results. To properly eliminate the gravitational effects, other measurement equipment than GPS should be

applied which will result in a more accurate contour map of the road. Examples of such measurement techniques are surveying or mobile mapping, which use a digital level and GPS in combination with lasers and camera's, respectively.

Even though the bike trailer measurement has some points of improvement, the measurement did determined the C_{rr} for variation in road surface, cycling velocity, tire width and tire pressure. The tested tire parameters were selected within the range to maintain puncture resistance and handling control. It could be concluded that the 28mm Corsa Pro at 4.8 bar minimizes the rolling losses for cycling on brick roads at 40 km/h, while the 28mm Corsa Pro at 5.3 bar does this for asphalt roads. The brick road has a higher surface roughness compared to asphalt. The optimum parameter set for both roads show that the rougher road surface has resulted in a decrease of optimal tire pressure. However, it should be noted that these observations are not significant due to the relative high standard of the mean.

Lastly, combining the result of the rolling losses with the results of the drum test was supposed to identify the individual contribution of rolling resistance and impedance to the total rolling losses. However, the results has shown that against expectation, the drum test resulted in higher estimation of rolling resistance compared to the estimated rolling losses, which is the sum of rolling resistance and rolling impedance. Combining results from different tests should be more carefully considered as it might be difficult to compare rolling resistance estimations from different experiments [44].

To create this distinction between rolling resistance and rolling impedance in future research, it would be advised to apply a method that assesses pure rolling resistance that is more comparable in test setup to the total rolling losses measurement. This will facilitate the comparison of the results from the different measurements, as equal surface conditions allow for generation of comparable vibrations at the tire-road interface. An example is the use of the tire trailer method discussed in table I. This method enables the exact same measurement as performed with the bike trailer, but without including the energy-absorbing cyclist responsible for the impedance losses.

When applying this method, two points need to be addressed. First, to prevent an overestimation of pure rolling losses, the tire trailer should not have any suspension features that result in dissipation of vibrational energy. The damping characteristics of the trailer should match that of the racing bicycle, which ensures that the only difference in test setup compared to the bike trailer is the exclusion of the energy absorbing cyclist. Second, the issue regarding sensitivity to trailer angle should be addressed to improve measurement accuracy on uneven roads. If both of these issues are addressed, then the two measurement will result in equal tire hysteresis losses, however, the addition of the energy-absorbing cyclist during the rolling losses measurement would result in an increase of energy losses due vibrational energy absorption by the cyclist.

A

Proof of concept: Bike Trailer

The bike trailer measurement is based on the assumption that a cover will eliminate the influence of air drag, as the air within the enclosed space of the trailer will move along with the cyclist. In case of testing on a leveled surface at constant speed, the only resistance experienced during cycling within this enclosed space is the rolling losses. It is needed to verify the proper elimination of air drag when using a moving cover. For this reason, a proof of concept is performed for the bike trailer measurements.

Method

A small trailer is created with an opening of 2.5 cm between the ground and the boarder of the trailer (see Fig. A.1B). An anemometer is placed within the enclosed space. As the anemometer doesn't have a logging mechanism, a camera is placed within the trailer and facing the anemometer (see Fig. A.1C).

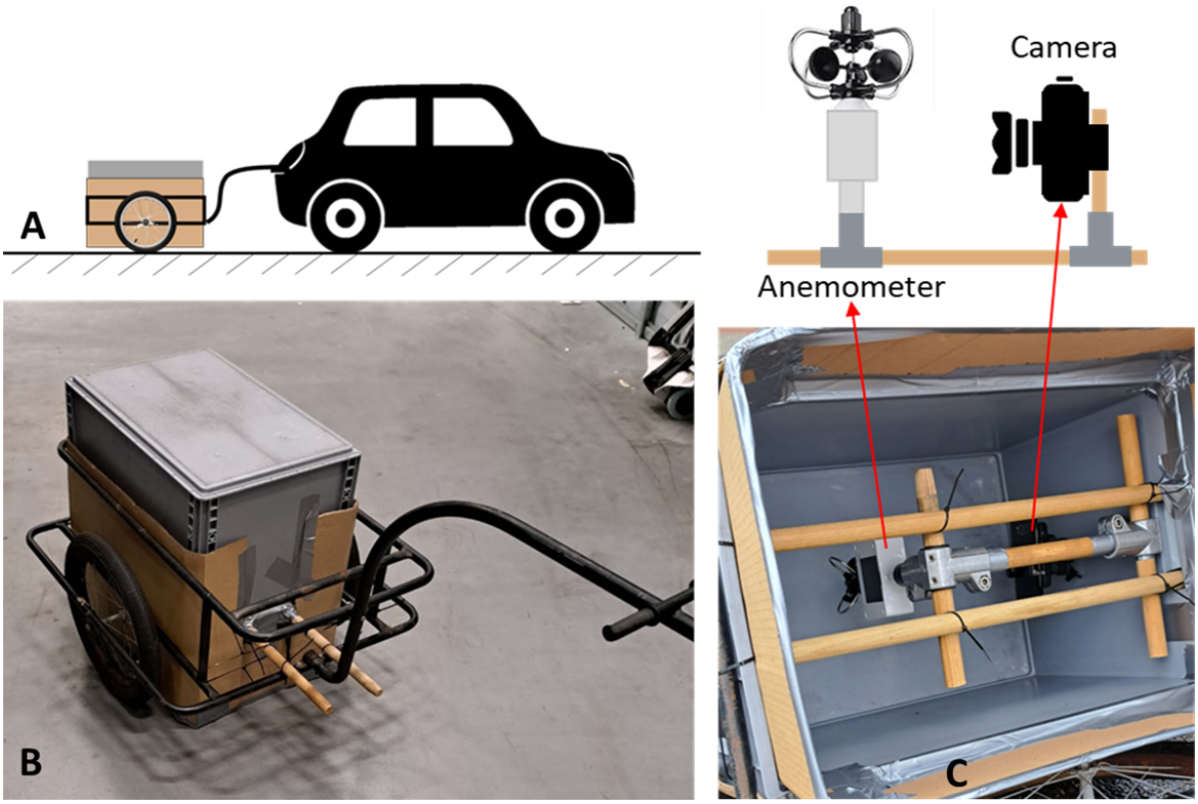

Figure A.1: Test setup used as proof of concept A) schematic of test setup B) Trailer C) Measurement equipment

The trailer is pulled behind a car, which is accelerating to 60 km/h and decelerating to a standstill (see Fig. A.1A). During this run the time on which the car is riding a specific speeds (15, 20, 25, 30, 35, 40, 45, 50, 55, 60 km/h) is recorded. This is done by synchronizing a stopwatch with the recording time of the camera. Afterwards, the video is analysed to verify whether air drag was experienced within the enclosed space. In addition, The wind conditions on the day of the measurement are extracted from the *KNMI*. They provide data regarding average and maximum wind speed for each day and each region of the Netherlands.

Results & Conclusion

The anemometer has recorded a maximum wind speed of 0.3 m/s, which corresponds to a driving velocity of 55 km/h (=15.3 m/s). For all driving velocity below 45 km/h (=12.5 m/s), the anemometer recorded a wind speed of 0.0 m/s. In addition, the average wind speed on the day of testing was 6 m/s.

It can be concluded that a cover will shield the cyclist from air resistance for velocity up to 45 km/h. For velocities higher than 45 km/h and up to 60km/h, most of the air resistance will be removed, however, the gap between the trailer and the road will allow for some air movement within the enclosed space. The concept of eliminating air drag by using a coverage is valid for the speeds tested within the proof of concept. It is not known what would happen to the air flow as speed is further increased.

B

Design Bike Trailer

The bike trailer is a type of windshield that creates an enclosed space around a cyclist and can be used to eliminate the air resistance experienced during cycling. During the experiments the bike trailer will be towed behind a car across a straight road section at a maximum speed of 40 km/h (see fig. B.1). This chapter will provide an overview of the design of the bike trailer and the measures taken to guarantee safety of the participant.

Figure B.1: Rolling loss measurements on a brick road

Design

The trailer is built from steel tubes (18x1 mm) and aluminum tubes (18x2 mm) (see Fig. B.2). The carrying beams are made of steel due to higher strength, the other beams are made of aluminum to minimize the weight. Bracing is applied to further strengthen the construction. The tubes are connected with the use of plastic lightweight clamps and solid aluminum clamps. At the critical points, such as wheel attachment and coupling, solid clamps are used. Otherwise, the lightweight clamps are used. The metal frame is covered with see-through plastic PVC sheet of 0.5 mm, creating an enclosed space within the trailer, which shields the cyclist from the wind while maintaining an overview of the surroundings (see fig. B.3). To minimize air entering the trailer through the gap between the trailer and the road, a brush strip is connected to the bottom of the trailer.

At the inside of the trailer double sided corrugated plastic is used to create a safety boarding between the enclosed space and the edges of the trailer. This boarding will create separation between the cyclist within the enclosed space and the rotating wheels and sharp edges of the bike trailer. In addition, to prevent the cyclist from getting stuck between the frame elements a Lexan polycarbonate (PC) plates are placed above the boarding of corrugated plastic. This plate has the dimension of 2050x1250 and is placed at the back part of the trailer. Lexan PC plates have a high impact resistance, which means that in case of a fall, the cyclist will not fall through the sides of the frame. Rather, the cyclist will be guided to the back of the trailer where the doors will open to create a safe passage for the cyclist out of the trailer.

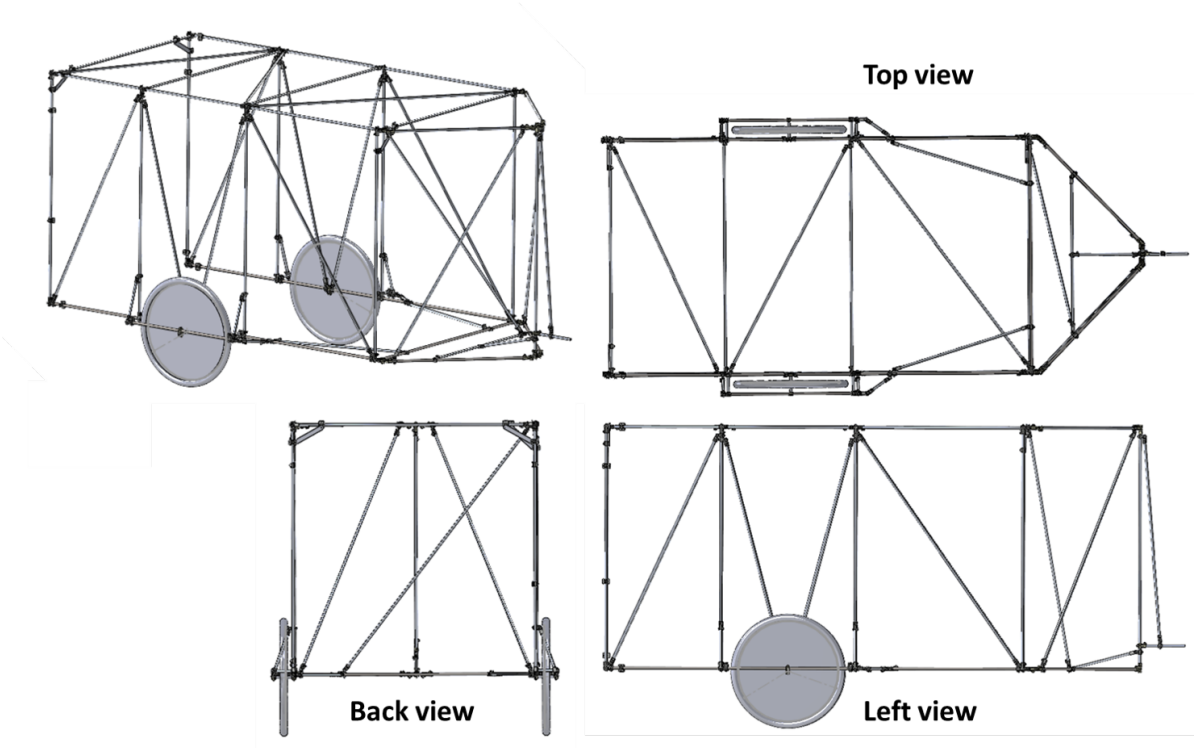

Figure B.2: Solid Works assembly from different perspectives

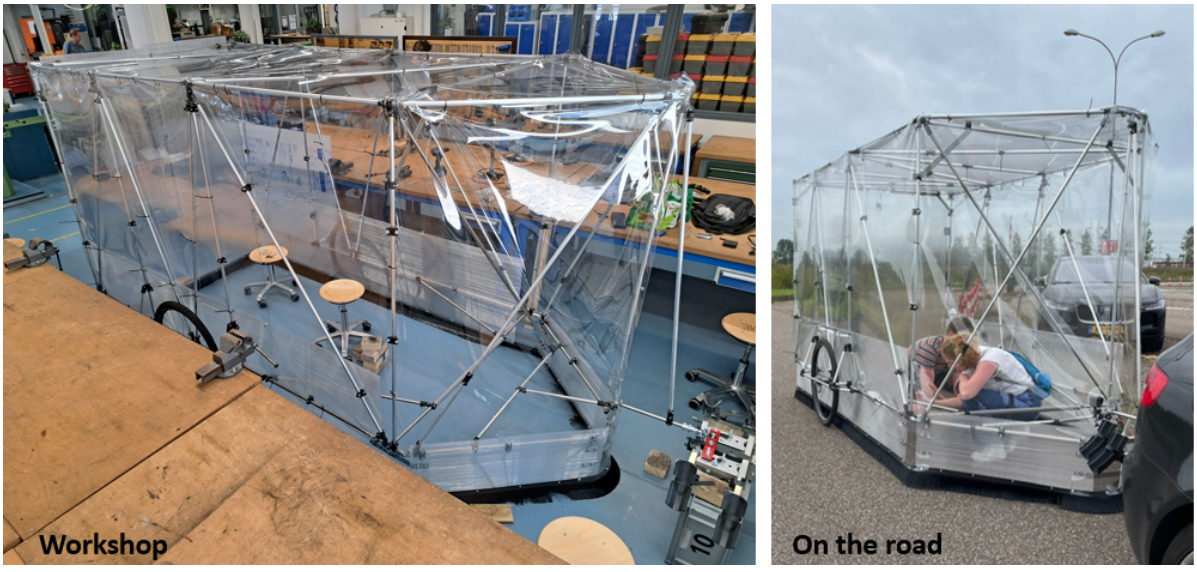

Figure B.3: The finalized build of the bike trailer in the workshop and the first time on the road

The trailer is supported by mountain bike wheels, which have wide tires that can be used on low tire pressure. These tires will serve as a suspension system for vibrations generated at the road surface. The wheels are attached at both sides and braced in all directions (see fig. B.5). This will help to divide forces generated at the road surface across the entire construction, rather than at one point.

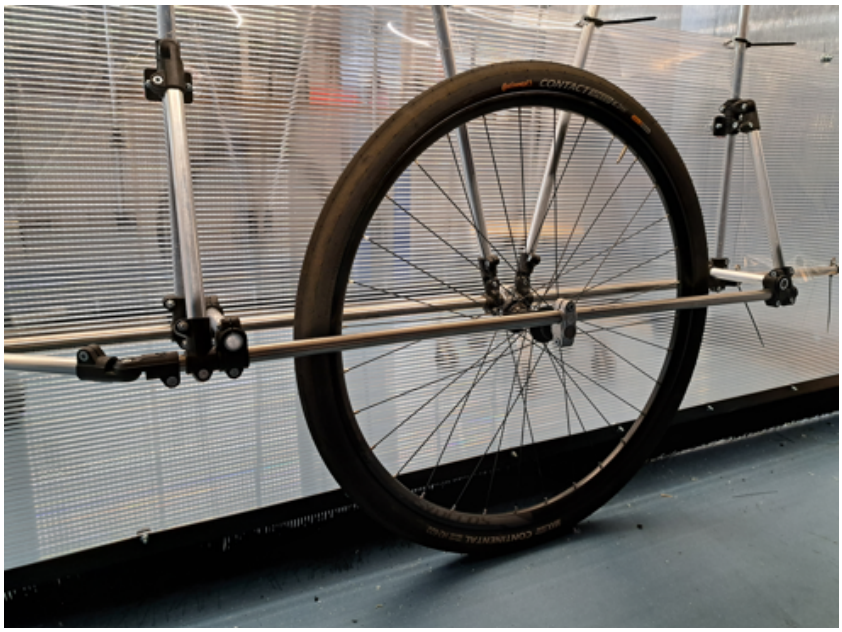

Figure B.4: Wheel attachment of the bike trailer

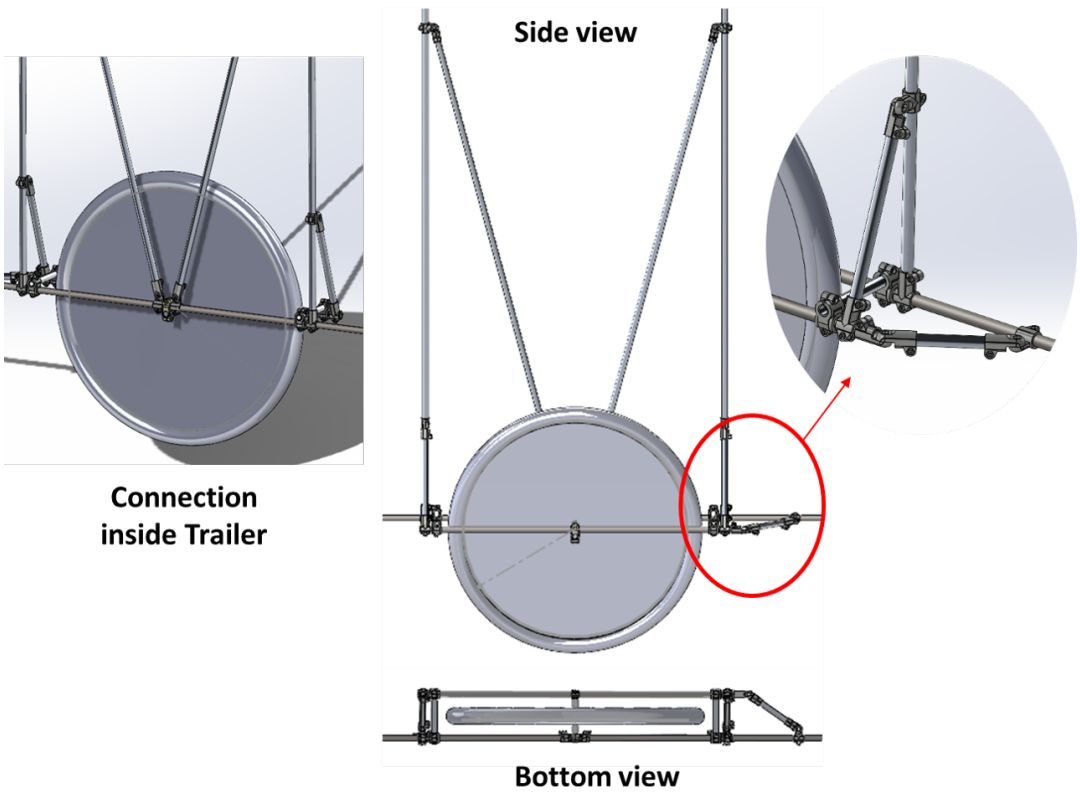

Figure B.5: Solid Works design of the wheel attachment

A Twinny load is placed onto the car's tow bar. A hinge is added to the Twinny load to connect the bike trailer to the car (see Fig. B.6). A safety cable is placed around the Twinny load and frame of the bike trailer to maintain a connection between the trailer and the car in case of failure of the coupling mechanism. In addition, to keep the trailer stable during the test, the weight on the tongue needs to be 10-15% of the total weight of the trailer.

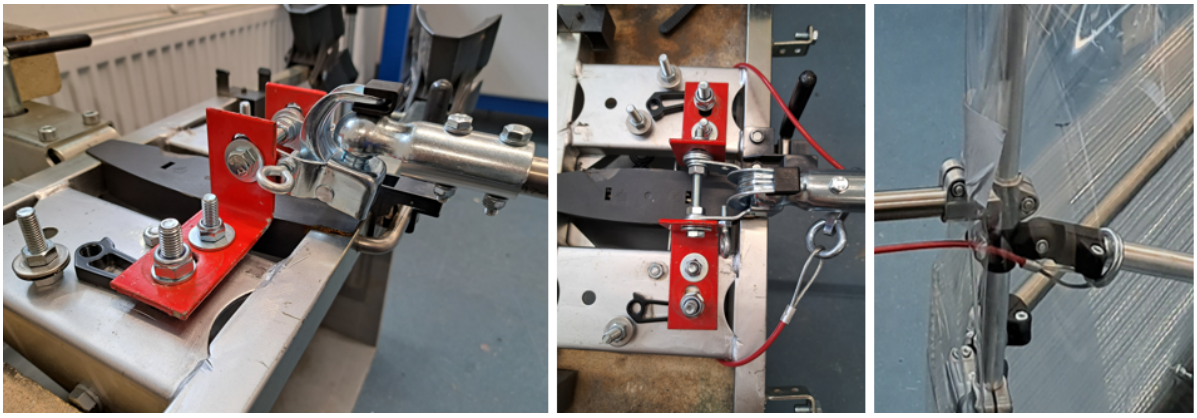

Figure B.6: Link between the bike trailer and Twinny load, which includes safety cable

The back of the trailer is closed with doors connected to the side plates of the trailer with hinges and kept together with magnets (see fig. B.7). The doors are made from a lightweight solid material (corrugated plastic) to prevent anything getting stuck between the rear wheel axis of the bicycle. The magnets, used to close the door, are placed in such a way that the doors will easily open when getting in contact with the rear wheel of the bicycle. Impact with the bike or cyclist will generate enough force to break the bond between the magnets and open the door. This will create safe passage of the cyclist out of the bike trailer both in the scenario that the cyclist cannot keep up his speed (cyclist will not fall) or if the cyclist has fallen. To prevent the doors from getting pushed inward by the tailwind, the doors will reach slightly above the top beam of the trailer's frame (see fig. B.8). This will obstruct inwards rotation.

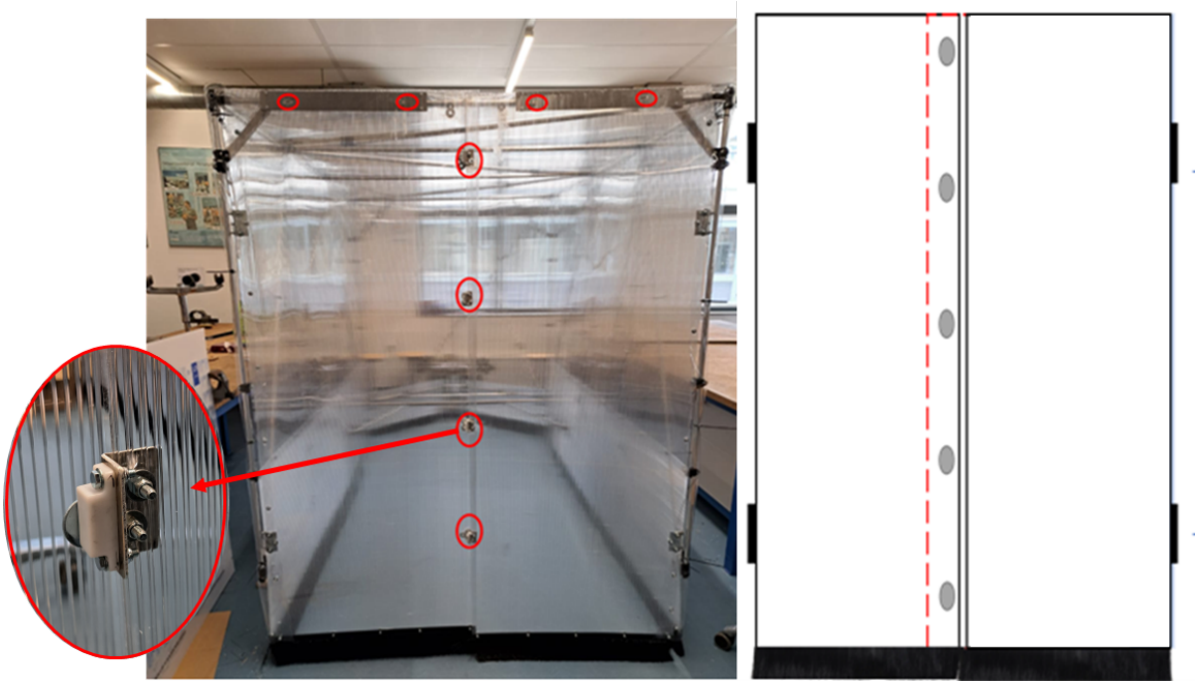

Figure B.7: Back door design

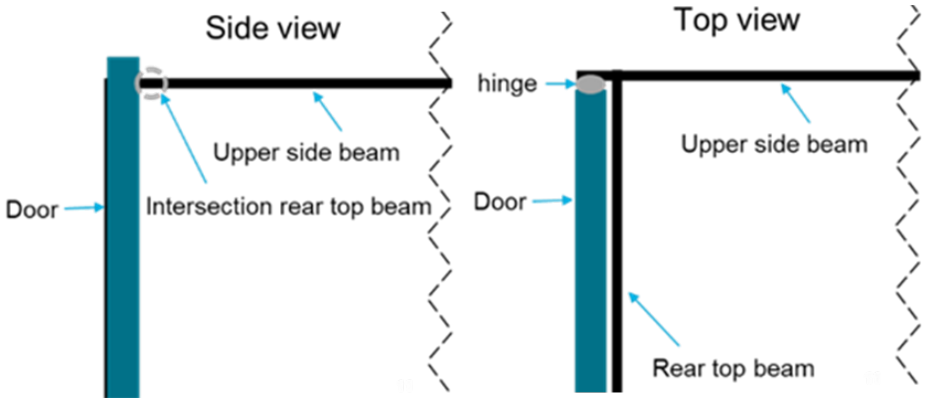

Figure B.8: Mechanism that prevents the doors from being pushed inwards

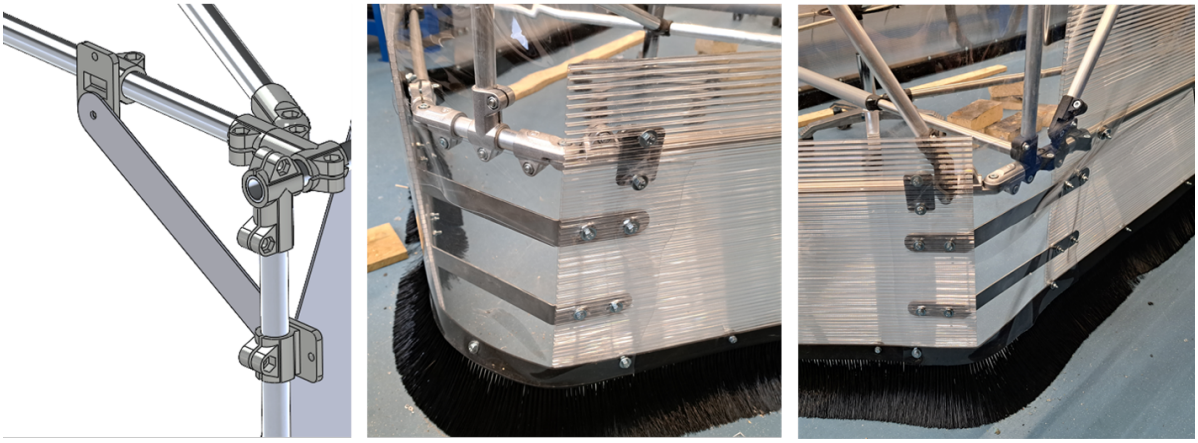

Figure B.9: Some bracing applied to strengthen the construction at the rear and front of the trailer

Safety Measures

The main concern of the test setup, is the risk of falling, which could injure the participant. Some general mitigation measures are taken to minimize the risk of falling, however, falling cannot always be prevented. This has been taken into account during the design of the bike trailer, as already been discussed in previous paragraphs. Some of the design details, which help to mitigate the risk of injury in case of falling, are the lightweight design of the trailer, the boarding at the inside of the trailer and the back doors that are hold together by magnets.

The risk of falling is minimized by selecting a (semi-)professional road cyclist as participant. Such a participant, familiar with riding within a peloton for extended periods, is less prone to falling due to their skill and experience in navigating confined spaces. The trailer will create an enclosed space with a minimal dimension of 2,80 m in cycling direction and 1,50 m in width. A bicycle has a length of approximately 1,80 m and maximum width of 0,50 m at the handlebars. This leaves 0,50 m spacing around the cyclist. The free space within the trailer is larger compared to the space within a peloton.

In addition, braking of the car could lead to a fall of the participant within the trailer. To minimize this risk, the car will be towed by someone who is experienced with cyclists drafting behind the car while driving. Such a driver, will be familiar with communicating with the cyclist, be able to appropriately accelerate/decelerate with the cyclist behind the car and can stay calm in case of emergency and not initiate emergency braking. During the test runs, the cyclist and the car driver will be able to communicate using a radio communication system, which will make it possible to abort the test at any moment. Braking can only be initiated when mutually agreed through the radio system after which the cyclist will be guided by brake lights of the car. Otherwise, both the cyclist and car driver will generally follow the rule of no braking, which is also applied when cycling within a peloton.

Last, a roll bar is placed at the front of the cycling space, which can be used by the cyclist to transfer energy when cycling faster than the speed of the trailer. This is created by adding a PVC tube around

the front beam of the cycling space (see Fig. B.10). To prevent falling over the beam, the beam is placed just above the wheel axis of the bike. Cyclists regularly rub wheels in the peloton and if the cyclist's wheel touches the roll bar we expect no destabilization.

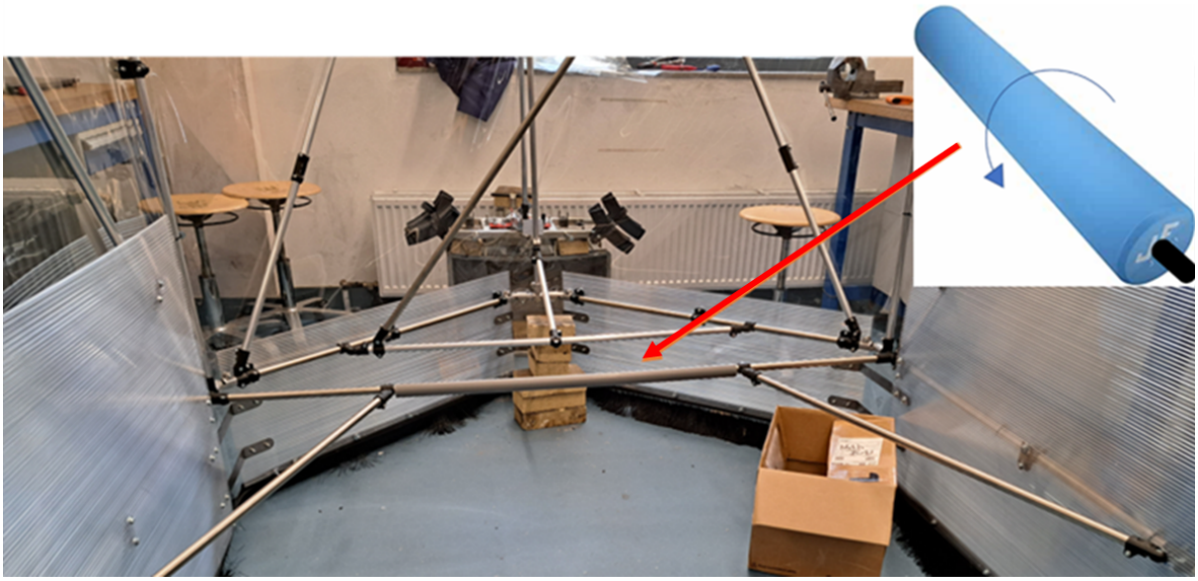

Figure B.10: Roll bar used by the cyclist to transfer energy

C

Validation Multiple Linear Regression

This chapter provides a validation of the assumptions for the four regression analysis conducted within this study. This includes assessment of collinearity, linearity, homoscedasticity and normality. The assumption of collinearity is met if the variance inflation factor (VIF) is smaller than 10. Linearity and homoscedasticity are visually assessed by plotting the standardized residuals against the fitted predicted values. The assumption of linearirty and homoscedasticity are met if the errors are equally and randomly distributed around zero. Last, the normality is assessed by inspecting the frequency distribution of the standardized residuals with a fitted normal distribution curve.

Ink Print test

The first two analysis focuses on understanding the impact of tire type, tire width, inflation pressure and vertical load on the length and width of the contact patch. Regarding collinearity, the VIF for tire width, inflation pressure and vertical load are 2.3904, 4.4260 and 1.0056, respectively. This indicates that the assumption of little to no collinearity is satisfied, as the VIF is lower than 10 for all continuous independent variables.

Figure C.1 provides a visual analyzes of linearity, homoscedasticity and normality for the prediction of contact patch length. The standardized residuals are distributed around zero and lie approximately between -2 and 2 for all predicted values. A few residuals lie outside this range, which could potentially be identified as outliers and might be associated with the deviating observations highlighted in the figures of section 5.1. Nonetheless, the standardized residuals seem randomly distributed, which supports the claim of linearity and homoscedasticity. The outliers can also be detected within the frequency plot, which is used to visualize normality of the residual distribution. However, the residuals roughly approximate the normal distribution.

Figure C.2 provides a visual analyzes of linearity, homoscedasticity and normality in prediction of the contact patch width. Similar to the residuals for the prediction of contact patch length, most residuals fall within the same range (-0.6 to 0.6), with a few exceptions. However, the standardized residuals appear to be randomly distributed, which supports the claim of linearity and homoscedasticity. In addition, residuals approximate the normal distribution. This results from a good fit between the frequency distribution of residuals and the fitted normal distribution.

Drum test

The third analysis focuses on the impact of tire type, tire width, inflation pressure, vertical load and velocity on the C_{rr} obtained with drum testing. Regarding collinearity, the VIF for tire width, inflation pressure, vertical load and velocity are 1.8449, 2.5676, 1.0384 and 1.0689, respectively. This indicates that the assumption of little to no collinearity is satisfied.

Figure C.3 offers a visual analysis of linearity, homoscedasticity, and normality of the regression analysis. The standardized residuals are randomly distributed around zero, which supports the claim of linearity. In addition, a slight heteroscedasticity can be observed, indicated by a somewhat larger spread of residuals for higher fitted values compared to lower fitted values. However, it has been stated that a minor degree of heteroscedasticity has minimal impact on the significance of the test. The observed heteroscedasticity is limited, with most of the residuals ranging from -$5\text{E}-5$ to $5\text{E}-5$, which

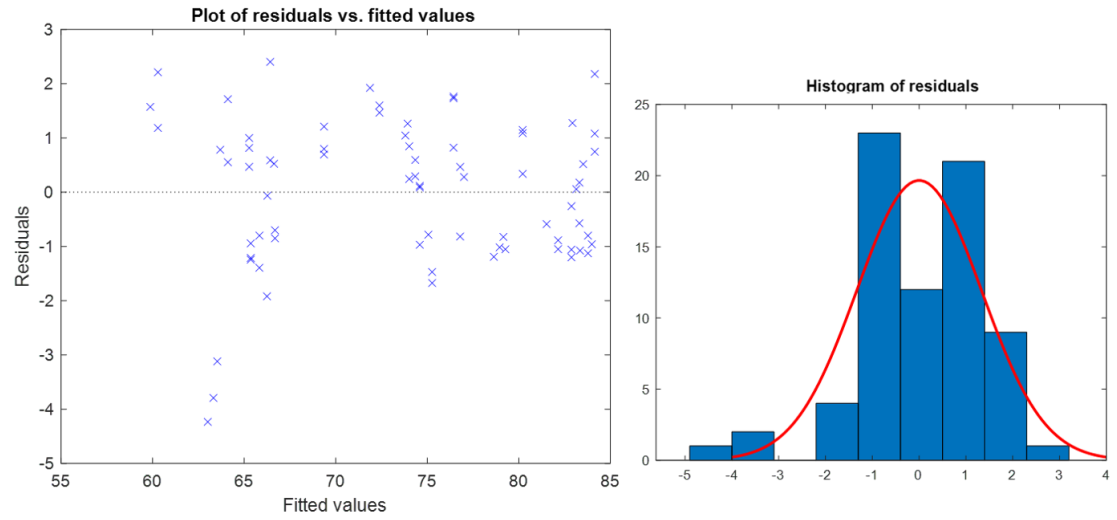

Figure C.1: Standardized residuals for prediction of contact patch length

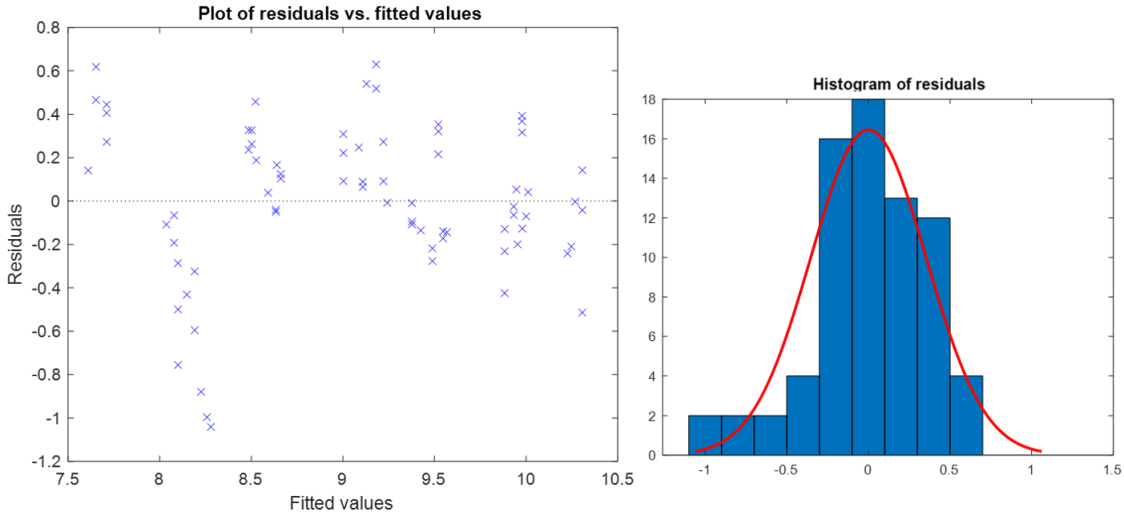

Figure C.2: Standardized residuals for prediction of contact patch width

makes it still appropriate to apply linear regression. Last, there is a good fit between the frequency distribution of the residuals and the fitted normal distribution. This suggests that the residuals are normally distributed.

Rolling losses measurement

The fourth analysis focuses on the impact of tire width, inflation pressure, velocity and road type on C_{rr} obtained with the rolling losses measurements. Regarding collinearity, the VIF for tire width, inflation pressure and velocity are 1.4050, 1.4075 and 1.0068, respectively. VIF is lower than 10 for all continuous independent variables, which indicates that the assumption of little to no collinearity is satisfied.

Figure C.4 presents a visual analysis of linearity, homoscedasticity, and normality of the regression analysis. The residuals are equally distributed around zero, which indicates linearity. Similar to the residual distribution shown for the drum test, a slight increase of residuals can be observed for the higher fitted values. However, generally, all residuals fall within the range of $-0.5\text{E}-3$ to $0.5\text{E}-3$, which approximates homoscedasticity. Last, the residuals can be assumed to be normally distributed, as the normal distribution provides a good fit for the frequency distribution of the residuals.

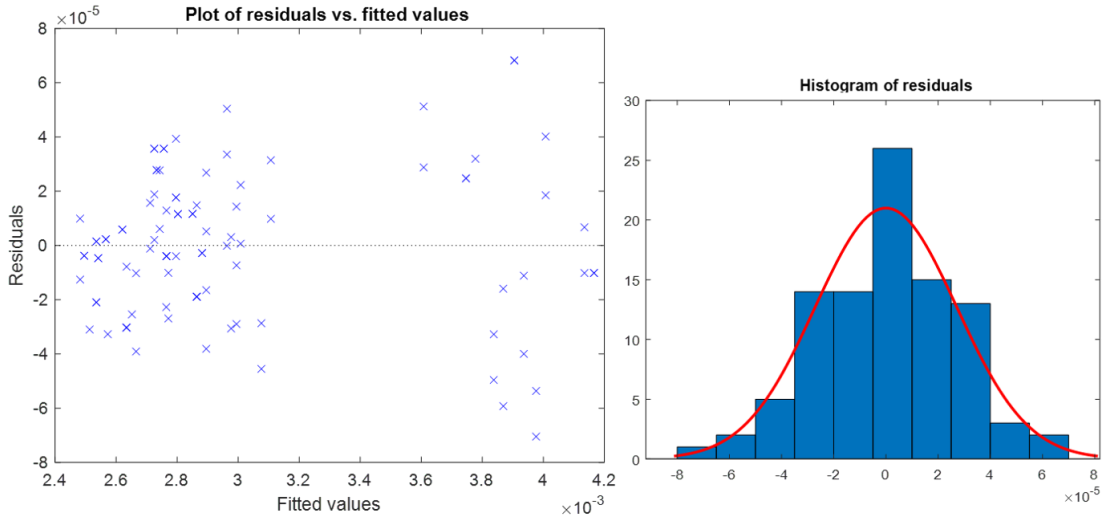

Figure C.3: Standardized residuals for prediction of C_{rr} obtained with drum test

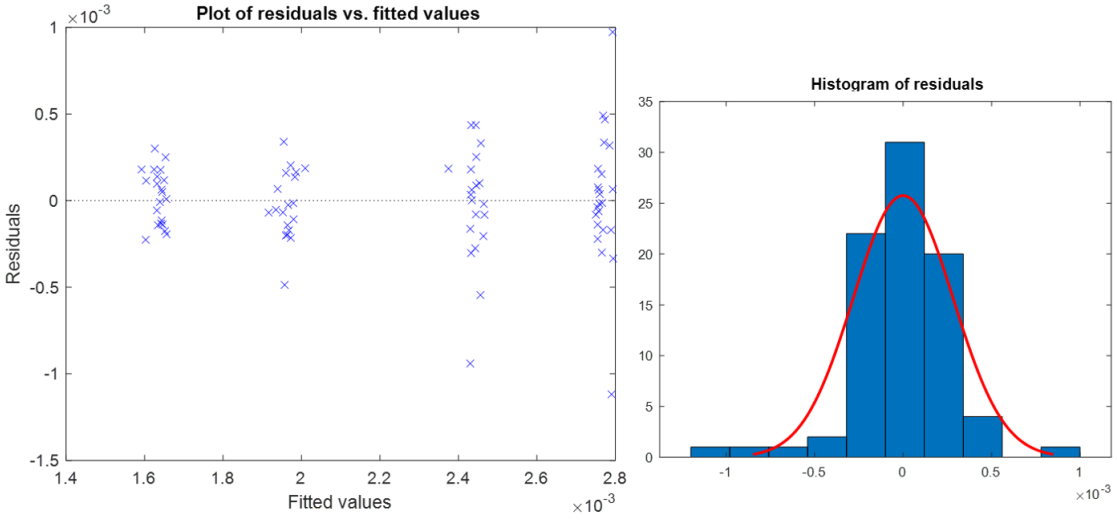

Figure C.4: Standardized residuals for prediction of C_{rr} obtained with rolling losses measurements

D

Individual Contact Patches

The assessment of the contact patch shape is done by taking a total of 73 ink footprints. This chapter presents each ink print with the fitted ellipse. Each figure reports the tire characteristics and the controlled variables, which are the tire type (tubeless/tubular), tire width, rim size, tire pressure and vertical load. In addition, the estimates of the width, length and area of the contact patch resulting from the fitted ellipse are reported for each ink print. The reported orientation angle could be disregarded, as this is not relevant for this research project.

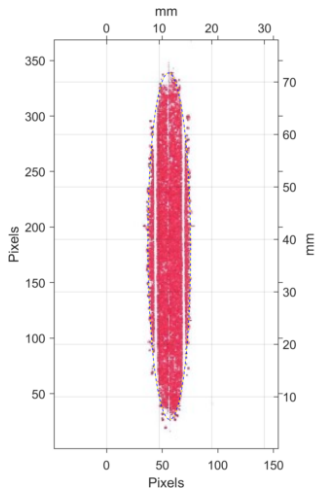

Vittoria Tubeless

Tire size = 26 mm
Rim size = 25 mm
Pressure = 5.3 bar (76.87 psi)
Load = 206.01 N (46.3129 lb)

Image
length = 312.2 pixels (66.1 mm)
width = 38.3 pixels (8.12 mm)
area = 9403 pixels^2 (421.3 mm^2)
orientation angle = 0.18°

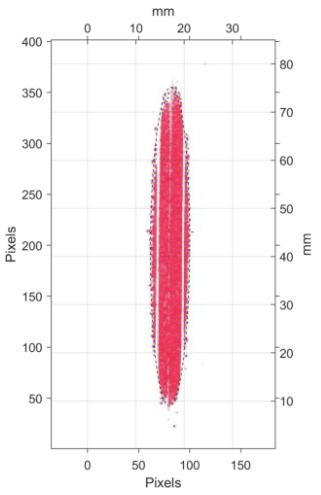

Vittoria Tubeless

Tire size = 26 mm
Rim size = 25 mm
Pressure = 5.3 bar (76.87 psi)
Load = 206.01 N (46.3129 lb)

Image
length = 313.1 pixels (66.3 mm)
width = 38.5 pixels (8.15 mm)
area = 9474 pixels^2 (424.5 mm^2)
orientation angle = -0.3°

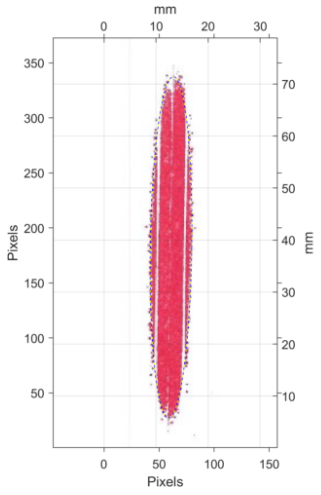

Vittoria Tubeless

Tire size = 26 mm
Rim size = 25 mm
Pressure = 5.3 bar (76.87 psi)
Load = 206.01 N (46.3129 lb)

Image
length = 310.6 pixels (65.7 mm)
width = 37.7 pixels (7.98 mm)
area = 9200 pixels^2 (412.2 mm^2)
orientation angle = -0.84°

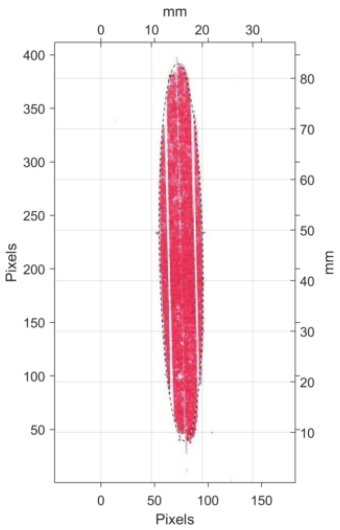

Vittoria Tubeless

Tire size = 26 mm
Rim size = 25 mm
Pressure = 5.3 bar (76.87 psi)
Load = 291.357 N (65.4997 lb)

Image
length = 352.6 pixels (74.6 mm)
width = 40.6 pixels (8.59 mm)
area = 11243 pixels^2 (503.7 mm^2)
orientation angle = 1.1°

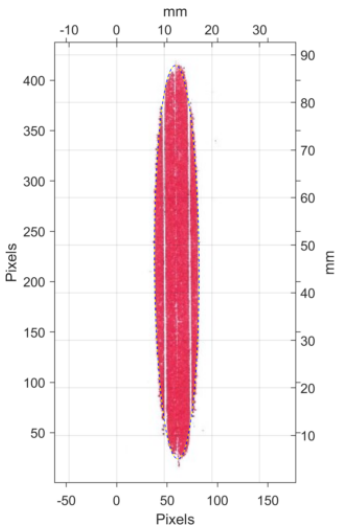

Vittoria Tubeless

Tire size = 26 mm
Rim size = 25 mm
Pressure = 5.3 bar (76.87 psi)
Load = 375.723 N (84.4659 lb)

Image
length = 390.9 pixels (82.7 mm)
width = 44.3 pixels (9.37 mm)
area = 13597 pixels^2 (609.2 mm^2)
orientation angle = 0.35°

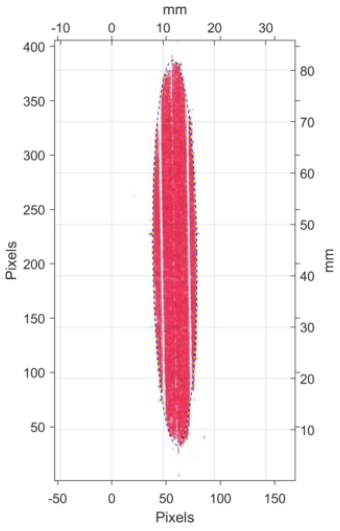

Vittoria Tubeless

Tire size = 26 mm
Rim size = 25 mm
Pressure = 5.3 bar (76.87 psi)
Load = 291.357 N (65.4997 lb)

Image
length = 354 pixels (74.9 mm)
width = 40.6 pixels (8.58 mm)
area = 11277 pixels^2 (505.2 mm^2)
orientation angle = 0.62°

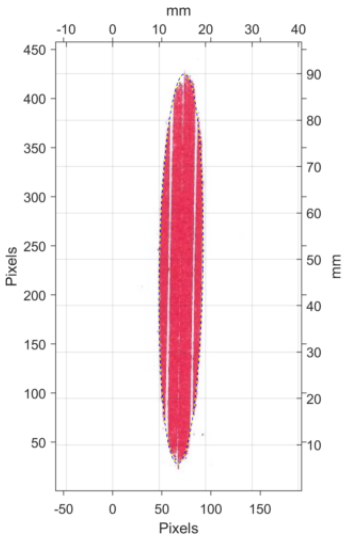

Vittoria Tubeless

Tire size = 26 mm
Rim size = 25 mm
Pressure = 5.3 bar (76.87 psi)
Load = 377.685 N (84.907 lb)

Image
length = 397 pixels (84 mm)
width = 44.5 pixels (9.42 mm)
area = 13884 pixels^2 (622 mm^2)
orientation angle = -0.98°

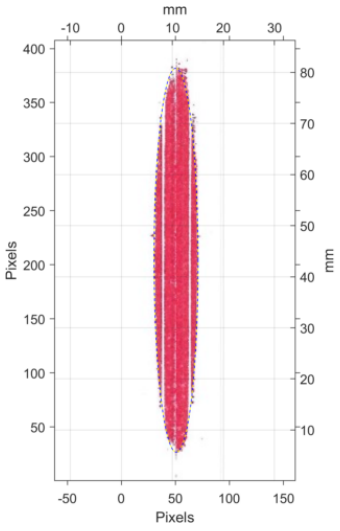

Vittoria Tubeless

Tire size = 26 mm
Rim size = 25 mm
Pressure = 5.3 bar (76.87 psi)
Load = 287.433 N (64.6175 lb)

Image
length = 355.2 pixels (75.2 mm)
width = 40.8 pixels (8.63 mm)
area = 11375 pixels^2 (509.6 mm^2)
orientation angle = 0.089°

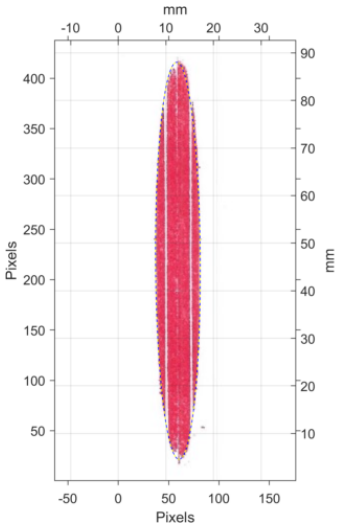

Vittoria Tubeless

Tire size = 26 mm
Rim size = 25 mm
Pressure = 5.3 bar (76.87 psi)
Load = 375.723 N (84.4659 lb)

Image
length = 394.4 pixels (83.5 mm)
width = 44.4 pixels (9.41 mm)
area = 13769 pixels^2 (616.9 mm^2)
orientation angle = 0.34°

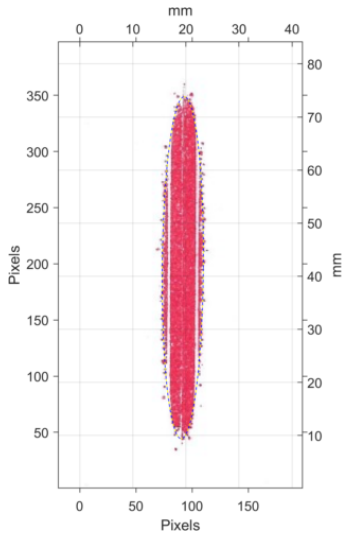

Vittoria Tubeless

Tire size = 26 mm
Rim size = 25 mm
Pressure = 6 bar (87.0226 psi)
Load = 203.067 N (45.6513 lb)

Image
length = 304.6 pixels (64.5 mm)
width = 36.6 pixels (7.75 mm)
area = 8760 pixels^2 (392.5 mm^2)
orientation angle = -0.51°

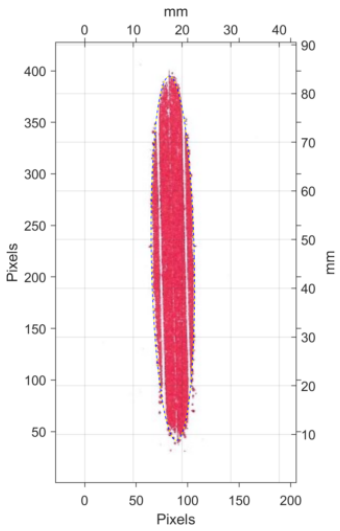

Vittoria Tubeless

Tire size = 26 mm
Rim size = 25 mm
Pressure = 6 bar (87.0226 psi)
Load = 298.224 N (67.0434 lb)

Image
length = 353.6 pixels (74.8 mm)
width = 41.6 pixels (8.81 mm)
area = 11554 pixels^2 (517.7 mm^2)
orientation angle = 1.1°

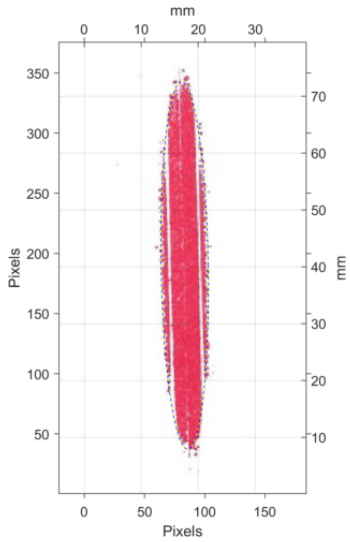

Vittoria Tubeless

Tire size = 26 mm
Rim size = 25 mm
Pressure = 6 bar (87.0226 psi)
Load = 206.991 N (46.5334 lb)

Image
length = 305.5 pixels (64.7 mm)
width = 39.1 pixels (8.27 mm)
area = 9375 pixels^2 (420 mm^2)
orientation angle = 0.95°

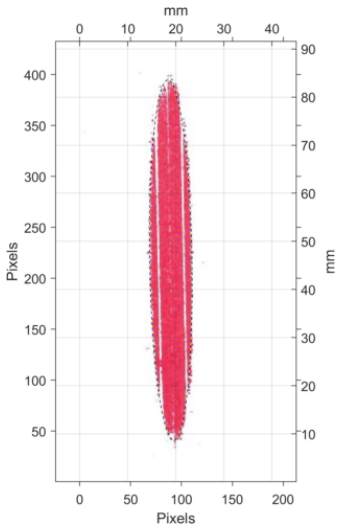

Vittoria Tubeless

Tire size = 26 mm
Rim size = 25 mm
Pressure = 6 bar (87.0226 psi)
Load = 300.186 N (67.4845 lb)

Image
length = 353.7 pixels (74.9 mm)
width = 41.5 pixels (8.79 mm)
area = 11529 pixels^2 (516.5 mm^2)
orientation angle = 0.95°

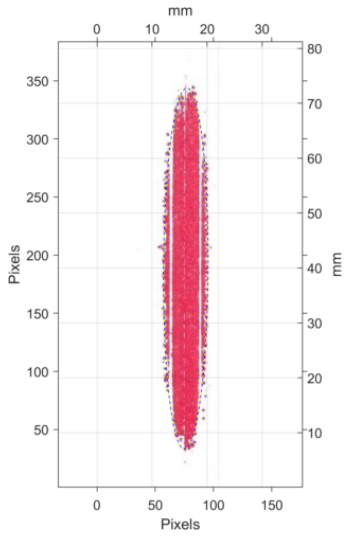

Vittoria Tubeless

Tire size = 26 mm
Rim size = 25 mm
Pressure = 6 bar (87.0226 psi)
Load = 206.991 N (46.5334 lb)

Image
length = 311 pixels (65.8 mm)
width = 38.4 pixels (8.12 mm)
area = 9367 pixels^2 (419.6 mm^2)
orientation angle = -0.38°

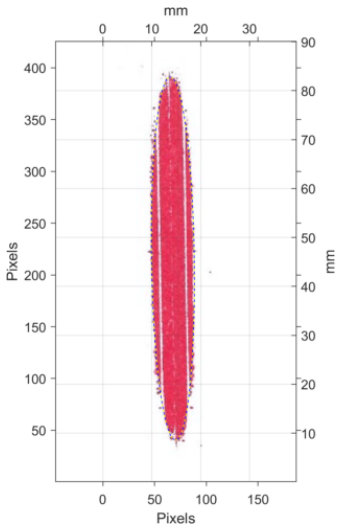

Vittoria Tubeless

Tire size = 26 mm
Rim size = 25 mm
Pressure = 6 bar (87.0226 psi)
Load = 300.186 N (67.4845 lb)

Image
length = 350.8 pixels (74.3 mm)
width = 41.4 pixels (8.76 mm)
area = 11409 pixels^2 (511.1 mm^2)
orientation angle = 0.85°

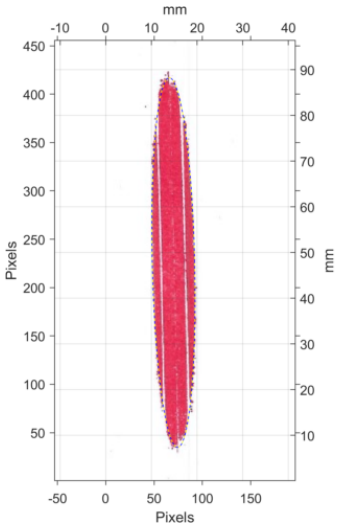

Vittoria Tubeless

Tire size = 26 mm
Rim size = 25 mm
Pressure = 6 bar (87.0226 psi)
Load = 370.818 N (83.3632 lb)

Image
length = 382.3 pixels (80.9 mm)
width = 43.9 pixels (9.29 mm)
area = 13180 pixels^2 (590.5 mm^2)
orientation angle = 1.3°

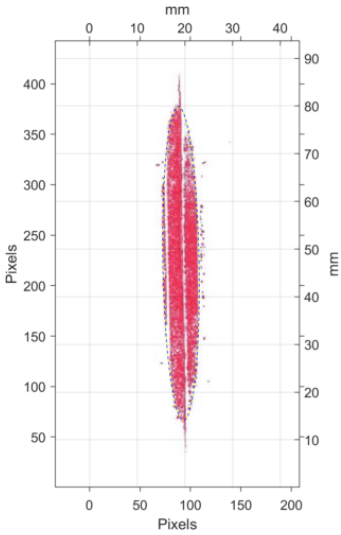

Vittoria Tubeless

Tire size = 28 mm
Rim size = 25 mm
Pressure = 4.8 bar (69.6181 psi)
Load = 211.896 N (47.6361 lb)

Image
length = 311 pixels (65.8 mm)
width = 35.9 pixels (7.6 mm)
area = 8766 pixels^2 (392.7 mm^2)
orientation angle = 0.99°

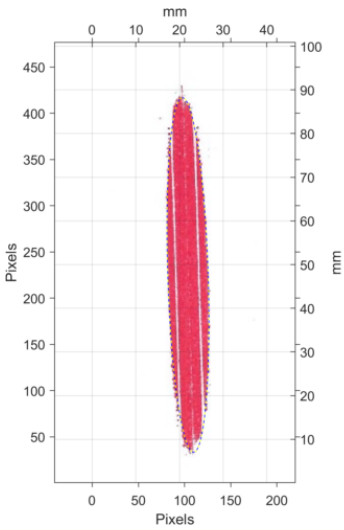

Vittoria Tubeless

Tire size = 26 mm
Rim size = 25 mm
Pressure = 6 bar (87.0226 psi)
Load = 376.704 N (84.6864 lb)

Image
length = 383.9 pixels (81.3 mm)
width = 43.8 pixels (9.27 mm)
area = 13206 pixels^2 (591.7 mm^2)
orientation angle = 1.8°

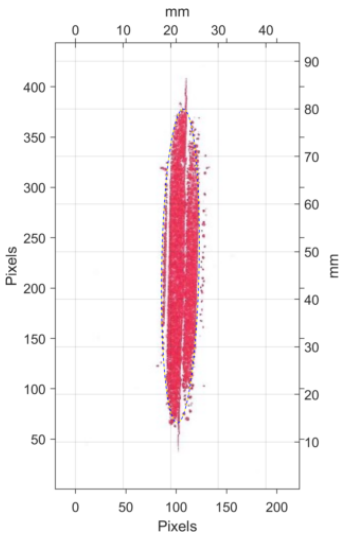

Vittoria Tubeless

Tire size = 28 mm
Rim size = 25 mm
Pressure = 4.8 bar (69.6181 psi)
Load = 211.896 N (47.6361 lb)

Image
length = 311.7 pixels (66 mm)
width = 37.2 pixels (7.87 mm)
area = 9099 pixels^2 (407.7 mm^2)
orientation angle = -1.1°

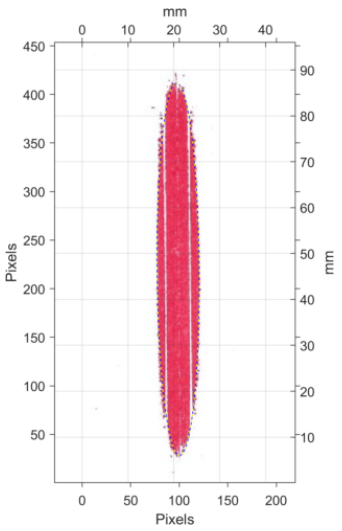

Vittoria Tubeless

Tire size = 26 mm
Rim size = 25 mm
Pressure = 6 bar (87.0226 psi)
Load = 376.704 N (84.6864 lb)

Image
length = 383.1 pixels (81.1 mm)
width = 43.5 pixels (9.21 mm)
area = 13096 pixels^2 (586.7 mm^2)
orientation angle = 0.46°

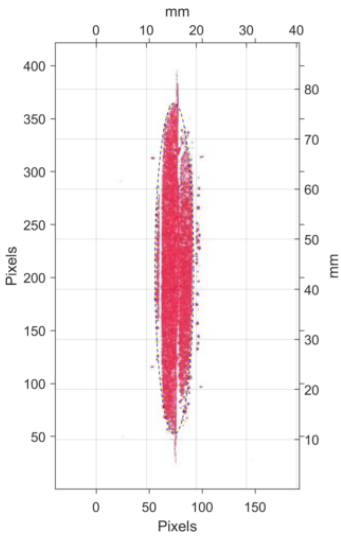

Vittoria Tubeless

Tire size = 28 mm
Rim size = 25 mm
Pressure = 4.8 bar (69.6181 psi)
Load = 207.972 N (46.754 lb)

Image
length = 312.8 pixels (66.2 mm)
width = 36.5 pixels (7.72 mm)
area = 8956 pixels^2 (401.3 mm^2)
orientation angle = -0°

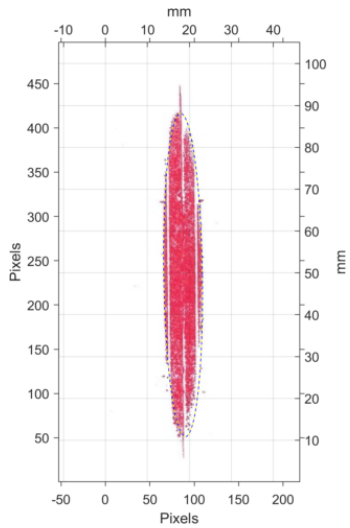

Vittoria Tubeless

Tire size = 28 mm
Rim size = 25 mm
Pressure = 4.8 bar (69.6181 psi)
Load = 309.015 N (69.4693 lb)

Image
length = 365.1 pixels (77.3 mm)
width = 43.6 pixels (9.23 mm)
area = 12511 pixels^2 (560.5 mm^2)
orientation angle = 0.84°

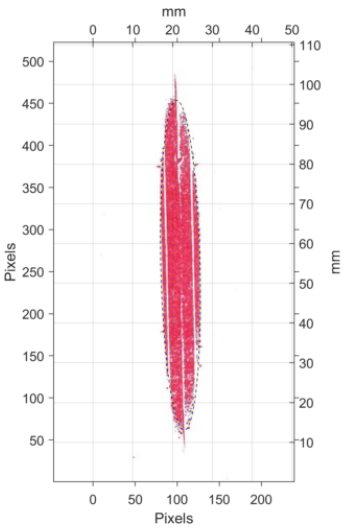

Vittoria Tubeless

Tire size = 28 mm
Rim size = 25 mm
Pressure = 4.8 bar (69.6181 psi)
Load = 372.78 N (83.8043 lb)

Image
length = 392 pixels (83 mm)
width = 46.6 pixels (9.87 mm)
area = 14354 pixels^2 (643.1 mm^2)
orientation angle = 1.3°

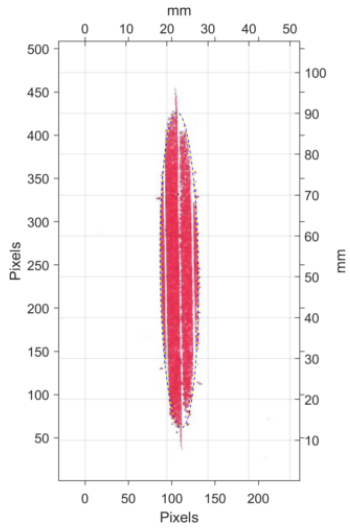

Vittoria Tubeless

Tire size = 28 mm
Rim size = 25 mm
Pressure = 4.8 bar (69.6181 psi)
Load = 307.053 N (69.0283 lb)

Image
length = 365 pixels (77.3 mm)
width = 44 pixels (9.31 mm)
area = 12613 pixels^2 (565.1 mm^2)
orientation angle = 0.76°

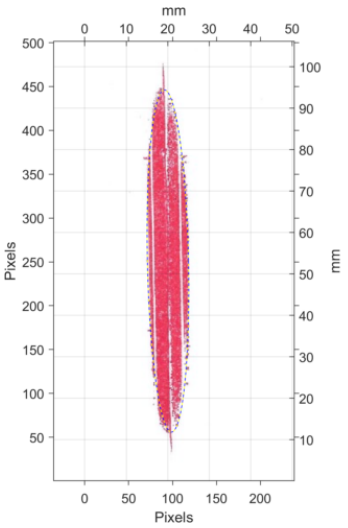

Vittoria Tubeless

Tire size = 28 mm
Rim size = 25 mm
Pressure = 4.8 bar (69.6181 psi)
Load = 372.78 N (83.8043 lb)

Image
length = 390.5 pixels (82.7 mm)
width = 46.8 pixels (9.91 mm)
area = 14354 pixels^2 (643.1 mm^2)
orientation angle = 1.2°

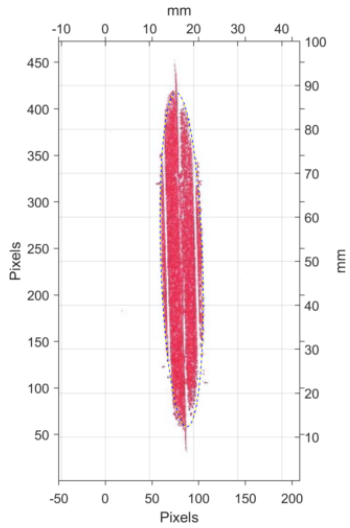

Vittoria Tubeless

Tire size = 28 mm
Rim size = 25 mm
Pressure = 4.8 bar (69.6181 psi)
Load = 307.053 N (69.0283 lb)

Image
length = 358.9 pixels (76 mm)
width = 44.9 pixels (9.49 mm)
area = 12644 pixels^2 (566.5 mm^2)
orientation angle = 1.8°

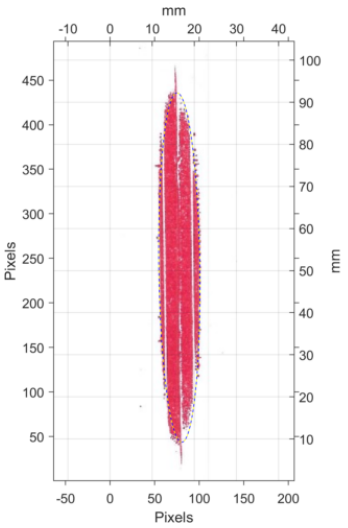

Vittoria Tubeless

Tire size = 28 mm
Rim size = 25 mm
Pressure = 4.8 bar (69.6181 psi)
Load = 374.742 N (84.2454 lb)

Image
length = 392.3 pixels (83 mm)
width = 46.1 pixels (9.75 mm)
area = 14197 pixels^2 (636.1 mm^2)
orientation angle = 0.78°

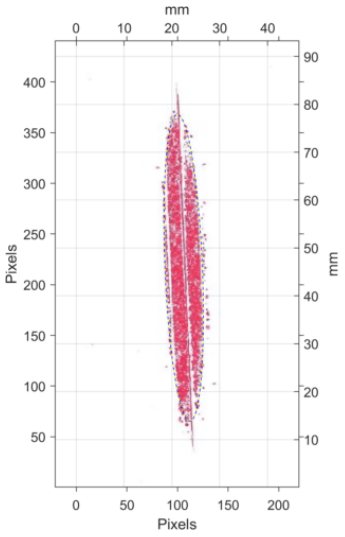

Vittoria Tubeless

Tire size = 28 mm
Rim size = 25 mm
Pressure = 5.3 bar (76.87 psi)
Load = 207.972 N (46.754 lb)

Image
length = 303.1 pixels (64.1 mm)
width = 36.9 pixels (7.81 mm)
area = 8786 pixels^2 (393.7 mm^2)
orientation angle = 2.4°

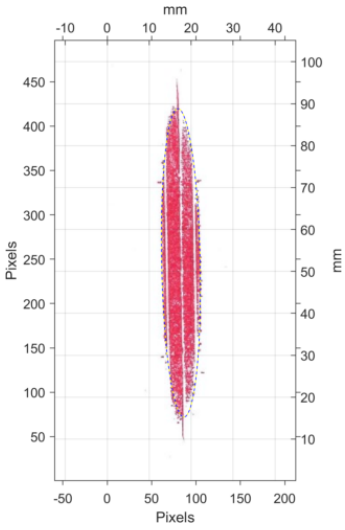

Vittoria Tubeless

Tire size = 28 mm
Rim size = 25 mm
Pressure = 5.3 bar (76.87 psi)
Load = 301.167 N (67.705 lb)

Image
length = 347.7 pixels (73.6 mm)
width = 43.4 pixels (9.2 mm)
area = 11864 pixels^2 (531.5 mm^2)
orientation angle = 1.1°

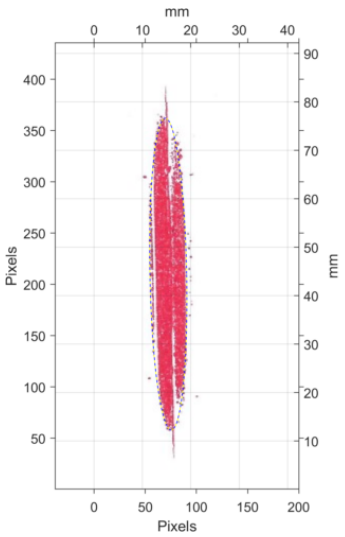

Vittoria Tubeless

Tire size = 28 mm
Rim size = 25 mm
Pressure = 5.3 bar (76.87 psi)
Load = 207.972 N (46.754 lb)

Image
length = 304.3 pixels (64.4 mm)
width = 35.9 pixels (7.6 mm)
area = 8582 pixels^2 (384.5 mm^2)
orientation angle = 1.1°

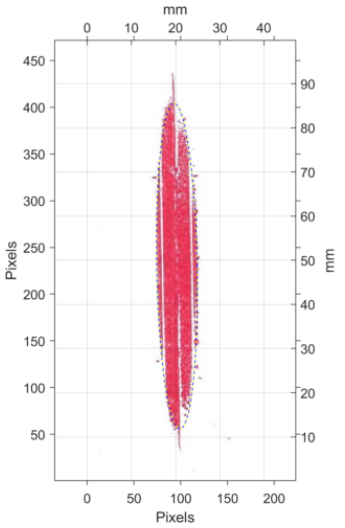

Vittoria Tubeless

Tire size = 28 mm
Rim size = 25 mm
Pressure = 5.3 bar (76.87 psi)
Load = 301.167 N (67.705 lb)

Image
length = 348.6 pixels (73.8 mm)
width = 43.3 pixels (9.17 mm)
area = 11867 pixels^2 (531.7 mm^2)
orientation angle = 1°

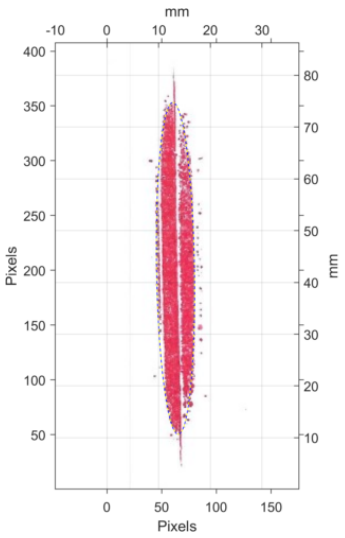

Vittoria Tubeless

Tire size = 28 mm
Rim size = 25 mm
Pressure = 5.3 bar (76.87 psi)
Load = 207.972 N (46.754 lb)

Image
length = 302.9 pixels (64.1 mm)
width = 34.7 pixels (7.34 mm)
area = 8255 pixels^2 (369.8 mm^2)
orientation angle = 0.94°

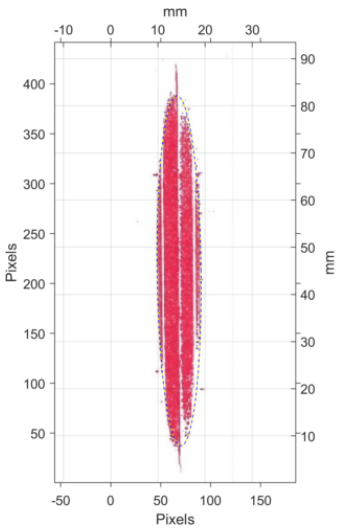

Vittoria Tubeless

Tire size = 28 mm
Rim size = 25 mm
Pressure = 5.3 bar (76.87 psi)
Load = 299.205 N (67.264 lb)

Image
length = 350.9 pixels (74.3 mm)
width = 44.1 pixels (9.33 mm)
area = 12152 pixels^2 (544.5 mm^2)
orientation angle = 0.68°

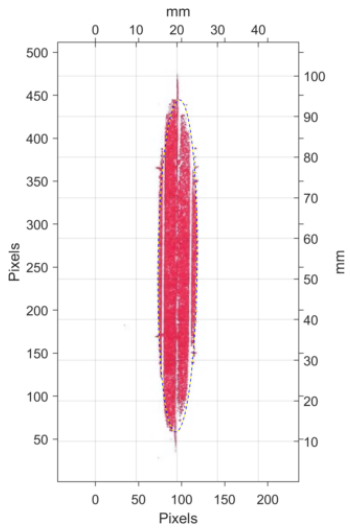

Vittoria Tubeless

Tire size = 28 mm
Rim size = 25 mm
Pressure = 5.3 bar (76.87 psi)
Load = 372.78 N (83.8043 lb)

Image
length = 386.5 pixels (81.8 mm)
width = 45.6 pixels (9.65 mm)
area = 13843 pixels^2 (620.2 mm^2)
orientation angle = -0.61°

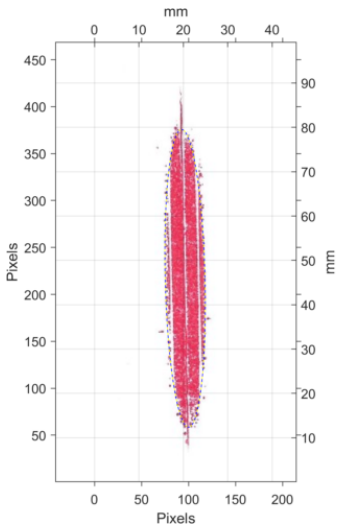

Vittoria Tubeless

Tire size = 30 mm
Rim size = 25 mm
Pressure = 4.3 bar (62.3662 psi)
Load = 204.048 N (45.8718 lb)

Image
length = 317.3 pixels (67.2 mm)
width = 42.4 pixels (8.98 mm)
area = 10573 pixels^2 (473.7 mm^2)
orientation angle = 1.4°

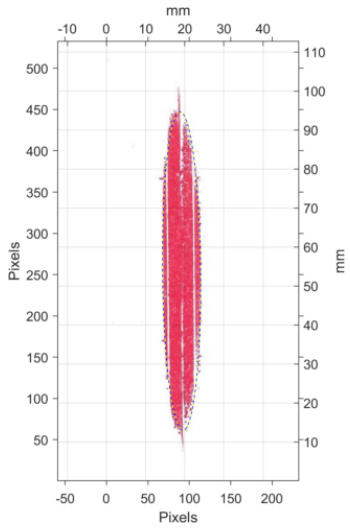

Vittoria Tubeless

Tire size = 28 mm
Rim size = 25 mm
Pressure = 5.3 bar (76.87 psi)
Load = 372.78 N (83.8043 lb)

Image
length = 385.9 pixels (81.7 mm)
width = 46.1 pixels (9.75 mm)
area = 13966 pixels^2 (625.7 mm^2)
orientation angle = 0.53°

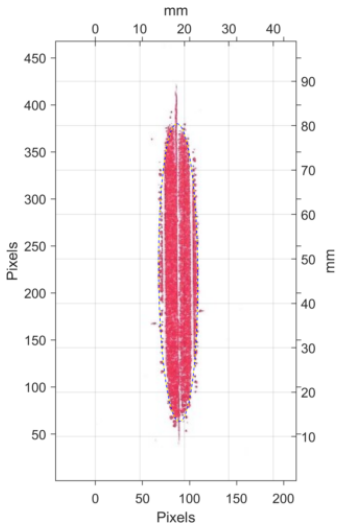

Vittoria Tubeless

Tire size = 30 mm
Rim size = 25 mm
Pressure = 4.3 bar (62.3662 psi)
Load = 202.086 N (45.4307 lb)

Image
length = 316.6 pixels (67 mm)
width = 41.7 pixels (8.83 mm)
area = 10371 pixels^2 (464.6 mm^2)
orientation angle = 0.46°

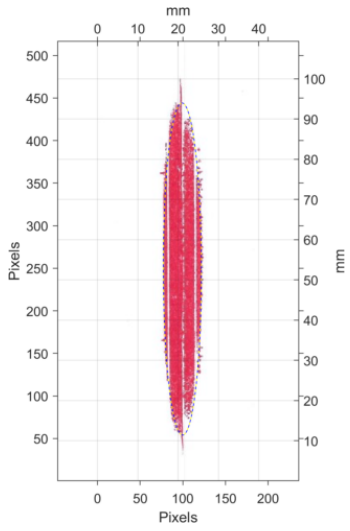

Vittoria Tubeless

Tire size = 28 mm
Rim size = 25 mm
Pressure = 5.3 bar (76.87 psi)
Load = 372.78 N (83.8043 lb)

Image
length = 390.3 pixels (82.6 mm)
width = 44.7 pixels (9.46 mm)
area = 13699 pixels^2 (613.8 mm^2)
orientation angle = 0.1°

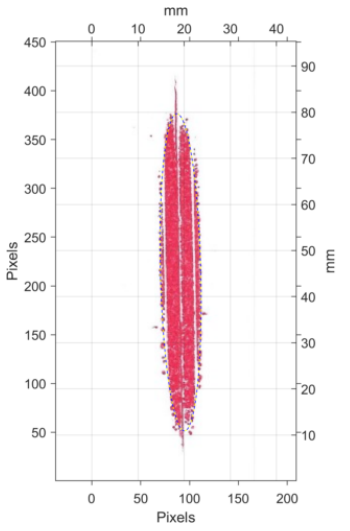

Vittoria Tubeless

Tire size = 30 mm
Rim size = 25 mm
Pressure = 4.3 bar (62.3662 psi)
Load = 202.086 N (45.4307 lb)

Image
length = 325.2 pixels (68.8 mm)
width = 41.4 pixels (8.76 mm)
area = 10575 pixels^2 (473.8 mm^2)
orientation angle = 1.4°

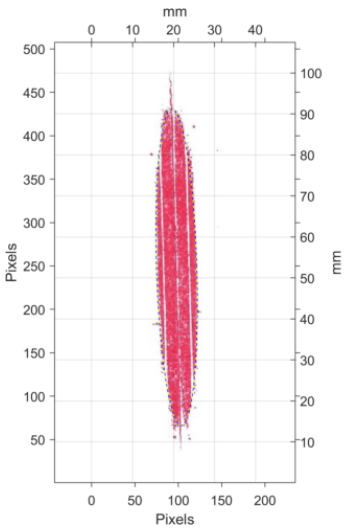

Vittoria Tubeless

Tire size = 30 mm
Rim size = 25 mm
Pressure = 4.3 bar (62.3662 psi)
Load = 296.262 N (66.6023 lb)

Image
length = 365 pixels (77.3 mm)
width = 46.7 pixels (9.87 mm)
area = 13373 pixels^2 (599.2 mm^2)
orientation angle = 1.7°

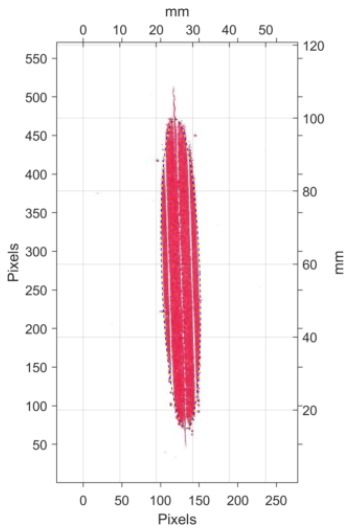

Vittoria Tubeless

Tire size = 30 mm
Rim size = 25 mm
Pressure = 4.3 bar (62.3662 psi)
Load = 368.856 N (82.9221 lb)

Image
length = 401.1 pixels (84.9 mm)
width = 49.4 pixels (10.4 mm)
area = 15550 pixels^2 (696.7 mm^2)
orientation angle = 2°

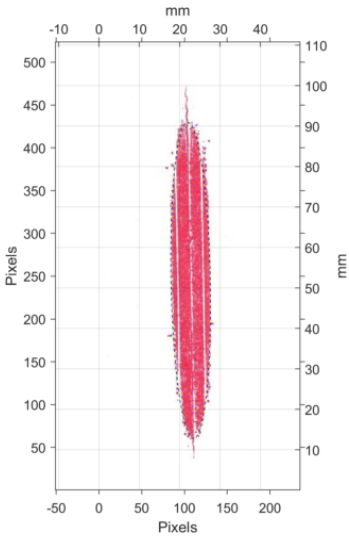

Vittoria Tubeless

Tire size = 30 mm
Rim size = 25 mm
Pressure = 4.3 bar (62.3662 psi)
Load = 296.262 N (66.6023 lb)

Image
length = 369.4 pixels (78.2 mm)
width = 46 pixels (9.74 mm)
area = 13347 pixels^2 (598 mm^2)
orientation angle = 1.1°

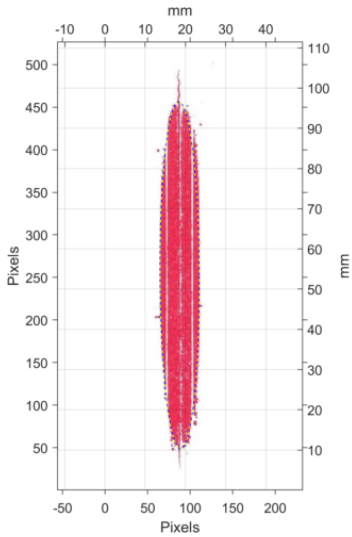

Vittoria Tubeless

Tire size = 30 mm
Rim size = 25 mm
Pressure = 4.3 bar (62.3662 psi)
Load = 368.856 N (82.9221 lb)

Image
length = 407.8 pixels (86.3 mm)
width = 46.3 pixels (9.79 mm)
area = 14820 pixels^2 (664 mm^2)
orientation angle = 0.3°

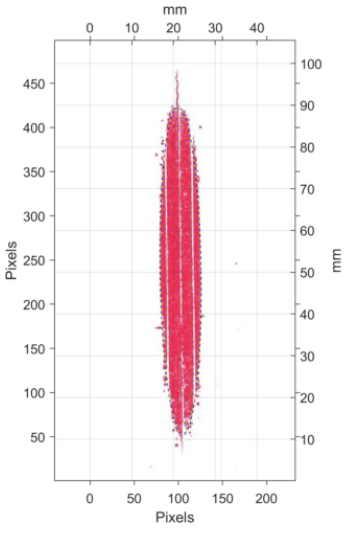

Vittoria Tubeless

Tire size = 30 mm
Rim size = 25 mm
Pressure = 4.3 bar (62.3662 psi)
Load = 296.262 N (66.6023 lb)

Image
length = 369.3 pixels (78.2 mm)
width = 46.5 pixels (9.84 mm)
area = 13486 pixels^2 (604.2 mm^2)
orientation angle = 0.84°

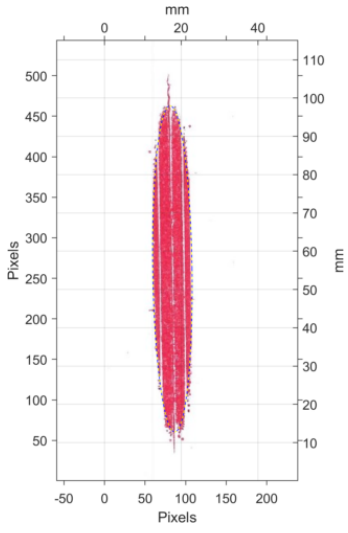

Vittoria Tubeless

Tire size = 30 mm
Rim size = 25 mm
Pressure = 4.3 bar (62.3662 psi)
Load = 368.856 N (82.9221 lb)

Image
length = 402.7 pixels (85.2 mm)
width = 48.5 pixels (10.3 mm)
area = 15336 pixels^2 (687.1 mm^2)
orientation angle = 0.84°

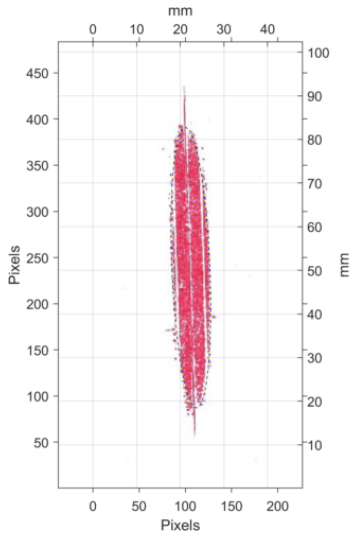

Vittoria Tubeless

Tire size = 30 mm
Rim size = 25 mm
Pressure = 4.8 bar (69.6181 psi)
Load = 208.953 N (46.9745 lb)

Image
length = 303.9 pixels (64.3 mm)
width = 41.2 pixels (8.72 mm)
area = 9829 pixels^2 (440.3 mm^2)
orientation angle = 2.3°

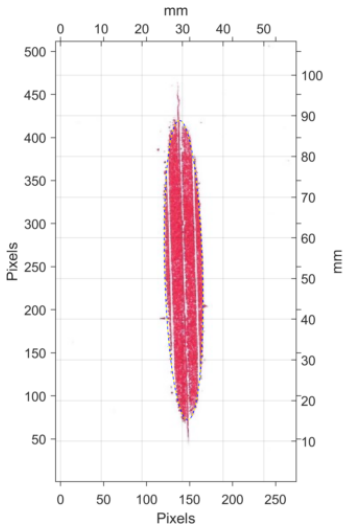

Vittoria Tubeless

Tire size = 30 mm
Rim size = 25 mm
Pressure = 4.8 bar (69.6181 psi)
Load = 287.433 N (64.6175 lb)

Image
length = 347.8 pixels (73.6 mm)
width = 44.3 pixels (9.37 mm)
area = 12089 pixels^2 (541.6 mm^2)
orientation angle = 1.6°

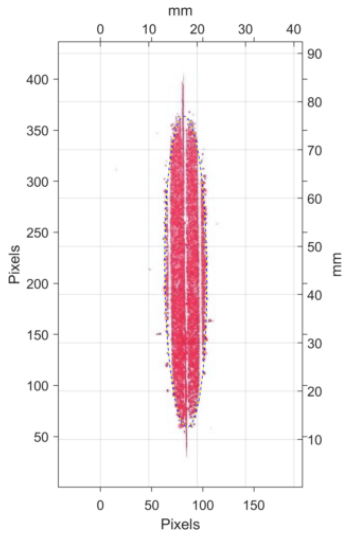

Vittoria Tubeless

Tire size = 30 mm
Rim size = 25 mm
Pressure = 4.8 bar (69.6181 psi)
Load = 205.029 N (46.0924 lb)

Image
length = 304.4 pixels (64.4 mm)
width = 41.2 pixels (8.72 mm)
area = 9851 pixels^2 (441.4 mm^2)
orientation angle = 0.56°

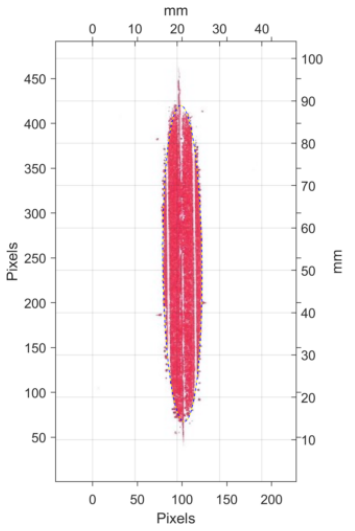

Vittoria Tubeless

Tire size = 30 mm
Rim size = 25 mm
Pressure = 4.8 bar (69.6181 psi)
Load = 287.433 N (64.6175 lb)

Image
length = 352.8 pixels (74.7 mm)
width = 43.9 pixels (9.28 mm)
area = 12151 pixels^2 (544.4 mm^2)
orientation angle = 0.65°

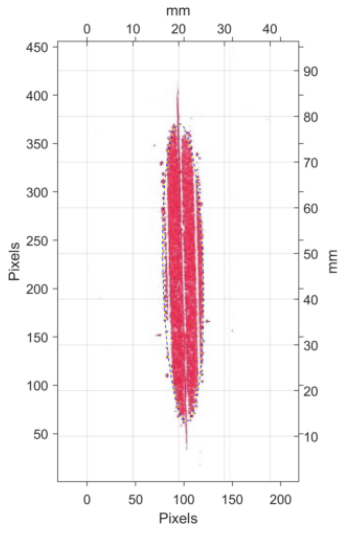

Vittoria Tubeless

Tire size = 30 mm
Rim size = 25 mm
Pressure = 4.8 bar (69.6181 psi)
Load = 205.029 N (46.0924 lb)

Image
length = 307.2 pixels (65 mm)
width = 41.6 pixels (8.81 mm)
area = 10045 pixels^2 (450.1 mm^2)
orientation angle = 1.4°

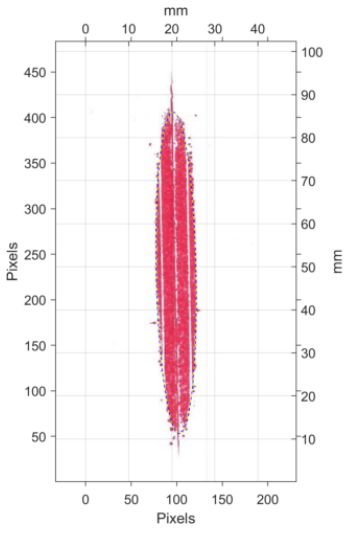

Vittoria Tubeless

Tire size = 30 mm
Rim size = 25 mm
Pressure = 4.8 bar (69.6181 psi)
Load = 287.433 N (64.6175 lb)

Image
length = 352.9 pixels (74.7 mm)
width = 43.8 pixels (9.27 mm)
area = 12138 pixels^2 (543.8 mm^2)
orientation angle = 1.2°

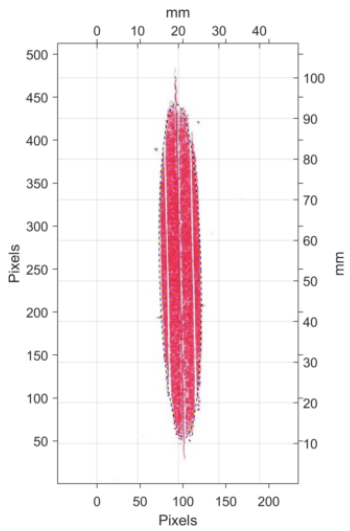

Vittoria Tubeless

Tire size = 30 mm
Rim size = 25 mm
Pressure = 4.8 bar (69.6181 psi)
Load = 369.837 N (83.1427 lb)

Image
length = 388.7 pixels (82.3 mm)
width = 48.5 pixels (10.3 mm)
area = 14805 pixels^2 (663.3 mm^2)
orientation angle = 1.4°

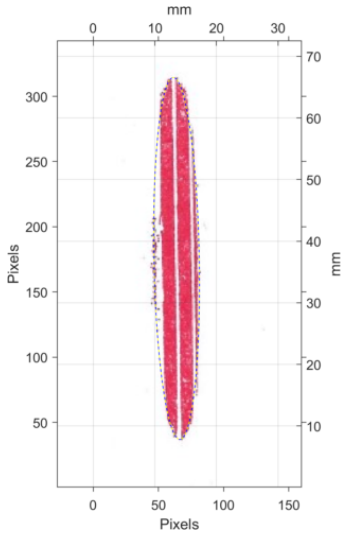

Vittoria Tubular

Tire size = 26 mm
Rim size = 25 mm
Pressure = 6 bar (87.0226 psi)
Load = 211.896 N (47.6361 lb)

Image
length = 277.7 pixels (58.8 mm)
width = 34.7 pixels (7.35 mm)
area = 7569 pixels^2 (339.1 mm^2)
orientation angle = 1.1°

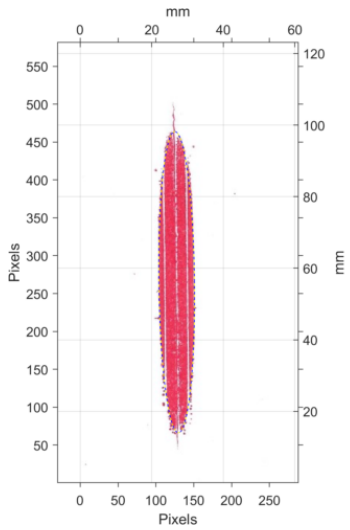

Vittoria Tubeless

Tire size = 30 mm
Rim size = 25 mm
Pressure = 4.8 bar (69.6181 psi)
Load = 365.913 N (82.2605 lb)

Image
length = 397.8 pixels (84.2 mm)
width = 47.2 pixels (9.98 mm)
area = 14739 pixels^2 (660.3 mm^2)
orientation angle = 0.68°

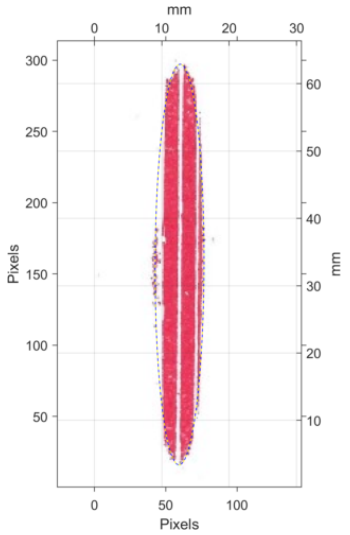

Vittoria Tubular

Tire size = 26 mm
Rim size = 25 mm
Pressure = 6 bar (87.0226 psi)
Load = 214.839 N (48.2977 lb)

Image
length = 281.2 pixels (59.5 mm)
width = 34.3 pixels (7.26 mm)
area = 7578 pixels^2 (339.5 mm^2)
orientation angle = -0.17°

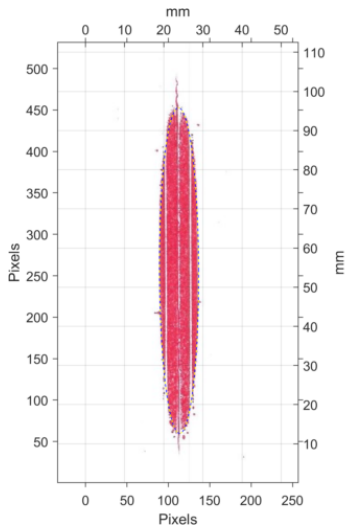

Vittoria Tubeless

Tire size = 30 mm
Rim size = 25 mm
Pressure = 4.8 bar (69.6181 psi)
Load = 367.875 N (82.7016 lb)

Image
length = 393 pixels (83.2 mm)
width = 47.4 pixels (10 mm)
area = 14639 pixels^2 (655.9 mm^2)
orientation angle = 0.21°

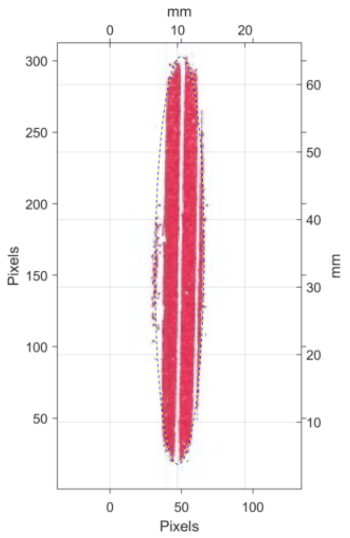

Vittoria Tubular

Tire size = 26 mm
Rim size = 25 mm
Pressure = 6 bar (87.0226 psi)
Load = 216.801 N (48.7388 lb)

Image
length = 285.4 pixels (60.4 mm)
width = 34.2 pixels (7.24 mm)
area = 7666 pixels^2 (343.4 mm^2)
orientation angle = -0.42°

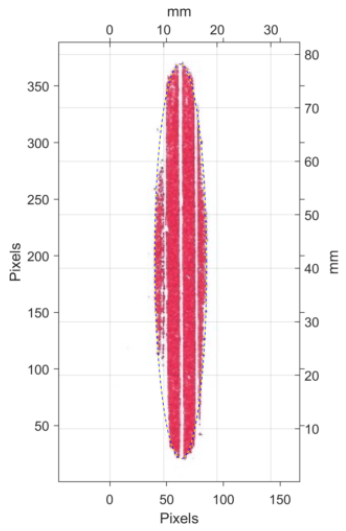

Vittoria Tubular

Tire size = 26 mm
Rim size = 25 mm
Pressure = 6 bar (87.0226 psi)
Load = 295.281 N (66.3818 lb)

Image
length = 348.6 pixels (73.8 mm)
width = 45.7 pixels (9.67 mm)
area = 12507 pixels^2 (560.3 mm^2)
orientation angle = 0.17°

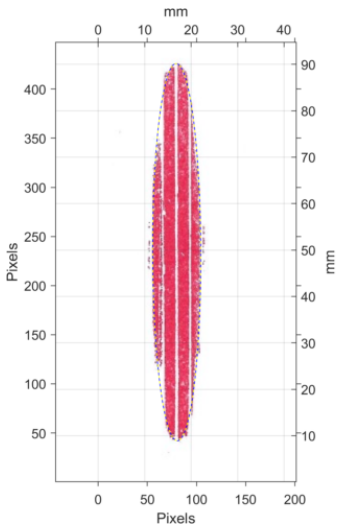

Vittoria Tubular

Tire size = 26 mm
Rim size = 25 mm
Pressure = 6 bar (87.0226 psi)
Load = 373.761 N (84.0248 lb)

Image
length = 384.1 pixels (81.3 mm)
width = 49 pixels (10.4 mm)
area = 14780 pixels^2 (662.2 mm^2)
orientation angle = 0.18°

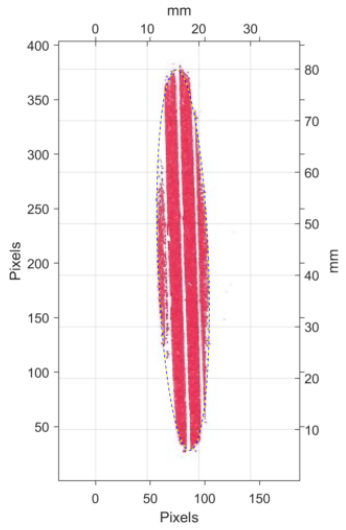

Vittoria Tubular

Tire size = 26 mm
Rim size = 25 mm
Pressure = 6 bar (87.0226 psi)
Load = 300.186 N (67.4845 lb)

Image
length = 349.6 pixels (74 mm)
width = 46.4 pixels (9.81 mm)
area = 12726 pixels^2 (570.2 mm^2)
orientation angle = 2.1°

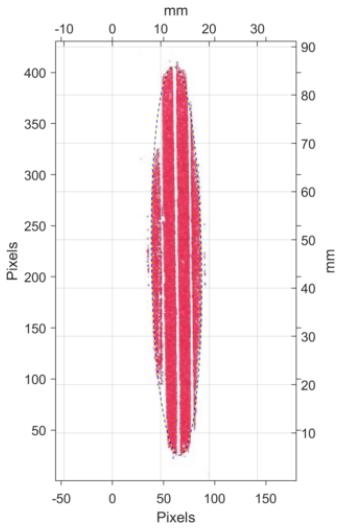

Vittoria Tubular

Tire size = 26 mm
Rim size = 25 mm
Pressure = 6 bar (87.0226 psi)
Load = 373.761 N (84.0248 lb)

Image
length = 380.5 pixels (80.5 mm)
width = 48.9 pixels (10.3 mm)
area = 14608 pixels^2 (654.5 mm^2)
orientation angle = 0.88°

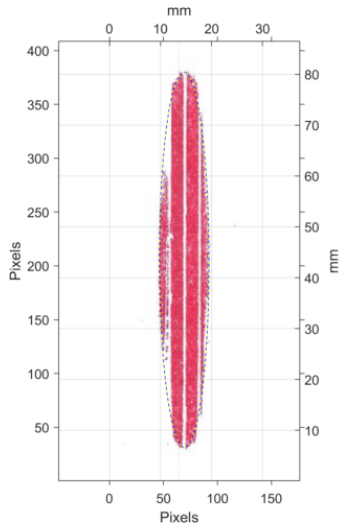

Vittoria Tubular

Tire size = 26 mm
Rim size = 25 mm
Pressure = 6 bar (87.0226 psi)
Load = 300.186 N (67.4845 lb)

Image
length = 348.9 pixels (73.9 mm)
width = 45.8 pixels (9.7 mm)
area = 12558 pixels^2 (562.6 mm^2)
orientation angle = 0.091°

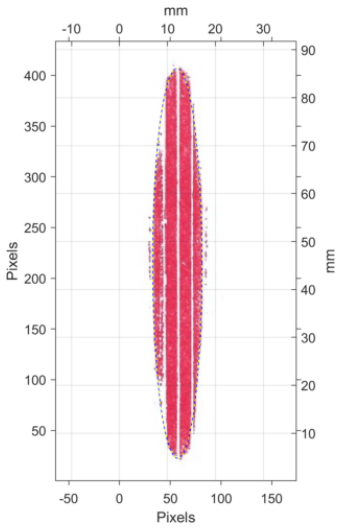

Vittoria Tubular

Tire size = 26 mm
Rim size = 25 mm
Pressure = 6 bar (87.0226 psi)
Load = 373.761 N (84.0248 lb)

Image
length = 384.4 pixels (81.4 mm)
width = 48.6 pixels (10.3 mm)
area = 14681 pixels^2 (657.8 mm^2)
orientation angle = 0.087°

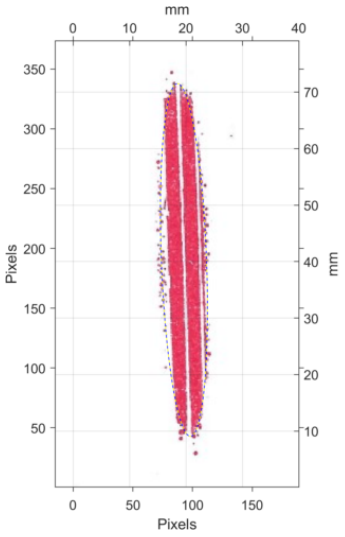

Vittoria Tubular

Tire size = 26 mm
Rim size = 25 mm
Pressure = 7.5 bar (108.778 psi)
Load = 211.896 N (47.6361 lb)

Image
length = 295.3 pixels (62.5 mm)
width = 37.9 pixels (8.01 mm)
area = 8779 pixels^2 (393.3 mm^2)
orientation angle = 2.2°

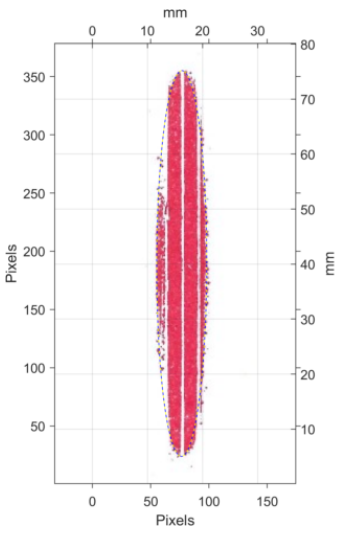

Vittoria Tubular

Tire size = 26 mm
Rim size = 25 mm
Pressure = 7.5 bar (108.778 psi)
Load = 297.243 N (66.8229 lb)

Image
length = 331.5 pixels (70.2 mm)
width = 43 pixels (9.09 mm)
area = 11185 pixels^2 (501.1 mm^2)
orientation angle = -0.088°

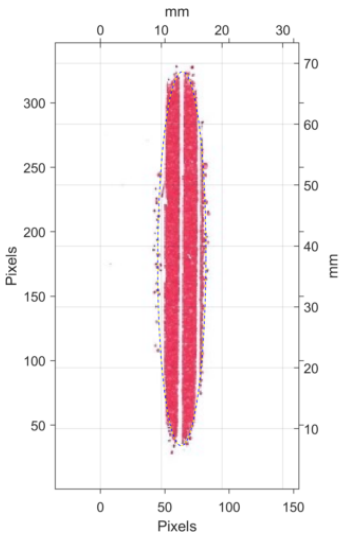

Vittoria Tubular

Tire size = 26 mm
Rim size = 25 mm
Pressure = 7.5 bar (108.778 psi)
Load = 207.972 N (46.754 lb)

Image
length = 290.3 pixels (61.4 mm)
width = 37.5 pixels (7.93 mm)
area = 8540 pixels^2 (382.6 mm^2)
orientation angle = -0.18°

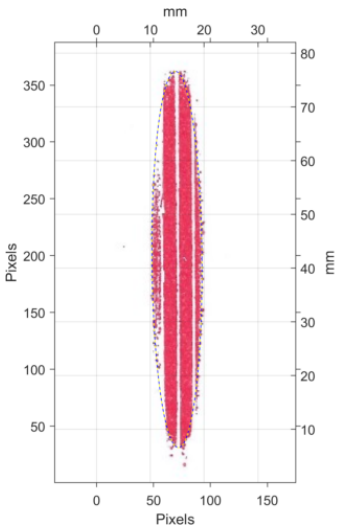

Vittoria Tubular

Tire size = 26 mm
Rim size = 25 mm
Pressure = 7.5 bar (108.778 psi)
Load = 297.243 N (66.8229 lb)

Image
length = 331 pixels (70.1 mm)
width = 44 pixels (9.31 mm)
area = 11435 pixels^2 (512.3 mm^2)
orientation angle = 0.45°

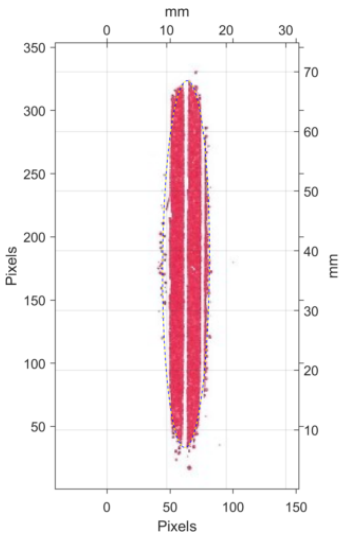

Vittoria Tubular

Tire size = 26 mm
Rim size = 25 mm
Pressure = 7.5 bar (108.778 psi)
Load = 211.896 N (47.6361 lb)

Image
length = 290.4 pixels (61.5 mm)
width = 37.3 pixels (7.89 mm)
area = 8499 pixels^2 (380.8 mm^2)
orientation angle = -0.38°

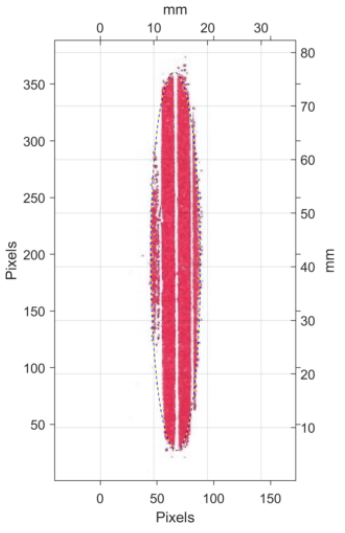

Vittoria Tubular

Tire size = 26 mm
Rim size = 25 mm
Pressure = 7.5 bar (108.778 psi)
Load = 297.243 N (66.8229 lb)

Image
length = 333.4 pixels (70.6 mm)
width = 43.6 pixels (9.22 mm)
area = 11411 pixels^2 (511.2 mm^2)
orientation angle = 0.27°

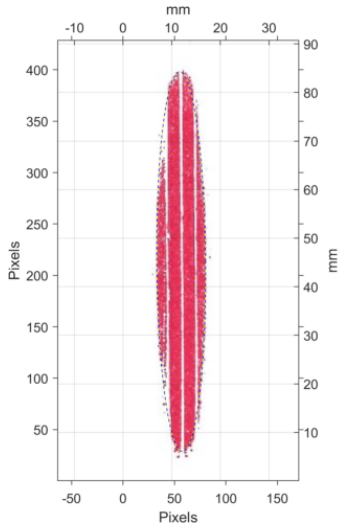

Vittoria Tubular

Tire size = 26 mm
Rim size = 25 mm
Pressure = 7.5 bar (108.778 psi)
Load = 390.438 N (87.774 lb)

Image
length = 369.5 pixels (78.2 mm)
width = 47.5 pixels (10.1 mm)
area = 13782 pixels^2 (617.5 mm^2)
orientation angle = 0.45°

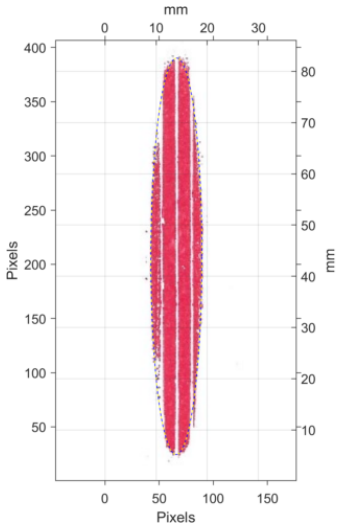

Vittoria Tubular

Tire size = 26 mm
Rim size = 25 mm
Pressure = 7.5 bar (108.778 psi)
Load = 384.552 N (86.4507 lb)

Image
length = 365.9 pixels (77.4 mm)
width = 47.2 pixels (10 mm)
area = 13578 pixels^2 (608.3 mm^2)
orientation angle = -0.086°

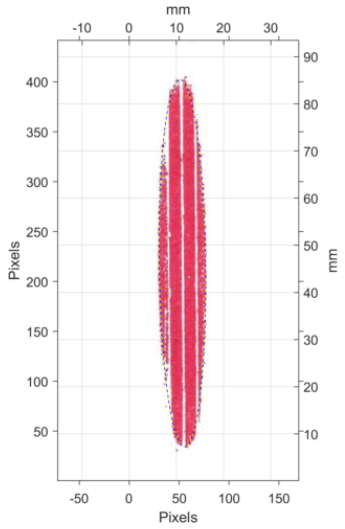

Vittoria Tubular

Tire size = 26 mm
Rim size = 25 mm
Pressure = 7.5 bar (108.778 psi)
Load = 387.495 N (87.1123 lb)

Image
length = 368.2 pixels (77.9 mm)
width = 46.5 pixels (9.85 mm)
area = 13460 pixels^2 (603.1 mm^2)
orientation angle = 0.74°

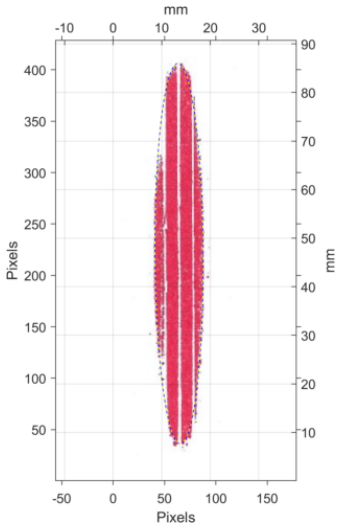

Vittoria Tubular

Tire size = 26 mm
Rim size = 25 mm
Pressure = 7.5 bar (108.778 psi)
Load = 389.457 N (87.5534 lb)

Image
length = 370.1 pixels (78.3 mm)
width = 46.9 pixels (9.93 mm)
area = 13636 pixels^2 (610.9 mm^2)
orientation angle = 0.36°

E

Data segments for rolling losses measurement

In section 4.4 and appendix **??**, the procedure regarding data selection for the rolling losses measurement are discussed. This chapter will present the data segments that are selected when following this procedure. The data selection is executed for each data file obtained with the Wahoo head unit. Each file include several runs corresponding to a specific tire and road surface. In some cases, files were also saved in between changes of inflation pressure. In these cases, the applied inflation pressure is also stored within the file name.

The segment selection will be presented by first showing the complete data set stored within one file. Followed by a representation of the selected data within a specific segment. It should be noted that some segment numbers are missing. These segments are deleted manually after the data selection procedure. This manual elimination of complete runs is based on the feedback of the cyclist regarding the execution of the run. The following list shows which segment are deleted and why these are removed from the results:

- 26mm 6b asphalt.csv Segment 1&2 - trial runs, no good feedback
- 26mm 6b asphalt.csv Segment 6&7 - no pedalling in the middle results in two separate sections of same run
- 26mm 6b asphalt.csv Segment 9 - does not accelerate fast enough at the start
- 26mm 57b asphalt.csv Segment 8 - cycling velocity is to low for 30 kmh test and to high for 40 kmh test (speed is around 34 kmh)
- 26mm 53b asphalt.csv Segment 1 - Hit doors during run
- 28mm asphalt.csv Segment 4 - Doors open during run
- 26mm brickroad.csv Segment 7 - stops pedalling during run
- 26mm brickroad reverse.csv Segment 2 - stops pedalling during run

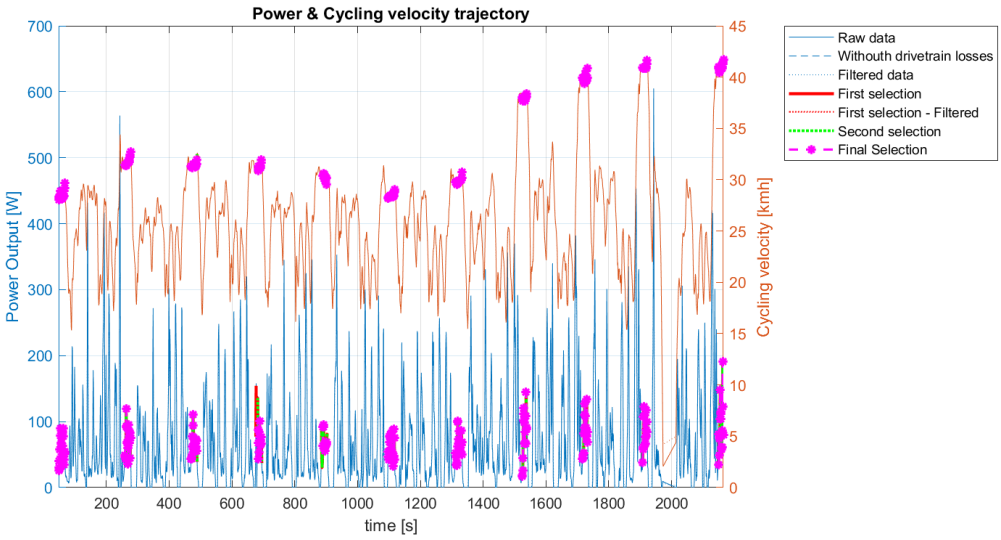

Figure E.1: Asphalt, 26mm Corsa Pro, 6 bar

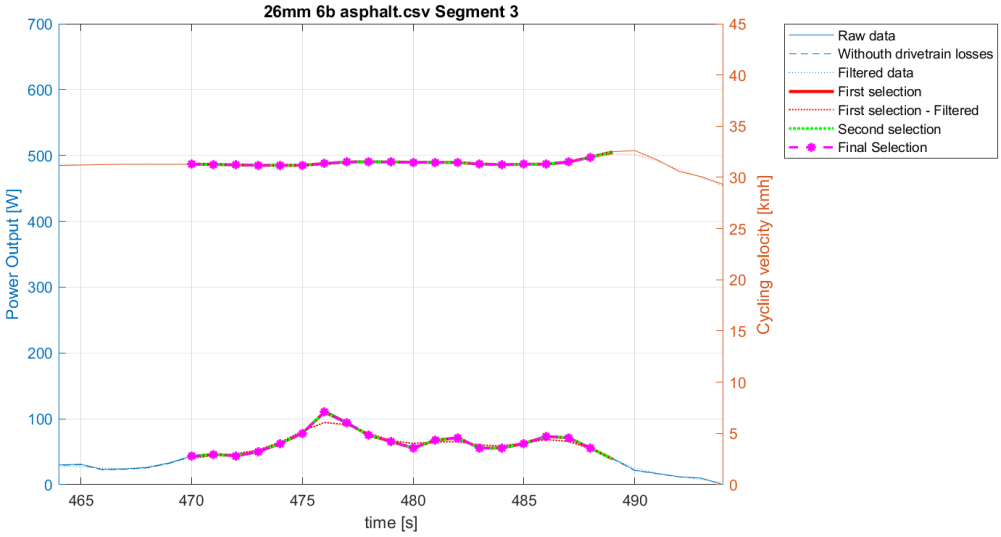

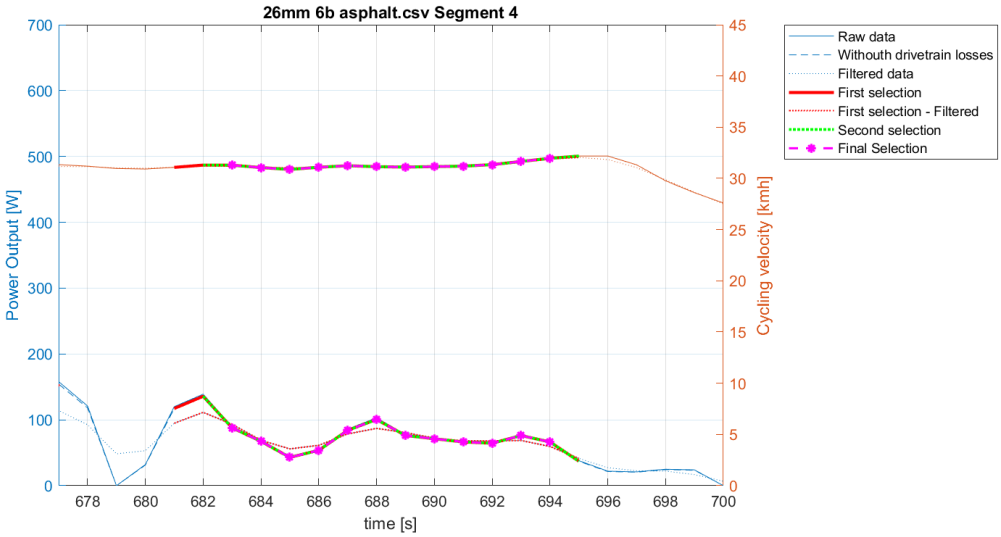

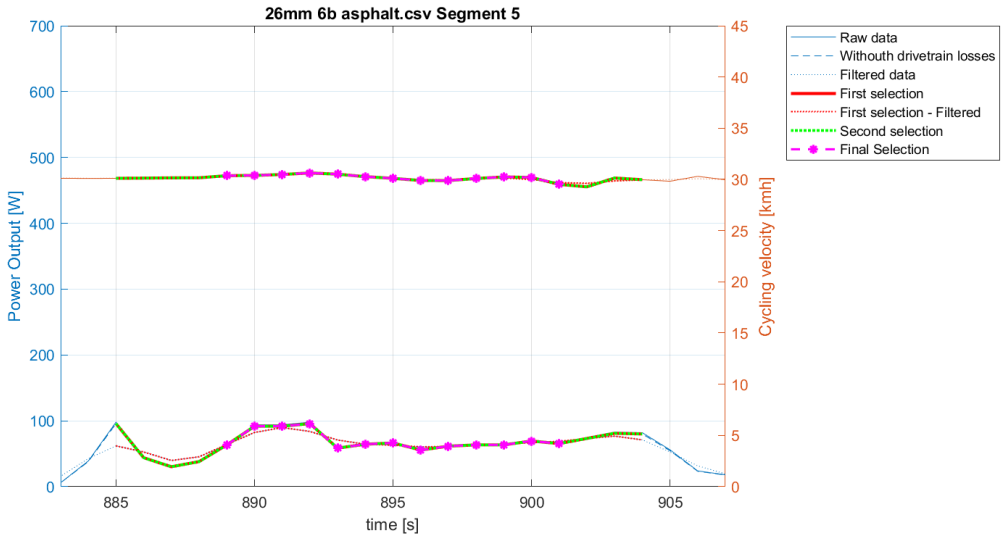
26mm 6b asphalt.csv Segment 5
Power Output [W]
Cycling velocity [kmh]
time [s]
Raw data
Withouth drivetrain losses
Filtered data
First selection
First selection - Filtered
Second selection
Final Selection

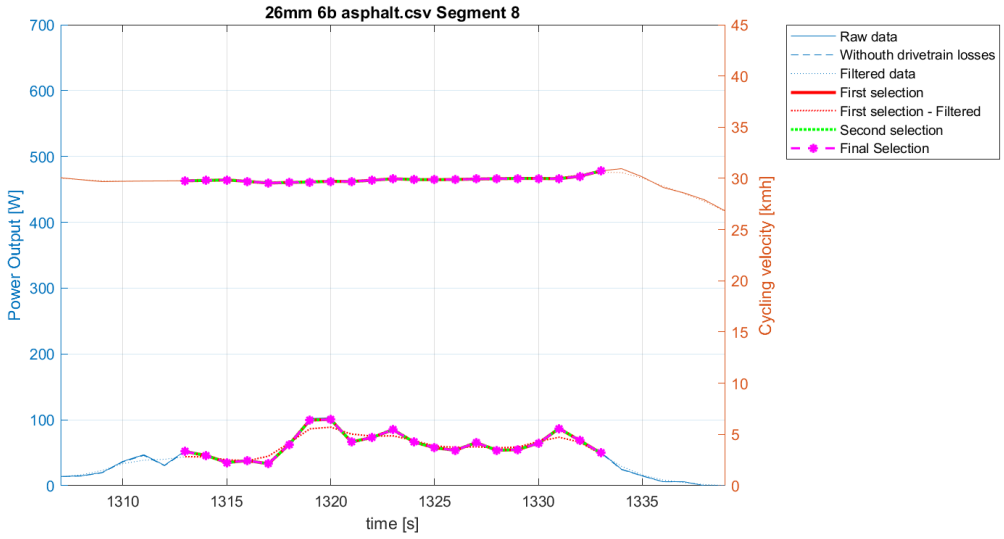
26mm 6b asphalt.csv Segment 8
Power Output [W]
Cycling velocity [kmh]
time [s]
Raw data
Withouth drivetrain losses
Filtered data
First selection
First selection - Filtered
Second selection
Final Selection

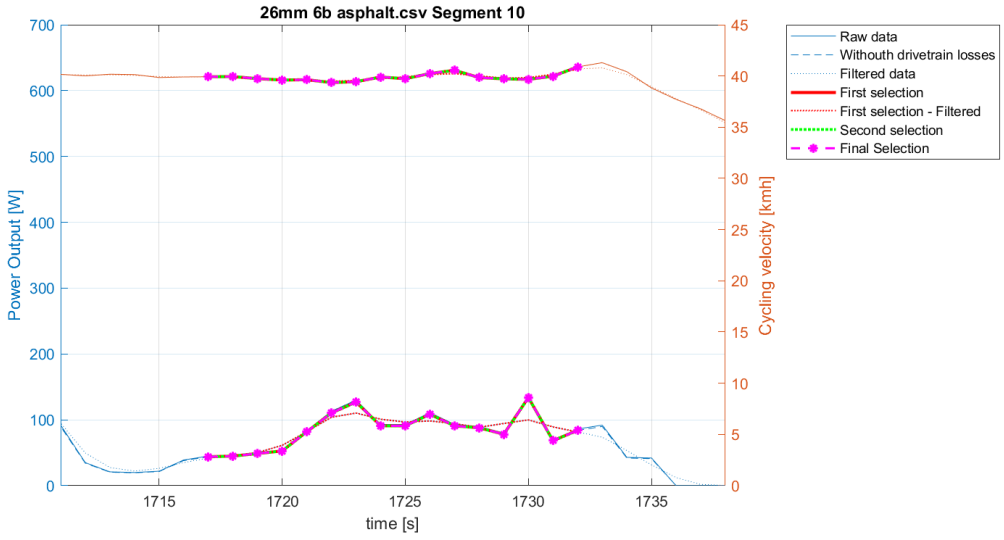
26mm 6b asphalt.csv Segment 10
Power Output [W]
Cycling velocity [kmh]
time [s]
Raw data
Withouth drivetrain losses
Filtered data
First selection
First selection - Filtered
Second selection
Final Selection

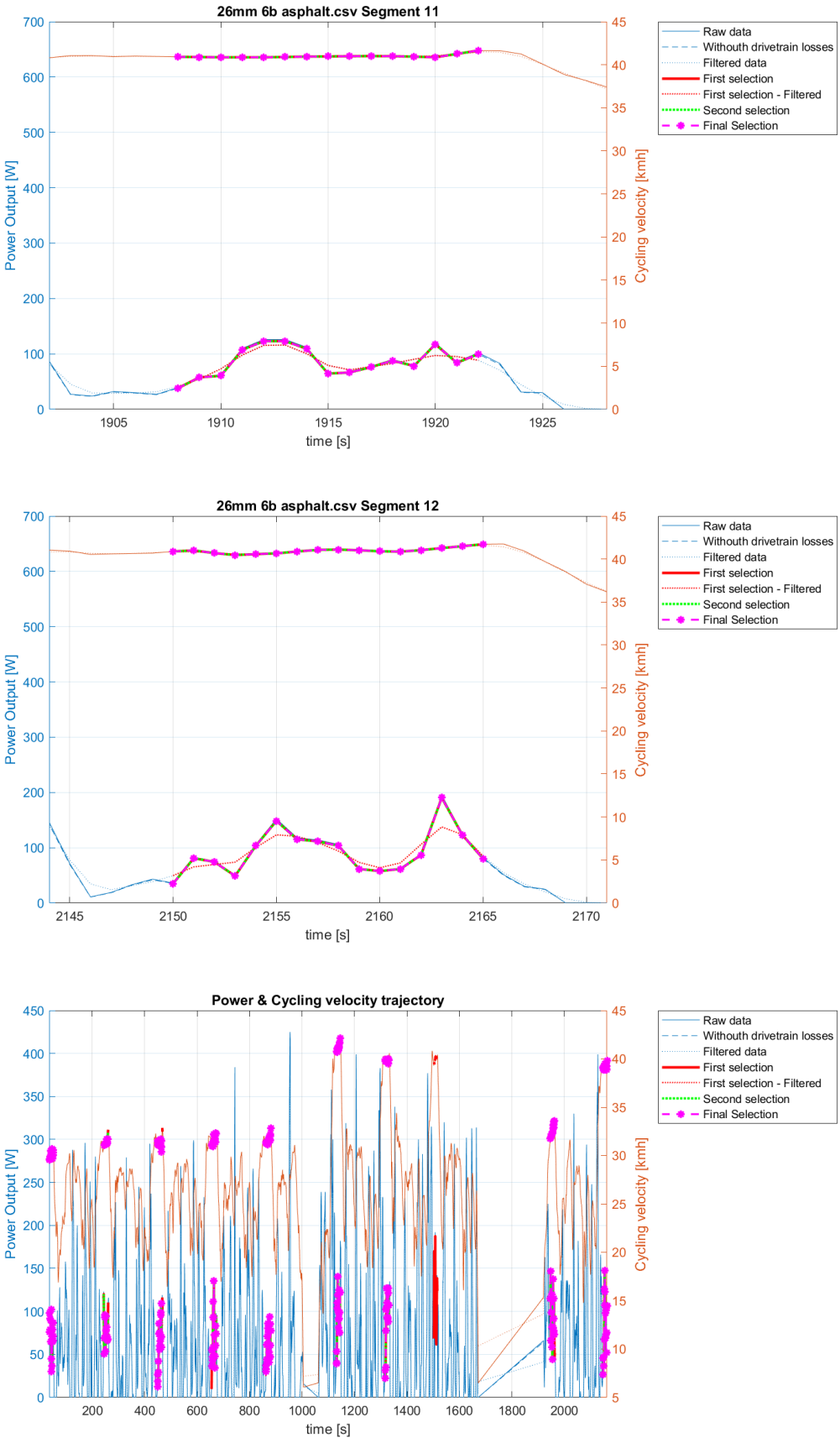

Figure E.2: Asphalt, 26mm Corsa Pro, 5.7 bar

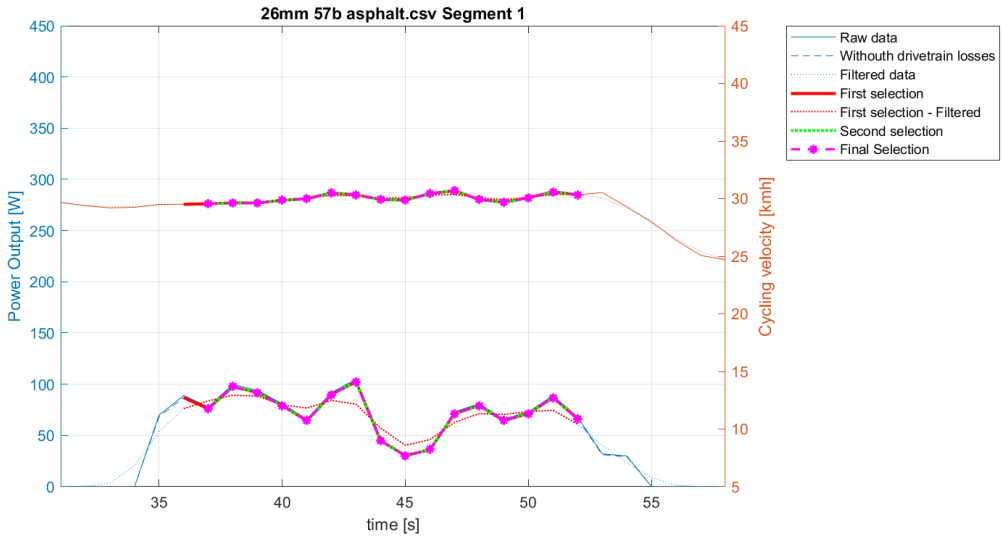
26mm 57b asphalt.csv Segment 1
Power Output [W]
Cycling velocity [kmh]
time [s]
Raw data
Withouth drivetrain losses
Filtered data
First selection
First selection - Filtered
Second selection
Final Selection

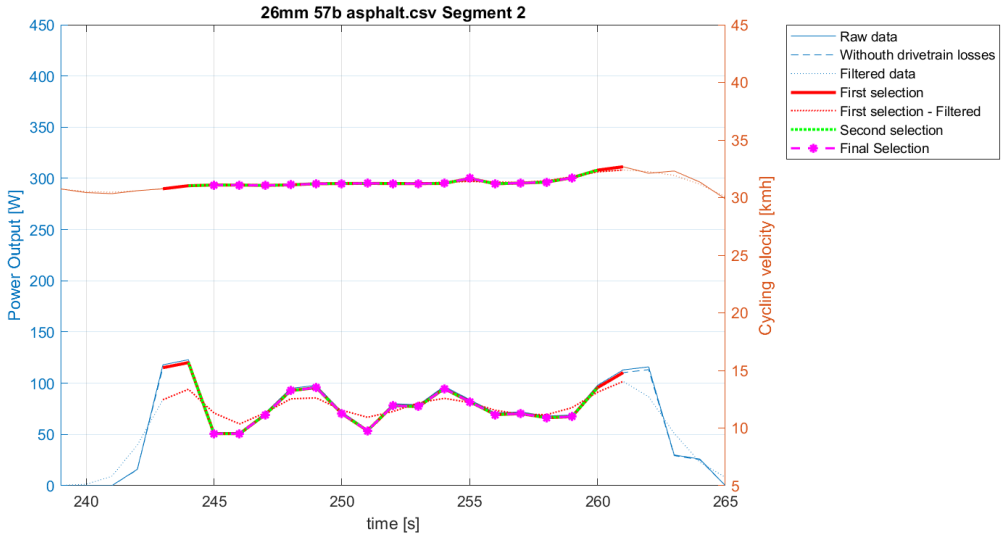
26mm 57b asphalt.csv Segment 2
Power Output [W]
Cycling velocity [kmh]
time [s]
Raw data
Withouth drivetrain losses
Filtered data
First selection
First selection - Filtered
Second selection
Final Selection

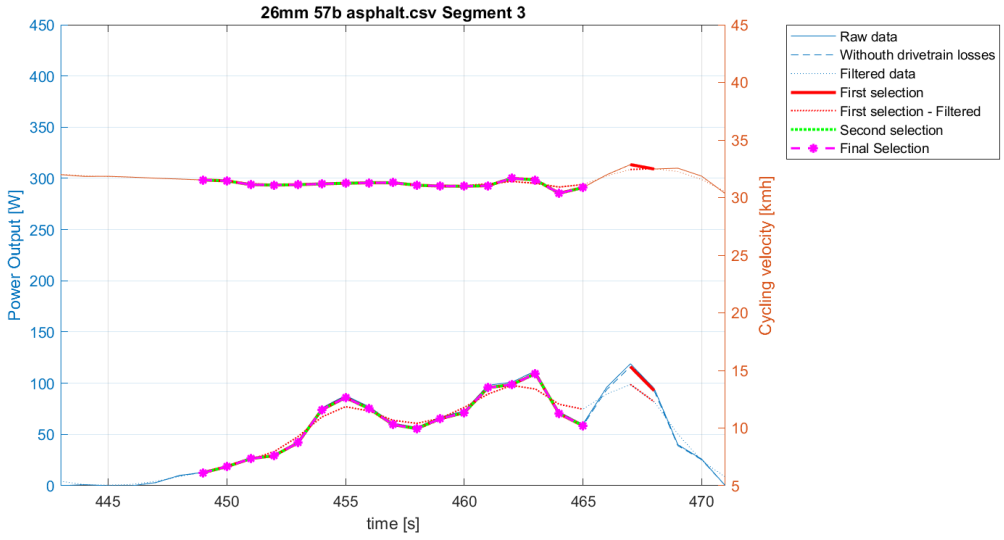
26mm 57b asphalt.csv Segment 3
Power Output [W]
Cycling velocity [kmh]
time [s]
Raw data
Withouth drivetrain losses
Filtered data
First selection
First selection - Filtered
Second selection
Final Selection

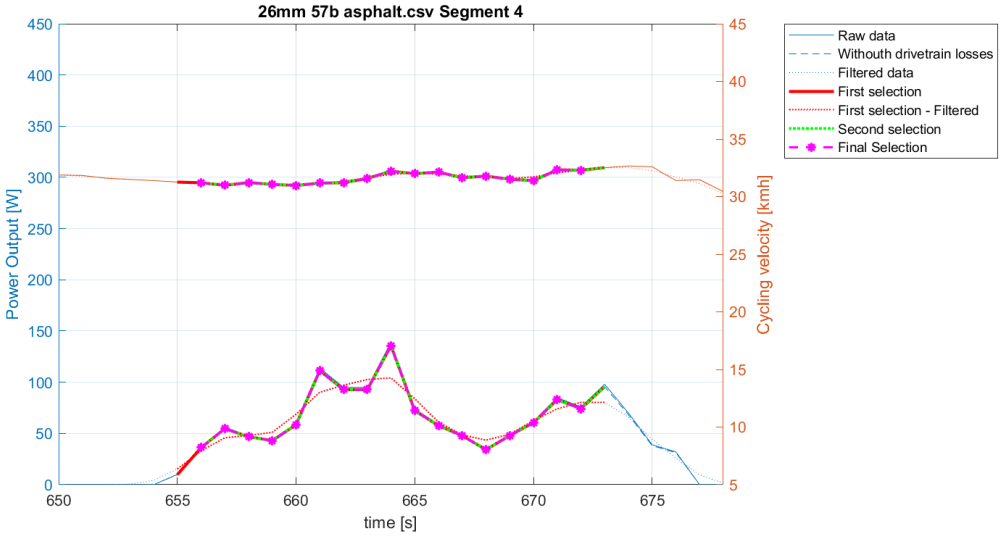
26mm 57b asphalt.csv Segment 4
Power Output [W]
Cycling velocity [kmh]
time [s]
Raw data
Withouth drivetrain losses
Filtered data
First selection
First selection - Filtered
Second selection
Final Selection

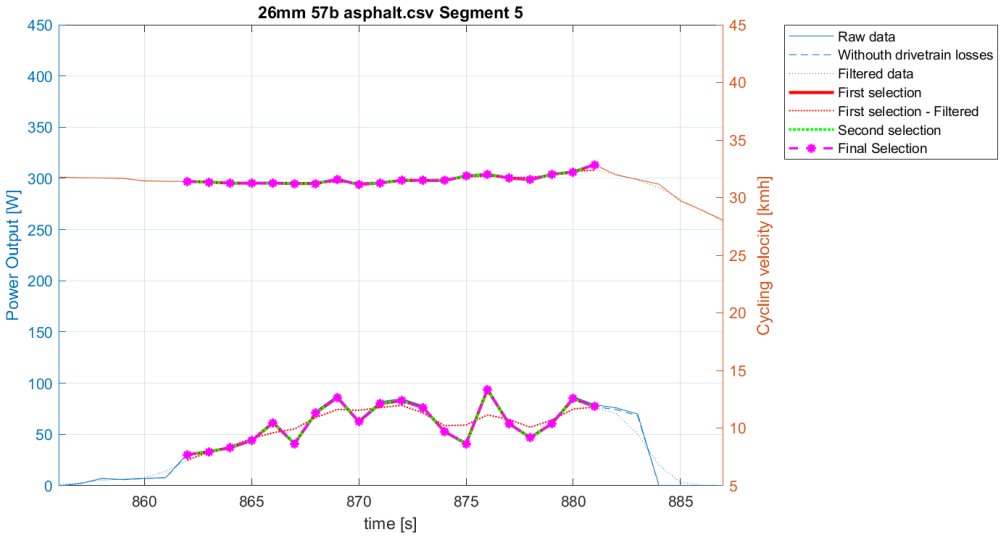
26mm 57b asphalt.csv Segment 5
Power Output [W]
Cycling velocity [kmh]
time [s]
Raw data
Withouth drivetrain losses
Filtered data
First selection
First selection - Filtered
Second selection
Final Selection

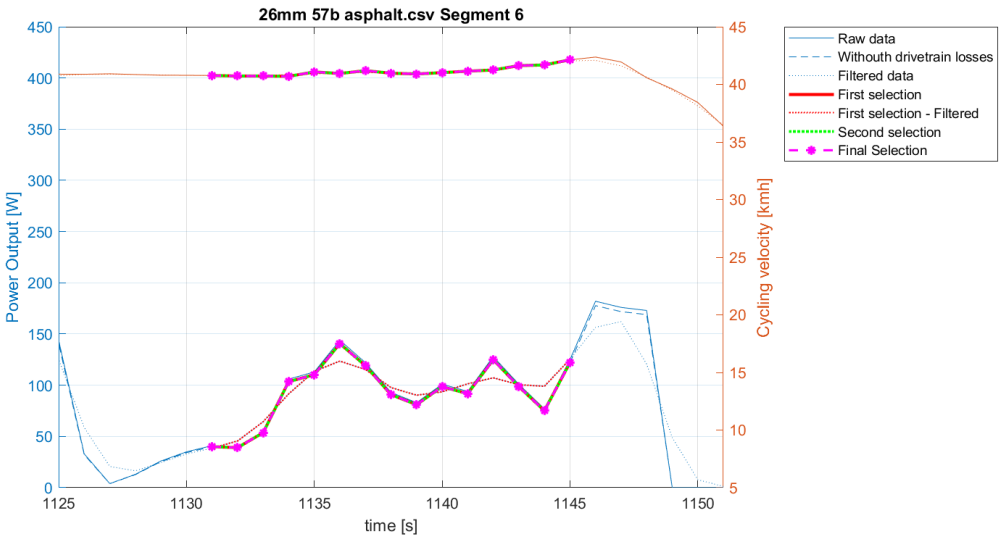
26mm 57b asphalt.csv Segment 6
Power Output [W]
Cycling velocity [kmh]
time [s]
Raw data
Withouth drivetrain losses
Filtered data
First selection
First selection - Filtered
Second selection
Final Selection

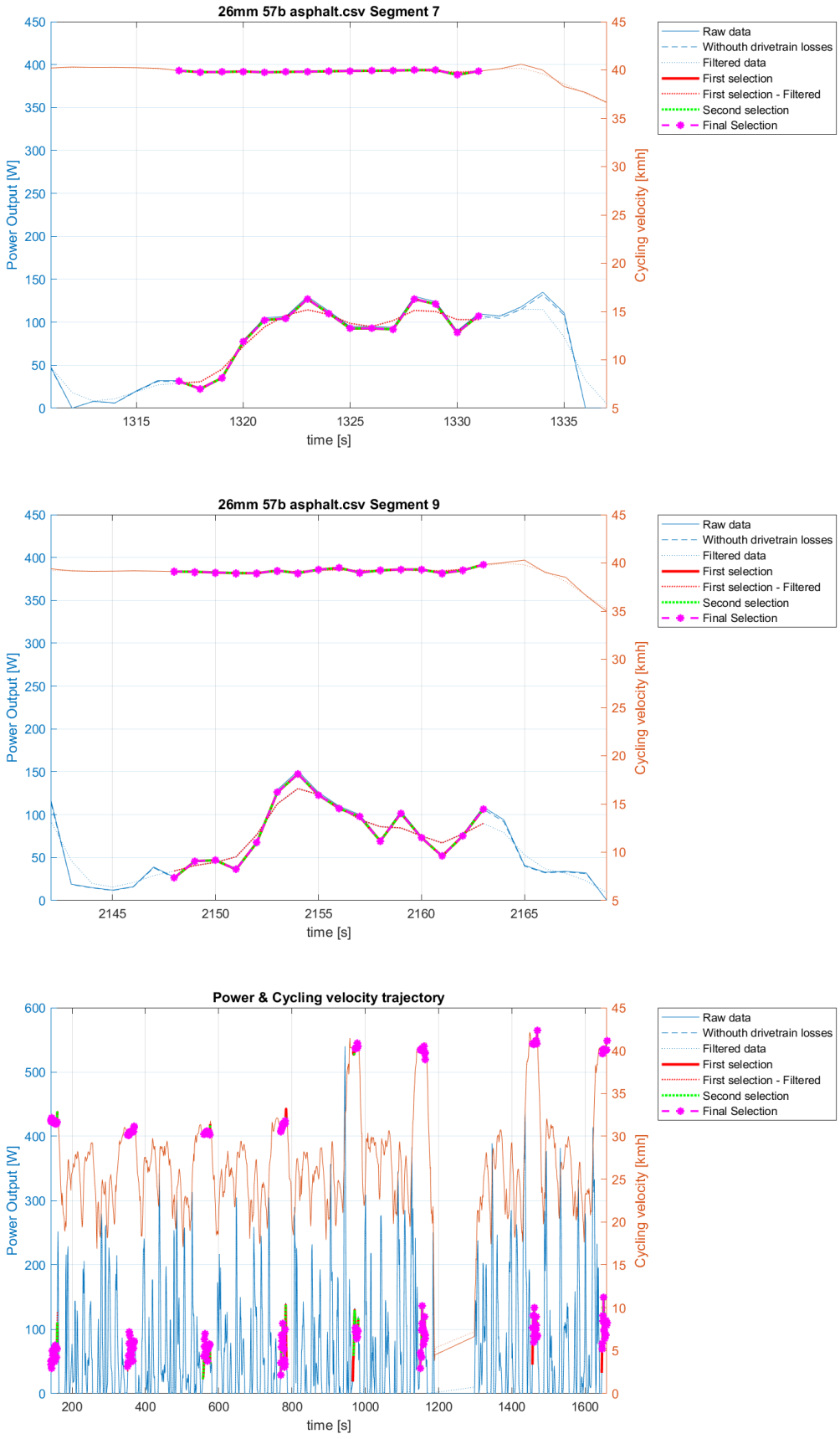

Figure E.3: Asphalt, 26mm Corsa Pro, 5.3 bar

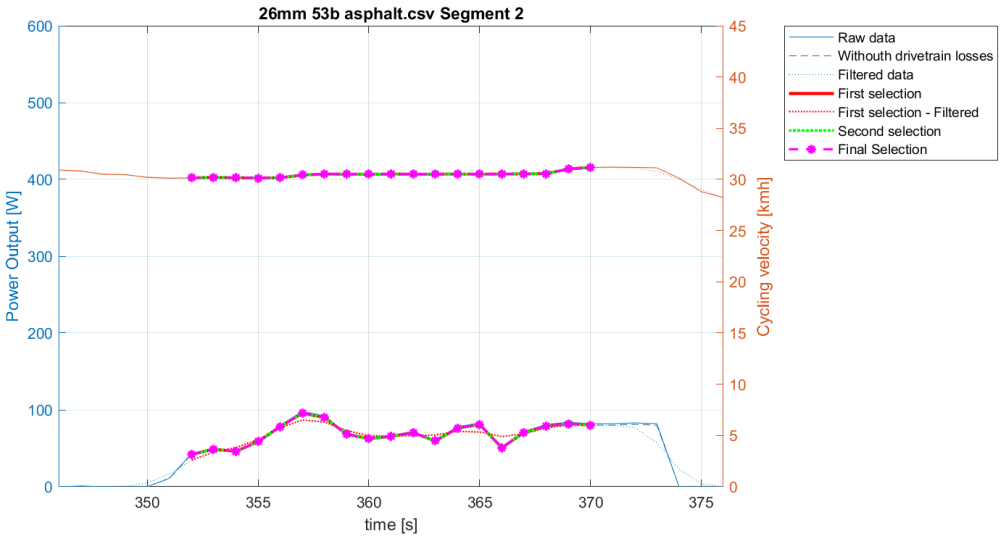
26mm 53b asphalt.csv Segment 2
Power Output [W]
Cycling velocity [kmh]
time [s]
Raw data
Withouth drivetrain losses
Filtered data
First selection
First selection - Filtered
Second selection
Final Selection

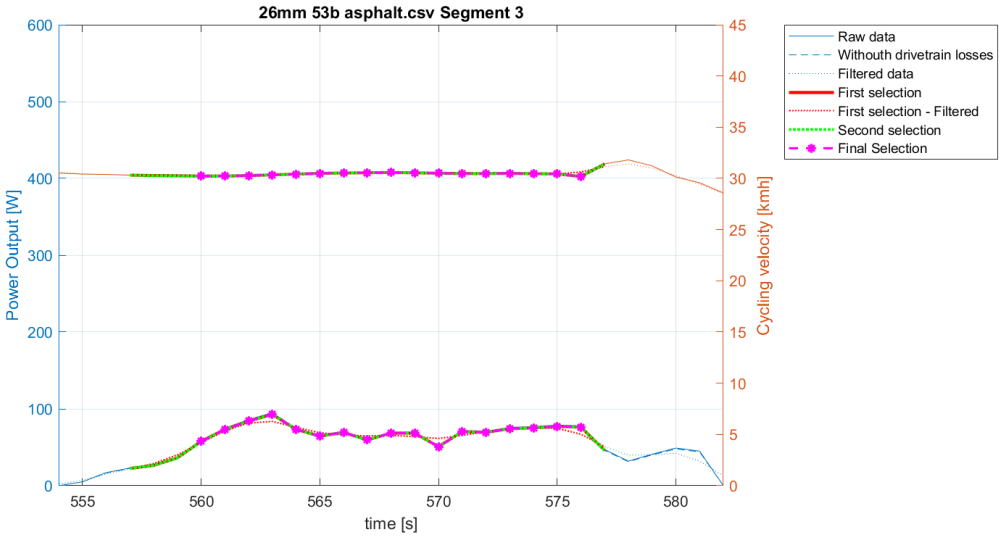
26mm 53b asphalt.csv Segment 3
Power Output [W]
Cycling velocity [kmh]
time [s]
Raw data
Withouth drivetrain losses
Filtered data
First selection
First selection - Filtered
Second selection
Final Selection

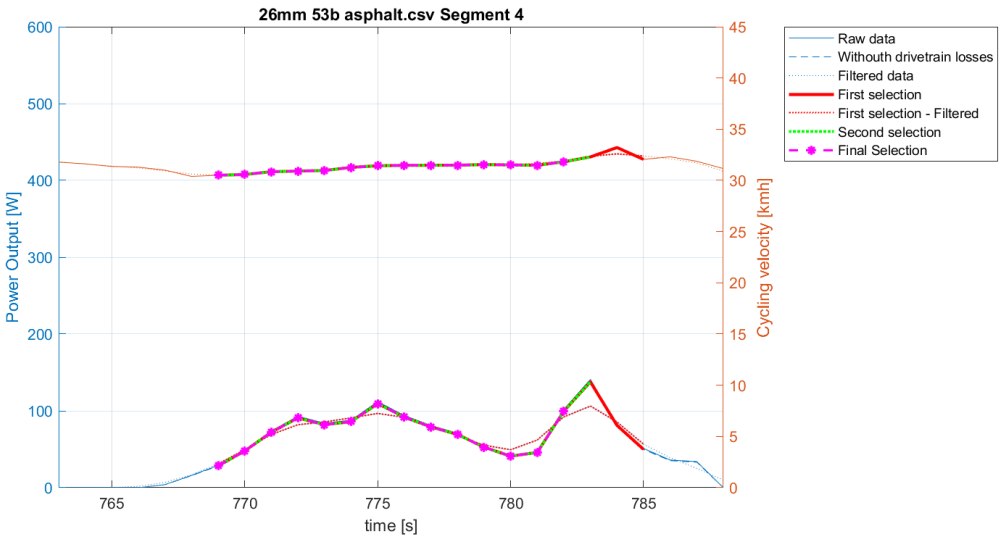
26mm 53b asphalt.csv Segment 4
Power Output [W]
Cycling velocity [kmh]
time [s]
Raw data
Withouth drivetrain losses
Filtered data
First selection
First selection - Filtered
Second selection
Final Selection

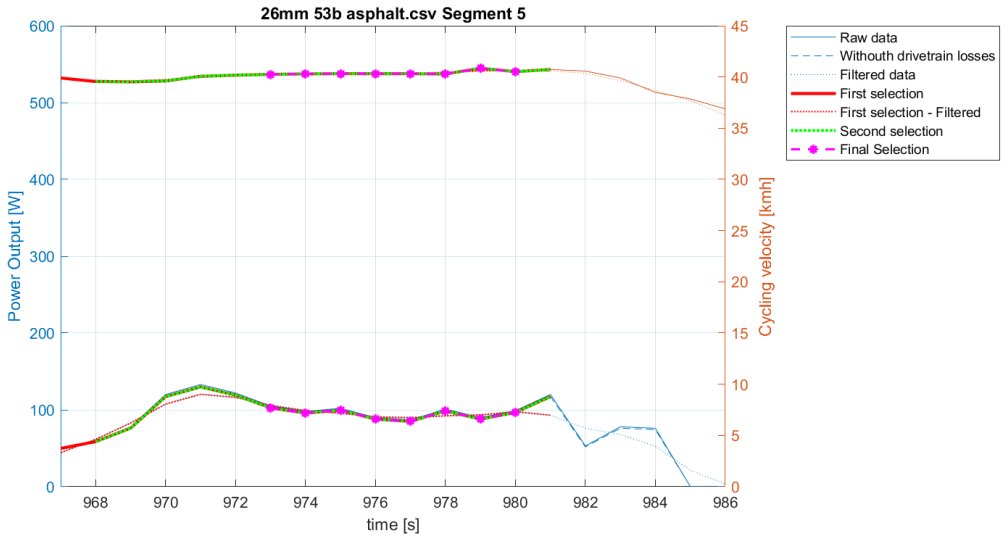
26mm 53b asphalt.csv Segment 5
Power Output [W]
Cycling velocity [kmh]
time [s]
Raw data
Withouth drivetrain losses
Filtered data
First selection
First selection - Filtered
Second selection
Final Selection

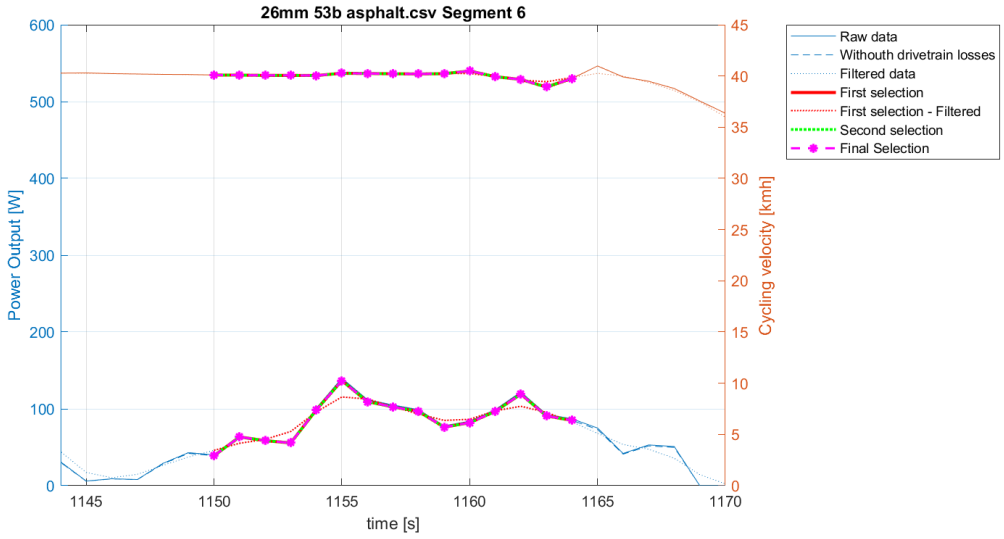
26mm 53b asphalt.csv Segment 6
Power Output [W]
Cycling velocity [kmh]
time [s]
Raw data
Withouth drivetrain losses
Filtered data
First selection
First selection - Filtered
Second selection
Final Selection

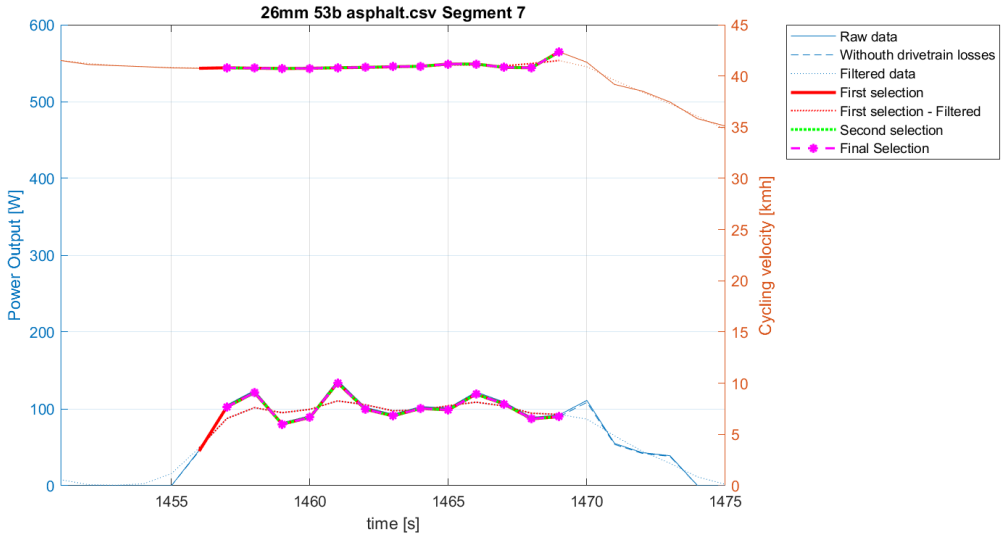
26mm 53b asphalt.csv Segment 7
Power Output [W]
Cycling velocity [kmh]
time [s]
Raw data
Withouth drivetrain losses
Filtered data
First selection
First selection - Filtered
Second selection
Final Selection

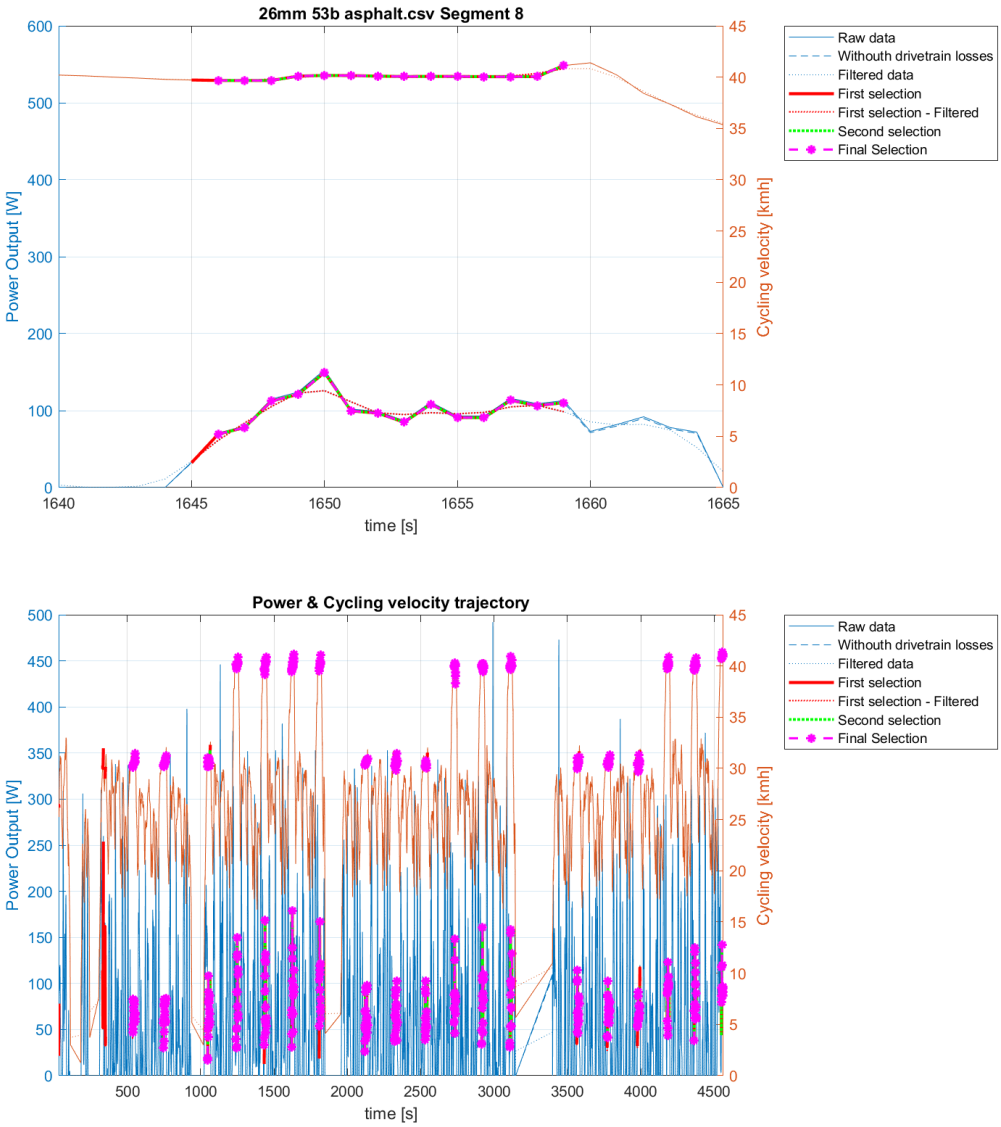

Figure E.4: Asphalt, 28mm Corsa Pro

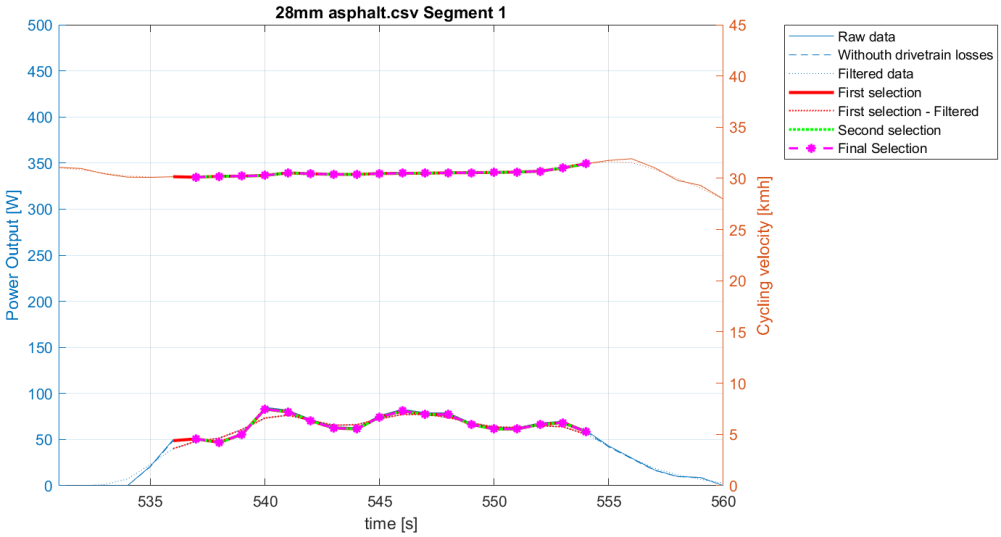

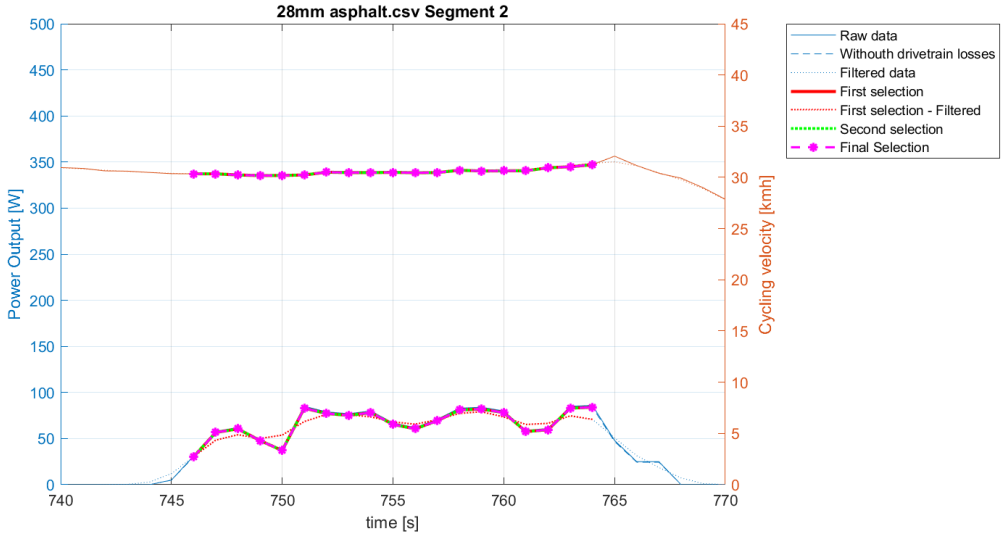
28mm asphalt.csv Segment 2
Power Output [W]
Cycling velocity [kmh]
time [s]
Raw data
Withouth drivetrain losses
Filtered data
First selection
First selection - Filtered
Second selection
Final Selection

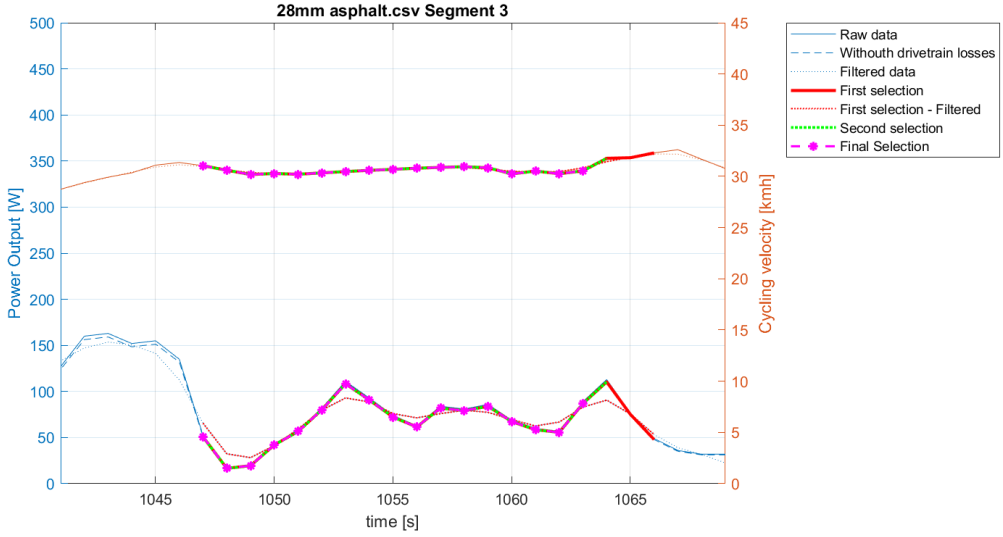
28mm asphalt.csv Segment 3
Power Output [W]
Cycling velocity [kmh]
time [s]
Raw data
Withouth drivetrain losses
Filtered data
First selection
First selection - Filtered
Second selection
Final Selection

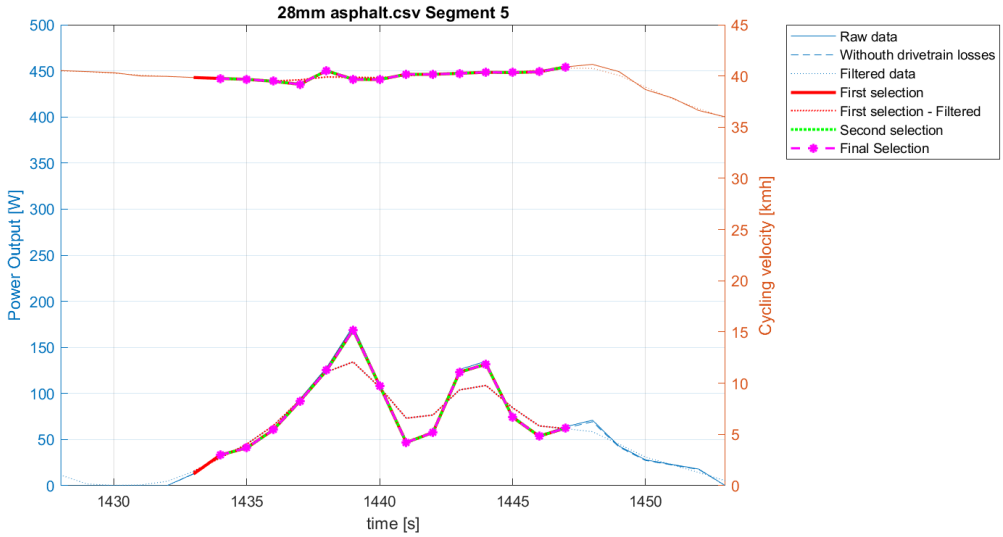
28mm asphalt.csv Segment 5
Power Output [W]
Cycling velocity [kmh]
time [s]
Raw data
Withouth drivetrain losses
Filtered data
First selection
First selection - Filtered
Second selection
Final Selection

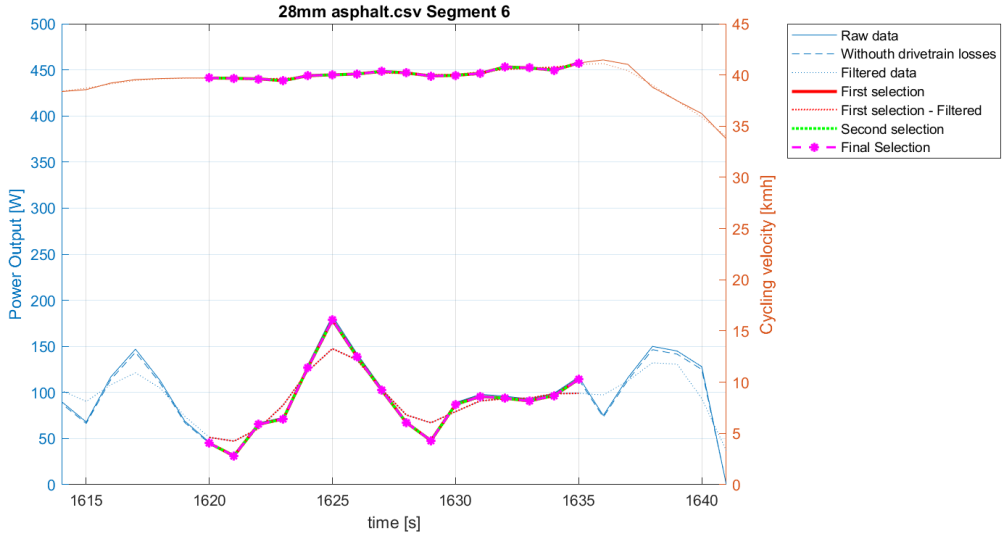
28mm asphalt.csv Segment 6
Power Output [W]
Cycling velocity [kmh]
time [s]
Raw data
Withouth drivetrain losses
Filtered data
First selection
First selection - Filtered
Second selection
Final Selection

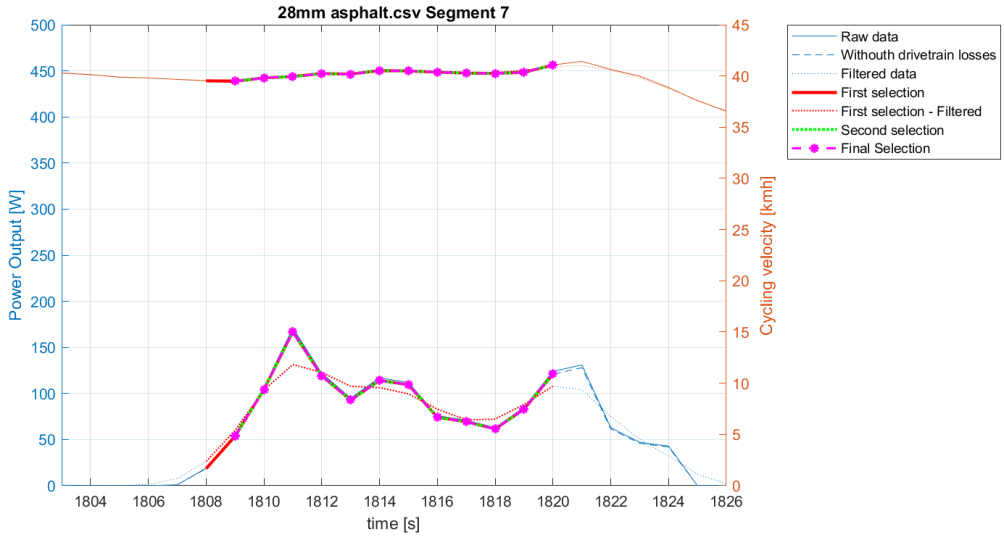
28mm asphalt.csv Segment 7
Power Output [W]
Cycling velocity [kmh]
time [s]
Raw data
Withouth drivetrain losses
Filtered data
First selection
First selection - Filtered
Second selection
Final Selection

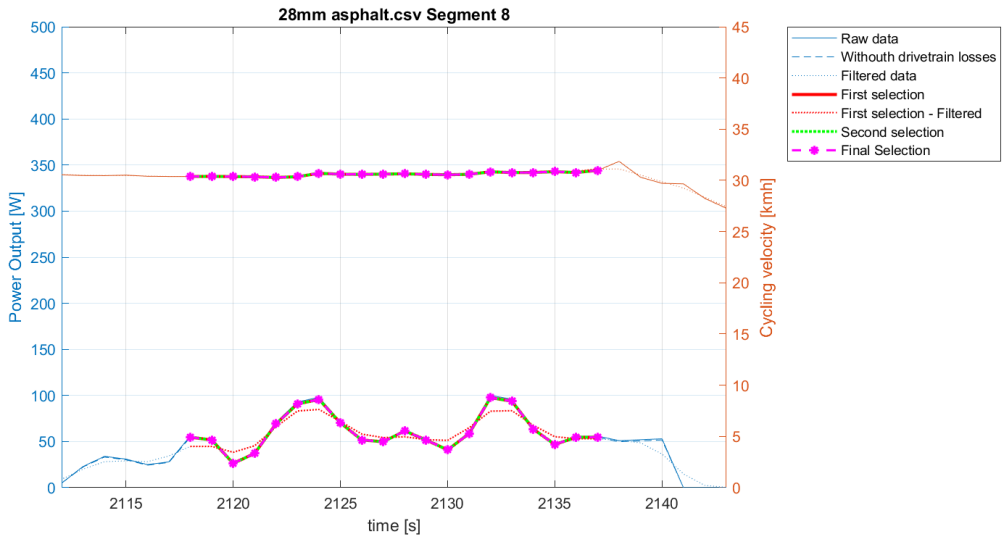
28mm asphalt.csv Segment 8
Power Output [W]
Cycling velocity [kmh]
time [s]
Raw data
Withouth drivetrain losses
Filtered data
First selection
First selection - Filtered
Second selection
Final Selection

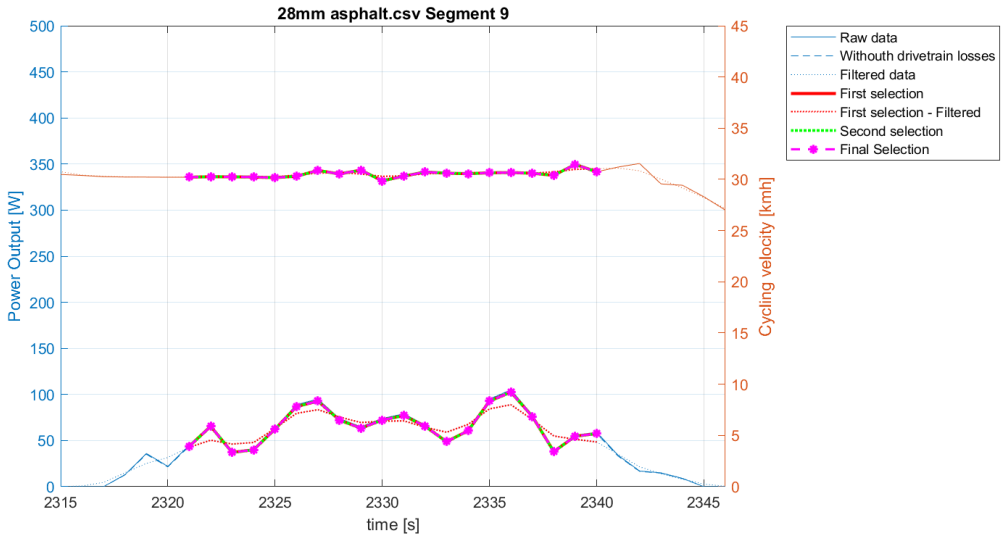
28mm asphalt.csv Segment 9
Power Output [W]
Cycling velocity [kmh]
time [s]
Raw data
Withouth drivetrain losses
Filtered data
First selection
First selection - Filtered
Second selection
Final Selection

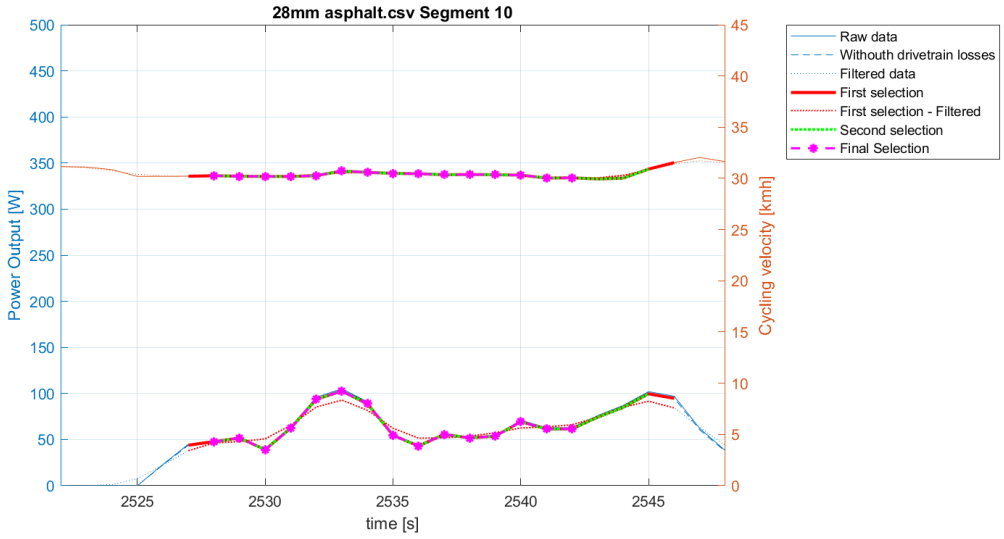
28mm asphalt.csv Segment 10
Power Output [W]
Cycling velocity [kmh]
time [s]
Raw data
Withouth drivetrain losses
Filtered data
First selection
First selection - Filtered
Second selection
Final Selection

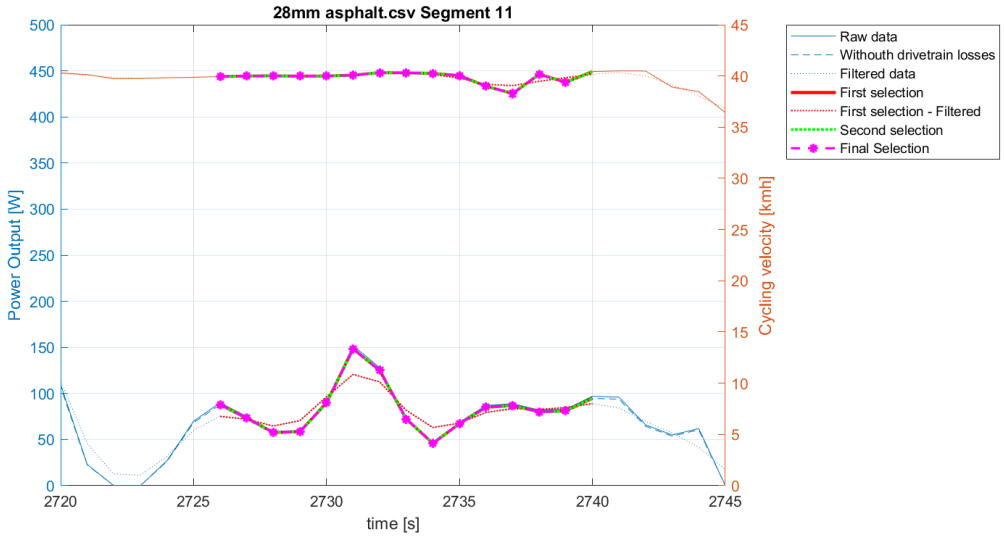
28mm asphalt.csv Segment 11
Power Output [W]
Cycling velocity [kmh]
time [s]
Raw data
Withouth drivetrain losses
Filtered data
First selection
First selection - Filtered
Second selection
Final Selection

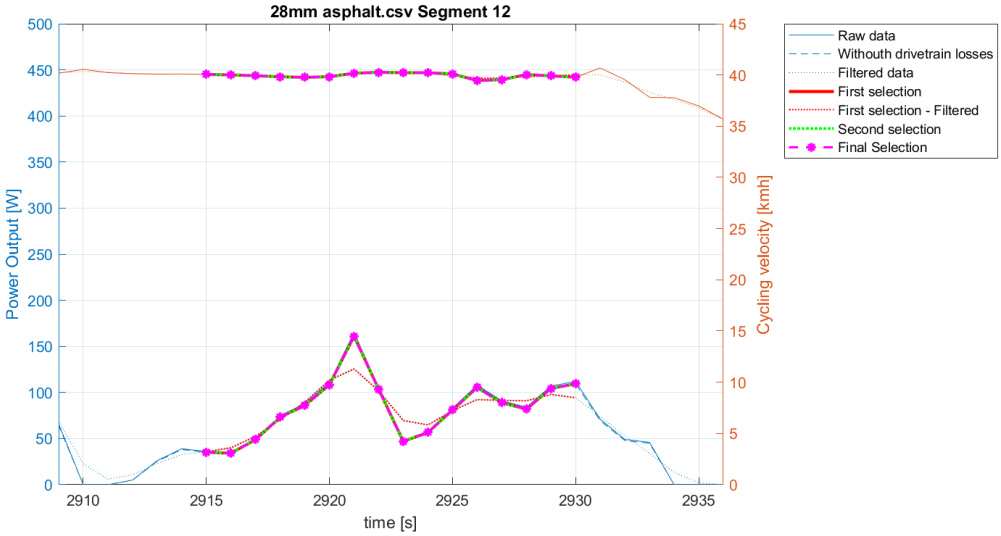
28mm asphalt.csv Segment 12
Power Output [W]
Cycling velocity [km/h]
time [s]
Raw data
Withouth drivetrain losses
Filtered data
First selection
First selection - Filtered
Second selection
Final Selection

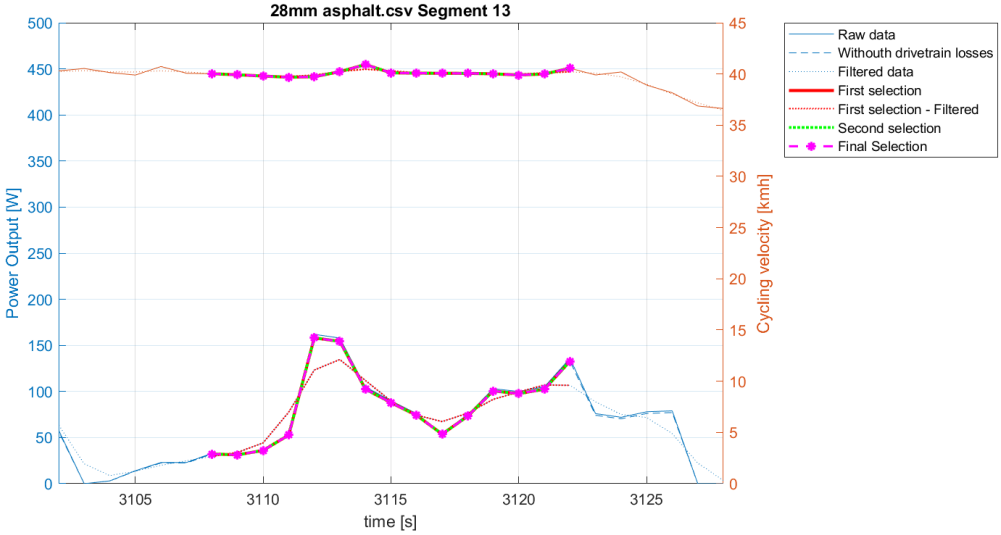
28mm asphalt.csv Segment 13
Power Output [W]
Cycling velocity [km/h]
time [s]
Raw data
Withouth drivetrain losses
Filtered data
First selection
First selection - Filtered
Second selection
Final Selection

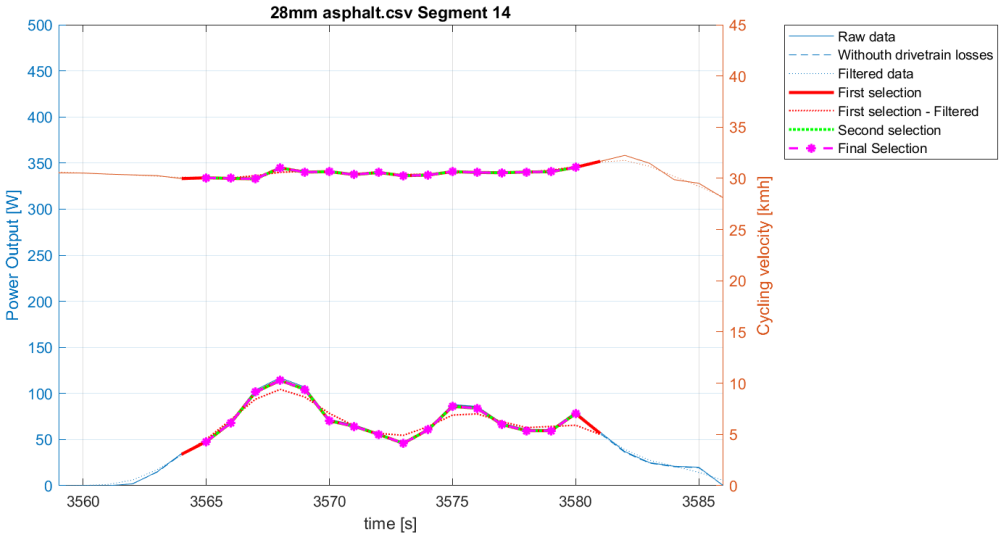
28mm asphalt.csv Segment 14
Power Output [W]
Cycling velocity [km/h]
time [s]
Raw data
Withouth drivetrain losses
Filtered data
First selection
First selection - Filtered
Second selection
Final Selection

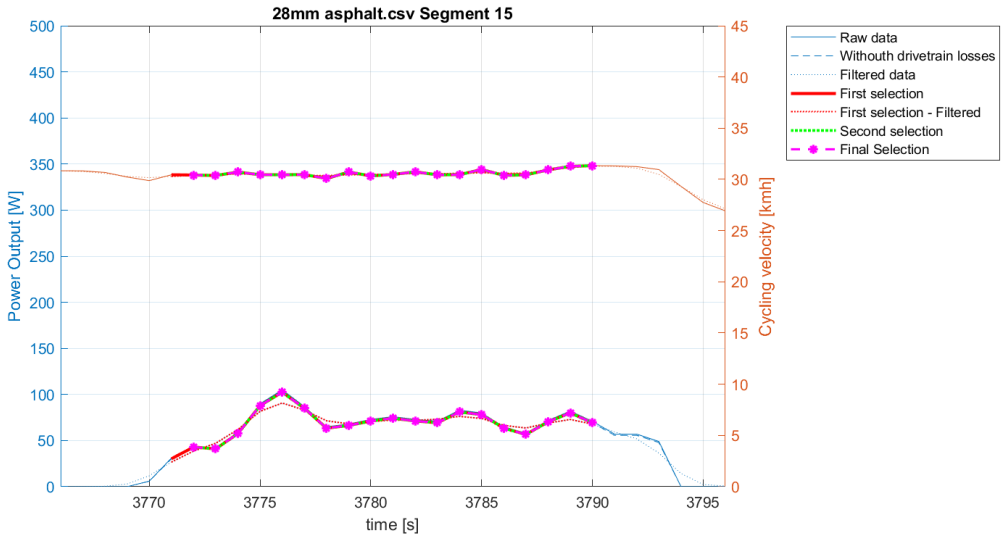
28mm asphalt.csv Segment 15
Power Output [W]
Cycling velocity [kmh]
time [s]
Raw data
Withouth drivetrain losses
Filtered data
First selection
First selection - Filtered
Second selection
Final Selection

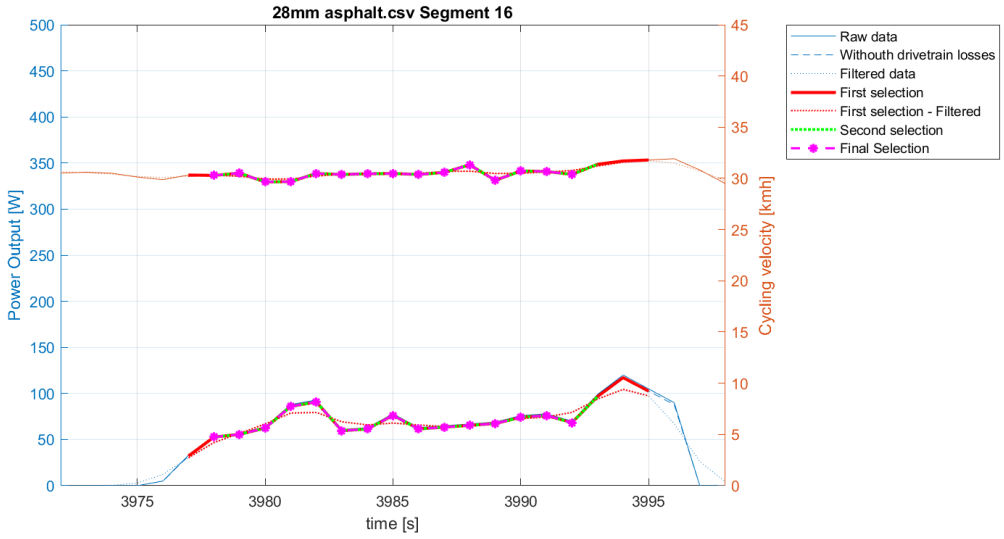
28mm asphalt.csv Segment 16
Power Output [W]
Cycling velocity [kmh]
time [s]
Raw data
Withouth drivetrain losses
Filtered data
First selection
First selection - Filtered
Second selection
Final Selection

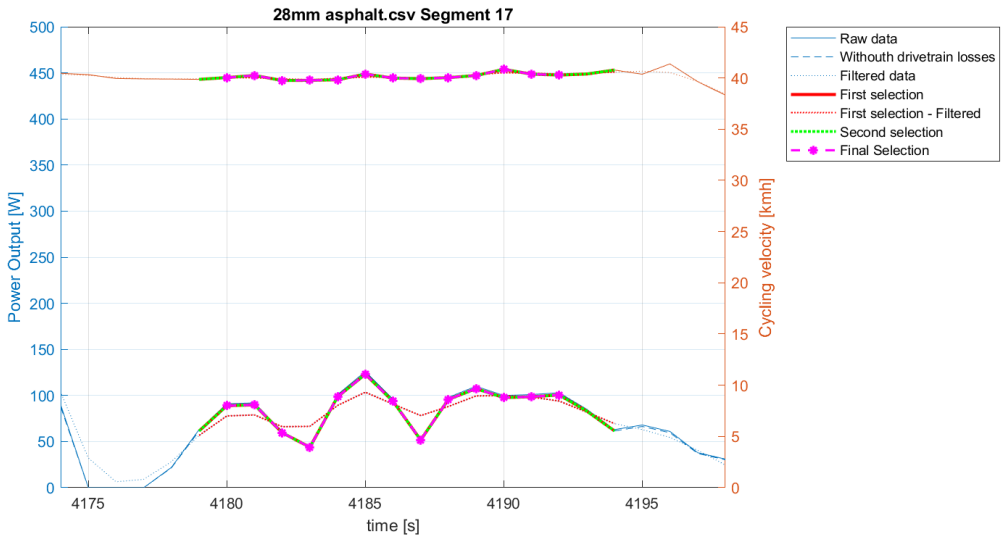
28mm asphalt.csv Segment 17
Power Output [W]
Cycling velocity [kmh]
time [s]
Raw data
Withouth drivetrain losses
Filtered data
First selection
First selection - Filtered
Second selection
Final Selection

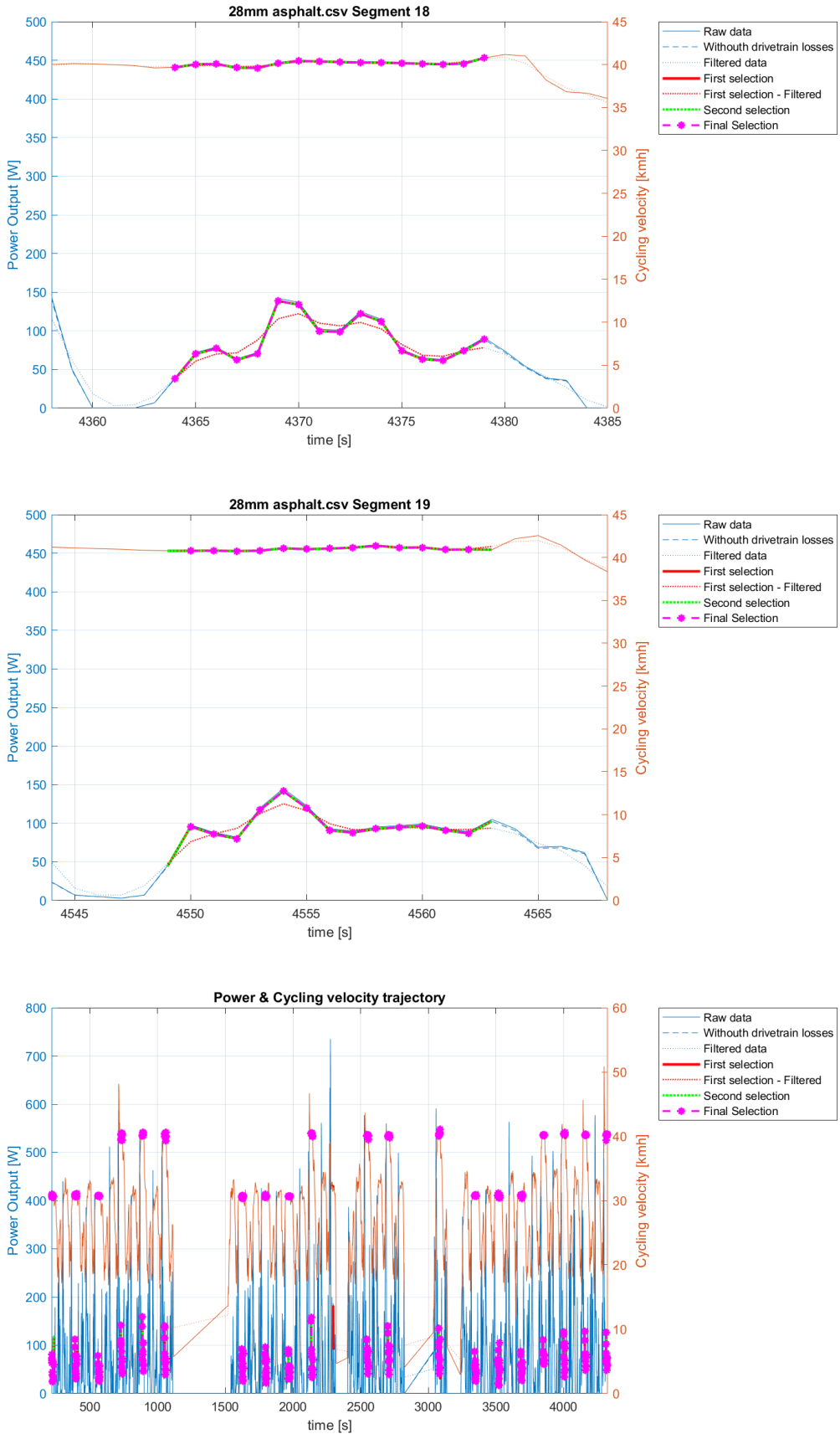

Figure E.5: Brickroad, 26mm Corsa Pro

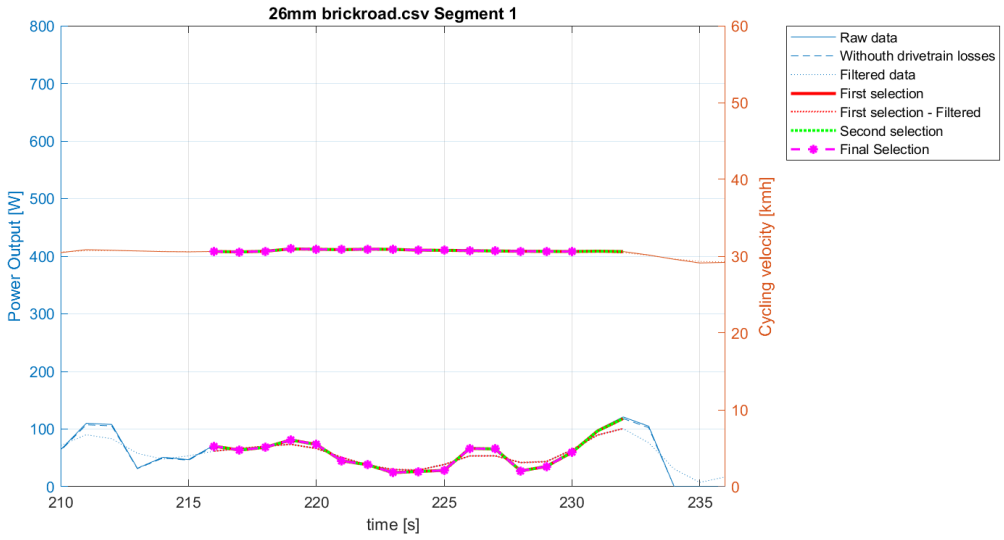
26mm brickroad.csv Segment 1
Power Output [W]
Cycling velocity [kmh]
time [s]
Raw data
Withouth drivetrain losses
Filtered data
First selection
First selection - Filtered
Second selection
Final Selection

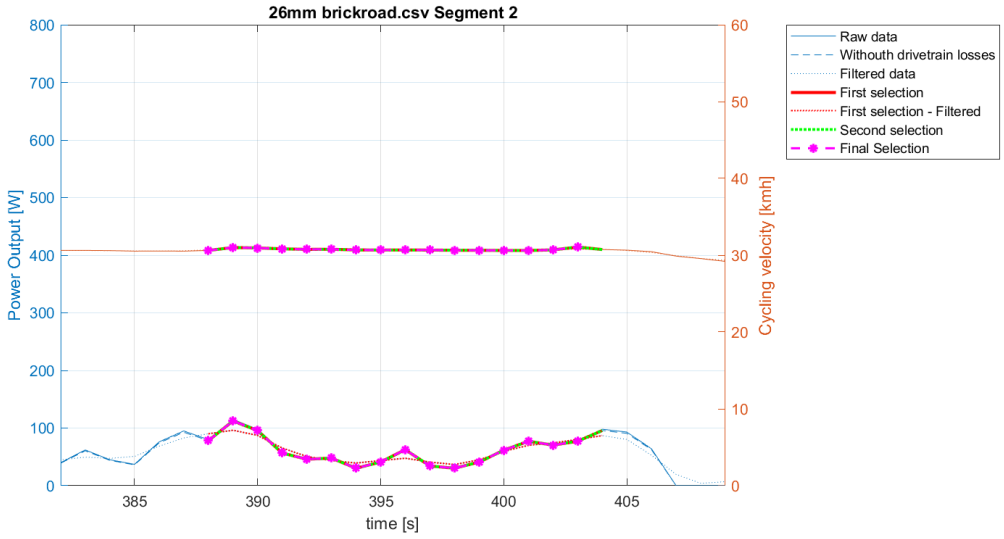
26mm brickroad.csv Segment 2
Power Output [W]
Cycling velocity [kmh]
time [s]
Raw data
Withouth drivetrain losses
Filtered data
First selection
First selection - Filtered
Second selection
Final Selection

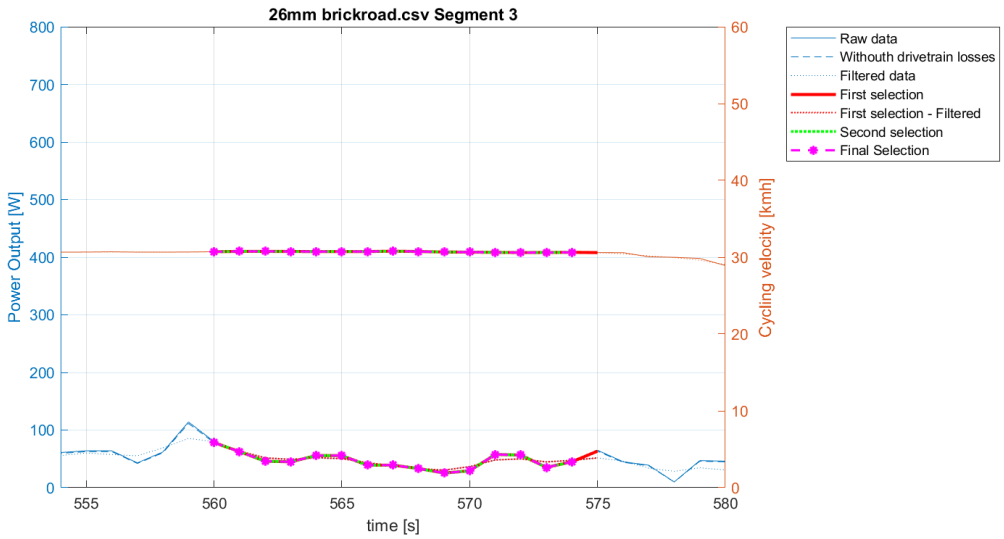
26mm brickroad.csv Segment 3
Power Output [W]
Cycling velocity [kmh]
time [s]
Raw data
Withouth drivetrain losses
Filtered data
First selection
First selection - Filtered
Second selection
Final Selection

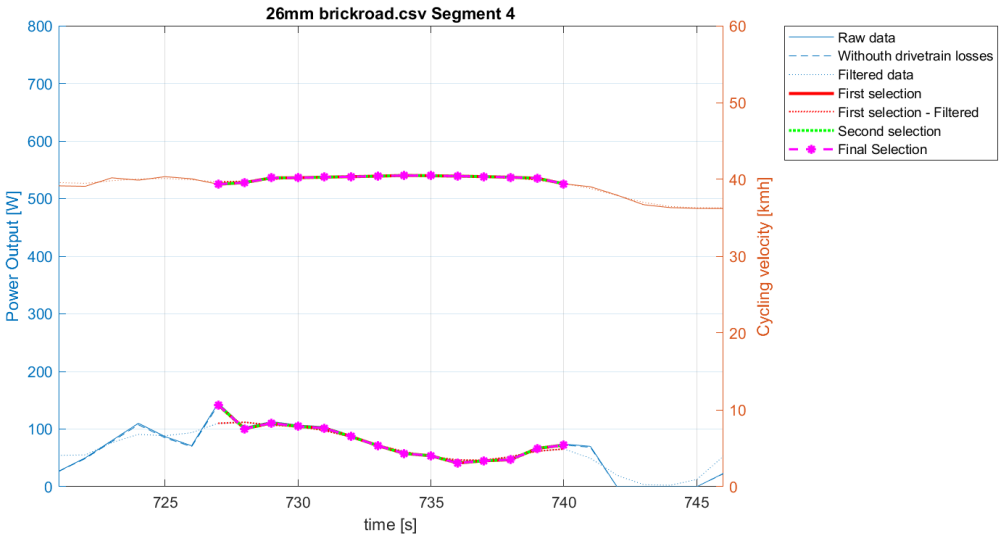
26mm brickroad.csv Segment 4
Power Output [W]
Cycling velocity [kmh]
time [s]
Raw data
Withouth drivetrain losses
Filtered data
First selection
First selection - Filtered
Second selection
Final Selection

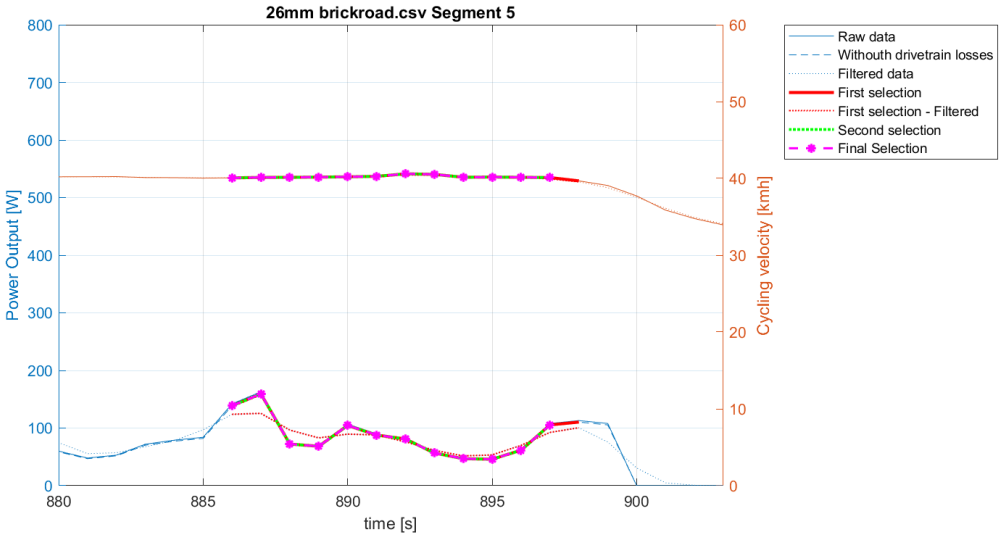
26mm brickroad.csv Segment 5
Power Output [W]
Cycling velocity [kmh]
time [s]
Raw data
Withouth drivetrain losses
Filtered data
First selection
First selection - Filtered
Second selection
Final Selection

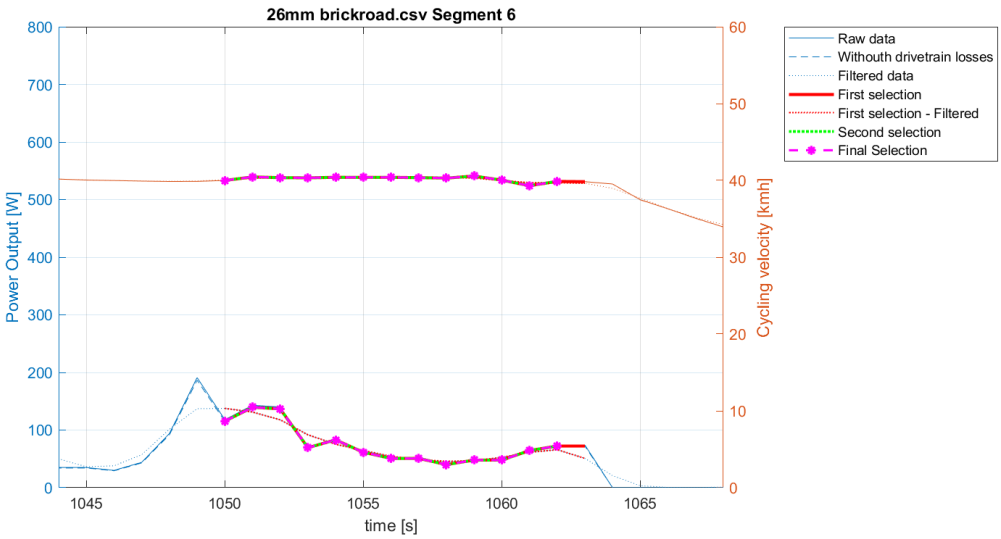
26mm brickroad.csv Segment 6
Power Output [W]
Cycling velocity [kmh]
time [s]
Raw data
Withouth drivetrain losses
Filtered data
First selection
First selection - Filtered
Second selection
Final Selection

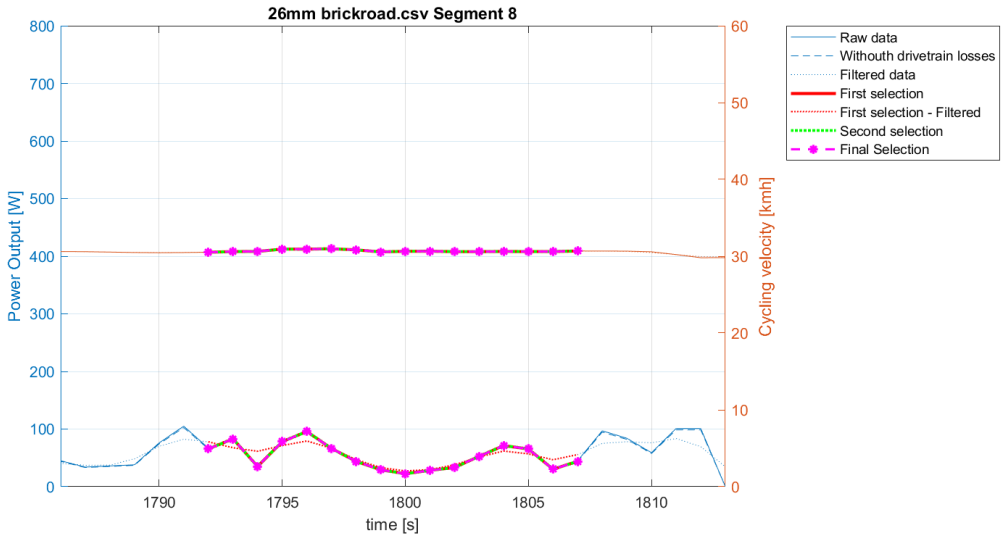
26mm brickroad.csv Segment 8
Power Output [W]
Cycling velocity [kmh]
time [s]
Raw data
Withouth drivetrain losses
Filtered data
First selection
First selection - Filtered
Second selection
Final Selection

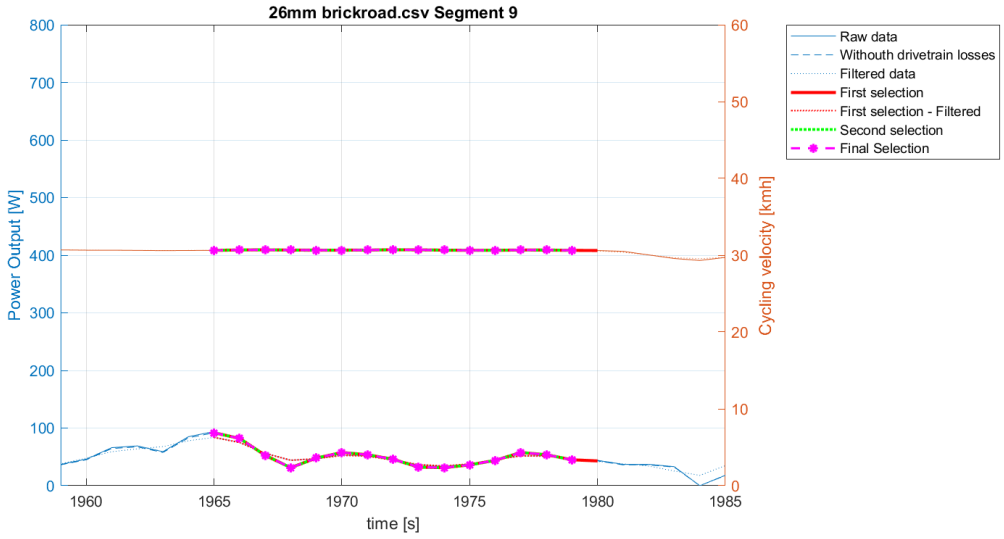
26mm brickroad.csv Segment 9
Power Output [W]
Cycling velocity [kmh]
time [s]
Raw data
Withouth drivetrain losses
Filtered data
First selection
First selection - Filtered
Second selection
Final Selection

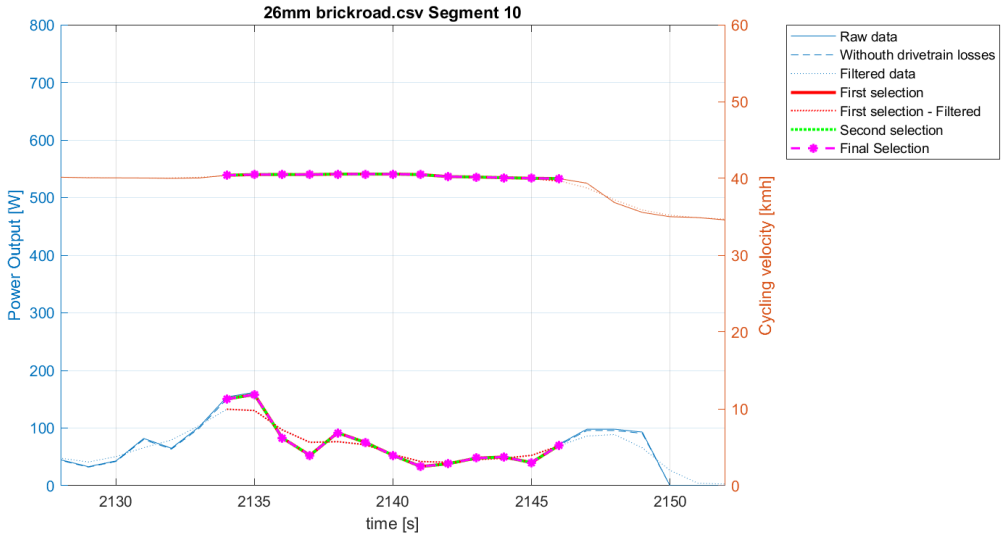
26mm brickroad.csv Segment 10
Power Output [W]
Cycling velocity [kmh]
time [s]
Raw data
Withouth drivetrain losses
Filtered data
First selection
First selection - Filtered
Second selection
Final Selection

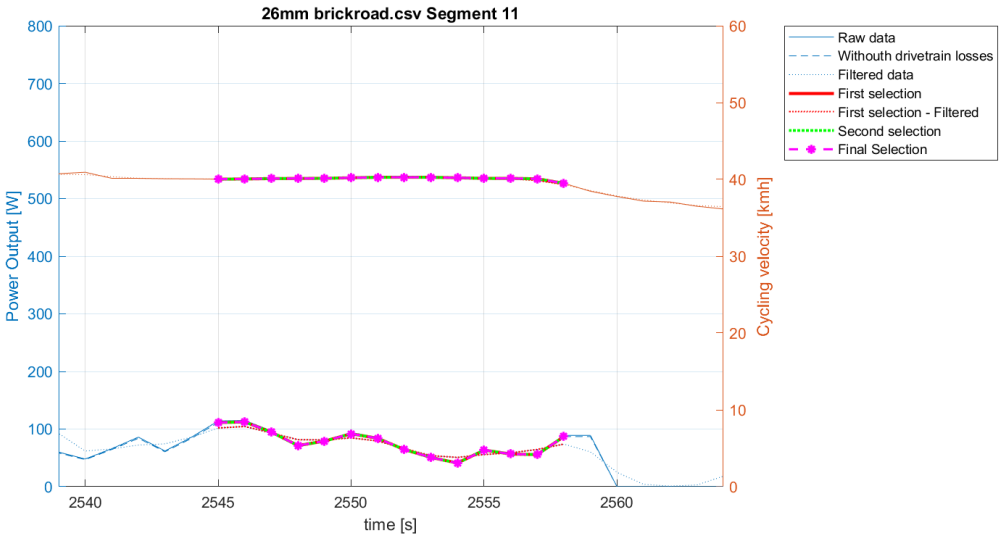
26mm brickroad.csv Segment 11
Power Output [W]
Cycling velocity [kmh]
time [s]
Raw data
Withouth drivetrain losses
Filtered data
First selection
First selection - Filtered
Second selection
Final Selection

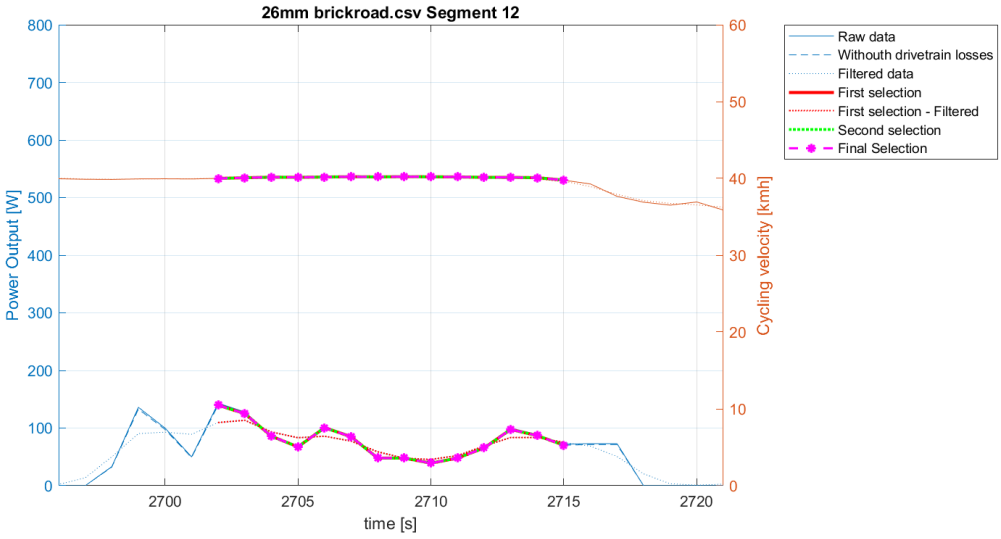
26mm brickroad.csv Segment 12
Power Output [W]
Cycling velocity [kmh]
time [s]
Raw data
Withouth drivetrain losses
Filtered data
First selection
First selection - Filtered
Second selection
Final Selection

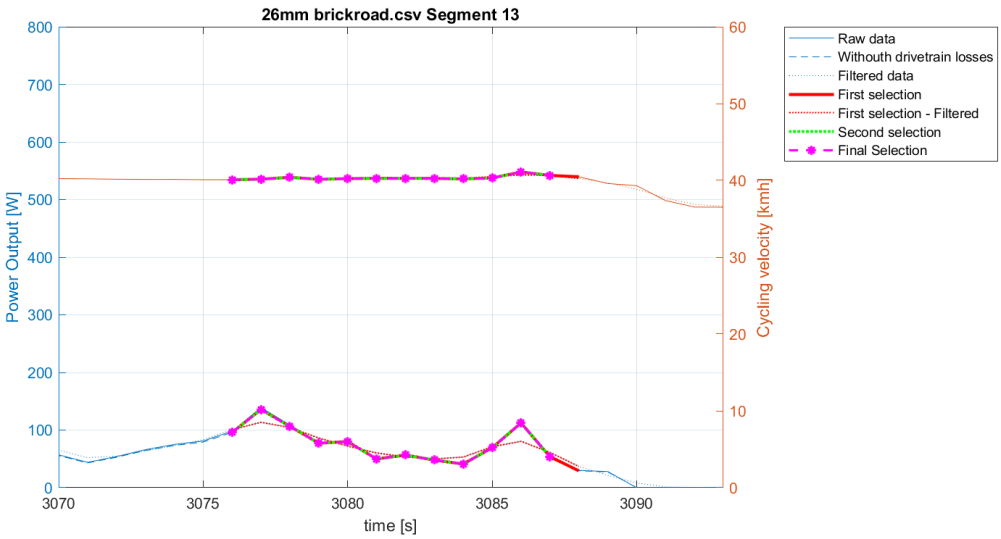
26mm brickroad.csv Segment 13
Power Output [W]
Cycling velocity [kmh]
time [s]
Raw data
Withouth drivetrain losses
Filtered data
First selection
First selection - Filtered
Second selection
Final Selection

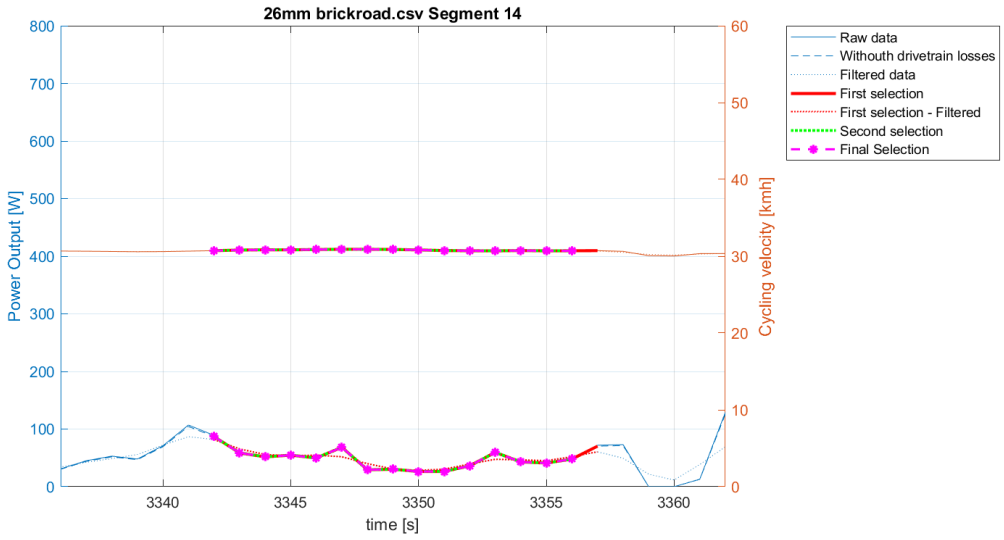
26mm brickroad.csv Segment 14
Power Output [W]
Cycling velocity [kmh]
time [s]
Raw data
Withouth drivetrain losses
Filtered data
First selection
First selection - Filtered
Second selection
Final Selection

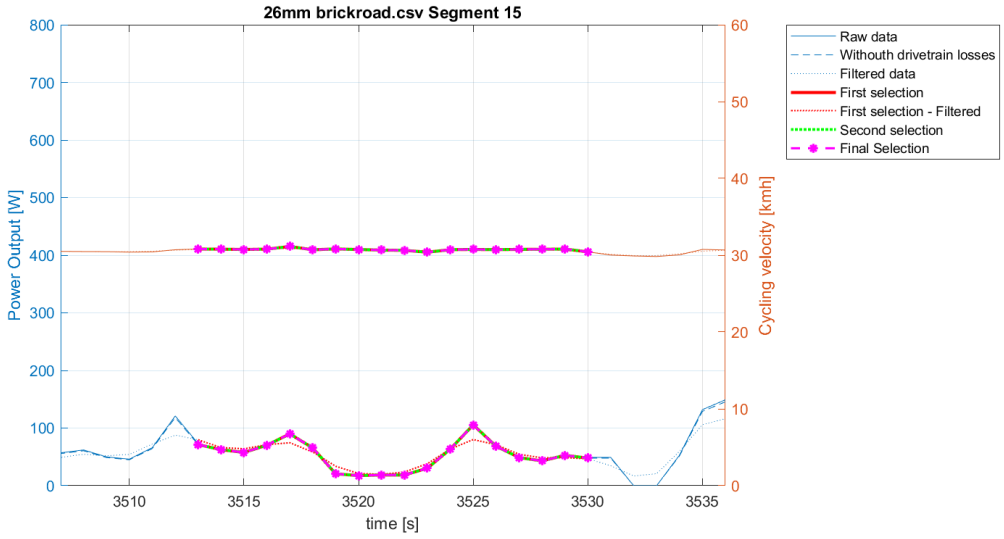
26mm brickroad.csv Segment 15
Power Output [W]
Cycling velocity [kmh]
time [s]
Raw data
Withouth drivetrain losses
Filtered data
First selection
First selection - Filtered
Second selection
Final Selection

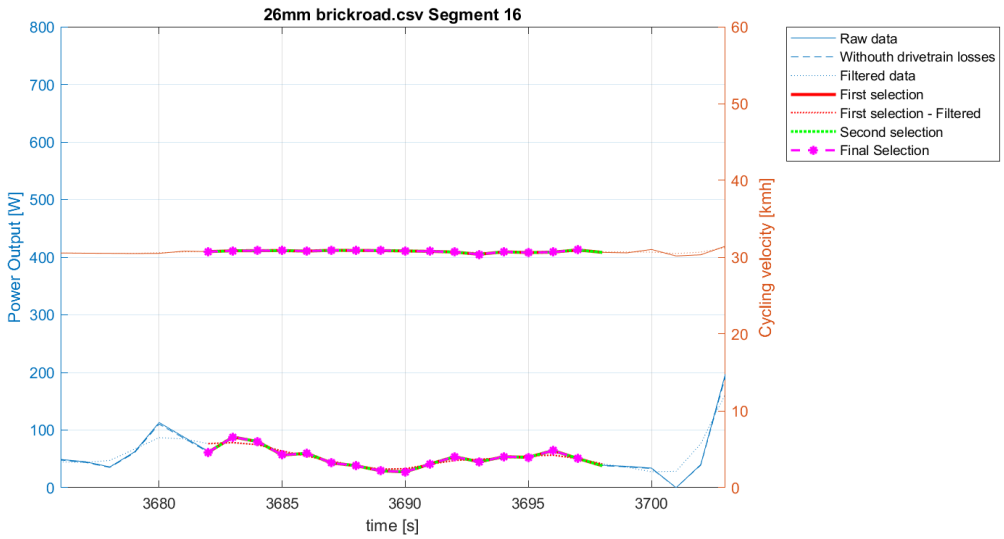
26mm brickroad.csv Segment 16
Power Output [W]
Cycling velocity [kmh]
time [s]
Raw data
Withouth drivetrain losses
Filtered data
First selection
First selection - Filtered
Second selection
Final Selection

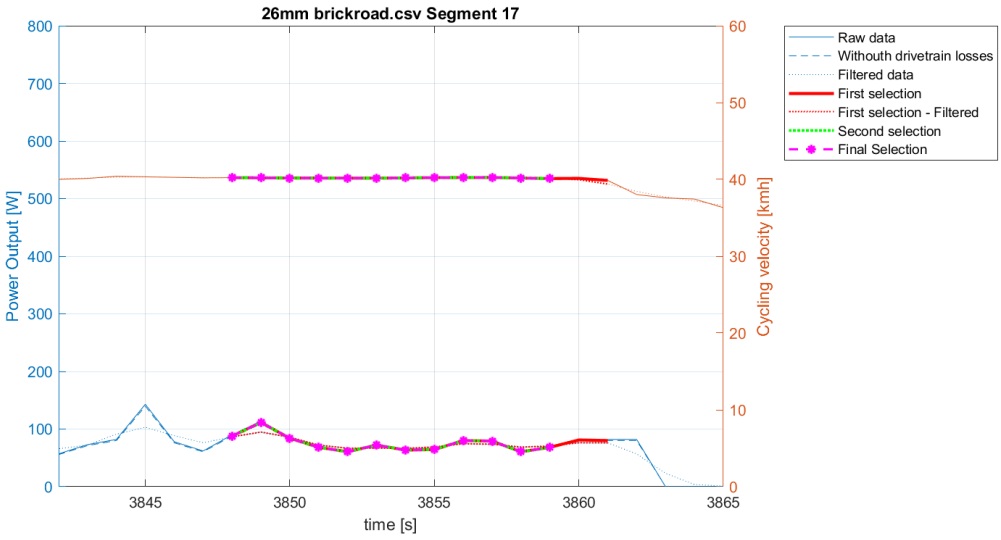
26mm brickroad.csv Segment 17
Power Output [W]
Cycling velocity [kmh]
time [s]
Raw data
Withouth drivetrain losses
Filtered data
First selection
First selection - Filtered
Second selection
Final Selection

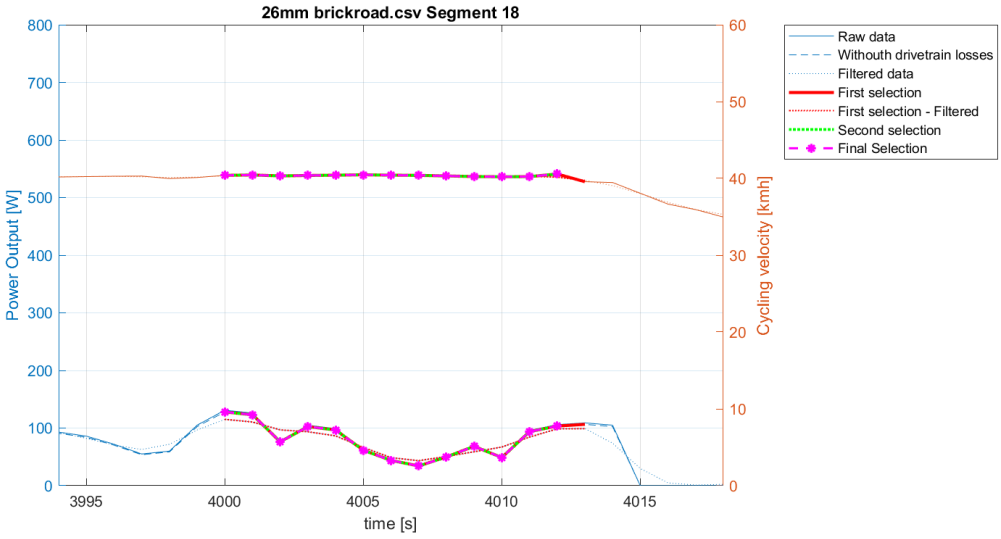
26mm brickroad.csv Segment 18
Power Output [W]
Cycling velocity [kmh]
time [s]
Raw data
Withouth drivetrain losses
Filtered data
First selection
First selection - Filtered
Second selection
Final Selection

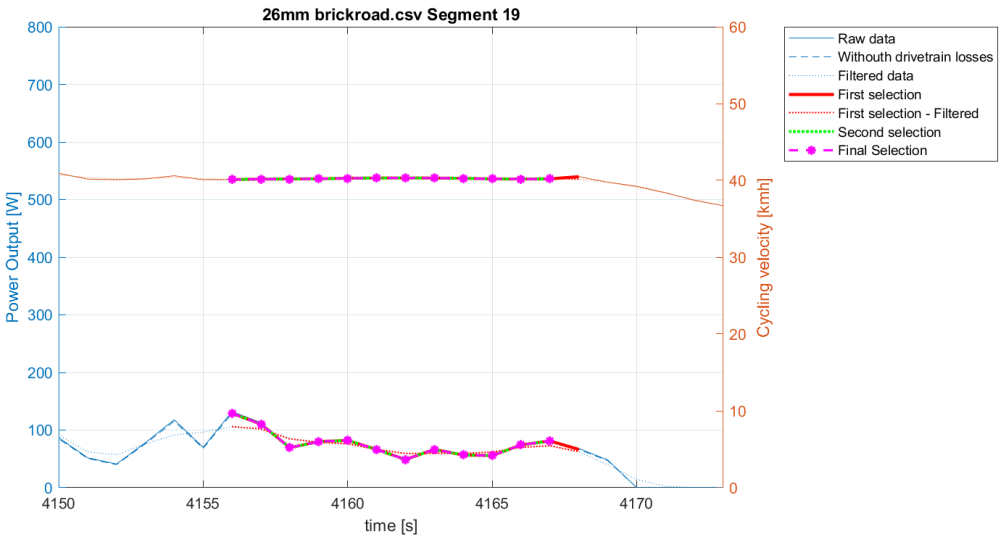
26mm brickroad.csv Segment 19
Power Output [W]
Cycling velocity [kmh]
time [s]
Raw data
Withouth drivetrain losses
Filtered data
First selection
First selection - Filtered
Second selection
Final Selection

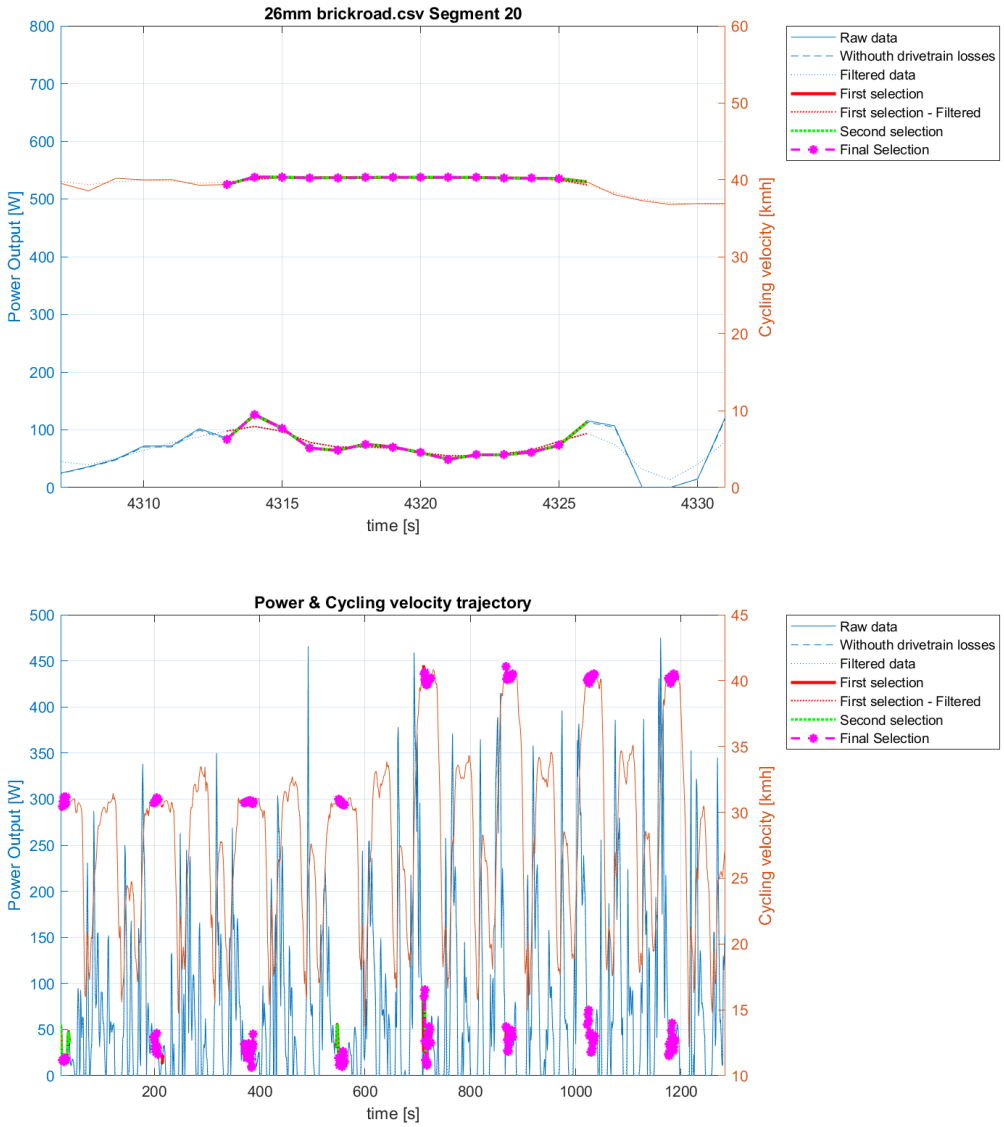

Figure E.6: Brickroad, 26mm Corsa Pro, reversed direction

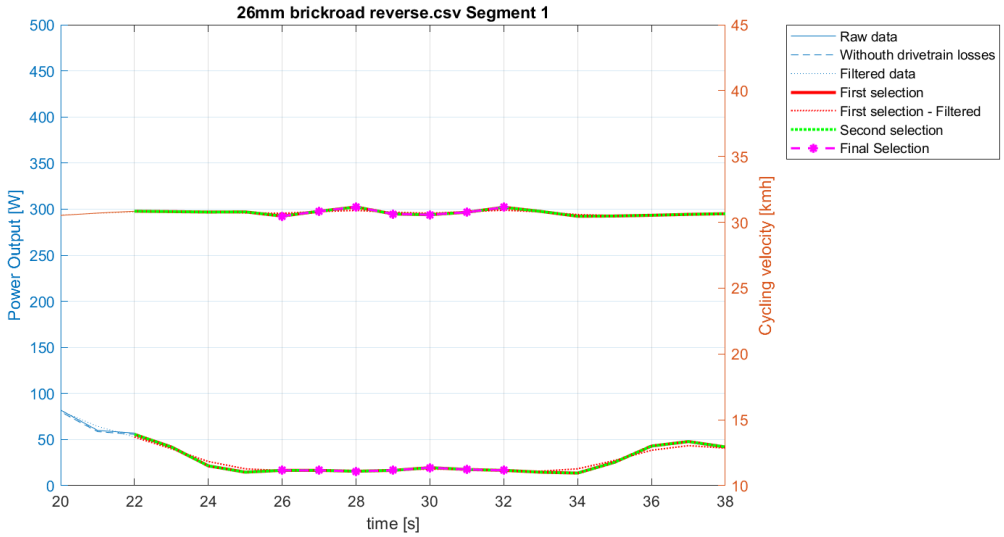

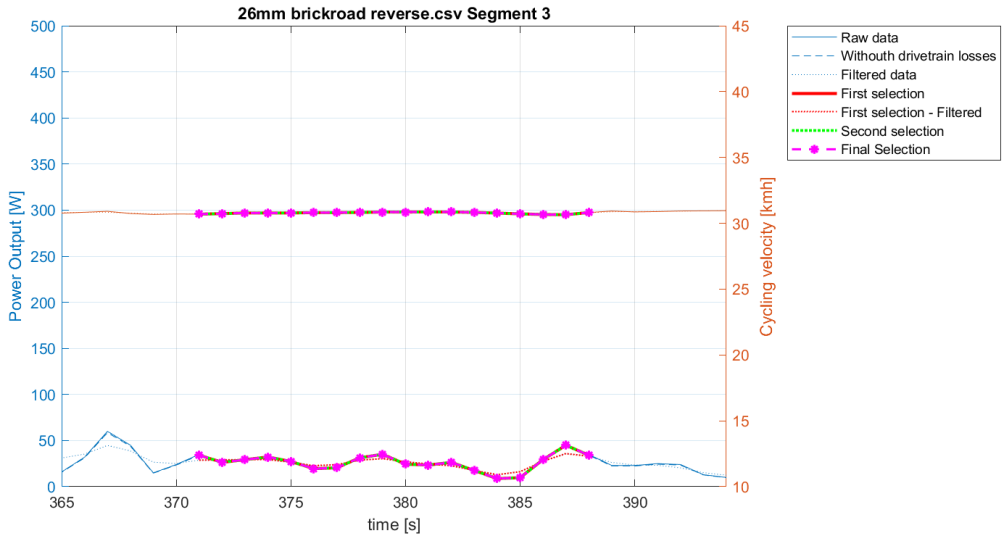
26mm brickroad reverse.csv Segment 3
Power Output [W]
Cycling velocity [kmh]
time [s]
Raw data
Withouth drivetrain losses
Filtered data
First selection
First selection - Filtered
Second selection
Final Selection

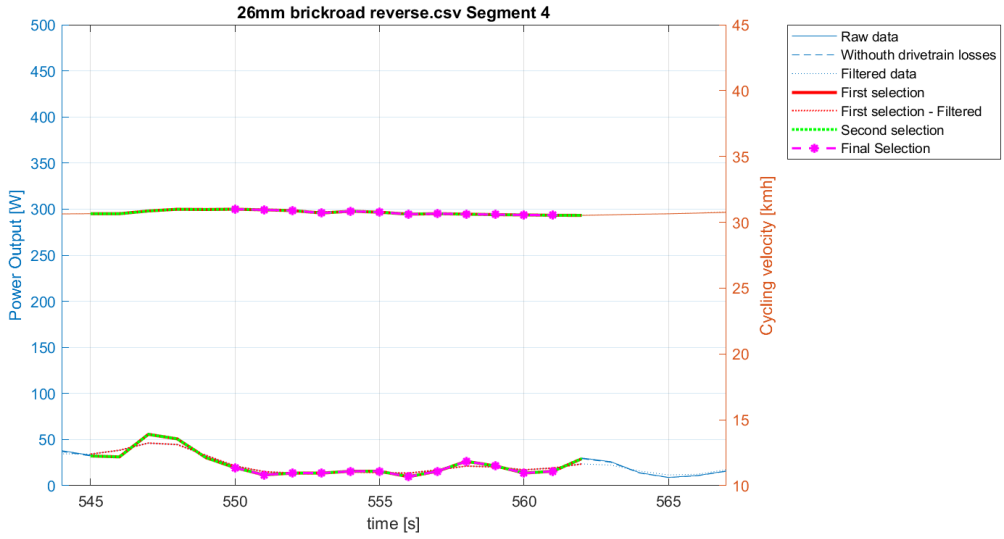
26mm brickroad reverse.csv Segment 4
Power Output [W]
Cycling velocity [kmh]
time [s]
Raw data
Withouth drivetrain losses
Filtered data
First selection
First selection - Filtered
Second selection
Final Selection

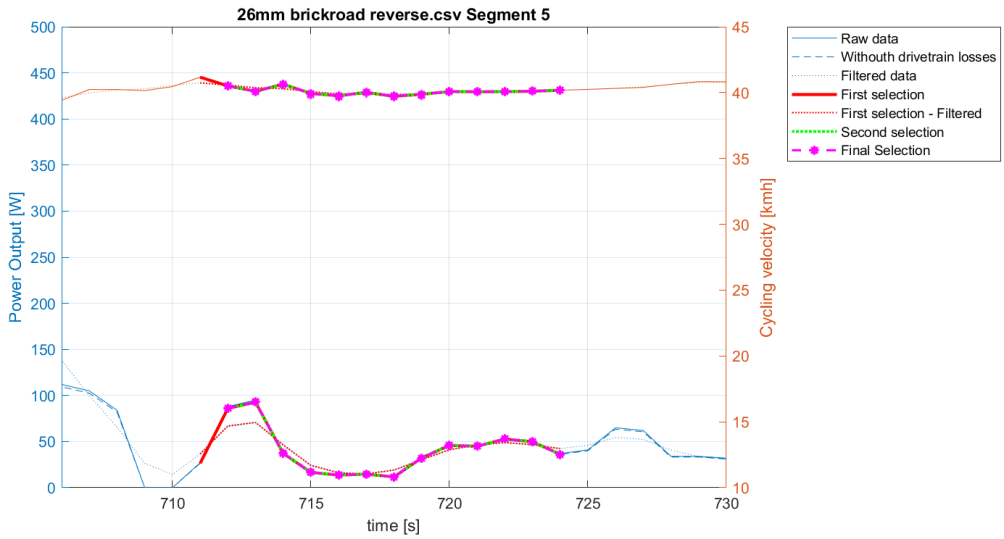
26mm brickroad reverse.csv Segment 5
Power Output [W]
Cycling velocity [kmh]
time [s]
Raw data
Withouth drivetrain losses
Filtered data
First selection
First selection - Filtered
Second selection
Final Selection

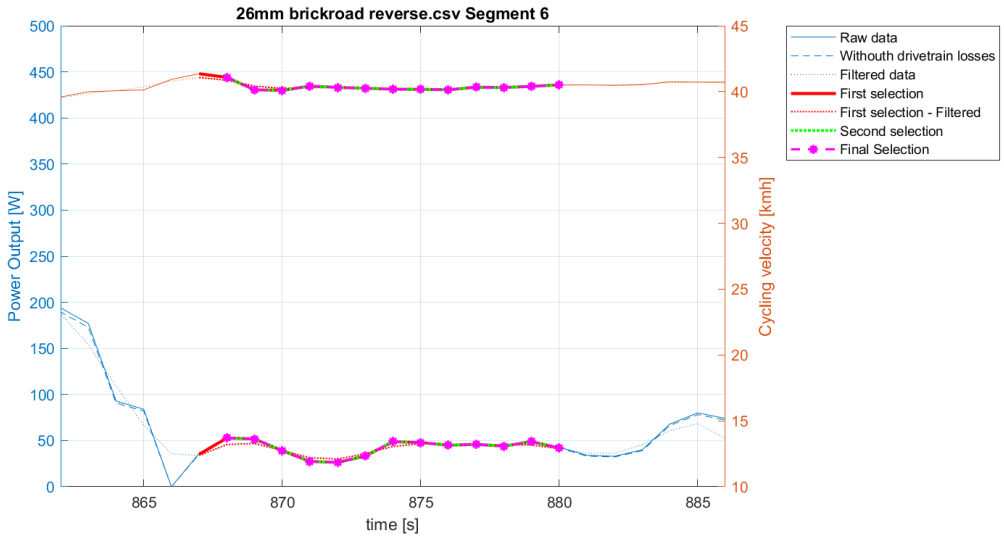
26mm brickroad reverse.csv Segment 6
Power Output [W]
Cycling velocity [kmh]
time [s]
Raw data
Withouth drivetrain losses
Filtered data
First selection
First selection - Filtered
Second selection
Final Selection

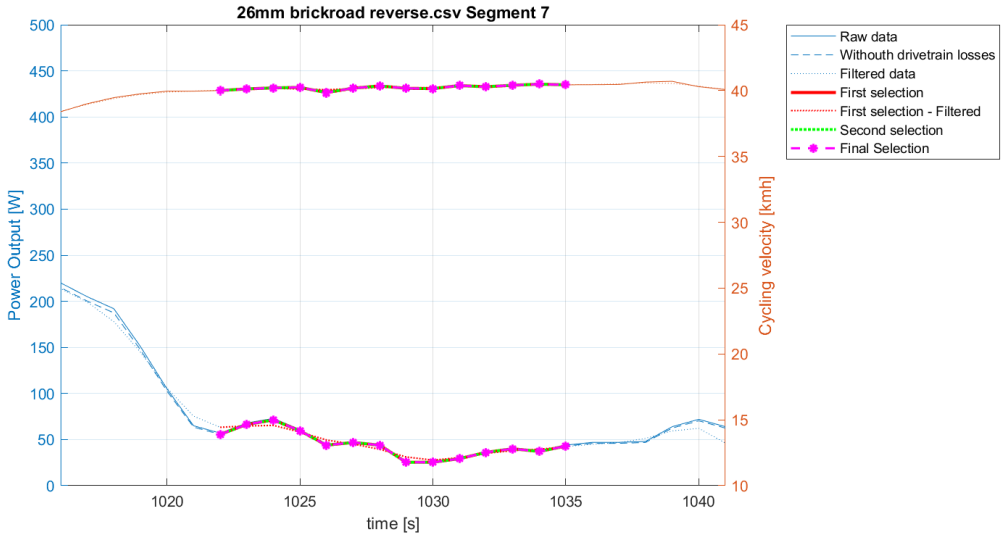
26mm brickroad reverse.csv Segment 7
Power Output [W]
Cycling velocity [kmh]
time [s]
Raw data
Withouth drivetrain losses
Filtered data
First selection
First selection - Filtered
Second selection
Final Selection

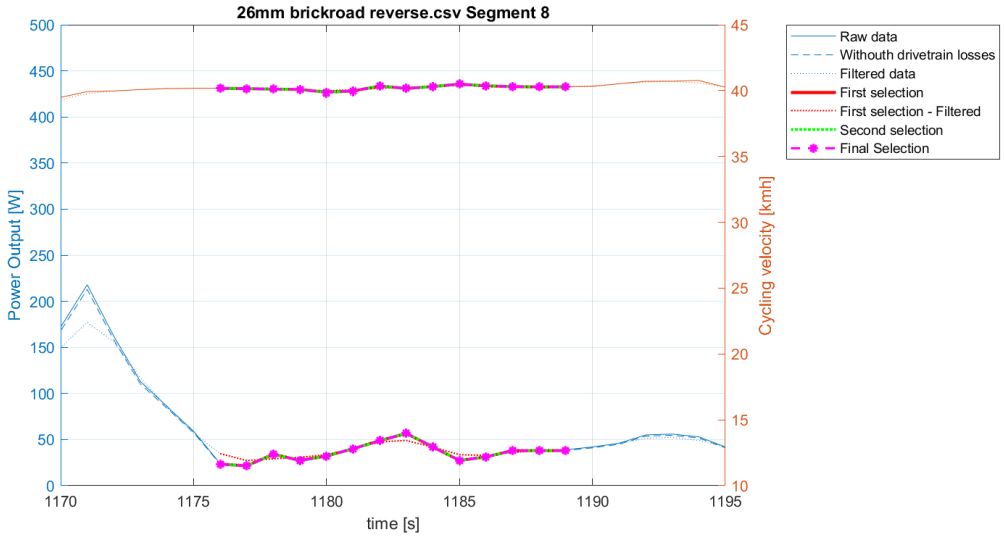
26mm brickroad reverse.csv Segment 8
Power Output [W]
Cycling velocity [kmh]
time [s]
Raw data
Withouth drivetrain losses
Filtered data
First selection
First selection - Filtered
Second selection
Final Selection

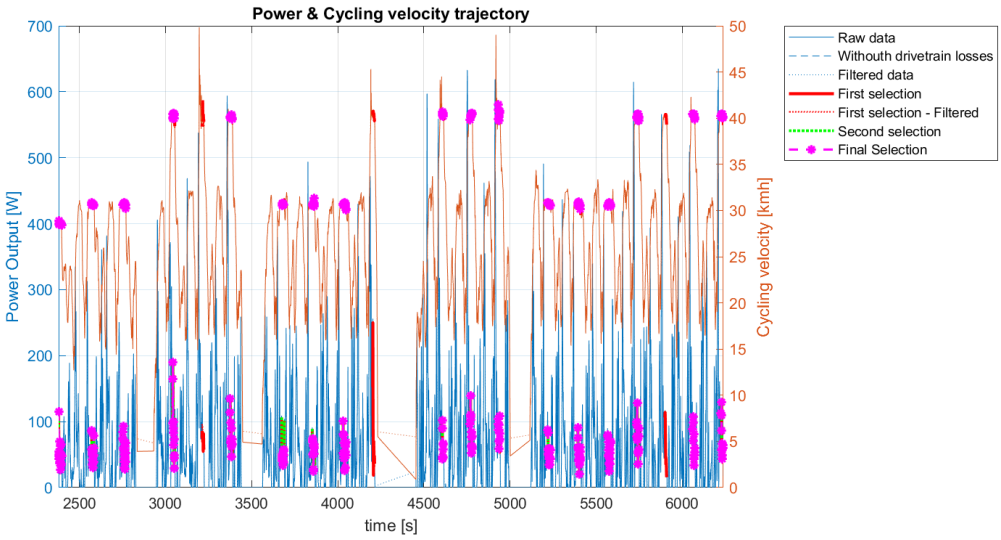

Figure E.7: Brickroad, 28mm Corsa Pro

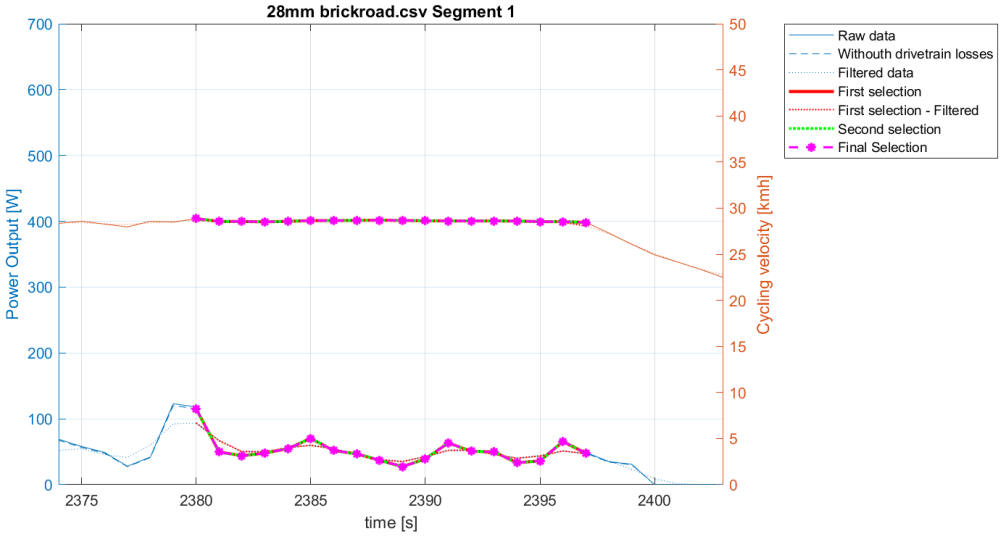

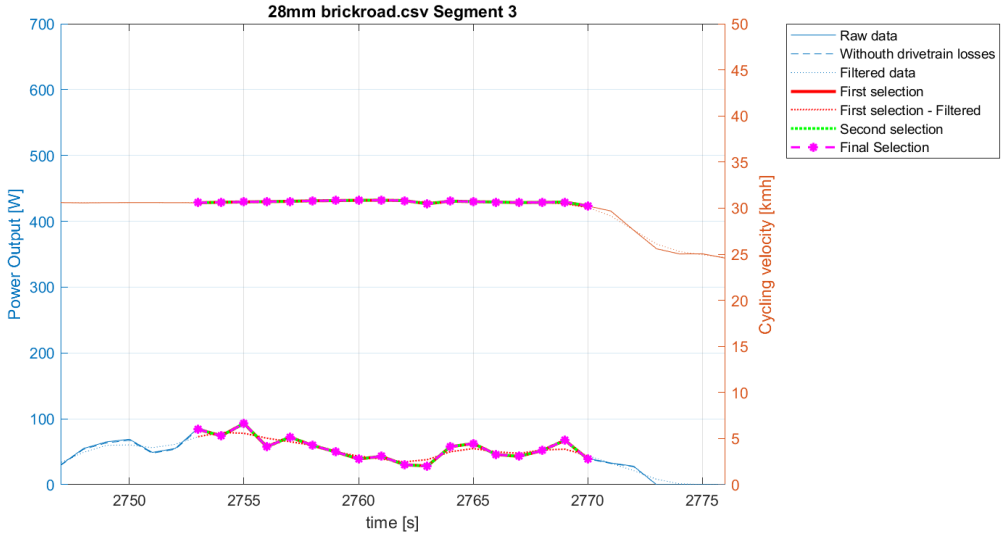
28mm brickroad.csv Segment 3
Power Output [W]
Cycling velocity [kmh]
time [s]
Raw data
Withouth drivetrain losses
Filtered data
First selection
First selection - Filtered
Second selection
Final Selection

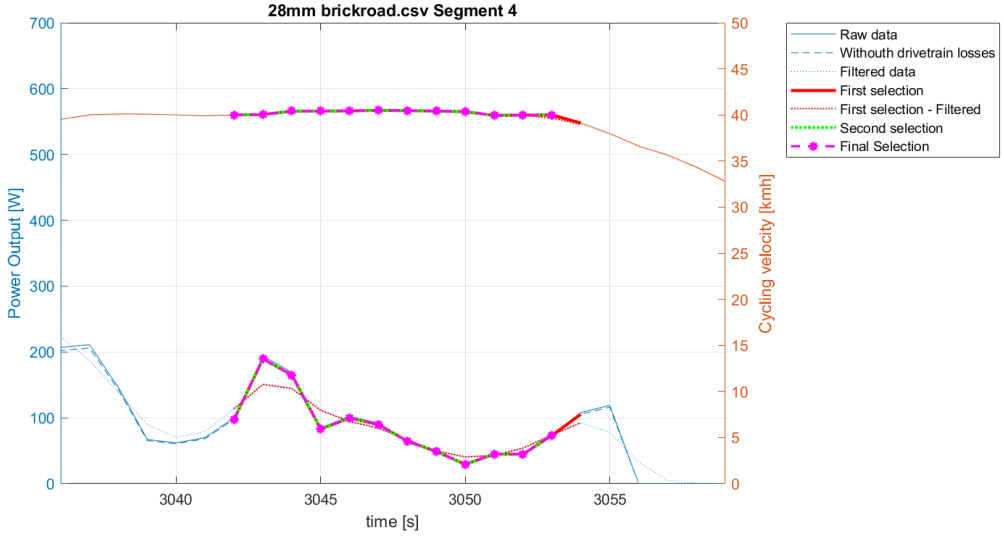
28mm brickroad.csv Segment 4
Power Output [W]
Cycling velocity [kmh]
time [s]
Raw data
Withouth drivetrain losses
Filtered data
First selection
First selection - Filtered
Second selection
Final Selection

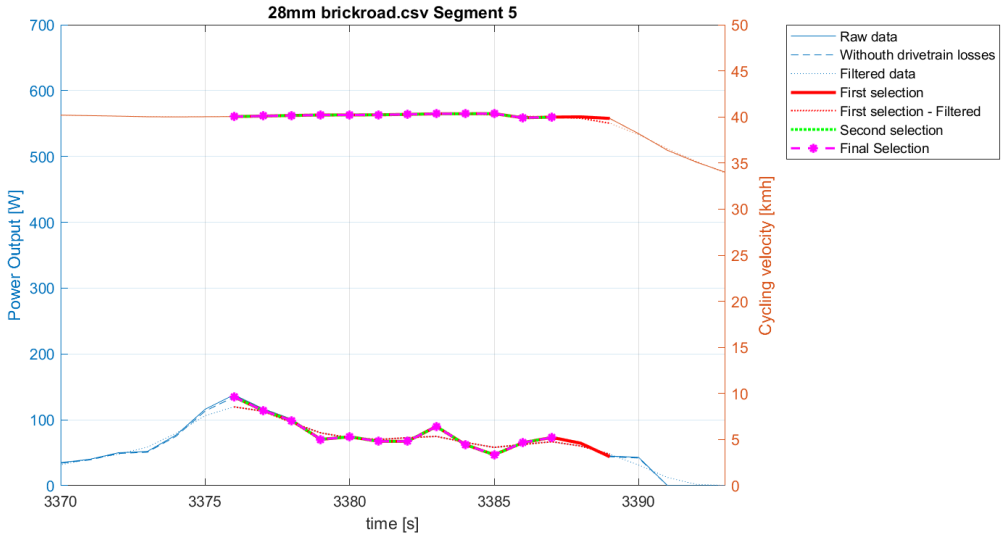
28mm brickroad.csv Segment 5
Power Output [W]
Cycling velocity [kmh]
time [s]
Raw data
Withouth drivetrain losses
Filtered data
First selection
First selection - Filtered
Second selection
Final Selection

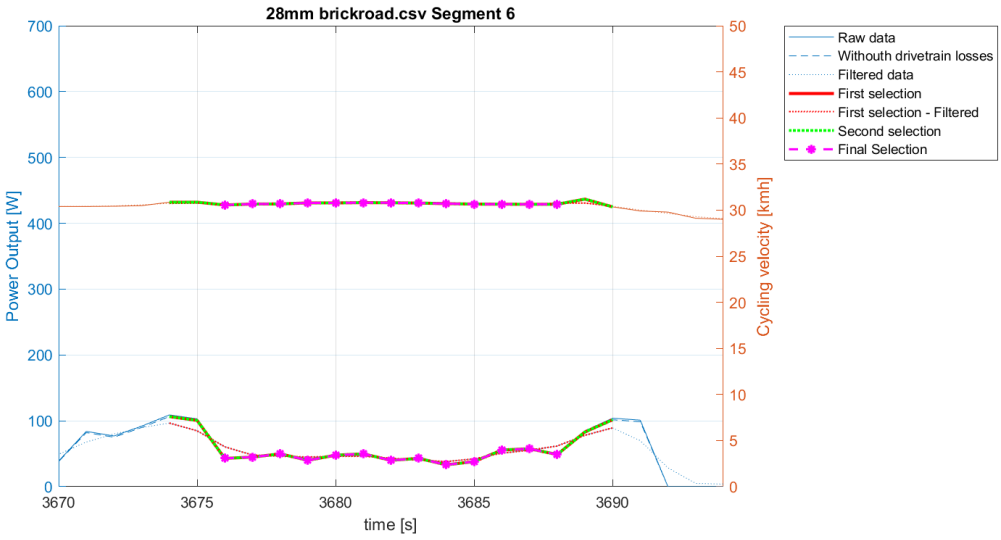
28mm brickroad.csv Segment 6
Power Output [W]
Cycling velocity [kmh]
time [s]
Raw data
Withouth drivetrain losses
Filtered data
First selection
First selection - Filtered
Second selection
Final Selection

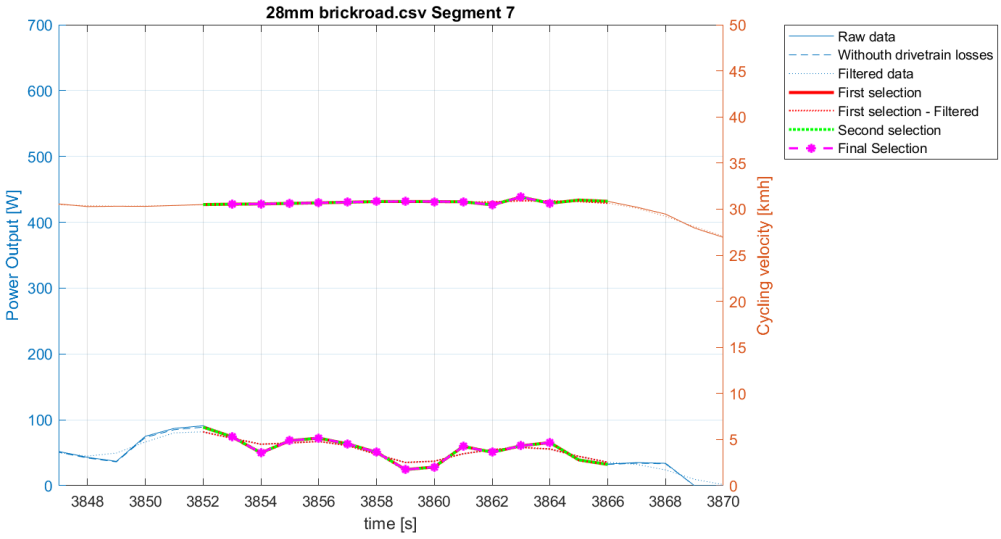
28mm brickroad.csv Segment 7
Power Output [W]
Cycling velocity [kmh]
time [s]
Raw data
Withouth drivetrain losses
Filtered data
First selection
First selection - Filtered
Second selection
Final Selection

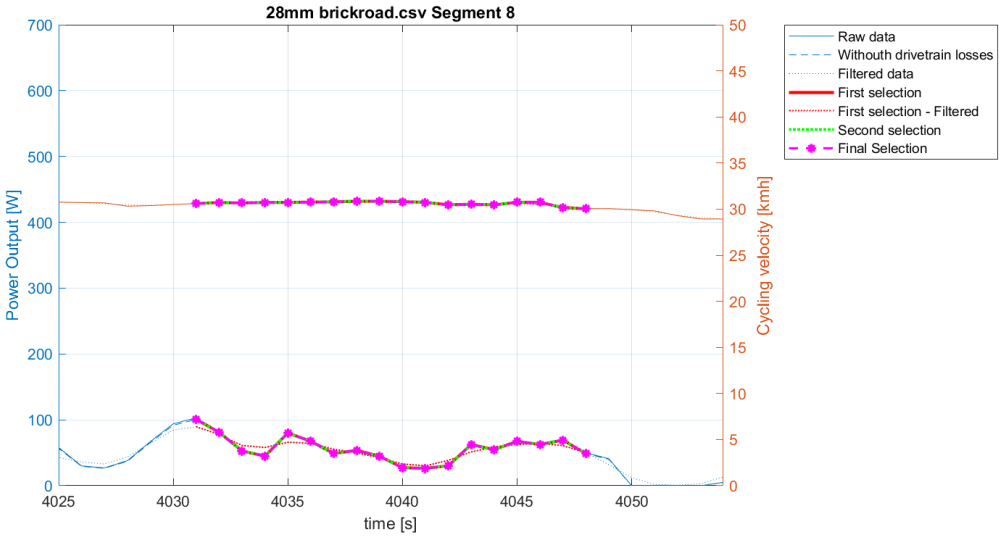
28mm brickroad.csv Segment 8
Power Output [W]
Cycling velocity [kmh]
time [s]
Raw data
Withouth drivetrain losses
Filtered data
First selection
First selection - Filtered
Second selection
Final Selection

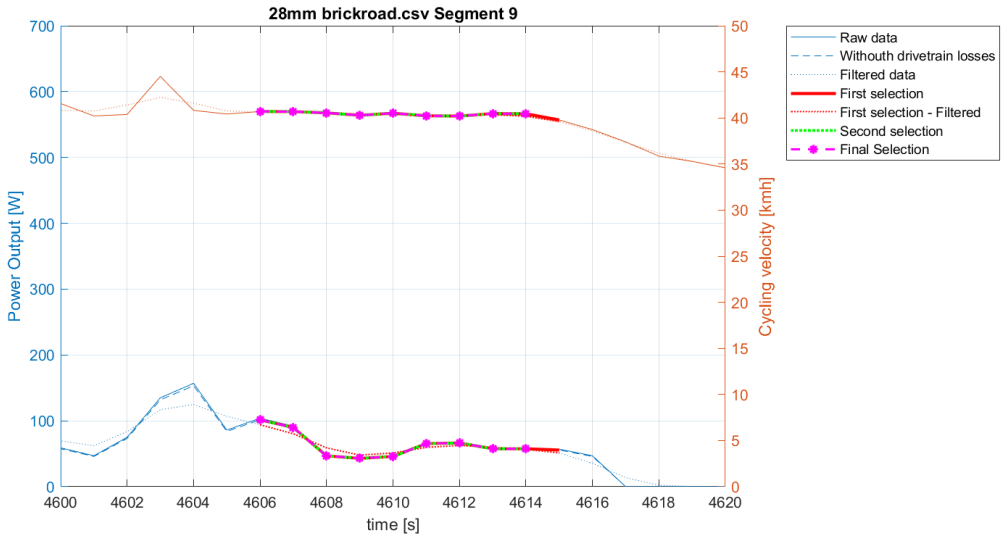
28mm brickroad.csv Segment 9
Power Output [W]
Cycling velocity [kmh]
time [s]
Raw data
Withouth drivetrain losses
Filtered data
First selection
First selection - Filtered
Second selection
Final Selection

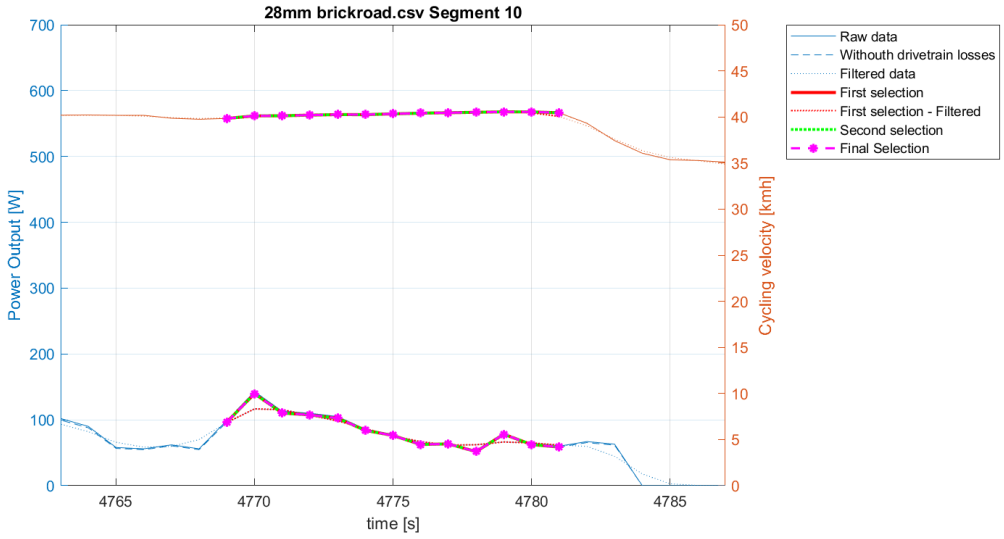
28mm brickroad.csv Segment 10
Power Output [W]
Cycling velocity [kmh]
time [s]
Raw data
Withouth drivetrain losses
Filtered data
First selection
First selection - Filtered
Second selection
Final Selection

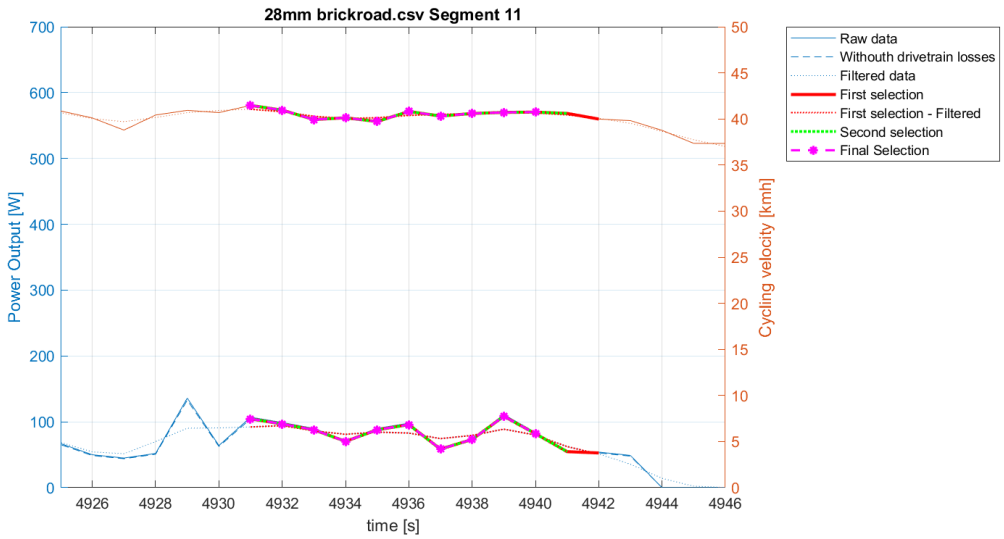
28mm brickroad.csv Segment 11
Power Output [W]
Cycling velocity [kmh]
time [s]
Raw data
Withouth drivetrain losses
Filtered data
First selection
First selection - Filtered
Second selection
Final Selection

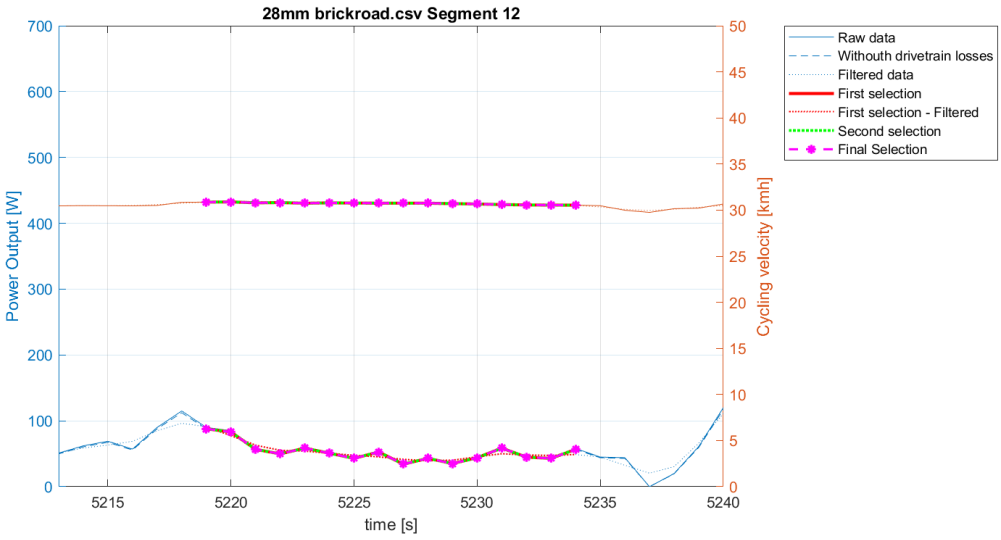
28mm brickroad.csv Segment 12
Power Output [W]
Cycling velocity [km/h]
time [s]
Raw data
Withouth drivetrain losses
Filtered data
First selection
First selection - Filtered
Second selection
Final Selection

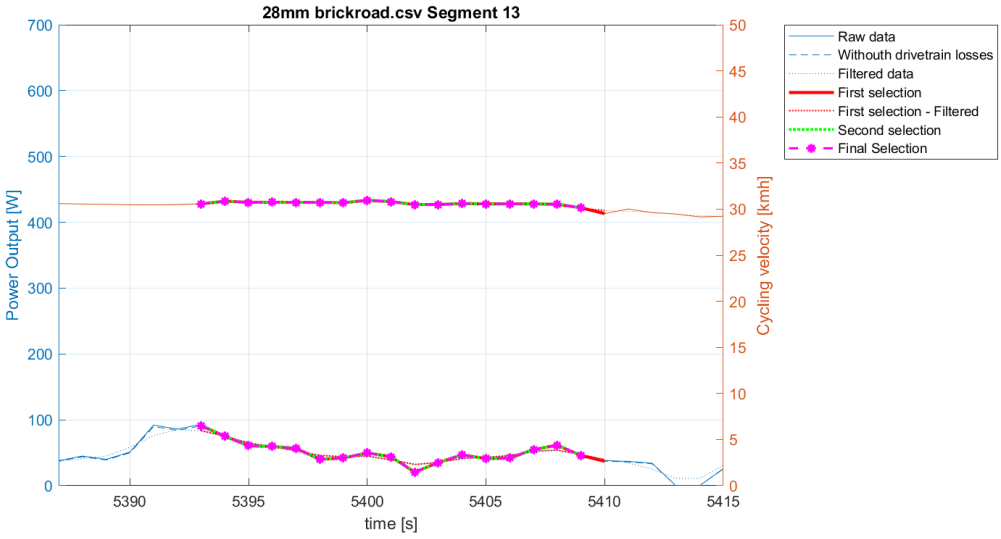
28mm brickroad.csv Segment 13
Power Output [W]
Cycling velocity [km/h]
time [s]
Raw data
Withouth drivetrain losses
Filtered data
First selection
First selection - Filtered
Second selection
Final Selection

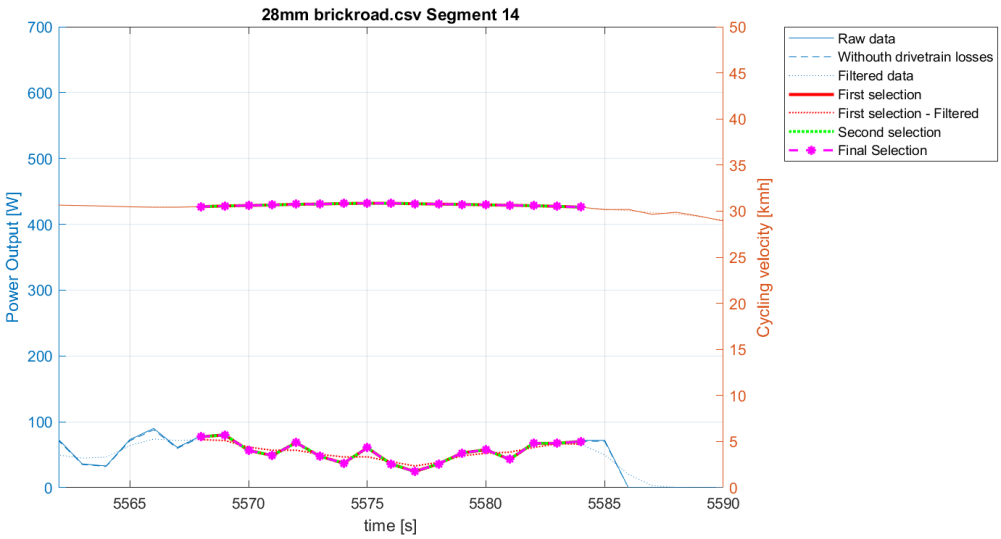
28mm brickroad.csv Segment 14
Power Output [W]
Cycling velocity [km/h]
time [s]
Raw data
Withouth drivetrain losses
Filtered data
First selection
First selection - Filtered
Second selection
Final Selection

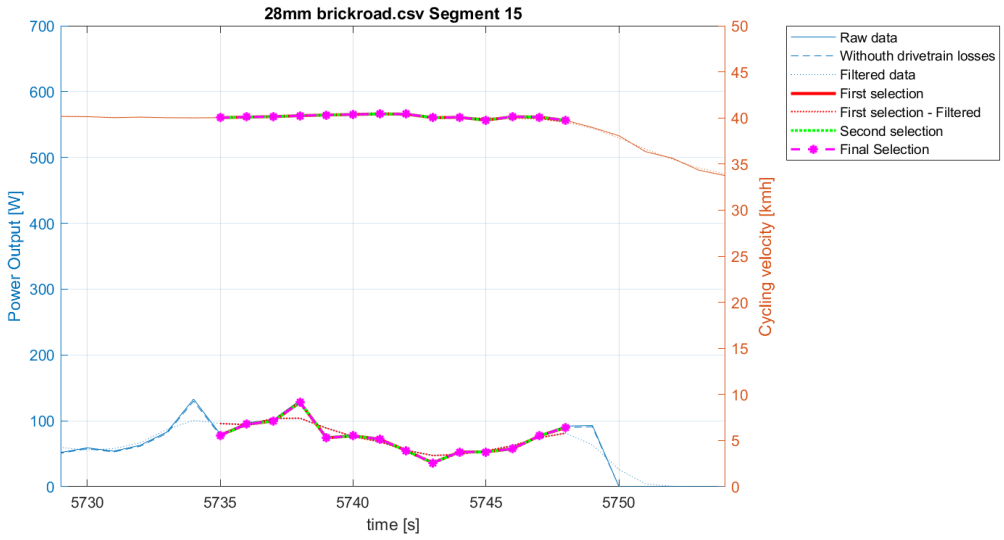
28mm brickroad.csv Segment 15
Power Output [W]
Cycling velocity [kmh]
time [s]
Raw data
Withouth drivetrain losses
Filtered data
First selection
First selection - Filtered
Second selection
Final Selection

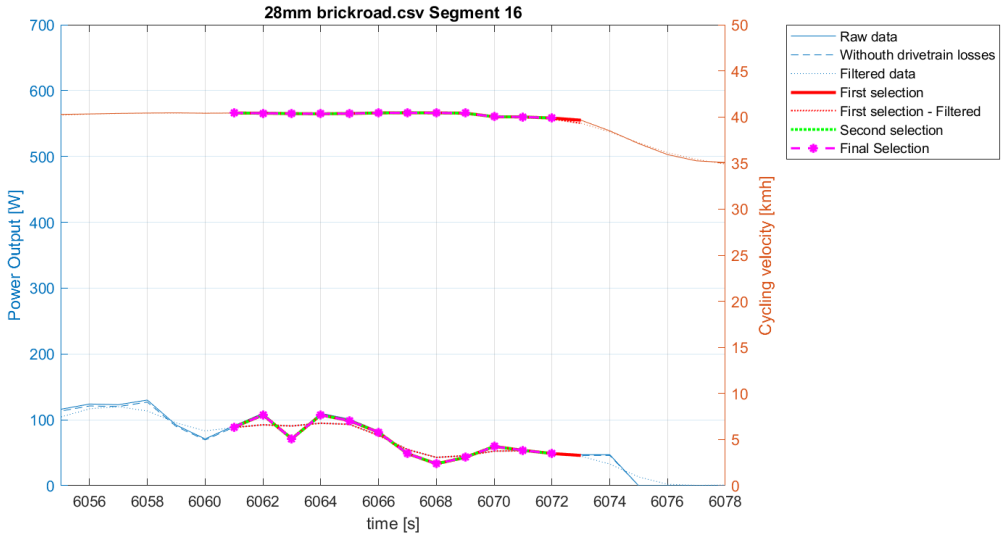
28mm brickroad.csv Segment 16
Power Output [W]
Cycling velocity [kmh]
time [s]
Raw data
Withouth drivetrain losses
Filtered data
First selection
First selection - Filtered
Second selection
Final Selection

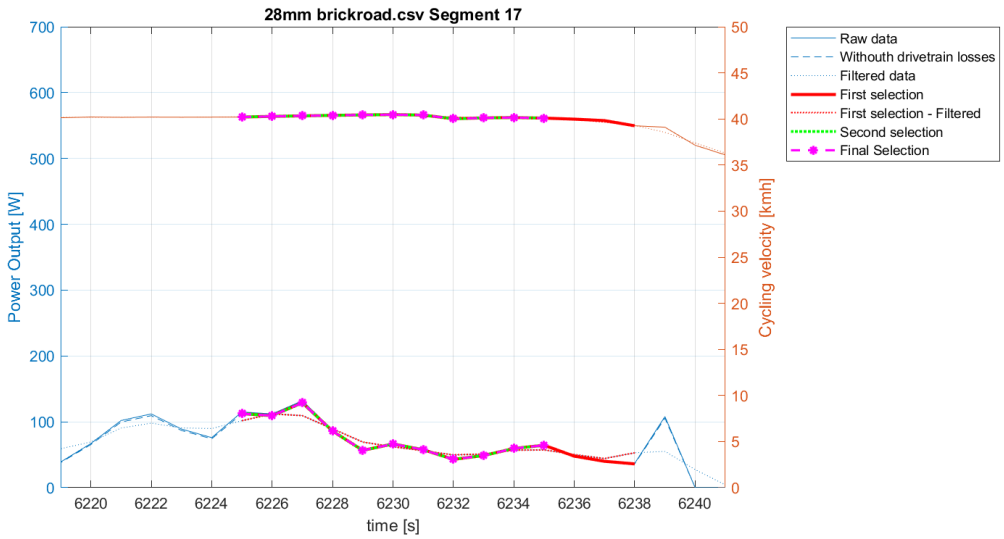
28mm brickroad.csv Segment 17
Power Output [W]
Cycling velocity [kmh]
time [s]
Raw data
Withouth drivetrain losses
Filtered data
First selection
First selection - Filtered
Second selection
Final Selection

Bibliography

[1] Erik W. Faria, Daryl L. Parker, and Irvin E. Faria. “The science of cycling”. In: *Sports Medicine* 35.4 (Jan. 2005), pp. 313–337. DOI: 10.2165/00007256-200535040-00002.

[2] Scope Cycling. *Scope Atmoz - Tire pressure control system*. [Online; accessed 16. Dec. 2023]. URL: https://www.scopecycling.com/product/atmoz.

[3] Liam Cahill. “Tyre pressure adjustment on the fly? Team DSM will use innovative €3,000 hubs to change tyre pressure mid-race for Paris-Roubaix”. In: *Road.cc* (Apr. 2022). URL: https://road.cc/content/tech-news/dsm-use-tyre-pressure-adjustment-hubs-paris-roubaix-291873.

[4] *About Us | Team DSM*. [Online; accessed 20. Jan. 2023]. URL: https://www.team-dsm.com/about-us.

[5] James C. Martin et al. “Validation of a mathematical model for road cycling power”. In: *Journal of Applied Biomechanics* 14.3 (Aug. 1998), pp. 276–291. DOI: 10.1123/jab.14.3.276. URL: https://doi.org/10.1123/jab.14.3.276.

[6] Mathis D. Fenre and Alex Klein-Paste. “Bicycle rolling resistance under winter conditions”. In: *Cold Reg. Sci. Technol.* 187 (July 2021). DOI: 10.1016/j.coldregions.2021.103282.

[7] Mathis D. Fenre and Alex Klein-Paste. “Rolling Resistance Measurements on Cycleways Using an Instrumented Bicycle”. In: *J. Cold Reg. Eng.* 35.2 (June 2021). DOI: 10.1061/(ASCE)CR.1943-5495.0000244.

[8] Malte Rothhämel. *On rolling resistance of bicycle tyres*. Jan. 2022, pp. 944–953. DOI: 10.1007/978-3-031-07305-2\{_}87. URL: https://doi.org/10.1007/978-3-031-07305-2_87.

[9] Thomas Maier et al. “Reliability of the virtual elevation method to evaluate rolling resistance of different mountain bike cross-country tyres”. In: *Journal of Sports Sciences* (Feb. 2017). DOI: 10.1080/02640414.2017.1287935. URL: https://doi.org/10.1080/02640414.2017.1287935.

[10] Daniel Meyer, Gideon Kloss, and Veit Senner. “What is Slowing Me Down? Estimation of Rolling Resistances During Cycling”. In: *Procedia Eng.* 147 (Jan. 2016), pp. 526–531. DOI: 10.1016/j.proeng.2016.06.232.

[11] Doris J. de Boer. *The Relative Importance of Different Aerodynamic and Mechanical Losses in Professional Road Race Cycling*. [Literature Review]. 2022.

[12] Robert.L. Jackson et al. *Synthesis of the effects of pavement properties on tire rolling resistance*. Tech. rep. Aug. 2011. URL: https://citeseerx.ist.psu.edu/document?repid=rep1&type=pdf&doi=08865e4ddd8d5c74645a02e3c5e223b33469cf73.

[13] Andy Herbener and Archibald. *A Direct Method of Measuring the Rolling Resistance of a Bicycle Tire*. Tech. rep. us, 2015.

[14] David Gordon Wilson. *Bicycling science*. Jan. 2004. DOI: 10.7551/mitpress/1601.001.0001. URL: https://doi.org/10.7551/mitpress/1601.001.0001.

[15] Cyclingabout. *Do Road Bikes Have Suspension?* [Online; accessed 14. Dec. 2023]. Oct. 2023. URL: https://cyclingabout.info/do-road-bikes-have-suspension.

[16] J. Poertner. “Part 4A: Rolling Resistance (The History and Previous Works)”. In: *SILCA* (Sept. 2021). URL: https://silca.cc/blogs/silca/part-4a-rolling-resistance-the-history-and-previous-works.

[17] ZIPP. *Total System Efficiency™*. Tech. rep. URL: https://www.sram.com/globalassets/publicsites/cms-campaign-pages-not-story-pages/zipp/totalsystemeffeciency/pdf-downloads/tse-explained2.pdf.

[18] Lennard Zinn. *Resistance is futile: How tire pressure and width affect rolling resistance*. Nov. 2012. URL: https://www.velonews.com/gear/resistance-futile-tire-pressure-width-affect-rolling-resistance/.

[19] Thomas Maier et al. “Influence of wheel rim width on rolling resistance and off-road speed in cross-country mountain biking”. In: *Journal of Sports Sciences* 37.7 (Dec. 2019), pp. 833–838. DOI: 10.1080/02640414.2018.1530057. URL: https://doi.org/10.1080/02640414.2018.1530057.

[20] J. Poertner. “Part 4B: Rolling Resistance and Impedance”. In: *SILCA* (Sept. 2022). URL: https://silca.cc/blogs/silca/part-4b-rolling-resistance-and-impedance.

[21] T. Gillespie. *Fundamentals of Vehicle Dynamics*. SAE International, 1992, pp. 110–118.

[22] A. Dressel. *Rolling Resistance for Special Topic in Sports Engineering*. June 2022.

[23] Schwalbe. *what exactly is rolling resistance?* [Online; accessed Dec. 2022]. URL: https://www.schwalbe.com/en/rollwiderstand.

[24] S.A. Velinsky and R.A. White. “Vehicle Energy Dissipation Due to Road Roughness”. In: *Vehicle System Dynamics* 9.6 (1980), pp. 359–384. DOI: 10.1080/00423118008968630.

[25] A.C. Lim et al. “Measuring changes in aerodynamic/rolling resistances by cycle-mounted power meters”. In: *Med. Sci. Sports Exerc.* 43.5 (May 2011), pp. 853–860. DOI: 10.1249/MSS.0b013e3181fcb140.

[26] FLO cycling. *Understanding Rolling Resistance & Impedance For Cyclists*. Apr. 2021. URL: https://blog.flocycling.com/aero-wheels/understanding-rolling-resistance-impedance-for-cyclists.

[27] Paolo Baldissera and Cristiana Delprete. “Rolling resistance, vertical load and optimal number of wheels in human-powered vehicle design”. In: *Proceedings of the Institution of Mechanical Engineers, Part P: Journal of Sports Engineering and Technology* 231.1 (Aug. 2016), pp. 33–42. DOI: 10.1177/1754337115625002. URL: https://doi.org/10.1177/1754337115625002.

[28] Dayi Zhang et al. “Compression mechanics of nickel-based superalloy metal rubber”. In: *Materials Science and Engineering: A* 580 (Sept. 2013), pp. 305–312. DOI: 10.1016/j.msea.2013.05.064.

[29] B.M. Redrouthu and S. Das. *Tyre modelling for rolling resistance*. [Master thesis]. 2014. URL: https://publications.lib.chalmers.se/records/fulltext/200040/200040.pdf.

[30] M.S. Sichani. *On Efficient Modelling of Wheel-Rail Contact in Vehicle Dynamics Simulation*. [Doctoral thesis]. 2016. URL: https://www.diva-portal.org/smash/get/diva2:899731/FULLTEXT01.pdf.

[31] E. Moyer. *Air resistance and rolling resistance losses*. Tech. rep. May 2014. URL: https://geosci.uchicago.edu/~moyer/GEOS24705/Readings/Air_and_rolling_resistance.pdf.

[32] Global Cycling Network. *What Is The Fastest Tyre Pressure For Road Bikes?* Jan. 2023. URL: https://www.youtube.com/watch?v=6rMnNI2RCgw.

[33] M. Munera, X. Chiementin, and W. Bertucci. “Mechanical equivalent model of vibration transmission in cycling”. In: *Computer Methods in Biomechanics and Biomedical Engineering* 16.sup1 (July 2013), pp. 86–87. DOI: 10.1080/10255842.2013.815850.

[34] Y. Champoux, J. Vanwallenghem, and J. M. Drouet. “Dynamic Calibration of an Instrumented Bike Brake Hood in Measuring Power Absorbed by the Hands”. In: *Procedia Engineering* 112 (2015), pp. 225–230. DOI: 10.1016/j.proeng.2015.07.204.

[35] T. Anhalt. *What’s in a tube?* Sept. 2009. URL: https://www.slowtwitch.com/Tech/What_s_in_a_tube__1034.html.

[36] J. Heine. *The Missing Piece: Suspension Losses*. Aug. 2016. URL: https://www.renehersecycles.com/the-missing-piece-suspension-losses/.

[37] Joachim Vanwalleghem. *Study of the damping and vibration behaviour of flax-carbon composite bicycle racing frames*. [Master thesis]. 2010. URL: https://libstore.ugent.be/fulltxt/RUG01/001/418/457/RUG01-001418457_2010_0001_AC.pdf.

[38] F. Grappe et al. “Influence of tyre pressure and vertical load on coefficient of rolling resistance and simulated cycling performance”. In: *Ergonomics* 42.10 (Oct. 1999), pp. 1361–1371. DOI: 10.1080/001401399185009.

[39] J. Bierman. *CRR Load Test | Bicycle Rolling Resistance*. Apr. 2022. URL: https://www.bicyclerollingresistance.com/specials/crr-load-test.

[40] SILCA. *Part 2: Tire Stiffness (Wider is Stiffer/Harsher?)* Sept. 2021. URL: https://silca.cc/blogs/silca/part-2-tire-stiffness-wider-is-stiffer-harsher.

[41] Lennard Zinn. *Technical FAQ: Tire rolling-resistance testing methodology and verification*. Jan. 2022. URL: https://www.velonews.com/gear/technical-faq-tire-rolling-resistance-testing-methodology-and-verification/.

[42] Lennard Zinn. “Technical FAQ: The science of tire pressure, rim width, and heat buildup”. In: *VeloNews* (Sept. 2021). URL: https://www.velonews.com/gear/technical-faq-science-tire-pressure-rim-width-heat-buildup.

[43] D.J. de Boer. *Modeling a Professional Road Cycling Race To Determine the Fastest Wheel-Tire Combination*. [Master thesis]. 2022.

[44] L.G. Andersen. *Rolling Resistance Modelling: From Functional Data Analysis to Asset Management System*. [PhD Dissertation]. 2015.

[45] U. Sandberg et al. *Rolling Resistance - Measurement Methods for Studies of Road Surface Effects*. Tech. rep. Feb. 2012. URL: https://www.diva-portal.org/smash/get/diva2:1505233/FULLTEXT01.pdf.

[46] R. Karlsson et al. *Road surface influence on rolling resistance*. Tech. rep. Nov. 2011. URL: http://www.diva-portal.org/smash/get/diva2:669244/FULLTEXT01.pdf.

[47] P. Múčka. “International Roughness Index specifications around the world”. In: *Road Materials and Pavement Design* 18.4 (June 2016), pp. 929–965. DOI: 10.1080/14680629.2016.1197144.

[48] Andrew. *How does Hysteresis in tires helps create friction?* Jan. 2018. URL: https://engineering.stackexchange.com/questions/18762/how-does-hysteresis-in-tires-helps-create-friction.

[49] C. Hölzel, F. Höchtl, and V. Senner. “Cycling comfort on different road surfaces”. In: *Procedia Eng.* 34 (2012), pp. 479–484. DOI: 10.1016/j.proeng.2012.04.082.

[50] J. Heine. *How to Test Tire Performance*. May 2018. URL: https://www.renehersecycles.com/testing-tires-isnt-easy/.

[51] SRAM. *LIFE ON THE ROLLINGROAD*. Dec. 2021. URL: https://www.sram.com/en/life/stories/life-on-the-rollingroad.

[52] ZIPP. *THE WORLD’S TOUGHEST TRAINER RIDE?* Mar. 2022. URL: https://www.sram.com/en/zipp/zipp-media/the-worlds-toughest-trainer-ride.

[53] Tracee Meyers. *Trek’s custom treadmill*. Dec. 2019. URL: https://www.woodway.com/treks-custom-treadmill.

[54] Trek Performance Research. *Trek’s custom treadmill - Trek Blog | Trek Bikes*. Sept. 2019. URL: https://blog.trekbikes.com/en/2019/08/27/treks-custom-treadmill.

[55] Alee Denham. *Lab Test: Lowering Your Tyre Pressure Will Greatly Improve Your Bike’s Comfort*. July 2023. URL: https://www.cyclingabout.com/lab-test-lowering-tyre-pressure-improve-bike-comfort.

[56] P. E. Di Prampero et al. “Equation of motion of a cyclist”. In: *Journal of Applied Physiology* 47.1 (July 1979), pp. 201–206. DOI: 10.1152/jappl.1979.47.1.201. URL: https://doi.org/10.1152/jappl.1979.47.1.201.

[57] Carlo Capelli et al. “Energy cost and efficiency of riding aerodynamic bicycles”. In: *European journal of applied physiology and occupational physiology* 67.2 (Aug. 1993), pp. 144–149. DOI: 10.1007/bf00376658. URL: https://doi.org/10.1007/bf00376658.

[58] Paul W. Macdermid, Philip W. Fink, and Stephen R. Stannard. “The influence of tyre characteristics on measures of rolling performance during cross-country mountain biking”. In: *Journal of Sports Sciences* 33.3 (July 2014), pp. 277–285. DOI: 10.1080/02640414.2014.942682. URL: https://doi.org/10.1080/02640414.2014.942682.

[59] Simone Tengattini and Alexander Bigazzi. “Physical characteristics and resistance parameters of typical urban cyclists”. In: *Journal of Sports Sciences* 36.20 (Mar. 2018), pp. 2383–2391. DOI: 10.1080/02640414.2018.1458587. URL: https://doi.org/10.1080/02640414.2018.1458587.

[60] Simone Tengattini and Alexander Bigazzi. “Validation of an outdoor Coast-Down test to measure bicycle resistance parameters”. In: *Journal of transportation engineering* 144.7 (July 2018). DOI: 10.1061/jtepbs.0000152. URL: https://doi.org/10.1061/jtepbs.0000152.

[61] Andrew Dressel. “Measuring and Modeling the Mechanical Properties of Bicycle Tires”. In: *The University of Wisconsin-Milwaukee* (Jan. 2013). URL: https://dc.uwm.edu/etd/386/.

[62] Andrew Dressel and James Sadauckas. “Characterization and modelling of various sized mountain bike tires and the effects of tire tread knobs and inflation pressure”. In: *Applied sciences* 10.9 (May 2020), p. 3156. DOI: 10.3390/app10093156. URL: https://doi.org/10.3390/app10093156.

[63] D Woodward et al. *The static contact patch of some friction measuring devices*. Tech. rep. 2013.

[64] S. Portas and M. Pau. “NOVEL EXPERIMENTAL CHARACTERIZATION OF THE TIRE-PAVEMENT SYSTEM”. In: 2007.

[65] Samuel Kelly Clark. “ROLLING RESISTANCE FORCES IN PNEUMATIC TIRES”. In: *National Technical Information Service* (Jan. 1976). URL: https://rosap.ntl.bts.gov/view/dot/9695.

[66] Anthony Martyr and M.A. Plint. *Chassis or Rolling-Road dynamometers*. Jan. 2012, pp. 451–482. DOI: 10.1016/b978-0-08-096949-7.00017-0. URL: https://doi.org/10.1016/b978-0-08-096949-7.00017-0.

[67] *DURA-ACE Dual-Sided Power Meter HOLLOWTECH II Crankset 2x12-speed | SHIMANO BIKE-EU*. [Online; accessed 14. Dec. 2023]. Dec. 2023. URL: https://bike.shimano.com/en-EU/product/component/dura-ace-r9200/FC-R9200-P.html.

[68] *ELEMNT ROAM v2 GPS Bicycle Computer Bundle*. [Online; accessed 14. Dec. 2023]. Dec. 2023. URL: https://eu.wahoofitness.com/devices/bike-computers/elemnt-roam-bundle-buy.

[69] Yuho Shimizu. “Multiple desirable methods in outlier detection of univariate data with R source codes”. In: *Frontiers in Psychology* 12 (Jan. 2022). DOI: 10.3389/fpsyg.2021.819854. URL: https://doi.org/10.3389/fpsyg.2021.819854.

[70] Rand R. Wilcox. *Introduction to robust estimation and hypothesis testing*. Academic Press, Sept. 2016, pp. 45–106.

[71] Marko Sarstedt and Erik Mooi. *A Concise Guide to Market Research*. July 2018, pp. 209–256. DOI: 10.1007/978-3-662-56707-4\{_}7.

[72] Gülden Kaya Uyanık and Neşe Güler. “A study on multiple linear regression analysis”. In: *Procedia - Social and Behavioral Sciences* 106 (Dec. 2013), pp. 234–240. DOI: 10.1016/j.sbspro.2013.12.027.

[73] M. Tranmer et al. *Multiple Linear Regression (2nd Edition)*. 2020. URL: https://hummedia.manchester.ac.uk/institutes/cmist/a%20rchive-publications/working-papers/2020/2020-1-%20multiple-linear-regression.pdf.

[74] Lynn E. Eberly. *Methods in molecular biology*. Jan. 2007, pp. 165–187. DOI: 10.1007/978-1-59745-530-5\{_}9. URL: https://doi.org/10.1007/978-1-59745-530-5_9.

[75] Jason W. Osbourne and Elaine Waters. “Four assumptions of multiple regression that researchers should always test.” In: *Practical Assessment, Research and Evaluation* 8.2 (Jan. 2002), pp. 2–. DOI: 10.7275/r222-hv23.

[76] Douglas Lind, William Marchal, and Samuel Wathen. *Statistical techniques in business and economics*. McGraw-Hill/Irwin, Jan. 2011.

[77] K.H. Dijkman. *Tire influence on energy loss during cycling*. [Literature Review]. 2023.